Lehrstuhl für Experimentalphysik E21

Investigation of interlayer exchange coupling in ferro-/antiferro-/ferromagnetic trilayers

Christian Schanzer

Vollständiger Abdruck der von der Fakultät für Physik der Technischen Universität München zur Erlangung des akademischen Grades eines

Doktors der Naturwissenschaften

genehmigten Dissertation.

Vorsitzender: Univ.-Prof. Dr. M. Kleber

Prüfer der Dissertation:

1. Univ.-Prof. Dr. P. Böni

2. Univ.-Prof. Dr. R. Gross

Die Dissertation wurde am 20.10.2005 bei der Technischen Universität München eingereicht und durch die Fakultät für Physik am 28.03.2006 angenommen.

Thesis Outline

Interfaces between ferromagnetic and antiferromagnetic layers have shown a variety of intriguing features like unidirectional anisotropy leading to exchange bias, enhancement of coercivity, rotational hysteresis etc.. When an antiferromagnet is sandwiched between two ferromagnetic layers a nonvanishing exchange interaction between the two ferromagnets has been observed. Theoretically, the existence of a non-collinear magnetic structure in the antiferromagnetic spacer has been proposed. Previous investigations deduced a linear dependence of the turn-angle between the magnetization of the ferromagnetic layers on the thickness of the antiferromagnet from bulk magnetization measurements. These experiments provided indirect evidence for a spiraling of the moments within the antiferromagnetic spacer.

The aim of the present work is to investigate the role of an antiferromagnet in mediating exchange interaction between two adjacent ferromagnetic layers as a function of the thickness of the antiferromagnetic spacer layer. In contrast to previous work, we probed directly the magnetization reversal of individual ferromagnetic layers using polarized neutron reflectometry with polarization analysis in order to obtain an insight into the mechanism of interlayer coupling.

For this purpose, we prepared samples of FeCoV (20 nm)/NiO (t_{NiO})/FeCoV (20 nm) trilayers with FeCoV as the ferromagnet and NiO as the antiferromagnet. The trilayer series covers a range of NiO thickness from 1.5 to 100 nm. Additionally, NiO and FeCoV single layers and FeCoV/NiO and NiO/FeCoV bilayers were produced to investigate systematically the individual properties of the layers and interfaces, which constitute the trilayer samples. All samples were deposited using DC magnetron sputtering while a reactive Ar:O_2 atmosphere was used to deposit NiO from a Ni metal target. In the series of NiO layers the composition of the sputter atmosphere was varied to find optimum conditions to obtain stoichiometric NiO with (111) out-of-plane texture. The stoichiometry and the texture were determined from the critical angle of X-ray total reflection and the X-ray diffraction pattern, respectively. Based on these results, NiO-FeCoV bilayers and FeCoV/NiO/FeCoV trilayers were prepared.

X-ray diffraction and reflectometry were applied to characterize the structure of the samples. The X-ray diffraction measurements show that the out-of-plane texture of the NiO layers depends on the underlying material. Predominant (111) texture is found for the NiO layers deposited on glass substrates as expected from the chosen preparation conditions. When NiO is grown on top of FeCoV, grains with (200) texture are present in addition. The out-of-plane texture of FeCoV layers is always (110). X-ray reflectivity measurements were employed to probe the chemical depth profiles of the multilayer samples. A detailed layer structure of the samples was deduced from the refinement of models of the depth profile. The models were developed systematically from FeCoV single layers to trilayers via NiO-FeCoV bilayers. Due to this systematic procedure, finer details about layer thickness, interface roughness, interfacial layers and surface oxidation were unraveled. The structural characterization confirms the consistent and

high quality of the samples prepared by DC magnetron sputtering.

Bulk magnetic properties of FeCoV single layers, bilayers and trilayers were obtained from DC magnetization measurements. Hysteresis loops were measured along different directions in the plane of the samples in order to determine coercive fields and to obtain any net magnetic in-plane anisotropy. In addition to experiments at room temperature, measurements were performed at temperatures T = 2, 400 and 530 K as well, for the investigation of the temperature dependence of magnetization reversal. At T = 530 K ($> T_N$), in the paramagnetic state of NiO, the magnetic properties of ferromagnetic layers in bilayers and trilayers were obtained without the contribution of interfacial exchange from antiferromagnetic NiO.

The single layers of FeCoV provide intrinsic magnetic properties of free FeCoV layers isolated from other magnetic layers. They show isotropic magnetic properties in the plane of the films with a relatively high coercivity compared to bulk. It is inferred that the magnetic properties are a consequence of a random distribution of local stress causing high local magnetic anisotropies because of the large magnetostriction of FeCoV. In addition, FeCoV layers with different layer thicknesses were investigated to test the sensitivity of the magnetic properties on the layer thickness. A variation of coercivity is found, which can be properly explained in terms of the random anisotropy model.

Separate information about the magnetic properties of the bottom FeCoV layer in the trilayers including the influence of antiferromagnetic NiO on top was obtained from the series of FeCoV/NiO (t_{NiO}) bilayers. At room temperature, the hysteresis loops of the bilayers are very similar to that of the FeCoV single layers indicating that the magnetic properties of the FeCoV/NiO bilayers are governed by the intrinsic properties of the ferromagnetic layer. Only a weak influence of the antiferromagnet is observed in the case of a thick NiO spacer layer, which manifests itself as small exchange bias. The influence of NiO becomes prominent at low temperature enhancing the exchange bias significantly. It is found that the direction of pinning is defined by the orientation of the magnetization of the ferromagnet during cooling. This result suggests that the ferromagnet causes a reorientation of the antiferromagnetic spins, which are stabilized when samples are cooled to low temperature.

NiO (t_{NiO})/FeCoV bilayers represent the upper part of the trilayer motif. These samples show a distinct magnetic anisotropy and rather low coercivity at room temperature, which is significantly different to FeCoV single layers and FeCoV/NiO bilayers. Weak exchange bias is observed for thick NiO layers. At low temperatures, significant exchange bias was measured for all thicknesses of the NiO layer. The unidirectional anisotropy could be tuned along either direction of the anisotropy axis dependent on the orientation of the ferromagnet during cooling, similar to the series of FeCoV/NiO bilayers. For paramagnetic NiO ($T > 523$ K) the easy axis of magnetization is observed perpendicular to the direction of the easy axis for antiferromagnetic NiO suggesting that the anisotropy below T_N is induced by the NiO layer and transferred to the FeCoV layer via exchange coupling across their common interface. From these results, it is inferred that at room temperature the antiferromagnetic spins are rotated between the two possible orientations of their uniaxial anisotropy axis initiated by the reversal of

the exchange coupled ferromagnet. At low temperature, the antiferromagnetic spins become stabilized inducing exchange bias.

The MH-loops of FeCoV/NiO (t_{NiO})/FeCoV trilayers show a strong dependence of the magnetization reversal on the thickness of the NiO spacer layer. For $t_{NiO} \leq 10$ nm, the reversal occurs via a single gradual transition whereas for $t_{NiO} \geq 20$ nm, the MH-loops exhibit two steps during the magnetization reversal. The first step shifts towards lower applied fields for increasing thickness of the NiO spacer layer. The second step remains constant at an applied field similar to the coercive field of the FeCoV single layer. For $t_{NiO} \geq 40$ nm, the intermediate plateau in between the two steps has almost zero net magnetization. The two step process is present unless NiO becomes paramagnetic. At $T = 530$ K the magnetization reversal for $t_{NiO} \geq 40$ nm occurs also in a single gradual process. At $T = 2$ K, trilayers with $t_{NiO} \geq 40$ nm shows exchange bias similar to the NiO-FeCoV bilayers whereas for trilayers with $t_{NiO} \leq 10$ nm almost no exchange bias is observed.

In order to resolve the magnetization reversal of individual ferromagnetic layers of the FeCoV/NiO/FeCoV trilayers, polarized neutron reflectometry with polarization analysis was employed. Measurements were performed on selected samples representing the different regimes observed in bulk magnetic measurements. The obtained reflectivity profiles were modeled, based on the detailed chemical layer structure deduced from X-ray reflectivity data and adjusting the magnetization vectors of each FeCoV layer. First measurements were performed at magnetic saturation of the samples providing the saturation magnetization of the individual FeCoV layers on an absolute scale. Consistently, for all samples a magnetic moment of FeCoV of $2.1\mu_B$ per f.u. was obtained. Of particular interest are the configurations of the magnetization vectors during the magnetization reversal. Therefore, the polarization dependent reflectivity profiles were measured at selected fields during the magnetization reversal. The obtained layer resolved magnetization shows that at small thicknesses of the NiO spacer the magnetization of the FeCoV layers reverse in a combined way, i.e. within an identical range of applied field. For thick NiO spacer layers the top FeCoV layer reverses first at a low field, followed by the bottom layer at a higher field. In between these two switching fields, the magnetization of top and bottom FeCoV layers are aligned antiparallel to each other.

In summary, the experimental results provide evidence for interfacial coupling across the interfaces between NiO and FeCoV layers. In particular, the observation of exchange bias at low temperature and the reorientation of the anisotropy axis in NiO/FeCoV bilayers when NiO becomes paramagnetic support this. The absence of exchange bias at room temperature can be explained because the antiferromagnetic spins rotate irreversibly with the magnetization of the ferromagnetic layer. At low temperatures, the antiferromagnetic spin structure becomes more rigid and exchange bias sets on. The contribution of the internal spins of the antiferromagnet is inferred from the comparison of trilayers and bilayers with $t_{NiO} \leq 10$ nm at $T = 2$ K. In contrast to bilayers, exchange bias is not observed for these trilayers. This observation is understood as that the reversal of both ferromagnetic layers drags also the spins of the antiferromagnet at both interfaces leading to a rotation of all antiferromagnetic

spins along the layer thickness as a unit and erasing the mechanism for exchange bias. An exchange coupling of the ferromagnetic layers for $t_{NiO} \leq 20$ nm is evident from the results of polarized neutron reflectometry. These reveal that the magnetization of the bottom FeCoV layer is further reversed compared to FeCoV single layers and FeCoV/NiO bilayer at identical applied field. For $t_{NiO} \geq 40$ nm, the magnetization of the ferromagnetic layers can be tuned to an antiparallel orientation by applying a adequate magnetic field manifesting a dependence of the interlayer exchange coupling on the thickness of the NiO spacer layer.

The experimental observations can be understood within the framework of theoretical postulations of Xi and White who discuss the interlayer exchange coupling between two ferromagnetic layers separated by an antiferromagnetic layer. They predict a twist of the antiferromagnetic spins when one ferromagnetic layer reverses while the other remains rigid. Depending on the strength of interfacial coupling with respect to the domain wall energy of the antiferromagnet and the ratio of thickness and domain wall width of the antiferromagnet, different scenarios are possible for the evolution of a spin twist in the antiferromagnetic spacer. Applying the ideas of Xi and White with a qualitative extension by introducing different but finite rigidity of both ferromagnetic layers, can explain the experimental observations on FeCoV/NiO/FeCoV trilayers in the present work. For thin NiO spacer layers the antiferromagnetic spins are rigid mediating a strong coupling between the ferromagnetic layers. When the thickness of NiO increases, a twist of the antiferromagnetic spins is created during the magnetization reversal of the ferromagnetic layers. For $t_{NiO} \geq 40$ nm, a complete 180° domain wall can be accommodated in the NiO spacer facilitating the observed antiparallel configuration of the magnetization of the ferromagnetic layers.

Contents

Chapter 1

Introduction

Interlayer exchange coupling between two ferromagnetic layers mediated by materials like metals, semiconductors, insulators etc. has been a fascinating topic in the recent years. The properties of such nanostructures often cannot be predicted from the individual properties of their bulk counterparts. Furthermore, the combination of materials in multilayers can result in different properties than expected from the cumulative properties of the constituent materials as a thin layer. It is even possible to tailor the properties of nanostructures in a wide range, which provides interesting physics and innovative ideas for a new generation of magnetic storage devices, magnetic field sensors and state of the art spintronic devices [1].

In general, the nature of interlayer exchange coupling depends on the type of spacer material and its thickness. In combinations of ferromagnetic and non-magnetic metals, exchange coupling was clearly first demonstrated by Grünberg et al. in multilayers of Fe/Cr [2]. Subsequently, Parkin et al. found an oscillatory behavior between ferro- and antiferromagnetic coupling dependent on the thickness of the non-magnetic spacer layer [3]. The interaction between the ferromagnetic layers is mediated by the itinerant electrons of the spacer layer and the oscillatory behavior is explained quite satisfactorily in terms of the Ruderman-Kittel-Kasuya-Yosida (RKKY) type of exchange interaction and the critical spanning vectors of the Fermi surface of the spacer layer [2, 4]. In addition, these multilayers show a significant difference of the electrical resistance depending on the relative orientation of the magnetization of adjacent ferromagnetic layers, which is known as giant magneto-resistance (GMR) [5]. Usually, the resistance is low for a parallel configuration of magnetization of the ferromagnetic layers but it is relatively high for an antiparallel alignment. In combination with the oscillatory nature of the exchange interaction, ferro/non-magnetic multilayers have found application in GMR read-heads which have had a significant impact on magnetic data storage.

Later, it was discovered that the use of insulating spacer layers (like MgO, Al_2O_3, etc.) in the tunneling regime (layer thickness $\approx$ few Å), would lead to a further enhancement of the magneto-resistance [6, 7]. The mechanism of exchange coupling across insulators can be understood as spin-polarized tunneling [8]. The tunneling occurs only for a very small thickness of the spacer layer since the tunneling current decays exponentially as the spacer thickness increases. The strength of the exchange coupling correspondingly decays exponentially with increasing spacer thickness. Faure-Vincent et al. found in Fe/MgO (t_{MgO})/Fe/Co tunnel junctions with $t_{MgO} = 0.45 - 1.7$ nm that the nature

of coupling changed with increasing thickness of the spacer layer at $t_{MgO} \approx 0.8$ nm from an antiferromagnetic to a ferromagnetic type [8]. However, no oscillatory type of exchange interaction has been observed in insulating spacer layers. Devices based on the tunneling magneto-resistance (TMR) are envisaged for being implemented in a magnetic random access memory (MRAM), which is non-volatile and thus expected to bring significant improvements over the conventional RAM.

An intermediate scenario is realized in a semi-conducting spacer layer. Using $Fe_{1-x}Si_x$ as a spacer layer, Grünberg et al. found a mixed type of exchange interaction between two Fe layers [9]. With increasing Si concentration the exchange coupling changed from an oscillatory behaviour to an exponentially decaying one. The study of ferromagnet-semiconductor interfaces and dilute magnetic semiconductors (DMS) is currently a hot topic as such systems are envisaged to play a key role in prospective spintronic devices that make use of the electron's charge and spin degree of freedom [10].

Another class of materials are antiferromagnets, which are of enormous interest because of the phenomenon of exchange bias when a ferromagnet is interfaced to an antiferromagnet, e.g. as thin films. Antiferromagnets can be either insulators like NiO, CoO or metals, e.g. FeMn, IrMn. Exchange bias was discovered in 1956 by Meiklejohn and Bean on small Co particles with a CoO shell [11]. They reported '*A new type of magnetic anisotropy has been discovered which is best described as an exchange anisotropy. This anisotropy is the result of an interaction between an antiferromagnetic material and a ferromagnetic material*'. The most typical feature of exchange bias is a shifted or biased hysteresis loop, i.e. the loop is not centered at zero field.

Phenomenologically, exchange bias is described as follows: Starting from the paramagnetic phase of the antiferromagnet above its Néel temperature T_N, the system of ferro-/antiferromagnet is cooled while the magnetization of the ferromagnet ($T_C > T_N$) is saturated by an applied magnetic field. When the antiferromagnetic spin structure establishes itself, the spins of the antiferromagnet at the interface are forced to align parallel to the adjacent spins of the ferromagnet. Due to the direct exchange coupling between the interfacial moments of ferro- and antiferromagnet, the moments of the antiferromagnet introduce a torque and hinder the rotation of the ferromagnetic moments during the magnetization reversal when the applied field is opposite to the cooling field direction. When the ferromagnet is rotated towards the direction of the cooling field, this torque assists the external field, resulting in an early reversal of the magnetization of the ferromagnet. As a result, the MH-loop of the ferromagnet is shifted along the field axis opposite to the cooling field direction. This is known as negative exchange bias and is characterized by the bias field H_{eb}. This phenomenological model assumes ideally flat, epitaxial films with a fully uncompensated spin structure of the antiferromagnet at the interface, i.e. all interfacial spins of the antiferromagnet are aligned parallel forming a ferromagnetic sheet. Perpendicular to the plane of the layer adjacent ferromagnetic sheets in the antiferromagnet are ordered antiparallel. Usually, the onset of exchange bias is observed below a temperature T_B (blocking temperature), which is lower than T_N of the bulk antiferromagnet. It is suspected that $T_B < T_N$ is related, at least partially, to finite size effects, introduced by small layer thickness and grain size of the antiferromagnet [12]. Exchange bias of the ferromagnet/antiferromagnet interface

is exploited to pin one ferromagnetic layer in the artificially engineered GMR heads (spin-valves), while the other layer is free to align with the external magnetic field.

Even after four decades since its discovery, the quantitative description of the exchange bias phenomenon remains a theoretical challenge. A quantitative prediction of the bias field from the phenomenological model of direct exchange at the interface yields values, which are two orders of magnitude larger than the experimental values [13]. In order to account for this discrepancy, the formation of domain walls in the ferromagnet or in the antiferromagnet was postulated. According to this view, not only interface moments of the layers are involved but also the internal spin structure is affected during magnetization reversal.

Mauri et al. [14] and Kiwi et al. [15] predicted the formation of planar or partial domain walls parallel to the interface (figure 1.1a) in both, antiferromagnet and ferromagnet, respectively. In such a case, the potential barrier to overcome for the magnetization reversal is determined by the energy of the antiferromagnetic domain wall. Hence, the exchange energy between ferro- and antiferromagnet is lowered since it is spread over several spins of the planar domain wall instead of only two spins as in the phenomenological model. In contrast to the previous models, Malozemoff considered that the interfacial spin structure of the antiferromagnet to be not fully uncompensated [16]. He proposed a random field model where the interface is only partially uncompensated due to roughness and defects. These interfacial inhomogeneities give rise to random fields acting at the interface. The random fields initiate the formation of lateral domains (figure 1.1b) in the antiferromagnet to minimize the interfacial energy. The interfacial energy decreases with increasing domain size, which is in competition with in-plane anisotropies of the antiferromagnet confining the domain size. As a result of this competition, domains of particular size are stabilized. In addition, the random field theory explains the training of exchange bias, i.e. the decrease of the bias field with increasing number of field cycles, as an annihilation of domains. In both models, either the formation of the domain wall parallel to the plane of the layers or the formation of lateral domains predict a reduction of the interface energy yielding exchange bias fields of the same order as obtained in experiments.

However, until recently, there was no experimental evidence for the formation of antiferromagnetic domain walls at the ferro-/antiferromagntic interfaces. Scholl et al. using X-ray magnetic linear dichroism technique (XMLD) in Co/NiO [17] demonstrated that indeed the antiferromagnetic spins would be twisted internally and that the twist angle could be varied by rotating the magnetization of the Co layer by applying an external magnetic field. These experiments hint at the fact that the internal spin structure of the antiferromagnet is affected by the interface exchange coupling between the ferro- and antiferromagnet.

In the extended system of trilayers, the antiferromagnet is sandwiched between two ferromagnetic layers, being the subject of the present work. Previous investigations using various ferromagnets (Fe, Co, Py etc.) and antiferromagnets (CoO, NiO, FeMn) revealed a rich variety of phenomena [18, 19, 20, 21, 22]. Both metallic and insulating antiferromagnets showed a non-vanishing exchange interaction between the two ferro-

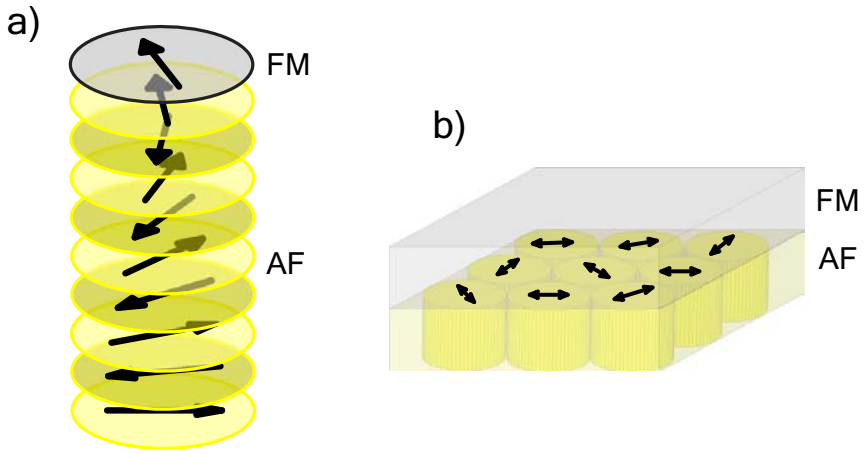

Figure 1.1: Illustration of the domain formation in the antiferromagnetic layer (AF) during the magnetization reversal of the ferromagnet (FM): a) planar (partial) domain wall and b) lateral domains.

magnetic layers.

Liu and Adenwalla investigated trilayers of $[Pt/Co]_3/NiO/[Co/Pt]_3$ in a regime of thin NiO layers $0.9 < t_{NiO} < 2.3$ nm [22]. The $[Pt/Co]_3$ multilayer blocks of this system had an out-of-plane anisotropy with different coercivities of the block on top and at the bottom of NiO. They deduced the strength of the interlayer coupling by measuring minor MH-loops of the layer block on top of NiO. The bias of the minor loop indicates the strength of the coupling. They observed an oscillation of the coupling as function of NiO thickness between a ferromagnetic and a antiferromagnetic type with a period of ≈ 0.5 nm. In addition, they found that the strength of the coupling decreases with increasing NiO thickness. Due to the (111) out-of-plane texture of their NiO layers, uncompensated sheets with opposite directions of magnetic moments alternate along the thickness of the NiO spacer. The observed oscillation period is roughly the same as twice the distance of NiO (111) planes. Subsequently, it was inferred that the relative orientation of the magnetization of the ferromagnets and therefore the type of coupling is defined by the relative orientation of the terminating spins at either side of the antiferromagnet [23]. These results indicate a rigid spin structure of the antiferromagnet during the magnetization reversal of the ferromagnetic layers and exchange coupling is described only as confined to the interfacial spins.

Further, Ernult et al. examined the coupling of ferromagnetic Co layers across a larger range of thickness of the NiO spacer [20]. In their work, one Co layer was part of Co/Cu/NiFe spin valve structure. They measured MH-loops and the magnetoresistance on a series of samples with varying NiO thickness up to $t_{NiO} = 20$ nm. From the combined analysis of MH-loops and magnetoresistance measurements, they deduced the orientation of magnetization of individual Co layers. They found that the Co layers are coupled ferromagnetically across the NiO spacer in the whole range of thickness.

Theoretical investigations on the role of an antiferromagnet in mediating interlayer

exchange in ferro-/antiferro-/ferromagnetic thin films are available in literature predicting interesting features [24, 25, 26]. The formation of a planar antiferromagnetic domain wall during the reversal of an adjacent exchange coupled ferromagnetic layer was treated by Stiles and McMichael [27] and by Xi and White [28]. Both discussed possible scenarios in dependence on the energy of the interfacial coupling relative to the energy of the antiferromagnetic domain wall as well as on the thickness of the antiferromagnetic layer relative to its domain wall width. Xi and White consider in [26] the configuration of two ferromagnetic layers exchange coupled across an antiferromagnetic spacer. The authors constructed magnetic phase diagrams characterizing the response of the internal spin structure of the antiferromagnet on the magnetization reversal of one ferromagnetic layer while the other remains rigid. In all phases a twist of the antiferromagnetic spins occurs, at least to a certain extent. The maximum twist depends on the strengths of the coupling at either interface, on the domain wall energy of the antiferromagnet and the thickness of the antiferromagnet relative to its domain wall width. It may occur that the coupling at one interface is weak and it breaks up when the twist of the antiferromagnetic spins would exceed a certain limit. In such a case, the antiferromagnetic spin structure can either return to its original equilibrium state or it springs to a new equilibrium. A particular situation exists for strong interfacial coupling at either side, i.e. the interfacial energies are larger than the domain wall energy. This configuration allows a twist of the antiferromagnetic spins beyond 180°. Hence, the ferromagnetic layers can align antiparallel while a complete planar domain wall is accommodated in the antiferromagnet.

The dependence of interlayer exchange coupling between adjacent ferromagnetic layers on the thickness of a metallic antiferromagnetic spacer layer in ferro-/antiferro-/ferromagnetic trilayers has been investigated by Yang and Chien [19]. A series of trilayers Py (20 nm)/FeMn (t_{FeMn})/Co (10 nm) with $t_{FeMn} = 5.3 - 15$ nm were field cooled from above the Néel temperature of the antiferromagnet down to room temperature. Consecutive bulk magnetic measurements revealed a dependence of the hysteresis loop on t_{FeMn}. They measured MH-loops along various direction, which enabled them to deduce the angles between the two ferromagnetic layers. In fact, the authors derived an empirical relation between the relative angle of the magnetization of the ferromagnet θ and the thickness of the antiferromagnet as $\theta = 0.176°/\text{nm} \cdot t_{FeMn}$, for $5.3 \leq t_{FeMn} \leq 9$ nm. At larger values of the thickness, θ remained constant at 180 °. This result suggests that the antiferromagnet plays an important role in mediating the interlayer exchange coupling, presumably by accommodating a spin twist within the antiferromagnet layer. In addition, they concluded the width of the antiferromagnetic domain wall of FeMn as 9 nm since beyond this limit the magnetization of the ferromagnetic layer can be aligned antiparallel applying a proper magnetic field.

Yang and Chien employed a macroscopic and indirect method to establish the interlayer coupling across the antiferromagnet by means of formation of a partial antiferromagnetic domain wall. Moreover, from the theoretical studies mentioned above, it is evident that formation of a partial domain wall in the antiferromagnet is a more complex scenario. The domain wall formation critically depends on the strength of exchange interactions, individually at both interfaces between the antiferromagnet and the ferromagnetic layers and their strength relative to the energy of the anti-

ferromagnetic domain wall as well. The observation of Yang and Chien is perhaps one of the many possibilities foreseen by the theoretical investigations. Therefore, it becomes necessary for a systematic and quantitative investigation, separately for antiferro-/ferromagnetic interfaces in bilayers with either sequence of deposition of the materials, a layer resolved investigation of the magnetization reversal of the ferromagnets in trilayers, element resolved magnetic properties of the antiferromagnetic layer etc. to get an insight into the physical phenomenon and to explain the observed dependence of the magnetization reversal on the thickness of the antiferromagnetic spacer in ferro-/antiferro-/ferromagnetic trilayer systems.

The aim of the present work is to investigate the role of antiferromagnetic spins in mediating exchange coupling between ferromagnetic layers in ferro-/antiferro-/ferromagnetic trilayers. It is supposed that the antiferromagnetic spins twist when the magnetization of one ferromagnetic layer reverses but the other remains still in its original orientation. In order to achieve a high twist angle of the antiferromagnetic spin structure, strong interfacial coupling is required [26]. Since interfacial coupling between ferro- and antiferromagnets is high for materials with large magnetic moments and high ordering temperatures (T_C, T_N) [28], ferromagnetic FeCoV and antiferromagnetic NiO are good candidates for our investigations. The interlayer exchange coupling in FeCoV/NiO/FeCoV trilayers is studied dependent on the thickness of the NiO spacer to reveal the evolution of the antiferromagnetic spins participating during the magnetization reversal of the ferromagnetic layers. Since the domain wall width of NiO as a thin film is reported to be ≈ 40 nm [29], a range of NiO thickness between 1.5 and 100 nm is covered in the present work. In previous work, the relative orientation of the ferromagnetic layers was deduced indirectly from bulk magnetic measurements. We have aimed to retrieve this information directly using polarized neutron reflectometry with polarization analysis, thus, obtaining an insight into the exchange coupling between ferromagnetic layers spaced by an antiferromagnet.

In order to characterize the exchange interaction between magnetic layers, one of the most desirable information is the knowledge of the magnetization vectors of individual layers. Neutron reflectometry using polarized neutrons enables to probe the depth profile of the magnetization in magnitude and direction. In general, neutron reflectometry measures the chemical depth profile of thin films and multilayers similar to X-ray reflectometry but with sensitivity to the nuclei, in contrast to the electron density as in the case of X-rays. The interaction strength for neutrons shows no systematic variation within the periodic table, even isotopes of the same material may have very different scattering strengths (e.g. hydrogen vs. deuterium). This enables to tailor the neutron reflectivity by isotope substitution while maintaining the electronic structure, e.g. the chemical properties. Due to their magnetic moment, neutrons also interact with magnetic fields, e.g. the magnetization of ferromagnetic layers. Using polarized neutrons adds additional sensitivity to measure the magnetization in magnetic thin films and multilayers as a function of depth.

For a non-collinear configuration of neutron polarization and magnetization of the sample two types of the scattering process are distinguished. First, the orientation of neutron polarization is conserved (non-spin flip) providing information about the

component of the magnetization parallel to the polarization. Second, during the scattering process the polarization of the neutron is inverted (spin flip) due to the torque acting on the magnetic moment of the neutron from the component of the magnetization perpendicular to the neutron polarization. Hence, the reflectivity of the spin flip process is sensitive to the perpendicular component of the magnetization. The information about the reflectivities of non-spin flip and spin flip is obtained by the analysis of the polarization of the reflected beam. In total, four cross-sections are probed in polarized neutron reflectometry with polarization analysis, according the four possible combinations of the polarization of the incident and the reflected beam with respect to the applied magnetic field. The combined information enables to deduce magnitude and direction of the magnetization of individual layers.

Polarized neutron reflectometry has been used to measure the absolute value of the magnetic moment per atom in films of thickness not exceeding a few atomic planes [30, 31], the penetration of magnetic fields in micron-thick superconductors [32, 33, 34] and the detailed magnetic coupling across non-magnetic spacers in multilayers and superlattices [35]. Recent reviews on polarized neutron reflectometry [36, 37, 38] contain compilations of experiments demonstrating the capability of this technique. We performed polarized neutron reflectivity with polarization analysis to probe the magnetic configurations of FeCoV/NiO/FeCoV trilayers during the magnetization reversal.

This work is structured in the following way: Chapter 2 describes the preparation of the samples (NiO, FeCoV single layers, NiO-FeCoV multilayers) using DC magnetron sputtering. It includes a brief presentation of the bulk properties of FeCoV and NiO. The sputtering facility TIPSI is described and a summary of the investigated samples is given at the end of the section including definitions of particular directions in the films, which will be references throughout this work. Chapter 3 is dedicated to the experimental methods and instruments used in this work. First, it describes the magnetometers used to measure bulk magnetic properties. Second, since reflectometry using X-ray and polarized neutrons finds large application in the present work, a brief introduction to the theory of reflectivity is given with a separate section focusing on polarized neutron reflectometry. Then, the instruments for X-ray reflectometry/diffraction and polarized neutron reflectometry are described. Chapter 4 presents the structural characterization of the samples. It shows the results from the series of NiO single layers, which provide the information about proper conditions for the reactive sputtering of NiO. FeCoV single layers and NiO-FeCoV multilayers are analyzed regarding their crystalline orientation out-of-plane using X-ray diffraction. Further, chemical depth profile of the films, i.e. layer thickness, interface roughness etc. is deduced in detail from X-ray reflectivity measurements. Chapter 5 presents the results of DC magnetometry and polarized neutron reflectometry including the discussion of the specific features of FeCoV single layers and NiO-FeCoV bilayers. The magnetic properties of FeCoV/NiO/FeCoV trilayers are discussed in chapter 6 focusing on the role of antiferromagnetic NiO in exchange coupling the ferromagnetic layers, as it appears to be consistent with the experimental observations. This work ends with the conclusions inferred from our investigations and an outlook on the scope of possible experiments to answer outstanding questions.

Chapter 2

Materials and sample preparation

For the investigation of the properties of ferro-/antiferro-/ferromagnetic trilayers, we prepared samples of FeCoV/NiO (t_{NiO})/FeCoV trilayers with FeCoV as the ferromagnet and NiO as the antiferromagnet. Additional series of NiO and FeCoV single layers and FeCoV/NiO and NiO/FeCoV bilayers were deposited to investigate systematically the individual properties of the layers and interfaces, which constitute the trilayer samples. The single layers provide information about the intrinsic properties of the materials as thin layers while the bilayers allow a separate analysis of the properties of FeCoV and the NiO-FeCoV interfaces dependent on the sequence of the materials. All samples were prepared using DC magnetron sputtering in which reactive sputtering was used for the deposition of NiO layers.

This chapter reviews briefly bulk properties of FeCoV and NiO. A description of the principles of DC magnetron sputtering and of the sputtering facility TIPSI, which was used for the production of the samples, follows. Finally, an overview of the samples, prepared for this project, is given including details about the sputter parameters used for the different materials.

2.1 Physical properties of the materials

This first section shall provide a brief overview on the bulk properties of the materials FeCoV and NiO, which were used in the present work as the ferromagnet and the antiferromagnet, respectively. Among other aspects, both materials are characterized by their high ordering temperatures. Therefore, they are good candidates for technical applications at elevated temperatures. Some details about their crystalline and magnetic structure are given in the following.

2.1.1 FeCoV

Fe-Co alloys are of technical interest because of their high Curie temperature of T_C = 1223 K, high saturation magnetization [39] and low magnetocrystalline anisotropy. These properties are beneficial for applications in devices, which are operated at high temperatures, e.g. for electrical devices in turbine engines or recording media [40, 41]. Moreover, Fe-Co alloys have a large positive magnetostriction coefficient λ_s making their magnetic properties very sensitive to internal strain, e.g. for bulk $Fe_{50}Co_{50}$

$\lambda_s = 8.34 \cdot 10^{-5}$ [42].

For concentrations around $Fe_{50}Co_{50}$ the crystalline structure is body-centered-cubic (bcc) where Fe and Co occupy different sublattices (B2-phase) [43]. At $T = 1000$ K an order-disorder transition takes place and Fe and Co are randomly distributed on the bcc lattice sites (A2-phase). A structural phase transformation from bcc to fcc occurs at $T = 1223$ K and the ferromagnetism disappears [43, 44]. The dependence of magnetic properties on the crystalline microstructure has been studied in detail for bulk Fe-Co alloys [45, 46].

For technical applications small amounts of vanadium are added because of metallurgical reasons. In addition, it increases alloy resistivity and therefore eddy current losses are reduced. The FeCoV alloy, which is used as the target material for the deposition of the ferromagnetic layers in this project, is of composition $Fe_{50}Co_{48}V_2$. It is commercially available in large quantities with a well defined composition. The FeCoV targets are supplied by Vacuumschmelze GmbH, Hanau, Germany under the product name Vacoflux50. Specifications of that product can be found in [47], e.g. the coercive field H_c (≈ 1 Oe), the saturation magnetization J_s ($= 2.35$ T), etc..

Magnetic properties of such FeCoV thin films spaced by non-magnetic titanium are reported previously [48, 49, 50, 51]. In general FeCoV in these multilayers exhibits semi-hard ferromagnetic properties. In particular, a dependence of the coercivity on the FeCoV layer thickness and a dependence of the mechanism of magnetization reversal on the preparation conditions are observed.

2.1.2 NiO

NiO is an antiferromagnetic insulator with a face-centered-cubic (fcc) crystal structure (figure 2.1). The antiferromagnetic order of the Ni magnetic moments is established via the oxygen atom by means of super exchange. The Néel temperature T_N of bulk NiO is 523 K. As the Néel temperature is relatively high, NiO is considered as a potential material for the pinning layer in spin valve structures [52]. Above T_N, the crystal structure is perfectly fcc (rocksalt structure). Below T_N, a small rhombohedral contraction ($\Delta l/l \approx 4.53 \cdot 10^{-3}$ [53]) of the crystal along different $\langle 111 \rangle$ axes exists and is accompanied by an anisotropy ($K_1 \approx 1 \cdot 10^6$ erg/cm^3 [54]), which forces the Ni moments to lie in $\{111\}$ planes. Within these easy planes, Ni moments are aligned ferromagnetically, whereas between neighboring $\{111\}$ planes, they are ordered antiferromagnetically with respect to each other. As four equivalent $\langle 111 \rangle$ directions exist, the contraction axis and therefore the planes of ferromagnetic sheets may vary spatially in a NiO crystal forming antiferromagnetic domains (T domains). Within antiferromagnetic domain walls the anisotropy axis varies gradually from one $\langle 111 \rangle$ direction of the crystal to another. A second three fold anisotropy (K_3) exists within the $\{111\}$ planes with spins along three possible directions (S domains), e.g. $[\bar{2}11]$, $[1\bar{2}1]$ and $[11\bar{2}]$. K_3 is roughly three orders of magnitude smaller than K_1. Consequently domain walls are larger here than those between anisotropy axes along different $\langle 111 \rangle$ directions as the domain wall width δ is proportional to $\sqrt{A_{AF}/K_u}$ [55] where A_{AF} and K_u are the exchange coefficient and the uniaxial anisotropy constant of the antiferromagnet, respectively.

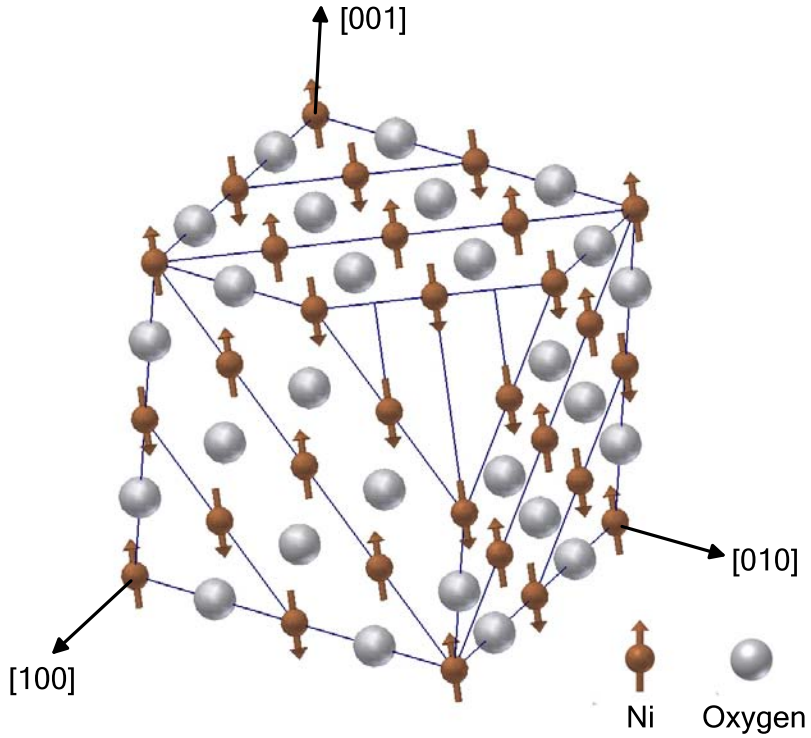

Figure 2.1: Crystal structure of NiO. Ni and O order in a rocksalt structure. The magnetic order is ferromagnetic between magnetic moments of Ni within {111} planes and is antiferromagnetic between neighboring {111} planes.

In exchange bias systems it is desired that the terminating crystal plane of the antiferromagnet has an uncompensated order of magnetic moments at the interface to the ferromagnet. In this configuration all moments point towards the same direction and it is expected that the highest exchange interaction is promoted between the antiferromagnet and the ferromagnet. As discussed above, in NiO the {111} planes are spin uncompensated. Thus, for thin film exchange bias systems the NiO layers shall exhibit a vertical (111) texture resulting in a termination with perfectly uncompensated spins when the interfaces are ideally smooth.

2.2 The DC magnetron sputtering facility TIPSI

DC magnetron sputtering is a widely used technique for thin film deposition. It is a rather fast process compared to molecular beam epitaxy using electron beam evaporation or pulsed laser deposition. Usually, thin films prepared by sputtering are vertically (out-of-plane) textured but grains have a random distribution of their crystal orientation in the plane of the films. The texture depends on the crystal structure of the bulk material and originates from the preference to grow with highest in-plane area density of the atoms [56], e.g. for bcc crystals the vertical texture will be (110) and for fcc (111), respectively. However, in sputtering the growth of thin films and therefore their crystalline orientation can be controlled by using adequate sputter conditions and single crystal substrates or special seed layers. DC magnetron sputtering is suited to

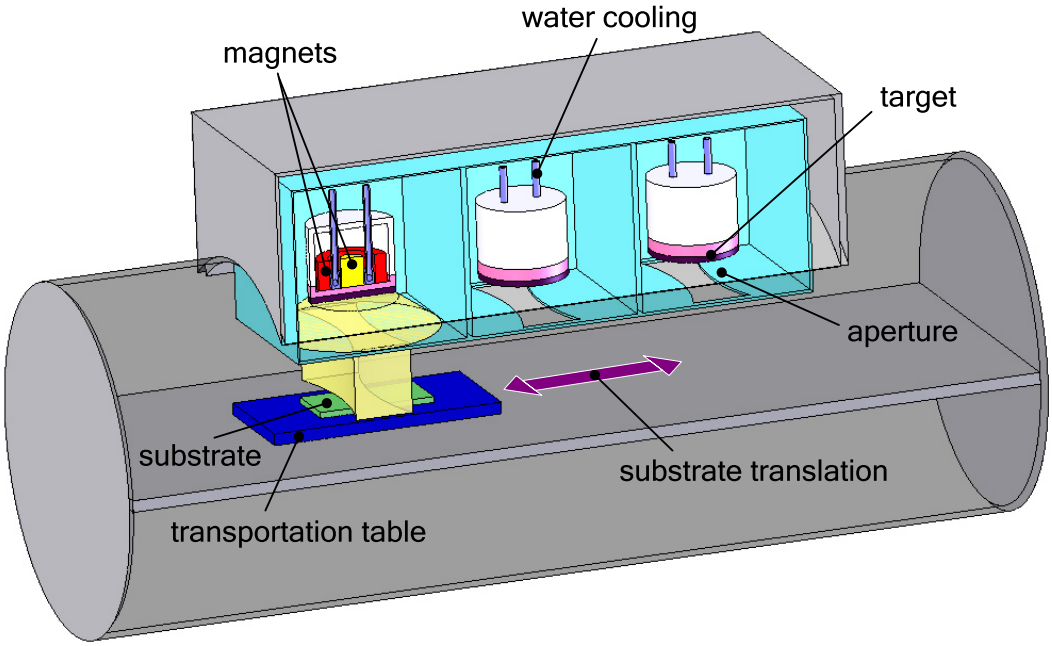

Figure 2.2: Scheme of TIPSI including basic components of the facility. Up to three targets can be mounted. Substrates are translated at a constant velocity alternately below the targets according to the desired sequence of layers. The sputter gas is supplied via a central gas inlet (not shown here).

deposit films with a very homogeneous thickness over a large area. In particular, this is beneficial when neutron reflectometry is intended for investigation, like in the present work, since the beam size on the sample under grazing incidence is typically 5 - 10 cm^2.

In sputtering, a target consisting of the material of the desired thin film is bombarded by ions, which are generated in a glow discharge. Normally argon is used as the sputter gas due to its inert properties and relatively high mass, which is beneficial to obtain high sputtering rates. In magnetron sputtering a magnetic field in front of the target confines the electrons there. They are forced to be on spiral trajectories around the magnetic field lines, which effectively increases the length of their path in the plasma. Therefore the glow discharge can be even preserved at relatively low pressure (typ. $\approx 10^{-3}$ mbar). The applied voltage for the glow discharge is typically several 100 V. When a gas ion hits the target, momentum transfer from the ion to the atoms of the target occurs. Target atoms are released when the transferred energy is higher than their binding energy. The emitted target atoms lose kinetic energy by elastic scattering at atoms of the sputter gas. Finally, they condense at surfaces of the environment, respectively the substrate as well. Using DC magnetron sputtering, thin films of pure metals and metallic alloys can be sputtered from their respective targets. For the latter, the composition of the target material is usually maintained in the film. In DC sputtering, the target represents the cathode, thus it is not possible to use insulators. Thin films of insulating materials can be deposited using RF sputtering. In DC magnetron systems, it is possible to prepare certain insulator films (e.g. NiO) from a

metallic target by reactive sputtering (see section 2.3). More details on sputtering are well described in [57, 58, 59].

For this project, we deposited series of NiO and FeCoV single layers and NiO-FeCoV multilayers as well using TIPSI, the small DC magnetron sputtering facility at the Paul Scherrer Institute (PSI) in Villigen, Switzerland. A schematic representation of TIPSI is shown in figure 2.2. TIPSI is equipped with three target stations. The targets are discs, which are mounted on a water cooled support of copper. The copper support also contains the arrangement of magnets, which provides the magnetic field in front of the target. Sputter gas flows into the sputter chamber via a central inlet. Reactive gases can be mixed with argon. The mixture as well as the total pressure are adjusted using mass flow controllers. A single power supply provides the voltage for the glow discharge. The desired target is connected by means of a toggle switch. Clean substrates are placed on a small transportation table and are translated at a constant velocity below the target for the deposition of layers. At a constant deposition rate, the layer thickness is controlled by the velocity of the translation. A constant velocity of translation assures homogeneous layers along the direction of translation. For a homogeneous layer thickness perpendicular to the translation an aperture is placed in front of the target. Thus, the variation of the layer thickness along the width of the samples is below 3% [60]. For the preparation of multilayers, power is supplied alternately to the desired targets and the substrate is translated below. The complete process is computer controlled. For the evacuation of the sputter chamber a turbo pump in combination with a membrane pump is installed.

2.3 Summary of prepared samples

We investigate the role of an antiferromagnetic layer sandwiched between two ferromagnetic layers on a series of FeCoV/NiO/FeCoV trilayers. The magnetization reversal of the FeCoV layers is studied dependent on the NiO thickness. Experiments on additional series of single layers and bilayers provide a separate information about the individual properties of the constituents of the trilayers. In summary, we prepared the following series:

1. Series NiO single layers - single layers of NiO at various sputter conditions:
   glass/NiO ($\approx$ 100 nm)

2. Series FeCoV single layers - single layers of FeCoV:
   glass/Ti (5 nm)/FeCoV (t_{FeCoV})/Ti (5 nm), t_{FeCoV} = 5, 20, 40 nm

3. Series FeCoV/NiO bilayers - bilayers with NiO on top of FeCoV:
   glass/Ti (5 nm)/FeCoV (20 nm)/NiO (t_{NiO}), t_{NiO} = 5, 60 nm

4. Series NiO/FeCoV bilayers - bilayers with FeCoV on top of NiO:
   glass/NiO (t_{NiO})/FeCoV (20 nm)/Ti (5 nm), t_{NiO} = 5, 10, 20, 40, 60 nm

5. Series trilayers - trilayers of FeCoV/NiO/FeCoV:
   glass/Ti (5 nm)/FeCoV (20 nm)/NiO (t_{NiO})/FeCoV (20 nm)/Ti (5 nm),
   t_{NiO} = 1.5, 5, 10, 20, 40, 60, 80, 100 nm

An illustration of the different series of samples is given in figure 2.3. Since the samples are differentiated on the basis of their magnetic layers, the Ti layers are not considered in the nomenclature. Additionally, in the nomenclature the order of the layers follows the order of deposition starting from the glass substrate.

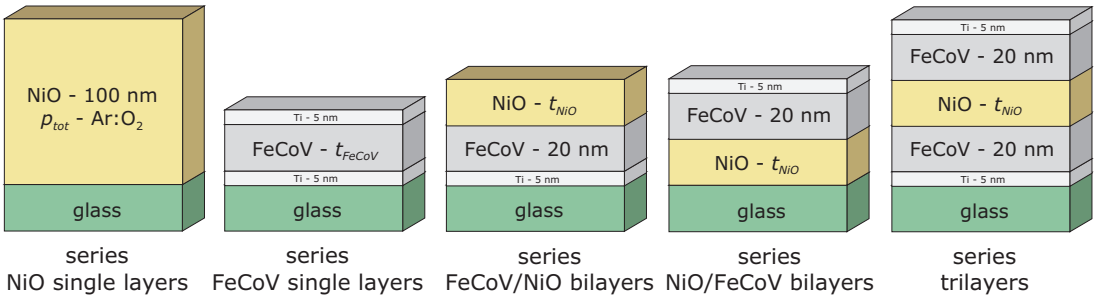

Figure 2.3: Schematic illustration of the different series of samples prepared for the systematic investigation of the properties of FeCoV/NiO/FeCoV trilayers. In addition to the trilayers, samples of bilayer counterparts and FeCoV single layers are prepared in order to study their individual properties. Proper parameters for the reactive sputtering of NiO layers are obtained from a series of NiO single layers.

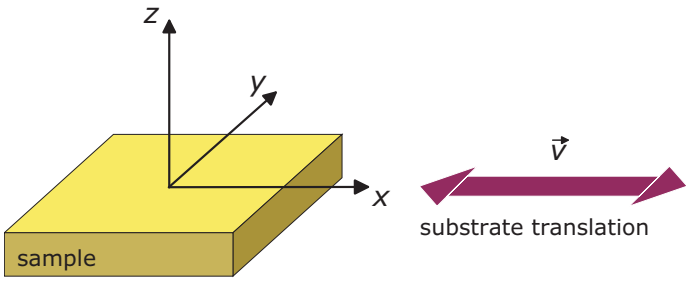

Figure 2.4: Representation of the coordinate system as used throughout the text to refer to particular axes of the sample.

Throughout the text, the presentation of results and the discussion will refer to particular directions in the samples. These are defined as an ortho-normal system (see also figure 2.4):

1. x-axis - parallel to the direction of substrate translation during deposition
2. y-axis - perpendicular (in-plane) to the direction of substrate translation during deposition
3. z-axis - perpendicular to the surface of the sample (out-of-plane axis)

The series of NiO single layers is dedicated to evaluate proper conditions for the preparation of NiO layers in this project using reactive sputtering. Here, oxygen is added to the argon sputter gas and causes oxidation of Ni atoms during the growth on the substrate. The stoichiometry of the NiO layers is expected to depend on the availability of oxygen for the process of oxidation. Regarding interfacial exchange coupling with adjacent ferromagnetic layers, aspects of the interface spin structure of the antiferromagnet have been already addressed in section 2.1.2. An uncompensated spin structure of the antiferromagnet at an ideally smooth interface is desired in order to promote highest interfacial coupling between the ferromagnetic and the antiferromagnet layer. For NiO, such a structure will be achieved if the terminating atomic layer is a (111) lattice plane. In summary, we aimed the following properties for the preparation of NiO layers:

i) proper stoichiometry of NiO to establish antiferromagnetism,

ii) texture of (111) along the growth direction for an uncompensated spin structure of the antiferromagnet at the interface,

iii) flat interfaces in order to preserve the uncompensated spin structure from the lattice structure of the antiferromagnet layer.

These properties could be controlled by the total pressure and the Ar:O_2 ratio of the sputter gas. In order to find the best conditions to achieve the properties mentioned above, NiO single layers at different total pressures (p_{tot} = 4, 6, 8 μbar) and various mixtures of Ar and O_2 were prepared. The mixture of Ar and O_2 was set by the flow rates of the individual gases and the Ar:O_2 ratios, as given below, correspond to the ratio of flow rates. The desired total pressure was adjusted by varying the flow rates of

	FeCoV	NiO	Ti
P [W]	200 ± 2	200 ± 2	200 ± 2
U [V]	480 ± 10	440 ± 10	355 ± 10
Ar flow rate [sccm]	5 ± 0.1	19 ± 0.1	4 ± 0.1
O_2 flow rate [sccm]	-	3.1	-
p_{tot} [μbar]	3.5 ± 0.1	6.0 ± 0.1	3.1 ± 0.1

Table 2.1: Typical sputter parameters for the deposition of the different materials of the multilayers. The flow rates are controlled by mass flow controllers. p_{tot} is the total pressure of the sputter gas as detected by a pressure gauge attached to the sputter chamber.

Ar and O_2 but maintaining their ratio. The analysis of NiO single layers using X-ray reflectivity and diffraction (section 4.1) showed that the desired properties would be achieved with an Ar:O_2 ratio of 86:14 and a total pressure of $p_{tot} = 6$ μbar. Thus, these parameters were used for the preparation of NiO-FeCoV multilayers.

The magnetic properties of free FeCoV layers i.e. without the proximity of NiO layers, are studied on the series of FeCoV single layers. The results for $t_{FeCoV} = 20$ nm are of particular interest because this thickness is chosen for the bilayer and trilayer series. The series FeCoV/NiO bilayers and NiO/FeCoV bilayers can be envisaged as constituents of the trilayer motif. Here, properties of FeCoV layers and their common interfaces with NiO layers are investigated depending on the sequence of the layers. These series allow to discriminate the individual properties of FeCoV layers in the trilayers. Finally, FeCoV/NiO/FeCoV trilayers were prepared for the investigation of a possible interaction between ferromagnetic FeCoV layers mediated by antiferromagnetic NiO layers and its dependence on t_{NiO}.

As mentioned above, NiO layers were prepared in a reactive Ar:O_2 atmosphere by sputtering from a pure Ni target. FeCoV layers were sputtered from an alloy target of composition $Fe_{50}Co_{48}V_2$ (see section 2.1.1) in a pure argon atmosphere. In addition, titanium layers were deposited on top of FeCoV layers in order to prevent oxidation of these layers when samples were exposed to ambient atmosphere. Titanium was also used as buffer layers between substrate and FeCoV layers since a profound knowledge of the magnetic properties of Ti/FeCoV layers has been acquired in our previous projects [48, 49, 50, 51]. Ti layers were sputtered from a pure Ti target in an argon atmosphere. Table 2.1 summarizes typical sputter parameters for the deposition of the different materials.

All samples were deposited on float glass of typical size of 50 x 100 mm^2 and thickness of 1 mm. The size of the glass substrates was chosen taking into consideration neutron reflectometry experiments with polarized neutrons (see section 3.4). Prior to the preparation of the films, the sputter chamber was evacuated until a base pressure better than $3 \cdot 10^{-5}$ mbar was reached.

Chapter 3

Experimental techniques

In magnetic nano-structures like thin films or multilayers, often only a few atoms, respectively magnetic moments, introduce specific magnetic properties. In exchange bias systems, e.g., only a few atomic planes at the interface between a ferromagnet and an antiferromagnet are responsible for the effect of exchange bias. For a direct investigation of such details, no unique technique exists. Therefore, a combined analysis using different techniques is required to elucidate the fundamental background of experimental observations. This chapter is dedicated to the various experimental techniques, which we employed in this project for the structural characterization and the measurement of magnetic properties. It describes the principles of the experimental techniques, the instruments with their features and particular aspects of the experiments.

In the present work, we have obtained bulk magnetic properties of the samples from DC magnetization measurements, which probe the static response of the sample magnetization to an external magnetic field. The structure of the samples has been characterized using X-ray reflectometry and diffraction. X-ray reflectometry probes the variation of the chemical composition vertical to the surface of the sample. The thickness of individual layers and the roughness of interfaces and surfaces are deduced from the reflectivity profile. X-ray diffraction measures the distance of the lattice planes of crystalline structures and the full diffraction pattern provides information about the crystal structure. In the present work, we employed X-ray diffraction to investigate the texture along the growth direction of the layers. Details on the magnetic configurations are unraveled using polarized neutron reflectometry. It enables to measure the magnetization vectors of individual layers at a particular magnetic state.

The first section of this chapter is dedicated to the instruments for DC magnetometry. Since complementary X-ray and polarized neutron reflectometry found large application in the present work, a brief introduction to the theory of reflectometry is given in the second section. The first part of the second section introduces the common formalism to describe the reflection of X-rays and neutrons from thin films and multilayers using refractive indices. Then, specialities using polarized neutrons are discussed. The third sections presents the facility for X-ray diffraction and reflectometry. The fourth section describes the basic setup of the neutron reflectometer, the general functioning and the option using polarized neutrons. A correction of the obtained data is necessary because of only finite polarization of the incident neutron beam and finite

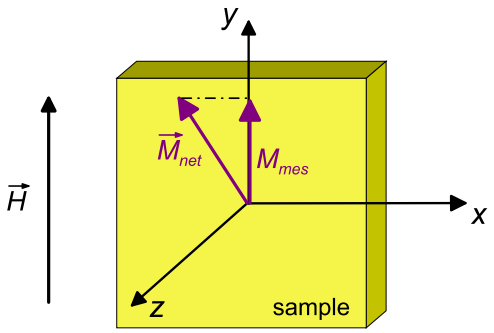

Figure 3.1: Geometry for DC magnetometry. The applied magnetic field $\vec{H}$ is in the plane of the sample, e.g. parallel to the y direction of the sample. The experiment measures the projection $\vec{M}_{mes}$ of the net magnetization $\vec{M}_{net}$ onto the field direction.

analysis of the polarization of the reflected beam. Here, the formalism is included, which is applied for data correction when, in particular, remanent supermirrors serve as beam polarizing and analyzing devices.

3.1 DC Magnetometry

We measured bulk magnetic properties of NiO-FeCoV multilayers using DC magnetometry. The experiments probed the component of the vector of the net magnetization parallel to the applied magnetic field. Complete hysteresis loops were recorded while sweeping the field from positive to negative saturation and vice versa. Samples were mounted in such a way that the applied field was along a defined direction in the plane of the samples. Figure 3.1 depicts the sample configuration with respect to the applied magnetic field and the measured magnetization.

Experiments were performed on commercial systems with dedicated options. For measurements at room and low temperature the magnetometer option of a Physical Property Measurement System was used (Institut E21, Technische Universität München). As the maximum temperature of this instrument was limited to $T = 350$ K for magnetization measurements, experiments at higher temperatures were conducted at the SQUID magnetometer at the Walther-Meissner-Institut (Technische Universität München). The principles of these instruments and general details about the measurements are described in the following sections.

3.1.1 The Physical Property Measurement System PPMS

The Physical Property Measurement System PPMS from Quantum Design (San Diego, USA) is a versatile instrument to perform a variety of experiments in an environment of precisely controlled temperature and external magnetic field. All experiments can run fully automated. The basic platform is a helium cryostat in a nitrogen-jacketed dewar with a superconducting coil to provide magnetic fields. The available temperature ranges from 1.9 to 400 K and magnetic fields up to ±9 T are possible. Several dedicated experimental options are available to perform magnetic, electro-transport,

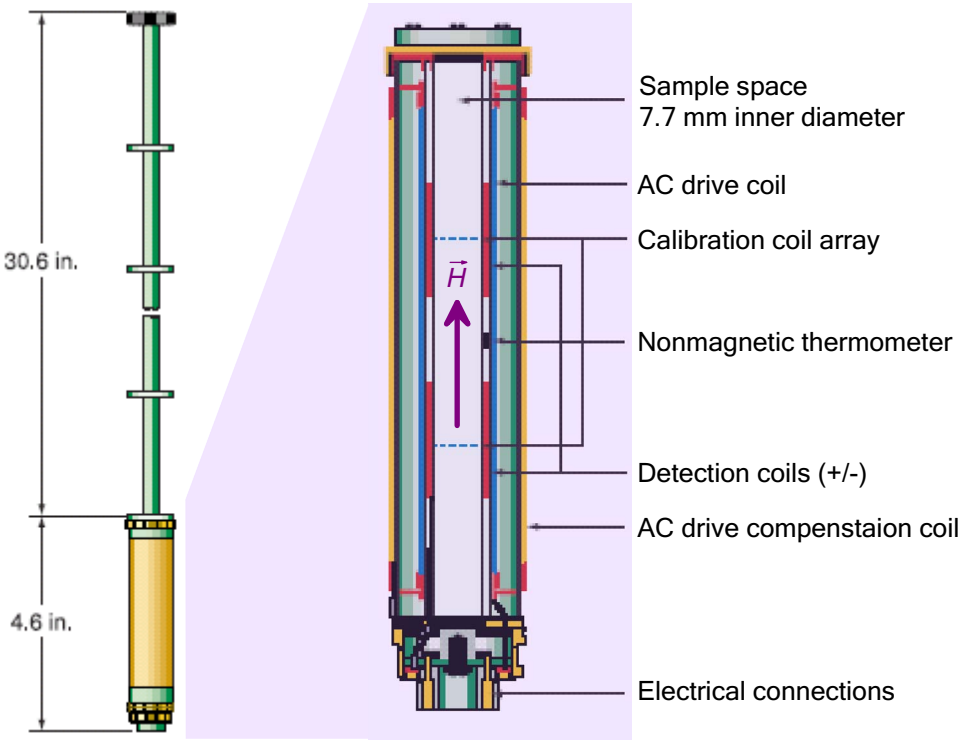

Figure 3.2: ACMS option for PPMS [61]. On the left side the ACMS insert is shown, which is introduced into the probe chamber of the cryostat. The coil set is magnified. In the detection coils a voltage is induced when a magnetic sample is moved through in DC magnetization measurements. The AC drive coils are used to apply a small alternating magnetic field. The response of the sample is again measured using the detection coils. The plug at the bottom connects the ACMS insert to the standard wiring of the basic platform.

or thermo-electric measurements. Each option is designed to be easily installed on the basic platform and ready for operation.

Magnetization measurements are conducted using the ACMS option, which combines AC susceptibility measurements and DC magnetometry in one setup. The hardware of this option consists of the ACMS coil set (figure 3.2) and on top of it a servo motor, which translates the sample through the coils. The coil set is inserted into the probe chamber of the cryostat, in the region of homogeneous magnetic field. The servo motor is attached externally.

The DC magnetometer option of PPMS is an extraction technique. In a constant, homogeneous field the sample is quickly moved (≈100 cm/s) by the servo motor through the detection coils of the ACMS coil set. Thereby the magnetization of the sample induces a voltage in the detection coils according to Faraday's Law. The amplitude of the induced voltage is proportional to the magnetic moment and the velocity of extraction of the sample. A voltage profile versus the position of the sample is recorded during the translation (figure 3.3). The magnetic moment of the sample is obtained by evaluating the detected signal. In order to minimize the statistical error the extraction can be repeated. Table 3.1 summarizes specifications of the DC magnetization option

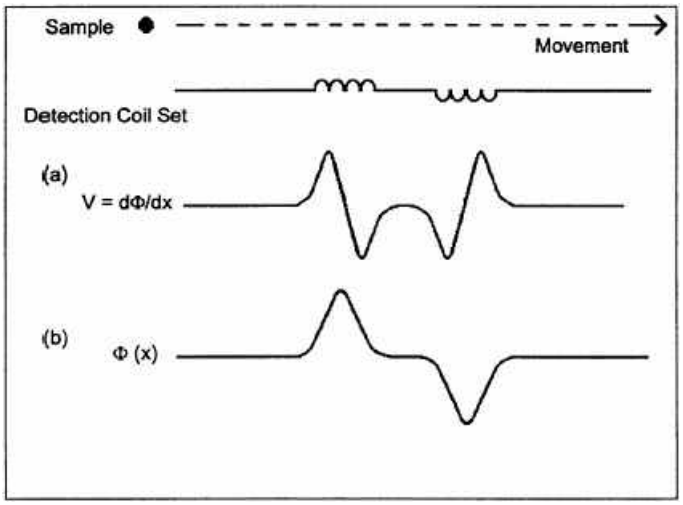

Figure 3.3: DC extraction signal. The sample is moved at a high velocity through the detection coils inducing a voltage, which is proportional to the rate of change of magnetic flux ϕ within the coils. Therefore the detected voltage profile is the time derivative $d\phi/dt$ of the magnetic flux, respectively $d\phi/dx$ because of $v = dx/dt$ with $v = const$. The magnetic moment of the sample is obtained by integrating the voltage profile numerically and fitting the measured data with the known waveform for a dipole moving through the coils [62].

of the PPMS.

Since the sample space is limited, small pieces of 5×5 mm^2 were cut from the original samples and are fixed onto a sample holder. In order to probe the in-plane magnetization the samples were mounted with their surface parallel to the magnetic field (see figure 3.1). Although the PPMS instrument possesses a high accuracy in controlling the experimental conditions and has a high sensitivity in measuring sample properties some details had to be considered in order to utilize its optimum performance. The low signal of the samples because of their small amount of material required a careful preparation and conduction of the experiments. We evaluated the systematic errors during the experiments of this work and developed strategies to minimize those, which are explained in the following.

	range	accuracy
temperature	1.9 - 350 K	±0.05%
magnetic field	±9 T	0.02 mT (< 1 T)
		0.2 mT (< 9 T)
signal	±5 emu ($\pm 5.4 \cdot 10^{20} \mu_B$)	2.5 $\cdot 10^{-5}$ emu ($2.7 \cdot 10^{15} \mu_B$)
sample size	≈ 5×12 mm^2	-

Table 3.1: Specifications for the ACMS option of PPMS [61, 62]. Using the ACMS option the maximum temperature is limited to 350 K since higher temperatures can cause damage of the electric insulation of the coil set. Regarding the accuracy of the magnetic field, effects of remanence of the sample environment must be taken into account additionally (see text).

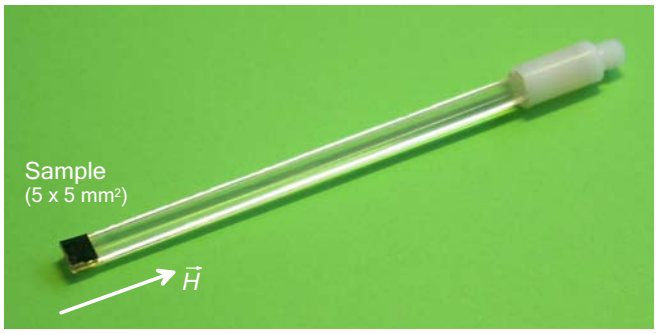

Figure 3.4: Sample holder for ACMS option of PPMS. The sample is mounted on one end of a quartz stick with a flat face. The quartz stick is fixed in an intermediate piece of polyacetal (Delrin), which allows attaching the ensemble to the standard transportation rod. Samples are glued on the sample holder using GE varnish.

In first experiments we used a plastic straw as a sample holder. The straw was established because it has no magnetic impurities and the ease of use. Unfortunately the measured signal was unstable, which was manifested in a reduced reproducibility and inconsistent absolute values for the saturation magnetization at positive and negative fields. In cooperation with Quantum Design we investigated these problems. Their origin was eventually found out to be electrostatic charging of the plastic straw from friction at the inner wall of the ACMS probe chamber during the measurements. In order to avoid this Quantum Design suggested to use quartz as the material for the sample holder. First prototypes were provided by Quantum Design and successfully tested in our laboratory measuring simple bulk Ni, Ni thin films on glass and finally samples of this project. Identical sample holders were reproduced for our laboratory. Figure 3.4 shows such a quartz sample holder. Samples are glued to the sample holder using GE varnish, which is stable down to 1.9 K, the minimum temperature of the system and exhibits no magnetic signal.

The accuracy of the magnetic field at the sample is influenced by the remanence of the environment. Especially below 0.1 T the relative error becomes significant. We studied the contribution from the remanence. As a result, we executed the following process before every experiment in order to minimize effects from remanence. First the magnetic field was set to $H = 1$ T. Then it was set back to zero in oscillatory mode where the field oscillates around zero reducing the amplitude steadily. Thus the environment of the sample in the cryostat became demagnetized. After that process the sample was installed and the measurement is started. Within a field range of ± 0.1 T highest accuracy could be preserved for low fields. Since the saturation field of the samples studied here is well within this range no limitations arise. In order to test the demagnetization procedure we measured the hysteresis of a FeCoV single layer after demagnetizing once from +1 T and once from -1 T. In each case, the loops showed a small shift of 2 - 3 Oe opposite to the starting field of the demagnetization process. As a result of these experiments the absolute accuracy of the magnetic field at the sample is estimated to be better than 3 Oe. Additional measurements of the zero field calibration using a separate low field Hall probe were consistent with the estimated accuracy.

3.1.2 The SQUID magnetometer

The SQUID magnetometer at the Walther-Meissner-Institut (Technische Universität München) provides a temperature range up to 800 K to measure DC magnetization. The hysteresis behaviors of the NiO-FeCoV samples above the Néel temperature of NiO ($T_N = 523$ K) are of great interest since the magnetic properties are expected to change significantly at the magnetic order-disorder transition of the antiferromagnet.

The SQUID magnetometer is also a product of Quantum Design, like the PPMS, which is described in the previous section. In the series of Quantum Design products it is called Magnetic Property Measurement System (MPMS). It uses a basic platform, which is very similar to the PPMS regarding the cryostat, the superconducting coil for the magnetic field and the control of the system. The MPMS is a dedicated magnetometer, which uses SQUID (Superconducting QUantum Interferometer Device) technology to measure AC susceptibility and DC magnetization with a very high sensitivity. In DC experiments the sample is stepped through the superconducting detection coils, which are liquid helium cooled. The induced voltage is measured, processed and the magnetic moment is computed.

An optional sample oven enables the MPMS to measure magnetic moments at high temperatures up to 800 K. The sample oven is directly installed into the probe chamber of the MPMS. A vacuum sleeve isolates the environment from the high temperature area. Thus, the probe chamber of the MPMS remains at ambient temperature. The residual sample space in the oven has a diameter of 3.5 mm. Therefore, we cut samples of 2×5 mm^2 from the big original pieces. Since the instrument has an excellent sensitivity ($\approx 10^{-7}$ emu) it was still possible to measure the magnetization accurately. Table 3.2 summarizes specifications of the SQUID magnetometer.

Experiments at the SQUID magnetometer are conducted identical to the PPMS. Systematic errors in the magnetic field due to remanence of the sample environment are corrected using results from samples exhibiting no exchange bias. Since the corrections obtained from various references are consistent, this procedure appears correct.

	range	accuracy
temperature	1.9 - 400 K	±0.5%
temperature with sample oven	ambient - 800 K	±0.5%
magnetic field	±7 T	0.02 mT (< 0.6 T) 0.2 mT (< 7 T)
signal	±5 emu	$< 10^{-8}$ emu (< 0.25 T) $\leq 6.7 \cdot 10^{-8}$ emu (< 7 T)
sample size (for sample oven)	≈ 3×12 mm^2	-

Table 3.2: Specifications of the SQUID magnetometer at the Walther-Meissner-Institut (Technische Universität München) [63]. An optional sample oven extends the available temperature range up to 800 K

3.2 Principles of reflectometry on thin films and multilayers

Reflectometry using X-rays and neutrons has itself established as a well suited experimental technique for the investigation of thin films and multilayers. Their difference in interaction with matter provides specific sensitivity and a complementary application of both techniques allows to unravel details of the layer structure, in particular regarding the magnetization vectors in magnetic multilayers.

The X-rays basically couple to the electrons and the scattering strength depends on the electron density, which varies according to the mass number of the elements. Therefore, X-rays are suited to distinguish multilayers composed of layers with large contrast in mass number. Nevertheless, the high brilliance of X-ray sources enables to tackle systems with only a small difference of the constituents regarding their interaction with X-rays. Neutrons interact with the nuclei of matter via the strong interaction. The interaction strength shows no systematic variation within the periodic table, even isotopes of the same material may have very different scattering strengths (e.g. hydrogen vs. deuterium). This can be used to manipulate the scattering length of a material by isotope substitution while maintaining the chemical properties. Additionally, because of their magnetic moment, neutrons interact with magnetic fields, e.g. originating from unpaired electrons in matter. Thus neutron reflectometry enables to probe the magnetic structure of thin films and multilayers using a polarized neutron beam.

The specular reflectivity probes the depth profile of the scattering length density within the coherence length of the probing beam obtaining the layer structure, the layer thicknesses and the roughness of surfaces and interfaces. Lateral inhomogeneities of the scattering strength within the coherence length give rise to diffuse scattering, which is measured in off-specular reflectometry [64, 65]. It provides information about the in-plane and vertical correlation of lateral structures, e.g. magnetic domains when using polarized neutrons.

In summary, X-ray and neutron reflectometry are complementary techniques and therefore well suited for the investigation of FM/AF/FM trilayers of this project. The following two sections contain a brief introduction to the principles of specular reflectometry using X-rays and neutrons in general and polarized neutrons in particular. More detailed descriptions about reflectometry can be found in [64], [65] and [66]. Recent reviews on polarized neutron reflectometry demonstrate its capability for the investigation of magnetic thin films and multilayers [37, 38, 67]. Although first results from off-specular X-ray reflectometry are shown in section 4.3 the theoretical approach for that is not included here as it requires an extensive formalism, which is beyond the scope of this work. A detailed theoretical treatment of off-specular reflectivity is presented e.g. in [64] and [65].

3.2.1 Specular reflectivity for X-rays and neutrons

In experiments measuring the specular reflectivity of X-rays or neutrons, a well collimated beam strikes the surface of a sample under grazing incidence and a detector

counts the intensity, which is reflected at an exit angle identical to the incident angle (figure 3.5). For the description of the interaction of X-rays and neutrons under grazing incidence it is convenient to use optical indices, which makes the formalism to calculate the reflectivity independent of the type of the probing beam. In the following, first, the definitions of the refractive indices for X-rays and neutrons are given. Second, the situation for an incident beam at an interface separating two media is mathematically described in terms of optical laws. Third, a method, known as matrix formalism is briefly described to calculate the reflectivity of a stack of layers.

In general the refractive index n is the ratio of wave vectors in matter k and in vacuum (air) k_0:

$$n = \frac{k}{k_0} \tag{3.1}$$

Refractive index for X-rays

For X-rays n is derived from Maxwell's equations and is given as:

$$n_{X-ray} = 1 - \frac{\lambda^2}{2\pi}\rho r_0(Z + f' + if'') \tag{3.2}$$

with r_0 the classical electron radius and λ the X-ray wavelength. ρ is the number of atoms per unit volume and Z is the number of protons per atom of the material. f' is the correction coefficient for dispersion. The imaginary part if'' leads to an exponentially decaying pre-factor in the wave function describing the absorption of X-rays.

An atomic scattering length b_{at} for X-ray radiation can be introduced

$$b_{at} = r_0(Z + f') \tag{3.3}$$

and equation 3.2 rewritten as

$$n_{X-ray} = 1 - \frac{\lambda^2}{2\pi}\rho b_{at} - i\lambda^2\rho\frac{r_0 f''}{2\pi}. \tag{3.4}$$

The second term describes the scattering strength in terms of the X-ray scattering length density ρb_{at}. The third term accounts for the absorption of X-rays in the material. This form for n_{X-ray} is similar to the common form for the neutron refractive index (see below) and is added here to emphasize that the formalism for X-ray and neutron reflectivity is the same.

Refractive index for neutrons

In the case of neutrons their equation of motion is described by the Schrödinger equation:

$$\triangle\Psi + k^2\Psi = 0 \tag{3.5}$$

with the wave vector k defined as:

$$k = \frac{1}{\hbar}\sqrt{2m_N(E-V)} \tag{3.6}$$

where E is the total energy of the neutron and V the potential experienced by the neutron. $V = 0$ for vacuum (air). In matter, V can be described using the Fermi-Pseudo potential [68]:

$$V = \frac{2\pi\hbar}{m_N}\rho b_{coh}. \tag{3.7}$$

b_{coh} is the coherent scattering length of the material and m_N the neutron mass. Then, the refractive index for neutrons is expressed as:

$$n_{neutron} = 1 - \frac{\lambda^2}{2\pi}\rho b_{coh} - i\lambda\rho\frac{\sigma_a + \sigma_{inc}}{4\pi}. \tag{3.8}$$

Similar to the case of X-rays (see equation 3.4), the scattering strength is described by the scattering length density ρb_{coh} for neutrons (2nd term). The third term includes absorption and incoherent scattering of neutrons with the respective cross-sections σ_a and σ_{inc}.

In summary, thin films and multilayers are characterized by their profile of the scattering length density ρb, either for X-rays or for neutrons, neglecting absorption. Vice versa, reflectometry probes the profile of the scattering length density, thus the sequence of the layers and their materials. For compound materials ρb is averaged according to the composition of the compound.

Reflectivity of smooth surfaces

Using refractive indices, the optical laws can be applied to describe phenomena like refraction, reflection and transmission of X-rays and neutrons when they pass from one medium into another under grazing incidence. The situation is illustrated in figure 3.5 for the vacuum/matter interface, which is also discussed in the following without loss of generality. In the case of an interface between two materials, n is the ratio n_2/n_1 of the individual refractive indices when the beam passes from material 1 into material 2.

Snell's law links the directions of propagation in vacuum and in the material:

$$\cos\theta_0 = n\cos\theta. \tag{3.9}$$

Since the refractive index n for X-rays and neutrons is slightly smaller than one (only few exceptions exist for neutrons, e.g. titanium) total reflection of the beam occurs when the incident angle θ_0 is less than a critical angle θ_c:

$$\theta_c = \arccos n \approx \sqrt{\frac{\rho b}{\pi}}\lambda, \tag{3.10}$$

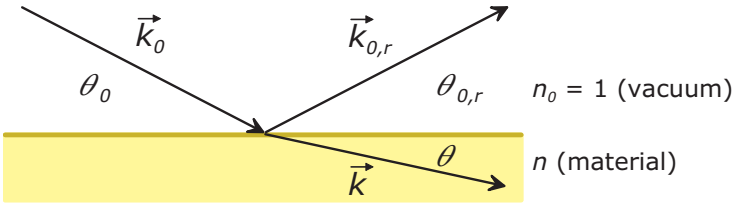

Figure 3.5: Scheme of a beam scattered at grazing incidence at an ideally flat surface separating two media of different refractive indices. The incident beam (k_0) is partially reflected ($k_{0,r}$) and partially transmitted (k). In addition, the transmitted beam is refracted at the interface. In specular reflectometry $\theta_0 = \theta_{0,r}$.

where ρb is the scattering length density either for X-rays or for neutrons.

The amplitudes of the reflected (α_r) and the transmitted (β_t) waves at the interface are given by the Fresnel coefficients [69][1]:

$$\alpha_r = \frac{\sin\theta_0 - n\sin\theta}{\sin\theta_0 + n\sin\theta} \tag{3.11}$$

$$\beta_t = \frac{2\sin\theta_0}{\sin\theta_0 + n\sin\theta} \tag{3.12}$$

In principle, for the case of X-rays, equations 3.11 and 3.12 are only valid for s-polarization but at grazing angles of incidence they are also a good approximation for p-polarization, e.g. $\alpha_r^{(s)} \approx \alpha_r^{(p)} \approx \alpha_r$.

Finally, in reflectometry experiments the reflectivity R is measured, which is the square of the modulus of the reflection coefficient:

$$R = |\alpha_r|^2 = \frac{I}{I_0} \tag{3.13}$$

with I and I_0 the intensities of the reflected and the incident beam in the experiment, respectively.

Reflectivity of multilayers

Up to here only one interface has been considered but already a sample of a single layer on a substrate contains two interfaces and a multilayer of N layers has $N + 1$ interfaces. At every interface, the situation as shown in figure 3.5 is repeated plus an additional k-vector, which represents the wave reflected from the interfaces below. This configuration of wave vectors is depicted in figure 3.6, exemplarily at one interface.

[1] Usually, the Fresnel coefficients are denoted by r and t for the reflected and transmitted amplitude. Since t is devoted for layer thicknesses throughout the text it is decided to use other symbols here but the original letters for the Fresnel coefficients appear as indices.

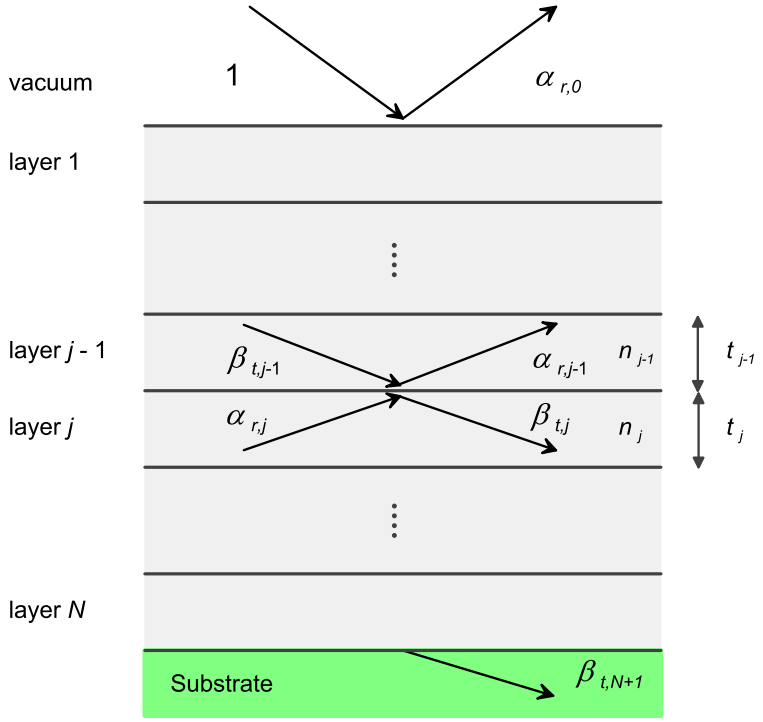

Figure 3.6: Illustration of the configuration of waves at interfaces of a multilayer. In general, α and β are the amplitudes of waves at an interface propagating up and down, respectively. The amplitude of the incident wave from vacuum is normalized to unity. $\alpha_{r,0}$ is the amplitude of the reflected wave, which is a superposition of all partial waves coming from the multilayer stack. As the substrate is usually very thick compared with the thin film layers, no wave is considered coming from the interior of the substrate.

A common way to compute the reflectivity of a stack of layers is based on a matrix formalism [64, 66]. Every interface is represented by a (2×2) matrix, which links the amplitudes of the waves in the two adjacent layers $j-1$ and j dependent on their refractive indices (equation 3.14). The propagation of the waves in layer $j-1$ is included in equation 3.14 by the additional matrix with diagonal elements describing the propagation towards $(-in_{j-1}k_{0z})$ and from $(+in_{j-1}k_{0z})$ the interface $j-1, j$. This matrix links the interfaces.

$$M_{j-1,j} = \begin{pmatrix} exp(-in_{j-1}k_{0z}t_{j-1}) & 0 \\ 0 & exp(+in_{j-1}k_{0z}t_{j-1}) \end{pmatrix} \times \begin{pmatrix} \frac{n_{j-1}+n_j}{2n_{j-1}} & \frac{n_{j-1}-n_j}{2n_{j-1}} \\ \frac{n_{j-1}-n_j}{2n_{j-1}} & \frac{n_{j-1}+n_j}{2n_{j-1}} \end{pmatrix} \tag{3.14}$$

k_{0z} is the perpendicular component of the incident wave vector with respect to the surface. The complete multilayer is then the product of all matrices $M_{j-1,j}$:

$$\begin{pmatrix} 1 \\ \alpha_{r,0} \end{pmatrix} = M_{0,1}M_{1,2}\cdots M_{j-1,j}\cdots M_{N,N+1}\begin{pmatrix} \beta_{t,N+1} \\ 0 \end{pmatrix} = M_{total}\begin{pmatrix} \beta_{t,N+1} \\ 0 \end{pmatrix} \tag{3.15}$$

with $\alpha_{r,0}$ being the amplitude of the wave finally reflected from the complete multilayer and $\beta_{t,N+1}$ the amplitude of the wave penetrating into the substrate. The amplitude

of the incident beam is normalized to unity. Consequently, the reflectivity R obtained from experiments is calculated as:

$$R = |\alpha_{r,0}|^2. \tag{3.16}$$

Another way to compute the reflectivity of a multilayer is the summation of partial waves from all interfaces [66] where the reflection coefficient α_r of each interface is determined in a recursive way known as Parrat formalism [70].

The Fresnel coefficient for the amplitude of the reflected wave (equation 3.11) indicates that the reflectivity depends on the angle of incidence of the probing beam and its wavelength. Latter is included in the refractive index n and the angle θ of the refracted beam. Usually, in experiments one of these parameters is fixed while the other is varied in order to measure a complete reflectivity profile. In principle, there is no difference between the two possibilities, e.g. in this work X-ray reflectometry was performed at constant wavelength while polarized neutron reflectivity was measured in a wavelength dispersive mode. The dependence of the specular reflectivity can be generalized introducing the wave vector transfer Q_z, which is defined as:

$$Q_z = |\vec{k}_{0,r} - \vec{k}_0| = \frac{4\pi}{\lambda} \sin\theta_0. \tag{3.17}$$

For the analysis, experimental data are compared with reflectivities computed from a proper model of the sample. In the present work, we use the software tool *Simulreflec* [71] to compute reflectivities for X-rays and neutrons on the basis of user defined models. In addition, *Simulreflec* enables fitting the experimental reflectivities to refine the model parameters.

3.2.2 Specular reflectivity for polarized neutrons with polarization analysis

The interaction of the magnetic moment of the neutron with magnetic fields makes neutron scattering experiments sensitive to magnetic structures and dynamics in matter. One of the most desirable information about magnetic thin films and multilayers is the knowledge of the magnetization vectors of individual layers. Neutron reflectometry using polarized neutrons enables to probe these[2]. Due to the dipolar nature of the magnetic interaction of neutrons with matter and the reflection geometry, polarized neutron reflectometry is limited to probe the in-plane component of the magnetization vector. For the investigation of most of magnetic thin films, which does not mean a restriction since the shape anisotropy effect confines the magnetization of thin ferromagnetic films in the plane of the sample. Particular benefits of this technique are to measure the magnetic moment per formula unit (f.u.) of a material on an absolute scale and to separate possible magnetic contributions from the substrate.

[2]The coherence length of the neutron beam in reflectometry is significantly larger than atomic distances. Thus, the magnetic structure in antiferromagnetic materials is averaged over a few atomic planes and the magnetic contribution to the scattering is zero because already neighboring magnetic moments in an antiferromagnet cancel each other.

This section shall provide a brief introduction to the basic aspects of neutron reflectometry with polarized neutrons. Usually the neutron polarization is in the plane of the sample. The first part of the introduction focuses on this conventional geometry. Additionally within this work, the feasibility of experiments with the neutron polarization perpendicular to the surface of the sample was examined. This configuration directly tests the collinearity of the magnetization vectors in magnetic multilayers and can measure the propagation of non-collinear arrangements. The second part of the present section is dedicated to the background of this type of experiment.

Prior to the introduction to polarized neutron reflectometry, it is worth to mention a few general aspects:

i) In experiments using polarized neutrons, a guide field $\vec{H}_G$ maintains the polarization of the neutron beam along its trajectory. There might be an additional magnetic field $\vec{H}$ applied to the sample, which differs in amplitude from $\vec{H}_G$ but $\vec{H}_G$ and $\vec{H}$ are always oriented parallel at the sample.

ii) The guide field $\vec{H}_G$ is the quantization axis for the neutron spin and neutrons will occupy one of two eigenstates, either parallel or antiparallel to $\vec{H}_G$.

iii) Throughout the text the selected eigenstate will be described by the polarization vector $\vec{P}$, which is parallel to the neutron spin $\vec{\sigma}$. The two states will be denoted as (+) for $\vec{P}$ parallel $\vec{H}_G$ and (-) for $\vec{P}$ antiparallel $\vec{H}_G$.

iv) The magnetic moment $\vec{\mu}$ of neutrons is opposite to their polarization $\vec{P}$, respectively their spin $\vec{\sigma}$ (see equation 3.18). This has to be considered carefully, e.g. in equations 3.21 and 3.22.

In section 3.2 the principles of neutron reflectometry are included. Due to the magnetic moment $\vec{\mu}$ of the neutrons additional aspects arise when the neutron reflectivity is measured on thin films or multilayers of ferromagnetic materials. The interaction of neutrons with a magnetic field $\vec{B}$ is expressed by the potential V_m:

$$V_m = -\vec{\mu} \cdot \vec{B} = -\gamma \mu_N \vec{\sigma} \vec{B}, \tag{3.18}$$

where $\gamma = -1.913$ is the gyromagnetic factor and μ_N the nuclear magneton. In ferromagnetic materials neutrons interact with the magnetic field created by unpaired electrons:

$$\vec{B} = \mu_0 \vec{M} \tag{3.19}$$

where μ_0 is the permeability of free space and $\vec{M}$ is the magnetization of the material. As a consequence of the dipolar nature of interaction between $\vec{\mu}$ and $\vec{M}$ magnetic scattering experiments probe only the component of $\vec{M}$ which is perpendicular to the wave vector transfer $\vec{Q}$ [72]. In specular reflectometry $\vec{Q}$ is always perpendicular to the surface of the sample ($= Q_z$), thus, polarized neutron reflectivity is only sensitive to the component of the magnetization vector in the plane of the sample. For the rest of the text $\vec{M}$ will refer only to this component.

The complete potential V including nuclear V_n and magnetic V_m interaction can be written as:

$$V = V_n + V_m = \frac{2\pi\hbar}{m_N}\rho b_{coh} - \mu_0\vec{\mu}\vec{M} - \vec{\mu}\vec{B}_0 \tag{3.20}$$

where the first term describes the nuclear contribution (see equation 3.7), the second the interaction with the magnetization of the layer and the third is the Zeeman energy of the neutrons in an external magnetic field $\vec{B}_0$.

For the special case when the neutron polarization $\vec{P}$ and the sample magnetization $\vec{M}$ are collinear, equation 3.20 simplifies to:

$$V = \frac{2\pi\hbar}{m_N}\rho b_{coh} \pm \mu_0\mu M \tag{3.21}$$

where (+) applies for $\vec{P}$ parallel $\vec{M}$ and (-) for $\vec{P}$ antiparallel $\vec{M}$. In addition it is assumed that B_0 (few 10 mT) is negligible compared to the contribution from M ($\approx$ 2 T). Furthermore, the magnetic part can be expressed in terms of a magnetic scattering length p_m and equation 3.21 becomes:

$$V = \frac{2\pi\hbar}{m_N}\rho(b_{coh} \pm p_m) \tag{3.22}$$

with

$$p_m = \frac{m_N}{2\pi\hbar}\frac{\mu_0\mu M}{\rho}. \tag{3.23}$$

Using p_m, the magnetic interaction can be directly included into the refractive index (equation 3.8) and therefore in the general formalism for neutron reflectivity as presented in section 3.2. As a result, e.g., the critical angle for total reflection depends on the polarization of the neutrons:

$$\theta_c = \sqrt{\frac{\rho}{\pi}(b_{coh} \pm p_m)}\lambda. \tag{3.24}$$

Figure 3.7 illustrates the spin dependent potential profile of a ferromagnetic/non-magnetic multilayer. The height of the potential of the ferromagnetic layers is enhanced (reduced) when $\vec{P}$ is parallel (antiparallel) to the magnetization $\vec{M}$ of the layers. As an example, a proper combination of ferromagnetic/non-magnetic materials (e.g. FeCoV/TiN [73]) allows to match the difference in potential for one spin state to be zero. Thus, neutrons of that particular spin state do not "see" the interfaces and are not reflected. This possibility is employed in polarizing neutron supermirrors (see section 3.4.2).

In general, when the polarization $\vec{P}$ of the neutrons forms some angle φ with the layer magnetization $\vec{M}$ (figures 3.8a and 3.8b) the interaction cannot be described using optical indices. The Schrödinger equation for a spin 1/2 particle has to be solved completely [74] where its potential is given by:

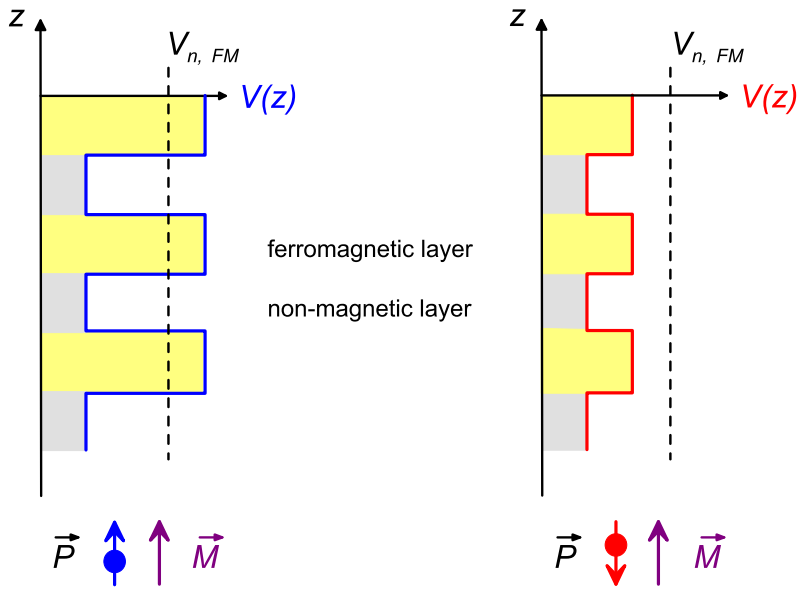

Figure 3.7: Depth profile of the potential structure of a ferromagnetic/non-magnetic multilayer for $\vec{P}$ parallel $\vec{M}$ and $\vec{P}$ antiparallel $\vec{M}$. The nuclear contribution $V_{n,FM}$ of the ferromagnetic layer is indicated by the dashed line. The spin dependent potential results in a different reflectivity profile dependent on the polarization of the neutrons.

$$V = \frac{2\pi\hbar}{m_N}\rho \begin{pmatrix} b_{coh} + p_m cos(\varphi) & p_m sin(\varphi) \\ p_m sin(\varphi) & b_{coh} + p_m cos(\varphi) \end{pmatrix}, \tag{3.25}$$

leading to four reflectivities R^{++}, R^{--}, R^{+-} and R^{-+} where the superscripts denote the neutron polarization of the incident and reflected beam, respectively. R^{++} and R^{--} are related to the diagonal elements of the matrix and therefore to the component of the in-plane magnetization parallel to the neutron polarization. They are called non spin flip (NSF) reflectivities since the neutron polarization is conserved during the scattering process (figure 3.8a). The off diagonal elements represent the perpendicular component of the in-plane magnetization. The perpendicular configuration of neutron polarization and magnetization creates a torque on the magnetic moment of the neutron, which results in a spin flip (SF) process where the neutron polarization inverts its orientation during the scattering process (figure 3.8b).

In summary, NSF and SF probe the components of the in-plane magnetization parallel and perpendicular to the neutron polarization. Measuring the four reflectivities enables to determine the magnitude and the orientation of the magnetization vector in ferromagnetic layers. It has to be noted that the retrieved orientation is invariant on mirroring the magnetization vector on the axis of the neutron polarization $\vec{P}$.

So far, the polarization of neutrons has been in the plane of the layer probing the depth profile of the in-plane magnetization vector. In another geometry, polarized neutron reflectometry is sensitive to the relative orientation of the magnetization vectors of adjacent ferromagnetic layers. Looking at the full scattering cross-section for polarized neutrons, it contains the following term $\sigma_{m''}$, which describes the interaction

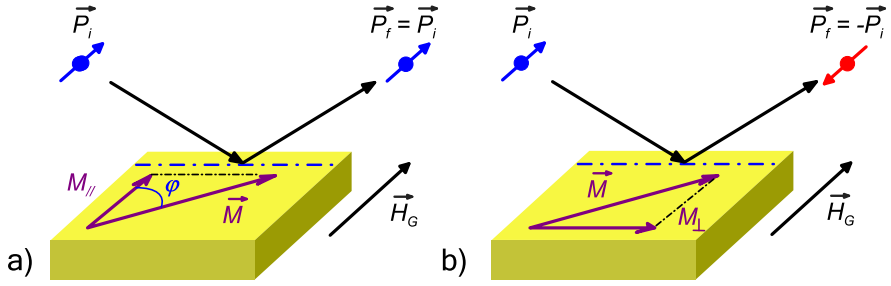

Figure 3.8: Reflections of polarized neutrons for a non-collinear configuration of $\vec{P}$ and $\vec{M}$. a) The polarization is conserved and the respective reflectivities R^{++} and R^{--} probe $M_{\parallel}$. b) The polarization of the neutron is flipped during the reflection because of $M_\perp$, thus, $R^{\pm\mp}$ are sensitive to $M_\perp$.

of a polarized neutron beam with a non-collinear magnetic structure [75]:

$$\sigma_{m''} = i(\vec{M}_{-Q} \times \vec{M}_Q)\vec{P} \tag{3.26}$$

where $\vec{M}_Q$ and $\vec{M}_{-Q}$ are the Fourier transform of the magnetization vector $\vec{M}$ and its conjugate, respectively. Equation 3.26 contains two important informations:

i) the experiment is most sensitive when the polarization of the neutron beam is parallel (antiparallel) to the axis of the spiral or partial spiral as defined by the evolution of non-collinear magnetic moments. The term is zero when $\vec{P}$ is coplanar with $\vec{M}$ like in conventional polarized neutron reflectometry.

ii) non-collinear magnetic moments give rise to an additional contribution to the spin flip reflectivity with a dependence on the polarization of the incident beam.

Since the polarization of the neutrons is always perpendicular to the magnetization vectors, all magnetic scattering is spin flip scattering and non spin flip reflectivities are of pure nuclear origin. An asymmetry of the spin flip reflectivities is the consequence of non-collinear magnetization vectors. When the magnetization of ferromagnetic layers is confined in the plane of the films (e.g. FeCoV here), a neutron polarization perpendicular to the film plane is essential to achieve the sensitivity for non-collinear magnetization vectors (figure 3.9). Consequently, the guide field for the neutrons must be perpendicular to the surface of the sample and no in-plane field can be applied to tune the magnetization of the sample. This kind of experiment is useful when the magnetization of samples can be prepared externally in an in-plane magnetic field and the state of magnetization is preserved when the field is removed.

Finally, it is important to note that in the above discussion of polarized neutron reflectometry the ferromagnetic layers are assumed to consist of a single domain. In case of multi domains the situation becomes rather complex and depends on the relative size of the domains to the in-plane coherence length of the neutron beam, which is typically a few ten microns. For domains larger than the in-plane coherence length, neutrons are still specularly reflected but depolarization occurs due to the different orientations

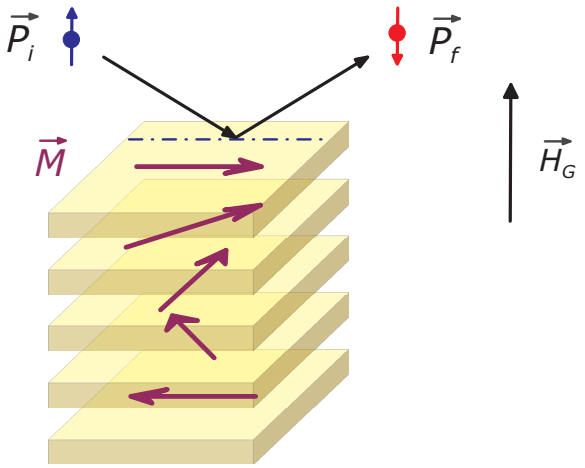

Figure 3.9: Reflection geometry with neutron polarization perpendicular to the sample surface. In this geometry the experiment is directly sensitive to a non-collinear arrangements of magnetic moments. The interaction of the polarized neutron beam with a non-collinear structure of magnetic moments is depicted leading to spin flip.

of the domains. When the size of the domains is smaller than the coherence length, the neutrons probe the average magnetization vector of the domain distribution within the coherence length. In addition, the lateral fluctuation of the magnetization vector leads to off-specular scattering.

3.3 X-ray reflectometry and diffraction

We performed X-ray reflectivity and X-ray diffraction measurements to characterize the chemical depth profile and the out-of-plane texture of the prepared samples. Both types of experiments are performed on a Siemens D5000 X-ray diffractometer (Institut E21, Technische Universität München).

The instrument runs with a copper source providing a X-ray beam with a wavelength $\lambda = 0.154$ nm ($Cu_{K\alpha}$). Originally, it is designed as a dedicated powder diffractometer but additionally, the instrument has been upgraded to perform high quality reflectivity measurements. Therefore, it has been equipped with commercially available components: a sample table including tilting facility, a high precision knife-edge collimator, an automatic attenuator and a secondary monochromator (figure 3.10).

The beam is collimated by a slit system, which can be varied in order to run the experiments with a proper beam divergence. One slit is introduced in the path of the incident beam close to the sample and two slits are placed in the reflected beam. The knife edge collimator, which acts as an additional slit, allows to narrow the beam divergence for the requirements of reflectometry experiments. The zero position of the knife edge is adjusted to the center of the straight X-ray beam, thus, it serves also as a reference for the alignment of the sample surface to the center of the beam. A monochromator (graphite) is installed in the reflected beam path, in front of the detector (scintillation counter), in order to filter out the K_β-line of the Cu source as well

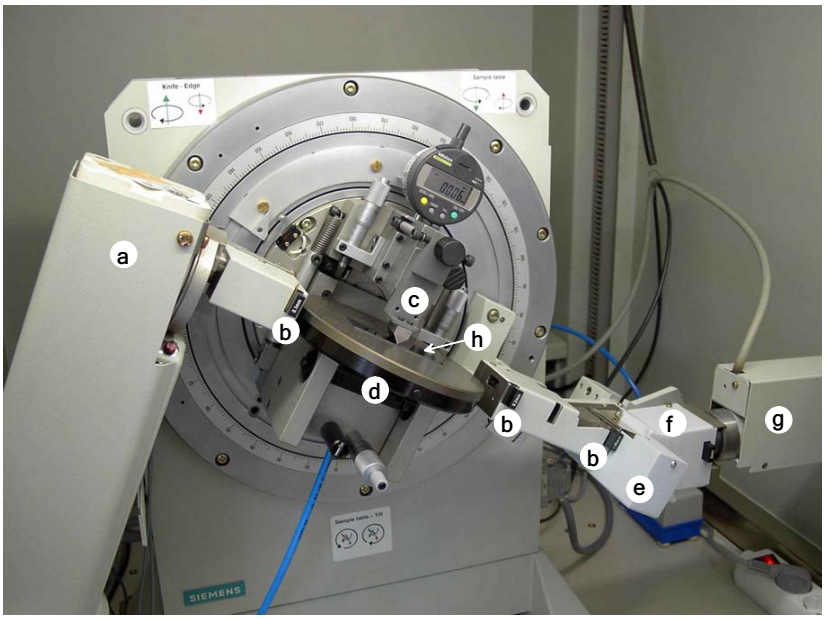

Figure 3.10: X-ray diffractometer Siemens D5000: standard $\theta/2\theta$-goniometer, upgraded for reflectivity measurements on thin films and multilayers. a) source (Cu), b) slits, c) knife edge collimator, d) sample table, e) automatic attenuator, f) secondary monochromator (graphite), g) detector (scintillation counter) and h) sample.

as fluorescence that might originate from the sample. Especially fluorescence from Fe in FeCoV layers is suppressed reducing the background in the experiments. The automatic attenuator allows reducing the beam intensity if it would cause saturation of the detector resulting in wrong counting rates. Especially for reflectometry, the automated attenuator enables to measure the range of total reflection with the attenuator in the beam and to continue the range of low reflectivity without attenuator, avoiding manual operation and interruption of the experiment.

The diffractometer is interfaced to a PC that controls the sample alignment and the experiments. The software is able to run various types of scans, which can even be combined to a sequence and executed one after the other. A complete set of experiments can be performed on one sample, fully automated. Data visualization during experiments and the processing afterwards as well is provided by adequate software tools including data treatment like merging, background correction etc..

For diffraction experiments, the slit width of 0.6 mm was chosen at every position resulting in a relaxed beam divergence of 0.18°. A well collimated beam is needed for reflectivity measurements. Therefore, an arrangement of slits was installed with widths of 0.1 mm in the incident beam and 0.2 and 0.05 mm in the reflected beam. In addition the knife edge collimator was inserted into the path of the beam, almost touching the surface of the sample. The gap between the film surface and the knife edge was set to 0.005 mm resulting in a divergence of $\approx 0.008°$. Table 3.3 summarizes the setups for beam collimation conducting either reflectometry or diffraction.

	Reflectometry	Diffraction
Width slit 1 [mm]	0.1	0.6
Width slit 2 [mm]	0.2	0.6
Width slit 3 [mm]	0.05	0.6
Position of knife edge [mm]	0.005 ± 0.002	out
Resolution $\Delta\theta$ [°]	≈ 0.008	0.18

Table 3.3: Configurations of the slits and the knife edge collimator for reflectometry and diffraction. The numbering of the slits follows the X-ray propagation with slit 1 in the incident beam and slit 2 and 3 in the reflected beam. The knife edge position is its distance to the sample surface.

Prior to the measurement the sample had to be aligned. Therefore, the knife edge was brought into its zero position representing the center of the beam. Then, the sample was moved from below towards the knife edge until it just did not touch. This step was in combination with the tilting facility, which enabled to adjust the sample surface parallel to the knife edge. After that, the knife edge was slightly lifted to create a narrow gap. For the final step of the sample alignment, a rocking scan at grazing incidence and a fixed detector angle was performed and the absolute sample angle was obtained from the center of the specular peak. The alignment of the sample was done using the beam collimation for reflectometry.

Specular reflectivity was typically measured from 0 to 3° of the incident angle in steps of 0.005°. The typical time for counting was 10 s per data point. The regime of total reflection was scanned with the attenuator in the beam until the intensity drops below 1000 counts/s. The rest of the scan was performed without beam attenuator. A small overlap of the two ranges was included, which enabled to merge the two parts of the reflectivity profile. In addition to the specular scan, a longitudinal scan was performed with a constant offset of the sample angle of 0.03° from the $\theta/2\theta$ geometry. This scan measured the diffuse intensity next to the specular rod including the background at the instrument. The intensity of the longitudinal scan was subtracted from the intensity of the specular scan providing the pure specular signal.

Off-specular reflectivity was measured on selected samples of the trilayer series. Therefore, a sequence of rocking scans was performed at various detector angles. The limits for the rocking scans were on either side the horizon of the sample surface with respect to the incident and the exit beam. This range increased with increasing 2θ angles. The detector angle was varied between $0.86° \leq 2\theta \leq 4°$ in order to limit the total time for the mapping of one sample. The step widths were 0.01° for θ and 0.02° for 2θ. The measuring time per data point was 10 s. A small C code was developed to link all rocking scans and arrange the data in columns of Q_x, Q_z and intensity.

Diffraction scans were performed in a $\theta/2\theta$ mode where the scattering vector remained perpendicular to the sample surface. Thus, the experiments probed the crystal structure of the layers along their growth direction, i.e the vertical texture. The scans typically covered a range of $33° \leq 2\theta \leq 68°$. The 2θ step size was 0.05° and at each data point the intensity was accumulated for 60 s. The background was determined

from the level of counts between the Bragg peaks and subtracted from the measured intensity.

3.4 Polarized neutron reflectometry

In section 3.2.2 the application and strength of neutron reflectometry in the field of magnetic thin films and multilayers using polarized neutrons are discussed. Therefore, it is a well suited technique to probe the magnetization profile of FM/AF/FM trilayer samples of this project at saturation and during the magnetization reversal providing an insight into the interlayer exchange coupling between the ferromagnetic layers.

Polarized neutron reflectometry for this project were performed at the Apparatus for Multi Optional Reflectometry (AMOR) at the Paul-Scherrer-Institut in Villigen, Switzerland. The instrument is a dedicated neutron reflectometer including options to use polarized neutrons and to analyze the state of polarization of the reflected neutron beam. The following sections provide details on the experimental setup of the instrument and the performed experiments. First, the basic setup of AMOR is presented including all experimental details, which are not related to the use of polarized neutrons. Second, the option of polarized neutron reflectometry on AMOR is described. Third, the procedure for the correction of the measured data regarding the finite polarization of the neutron beam is explained.

3.4.1 Basic setup of the neutron reflectometer AMOR

The AMOR instrument is located in the neutron guide hall of the Swiss Spallation Neutron Source SINQ. It is attached to the neutron guide 1RNRlb, which transports neutrons from the cold source moderator to the instrument.

At AMOR the Time-of-Flight (ToF) technique is employed to measure the reflectivity dependent on the momentum transfer Q_z. A pulsed neutron beam of a spectrum of neutron wavelengths hits the sample at a defined angle of incidence θ_0. The beam is reflected at the sample and finally the neutrons are counted in different registers dependent on their arrival time at the detector. Knowing the time of flight T and the path length L of the neutron trajectory, the respective neutron wavelength λ is assigned to every register

$$\lambda = \frac{h}{m_N L} T = \frac{T[\mu s]}{2527 \cdot L[m]} \tag{3.27}$$

and the associated Q_z can be calculated (equation 3.17). h is the Planck constant and m_N the neutron mass. The reflectivity is obtained by normalizing the measured spectrum of the reflected beam by the spectrum of the incident beam. The latter spectrum is measured with identical instrumental setup but without sample.

Figure 3.11 shows a schematic representation of AMOR. A neutron chopper is introduced into the neutron beam chopping the continuous beam into pulses. It consists of two disks (⌀ 700 mm) side by side and phase coupled. The phase shift defines a

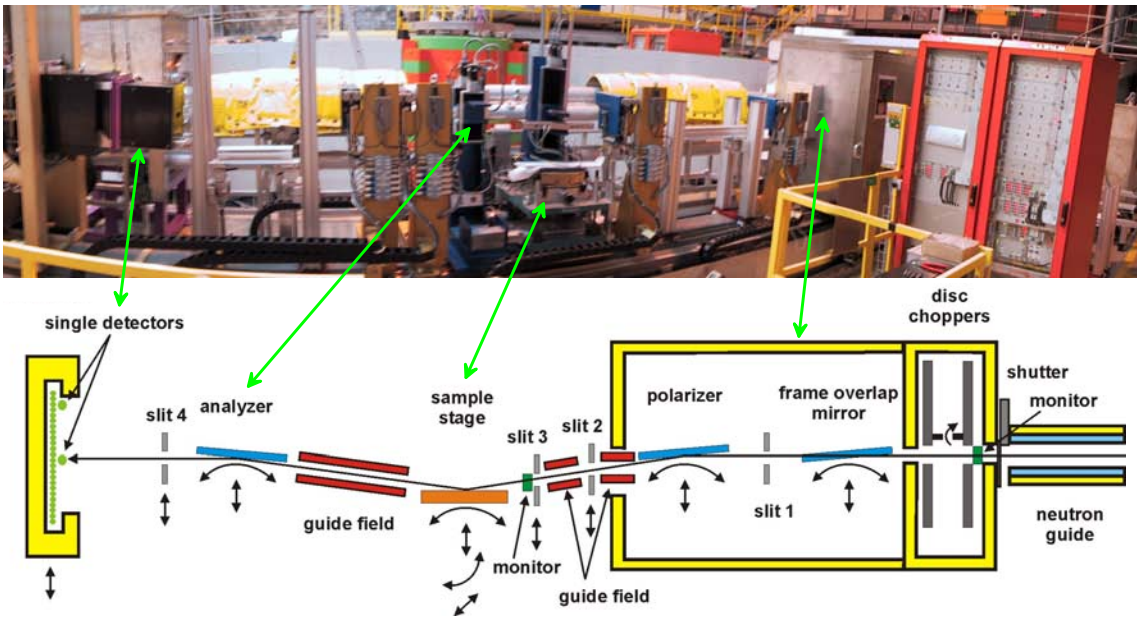

Figure 3.11: The Time-Of-Flight reflectometer AMOR. Optionally, polarized neutrons can be used with polarization analysis of the reflected beam. Therefore remanent polarizing supermirrors are introduced in the incident and reflected beam as polarizer and analyzer, respectively. (courtesy of Dr. T. Gutberlet, Paul-Scherrer-Institut, Switzerland)

window during that the chopper allows neutrons to pass. For the rest of the time neutrons are absorbed by the chopper disks. The rotation speed and the phase shift are variable in order to tune the wavelength resolution dependent on the requirements of the experiment. Typically these parameters are set to 1500 rev/min and 11°, respectively for the experiments within this project.

A frame overlap mirror reflects neutrons beyond a certain wavelength out of the beam. These slow neutrons may contaminate the fastest utilized neutrons of the next pulse. The cut-off wavelength is adjusted by the inclination of the mirror. The mirror is especially needed when highest resolution is desired and therefore the chopper to detector distance is very large. This was not necessary for the experiments of this work. Therefore the frame overlap mirror was not introduced. In addition, when using polarized neutrons, the polarizing mirrors already define a bandwidth of wavelengths, which can be utilized (see section 3.4.2).

Two diaphragms in the primary beam, separated by $d = 685$ mm define the shape and divergence of the neutron beam. Since the scattering plane is vertical the beam divergence in the vertical direction must be limited. Therefore the vertical opening widths were only 0.5 mm. The divergence in the horizontal direction can be relaxed in order to increase the intensity of the neutron beam. The horizontal slit widths were 20 mm. Optionally one more diaphragm can be introduced in the reflected beam i) to reduce background from diffuse scattered neutrons and ii) to reduce the divergence of the beam.

Samples are mounted horizontally on a sample stage, which has all degrees of freedom in order to align the samples with respect to the neutron beam and to set the desired angle of incidence. Neutrons of the reflected beam are counted using a single ^{3}He detector, which is at a distance of $L = 7200$ mm from the chopper.

The complete alignment of the instrument including the samples was performed by the instrument team of AMOR. The spectrum, which could be utilized ranged from approximately $\lambda = 0.3$ to 1.2 nm. Measurements were performed at two different angles of incidence in order to cover a larger Q_z range. The first angle was set to $\theta_0 \approx 0.5°$ and included the regime of total reflection. The adjacent Q_z range was measured at $\theta_0 \approx 1.4°$. Totally, a Q_z range of approximately 0.1 to 1 nm^{-1} could be covered. At larger Q_z the reflected intensity was only of the order of the background.

An important parameter of the experiments is the Q-resolution, especially regarding proper reproduction of experimental reflectivity profiles by computed profiles. Therefore, aspects on the instrumental resolution are discussed in the following, which have entered the computation of reflectivity in this work.

As usual in neutron scattering experiments the Q-resolution ΔQ_z is defined by the wavelength dispersion $\Delta\lambda$ and the angular divergence $\Delta\theta$ of the neutron beam. The relative resolution is derived from equation 3.17:

$$\frac{\Delta Q_z}{Q_z} = \frac{1}{\lambda}\Delta\lambda + \cot(\theta)\Delta\theta \tag{3.28}$$

where θ is the reflection angle of the neutron beam. From equation 3.28, one can see that the resolution depends on λ and therefore it varies along the reflectivity profile in Time-of-Flight experiments. The wavelength dispersion $\Delta\lambda$ is related to the uncertainty ΔT in the time of flight (see equation 3.27):

$$\Delta\lambda = \frac{h}{m_N L}\Delta T \tag{3.29}$$

Since the time of flight T is the difference between the time $t_{chopper}$ when the neutrons pass the chopper and the time $t_{detector}$ when they arrive at the detector, ΔT is given by the uncertainties of $t_{chopper}$ and $t_{detector}$:

$$\Delta T = \sqrt{\Delta t_{chopper}^2 + \Delta t_{detector}^2} \tag{3.30}$$

where $\Delta t_{chopper}$ is the time frame during that the chopper is open and neutrons can pass through. For the chopper system at AMOR, $\Delta t_{chopper}$ is related to the speed of rotation and the phase shift of the chopper disks. $\Delta t_{detector}$ is the width of the time channels in which neutrons are counted. Table 3.4 summarizes typical parameters of the setup of AMOR, which define the Q-resolution of the probing neutron beam.

Since in reflectometry experiments the angle of incidence is very small and the sample

w_1 [mm]	0.5	$t_{chopper}$ [μs]	440
w_2 [mm]	0.5	$t_{detector}$ [μs]	150
d [mm]	685	L [mm]	7200
$\Delta\theta$	0.08°	$\Delta\lambda$ [nm]	0.025

Table 3.4: Typical setup parameters of AMOR for the experiments conducted within this project. $t_{chopper}$ is defined by the speed of rotation of the chopper disks and their phase shift. A phase shift of 11° corresponds to an opening angle of the chopper of ≈4°.

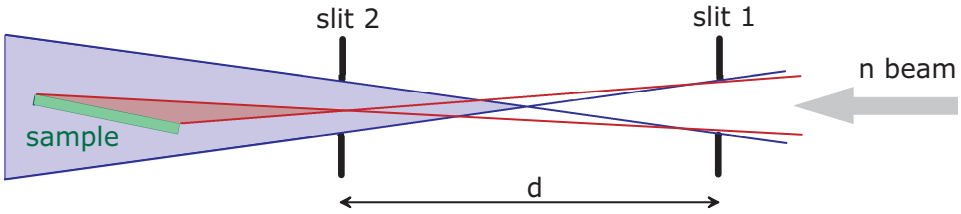

Figure 3.12: Illustration of the beam divergence defined by i) the geometry of the slits (blue triangle) and ii) the combination of slit geometry and size of sample (red triangle). For the latter the divergence is reduced since only a part of the beam is accepted by the sample.

size usually not very large the projection of the beam on the sample (footprint) has to be considered in determining the Q-resolution. The beam divergence $\Delta\theta$ is determined by the geometry of the slits when the footprint is smaller than the sample size. When the footprint is larger than the sample size, $\Delta\theta$ includes the acceptance of the sample and the divergence is smaller than defined by the slits. An illustration of this particular situation is shown in figure 3.12. For the experiments at AMOR both situations occur. At the first angle of incidence ($\theta_0 \approx 0.5°$) the situation is like shown in figure 3.12 by the red geometry and $\Delta\theta \approx 0.04°$. At the second angle ($\theta_0 \approx 1.4°$) the footprint of the beam on the sample is smaller than the sample size and $\Delta\theta \approx 0.08°$ (see table 3.4). The different $\Delta\theta$-resolution of the two Q_z ranges is considered in the computation of reflectivity profiles.

3.4.2 Setup for polarized neutrons and polarization analysis

AMOR provides the option using a polarized neutron beam and analysis of the polarization of the reflected beam. Devices for both, polarization and analysis of the neutron beam, are remanent supermirrors of FeCoV/TiN$_x$ [73]. When the mirrors are magnetically saturated the reflectivity depends on the spin state of the neutrons due to the magnetic contribution to the scattering length density from the ferromagnetic FeCoV layers (see section 3.2.2). For one spin state the contrast in scattering length density of the two materials is enhanced resulting in a high reflectivity. For the opposite spin state the contrast is reduced. In addition, for the latter, the contrast is matched to be ideally zero by adding the proper amount of nitrogen in the TiN layers. Thus the reflectivity is almost zero as well (figure 3.13).

A high polarization of the neutron beam of ≈95% is achieved by means of such supermirrors. An additional feature of the polarizing supermirrors employed at AMOR is

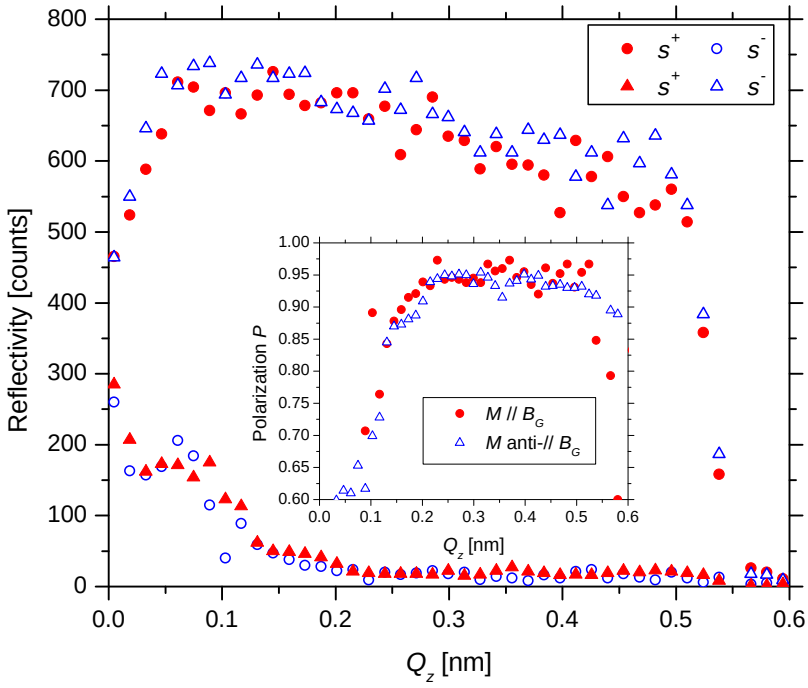

Figure 3.13: Spin dependent reflectivity of a remanent polarizing supermirror measured at different orientations of magnetization $\vec{M}$ with respect to the applied guide field $\vec{H}_G$: i) $\vec{M}$ parallel $\vec{H}_G$ (circles) and ii) $\vec{M}$ antiparallel $\vec{H}_G$ (triangles). In ii) the supermirror was saturated in an external magnetic field of ≈ -20 mT prior to the experiment. Due to the different orientation of $\vec{M}$ the reflectivities for spin up and spin down are inverted from i) to ii). In addition (inset) the experiments show that the polarization performance is almost independent of the relative orientation of $\vec{M}$ and $\vec{H}_G$.

their high remanence at zero field or even at small reverse fields, which is due to a net magnetic anisotropy originating from a net anisotropy of the internal stress [76]. This allows to switch the magnetization, consequently the polarization/analysis orientation, by a short magnetic field pulse (≈ 40 mT). The magnetization of the mirrors remains aligned, even when a reverse field of ≈ 1 mT is present (figure 3.13), which is always needed as a guide field to retain the neutron polarization. The guide field spans from the polarizer to the analyzer without gap.

For the experiments with the polarization of the neutron in the plane of the sample a large electro magnet provides magnetic fields up to ≈ ±1T at the sample position in order to tune the magnetization of the samples to the desired state of their hysteresis. The accuracy of the applied field is ≈ ±10 G. The field needs to have the same orientation as the guide field when reflectivity is measured.

In section 3.2.2 an alternative experiment is discussed, which is sensitive to the relative orientation of the magnetization vectors in the adjacent ferromagnetic layers and therefore enables to discriminate collinear from non-collinear structures directly. This kind of reflectometry experiment requires a polarization of the neutron beam perpendicu-

lar to the sample surface, which is in contrast to the conventional geometry described above. We realized the particular setup at the AMOR reflectometer by providing a small perpendicular magnetic field over a finite sample region. An appropriate overlap of the perpendicular field at the sample with the guide field of the incident and reflected beam enabled an adiabatic transformation of the neutron polarization from in-plane to perpendicular and vice versa. Figure 3.14 illustrates the setup and the transformation of the neutron polarization.

Since the external field had to be perpendicular to the sample surface, application of an in-plane magnetic field was not possible to hold the magnetization of the layers in a particular state during the experiment. Therefore, prior to the experiment, samples were magnetized externally to a desired state which then was brought to the respective remanent state before the polarized neutron reflectivity was measured.

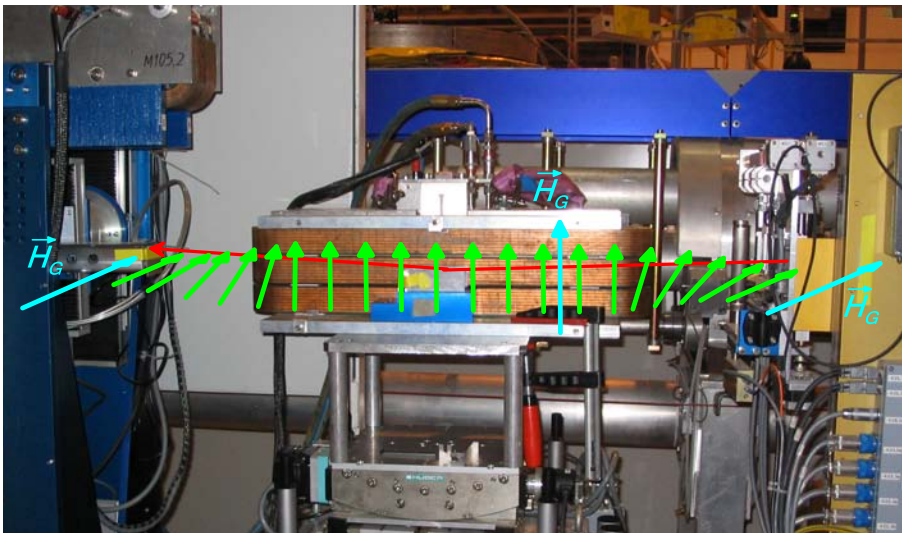

Figure 3.14: Setup at AMOR for the neutron polarization perpendicular to the sample surface. The vertical field at the sample position overlaps with the horizontal guide field of the incident and reflected beam. Thus an adiabatic transformation of the neutron polarization is achieved as schematically illustrated in the picture (green arrows). The red line describes the trajectory of the neutron beam. Using this setup, the conventional geometry of the polarizer/analyzer mirrors can be utilized.

3.4.3 Data correction of finite beam polarization and analysis

In polarized neutron reflectometry with polarization analysis of the reflected beam four reflectivity cross-sections (R^{++}, R^{--}, R^{+-}, R^{-+}) of the sample are probed (see section 3.2.2). Respective intensities (I^{++}, I^{--}, I^{+-}, I^{-+}) are measured by varying the state of polarizer and analyzer accordingly. Since polarizing and analyzing devices have only finite efficiencies the measured intensities contain a mixture of the four reflectivity cross-sections. Finite efficiencies result in a contamination of the polarized beam with neutrons of undesired spin state. In order to retrieve the reflectivity cross-sections the measured intensities have to be corrected, especially for the detailed analysis of the

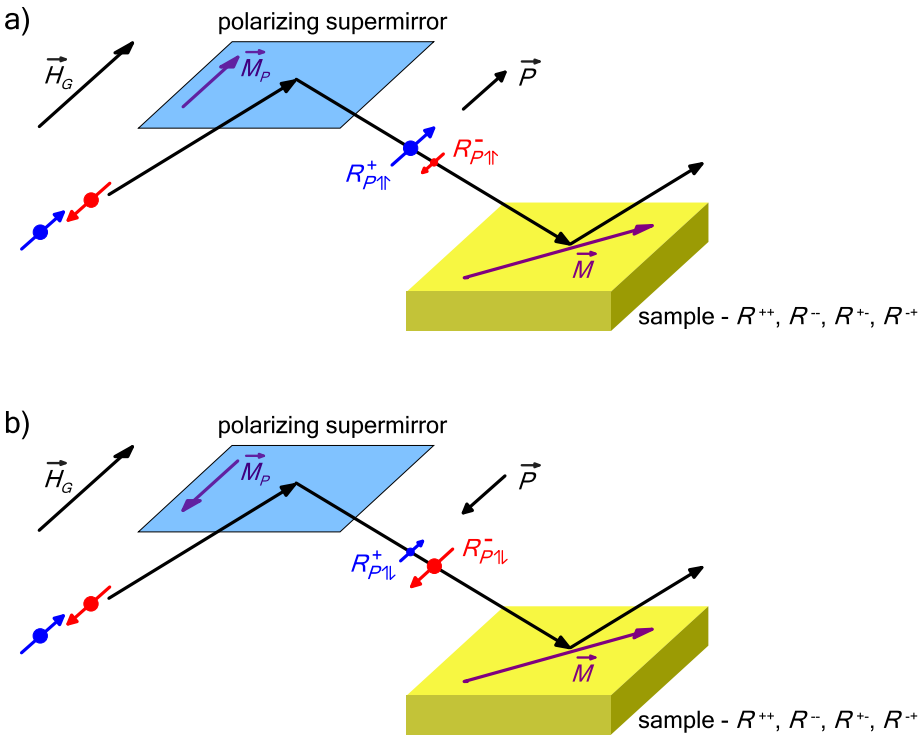

Figure 3.15: Illustration of neutron beam polarization using a remanent polarizing supermirror: a) $\vec{M}_P \uparrow\uparrow \vec{H}_G$, the supermirror has a high (low) reflectivity $R^+_{P1\uparrow}$ ($R^-_{P1\uparrow}$) for neutrons with spin parallel (antiparallel) $\vec{H}_G$, thus the polarization $\vec{P}$ of the probing beam is parallel $\vec{H}_G$. b) $\vec{M}_P \uparrow\downarrow \vec{H}_G$, the supermirror has a low (high) reflectivity $R^+_{P1\downarrow}$ ($R^-_{P1\downarrow}$) for neutrons with spin parallel (antiparallel) $\vec{H}_G$ and the polarization $\vec{P}$ of the beam is antiparallel $\vec{H}_G$.

reflectivity profiles by proper modeling. In the following the correction procedure is described, which is specifically employed for the setup at AMOR using remanent polarizing supermirrors.

It shall be emphasized again that (+) and (-) denote a polarization $\vec{P}$ of the neutron beam being parallel and antiparallel to the guide field $\vec{H}_G$, respectively. The orientation of $\vec{P}$ is selected dependent on the magnetization $\vec{M}_P$ of the polarizing supermirror, which is either parallel ($\uparrow\uparrow$) or antiparallel ($\uparrow\downarrow$) to $\vec{H}_G$. For the parallel (antiparallel) configuration the polarizing supermirror has a high reflectivity $R^+_{P1\uparrow}$ ($R^-_{P1\downarrow}$) for neutrons with spin parallel (antiparallel) to $\vec{H}_G$ and low reflectivity $R^-_{P1\uparrow}$ ($R^+_{P1\downarrow}$) for neutrons with spin antiparallel (parallel) to $\vec{H}_G$ resulting in a polarization $\vec{P}$ being parallel (antiparallel) to $\vec{H}_G$. The configuration of $\vec{P}$, $\vec{H}_G$ and $\vec{M}_P$ including the reflectivities of the polarizing supermirror is illustrated in figure 3.15. The relations are identical for the analyzing supermirror whose symbols have the subscript A in the following. The performance of polarizing supermirrors regarding neutron beam polarization and analysis is described in the most general way using their neutron spin dependent reflectivities.

The intensity I^{++} is measured with the magnetization of polarizer and analyzer supermirrors parallel to the guide field. It can be mathematically formulated as:

$$I^{++} = (\varepsilon_+, \varepsilon_-) \begin{pmatrix} R^+_{A\uparrow\uparrow} & 0 \\ 0 & R^-_{A\uparrow\uparrow} \end{pmatrix} \begin{pmatrix} R^{++} & R^{-+} \\ R^{+-} & R^{--} \end{pmatrix} \begin{pmatrix} R^+_{P\uparrow\uparrow} & 0 \\ 0 & R^-_{P\uparrow\uparrow} \end{pmatrix} \begin{pmatrix} n_+ \\ n_- \end{pmatrix} I_0. \quad (3.31)$$

Following the propagation of the neutron beam, equation 3.31 is read from right to left. I_0 is the initial intensity of the incoming beam. n_+ and n_- represent the probabilities for the neutron spin being parallel or antiparallel $\vec{H}_G$, respectively. Thus

$$n_+ + n_- = 1 \quad (3.32)$$

and for a unpolarized beam

$$n_+ = n_- = 1/2. \quad (3.33)$$

First, the incoming unpolarized beam is reflected at the polarizing supermirror with high and low reflectivities ($R^+_{P\uparrow\uparrow}$, $R^-_{P\uparrow\uparrow}$) for the two spin states of the neutrons. Second, the polarized beam hits the sample, which is characterized by the four reflectivity cross-sections R^{++}, R^{--}, R^{+-} and R^{-+}. Third, the beam reflected from the sample is analyzed by means of the spin dependent reflectivity ($R^+_{A\uparrow\uparrow}$, $R^-_{A\uparrow\uparrow}$) of the second supermirror. Finally, a detector counts the neutrons. To satisfy the mathematical formalism the detector is expressed as $(\varepsilon_+, \varepsilon_-)$ where ε_+, ε_- are the detector efficiencies [77]. Since the efficiency of ^{3}He detectors is not sensitive to the spin state of the neutron $\varepsilon_+ = \varepsilon_- = \varepsilon$.

The residual equations to describe polarized neutron reflectometry with polarization analysis are:

$$I^{--} = (\varepsilon_+, \varepsilon_-) \begin{pmatrix} R^+_{A\uparrow\downarrow} & 0 \\ 0 & R^-_{A\uparrow\downarrow} \end{pmatrix} \begin{pmatrix} R^{++} & R^{-+} \\ R^{+-} & R^{--} \end{pmatrix} \begin{pmatrix} R^+_{P\uparrow\downarrow} & 0 \\ 0 & R^-_{P\uparrow\downarrow} \end{pmatrix} \begin{pmatrix} n_+ \\ n_- \end{pmatrix} I_0, \quad (3.34)$$

$$I^{+-} = (\varepsilon_+, \varepsilon_-) \begin{pmatrix} R^+_{A\uparrow\downarrow} & 0 \\ 0 & R^-_{A\uparrow\downarrow} \end{pmatrix} \begin{pmatrix} R^{++} & R^{-+} \\ R^{+-} & R^{--} \end{pmatrix} \begin{pmatrix} R^+_{P\uparrow\uparrow} & 0 \\ 0 & R^-_{P\uparrow\uparrow} \end{pmatrix} \begin{pmatrix} n_+ \\ n_- \end{pmatrix} I_0, \quad (3.35)$$

$$I^{-+} = (\varepsilon_+, \varepsilon_-) \begin{pmatrix} R^+_{A\uparrow\uparrow} & 0 \\ 0 & R^-_{A\uparrow\uparrow} \end{pmatrix} \begin{pmatrix} R^{++} & R^{-+} \\ R^{+-} & R^{--} \end{pmatrix} \begin{pmatrix} R^+_{P\uparrow\downarrow} & 0 \\ 0 & R^-_{P\uparrow\downarrow} \end{pmatrix} \begin{pmatrix} n_+ \\ n_- \end{pmatrix} I_0, \quad (3.36)$$

where the subscripts of the reflectivities of polarizer and analyzer are related to the relative orientation of $\vec{M}_P$ and $\vec{M}_A$ with respect to $\vec{H}_G$. They are varied according to the desired spin selection.

Equations 3.31, 3.34, 3.35 and 3.36 form a set of equations describing the experiment, which can be expressed in a matrix notation:

$$\begin{pmatrix} I^{++} \\ I^{+-} \\ I^{--} \\ I^{-+} \end{pmatrix} = \frac{\varepsilon}{2} \begin{pmatrix} R^+_{A\uparrow\uparrow}R^+_{P\uparrow\uparrow} & R^-_{A\uparrow\uparrow}R^+_{P\uparrow\uparrow} & R^-_{A\uparrow\uparrow}R^-_{P\uparrow\uparrow} & R^+_{A\uparrow\uparrow}R^-_{P\uparrow\uparrow} \\ R^-_{A\uparrow\downarrow}R^+_{P\uparrow\uparrow} & R^+_{A\uparrow\downarrow}R^+_{P\uparrow\uparrow} & R^+_{A\uparrow\downarrow}R^-_{P\uparrow\uparrow} & R^-_{A\uparrow\downarrow}R^-_{P\uparrow\uparrow} \\ R^-_{A\uparrow\downarrow}R^-_{P\uparrow\downarrow} & R^+_{A\uparrow\downarrow}R^-_{P\uparrow\downarrow} & R^+_{A\uparrow\downarrow}R^+_{P\uparrow\downarrow} & R^-_{A\uparrow\downarrow}R^+_{P\uparrow\downarrow} \\ R^+_{A\uparrow\uparrow}R^-_{P\uparrow\downarrow} & R^-_{A\uparrow\uparrow}R^-_{P\uparrow\downarrow} & R^-_{A\uparrow\uparrow}R^+_{P\uparrow\downarrow} & R^+_{A\uparrow\uparrow}R^+_{P\uparrow\downarrow} \end{pmatrix} \begin{pmatrix} R^{++} \\ R^{+-} \\ R^{--} \\ R^{-+} \end{pmatrix} I_0. \quad (3.37)$$

Now, once the properties of polarizer and analyzer are known the reflectivities of the sample can be deduced from the measured intensities. The matrix in equation 3.37 contains eight unknowns, which are usually not determined easily. In the following these parameters are estimated for the particular conditions at AMOR.

At AMOR, the supermirrors for polarizer and analyzer have been produced in one run side by side during sputtering [78]. Therefore their properties might be considered identical, which has been confirmed by reflectivity measurements [79]. Figure 3.13 shows the performance of such remanent polarizing supermirrors dependent on the orientation of magnetization with respect to a small applied field, e.g. the guide field at AMOR. The performance appears to be almost identical for the two configurations. In the experimental setup at AMOR both mirrors are set to form the same angle (0.5°) with the respective incident neutron beam, which is the unpolarized beam from the neutron guide in case of the polarizer mirror and the beam reflected from the sample in case of the analyzer mirror. This is in particular important because in Time-of-Flight mode the complete reflectivity range of the supermirrors is utilized to polarize/analyze the wavelength dispersive spectrum of the neutron beam. Only with an identical reflection geometry of the polarizer and analyzer mirrors their properties can be identical within the complete spectrum.

The afore mentioned aspects make the assumption reasonable that the performance of polarizer and analyzer are identical and independent of their state of spin selection. Thus,

$$R^+ = R^+_{P\uparrow\uparrow} = R^+_{A\uparrow\uparrow} = R^-_{P\uparrow\downarrow} = R^-_{A\uparrow\downarrow} \tag{3.38}$$

and

$$R^- = R^-_{P\uparrow\uparrow} = R^-_{A\uparrow\uparrow} = R^+_{P\uparrow\downarrow} = R^+_{A\uparrow\downarrow}. \tag{3.39}$$

In general, the polarization P or the flipping ratio η are used to describe the efficiency of polarizing/analyzing devices. These can be expressed in terms of the supermirror reflectivities R^+ and R^- for the two spin states of the neutrons:

$$P = \frac{I^+ - I^-}{I^+ + I^-} = \frac{R^+ I_0 - R^- I_0}{R^+ I_0 + R^- I_0} = \frac{R^+ - R^-}{R^+ + R^-} \tag{3.40}$$

$$\eta = \frac{I^+}{I^-} = \frac{R^+ I_0}{R^- I_0} = \frac{R^+}{R^-}, \tag{3.41}$$

where I^+ and I^- are the intensities of the two spin states in the neutron beam after the polarizing device.

With the assumptions of equations 3.38, 3.39 and introducing the flipping ratio η (equation 3.41) equation 3.37 can be rewritten:

$$\begin{pmatrix} I^{++} \\ I^{+-} \\ I^{--} \\ I^{-+} \end{pmatrix} = \frac{\varepsilon I_0}{2R^- R^-} \begin{pmatrix} \eta^2 & \eta & 1 & \eta \\ \eta & \eta^2 & \eta & 1 \\ 1 & \eta & \eta^2 & \eta \\ \eta & 1 & \eta & \eta^2 \end{pmatrix} \begin{pmatrix} R^{++} \\ R^{+-} \\ R^{--} \\ R^{-+} \end{pmatrix}. \tag{3.42}$$

The number of unknowns in the matrix (incl. pre-factor) is significantly reduced now, and the residual parameters can be determined experimentally. Therefore, the polarized beam from the polarizer mirror is analyzed by the analyzer mirror. In terms of equation 3.42, this experiment is described with $R^{++} = R^{--} = 1$ and $R^{+-} = R^{-+} = 0$ resulting in:

$$\begin{pmatrix} I^{++} \\ I^{+-} \\ I^{--} \\ I^{-+} \end{pmatrix} = \frac{\varepsilon I_0}{2R^- R^-} \begin{pmatrix} \eta^2 + 1 \\ \eta + \eta \\ 1 + \eta^2 \\ \eta + \eta \end{pmatrix}. \tag{3.43}$$

Two of those four equations (e.g. I^{++} and I^{+-}) are sufficient to determine the residual unknowns in equation 3.42:

$$\eta = \frac{I^{++}}{I^{+-}} + \sqrt{\left(\frac{I^{++}}{I^{+-}}\right)^2 - 1} \tag{3.44}$$

$$\frac{\varepsilon I_0}{2R^- R^-} = \frac{I^{+-}}{\eta} \tag{3.45}$$

As AMOR is a ToF reflectometer these parameters are wavelength dependent and have to be determined for the full spectrum used in the experiment. Figure 3.16 depicts the wavelength dependent flipping ratio and polarization of the polarizing supermirrors. The measurement shows that a spectrum from $\lambda \approx 0.2$ to 1.2 nm can be reasonably utilized regarding the performance of the polarizing supermirrors. Smaller wavelengths are beyond the reflectivity range of the supermirror. At large wavelength, due to only finite absorption of the anti-reflection coating underneath the polarizing supermirror, residual neutrons with undesired spin state are totally reflected from the substrate, thus reducing the efficiency of polarization. Large fluctuations in the flipping ratio exist around $\lambda = 0.2$ and 0.6 nm, which correspond to the critical edge of the supermirror and to the transition from the regime of total reflection to the supermirror regime, respectively. Usually at those positions the reflectivity profiles of supermirrors show small fluctuations, which become emphasized in terms of the flipping ratio (equation 3.44). We apply the distribution of flipping ratio in figure 3.16 together with equation 3.42 to retrieve the spin dependent reflectivities of the sample from the measured intensities.

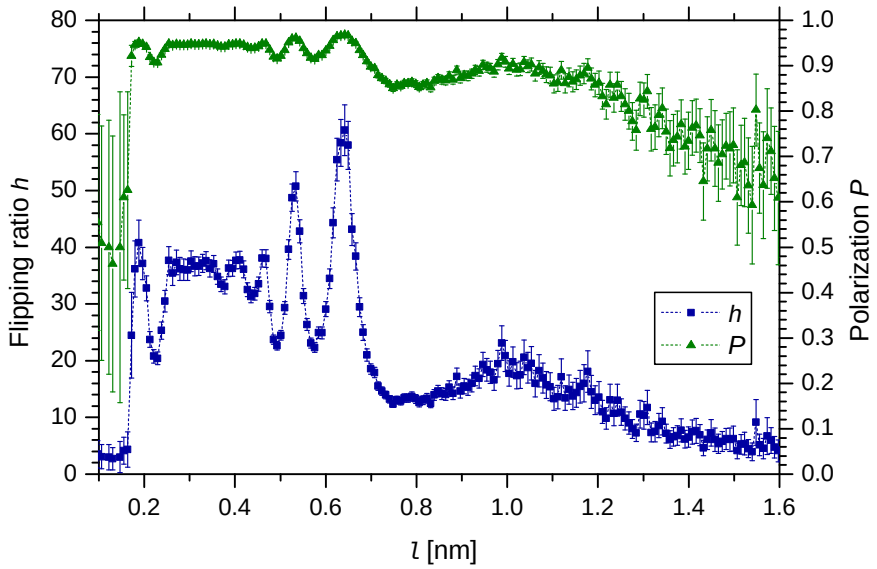

Figure 3.16: Wavelength dependent flipping ratio and polarization of the polarizing supermirrors employed at AMOR as beam polarizing and analyzing devices. Identical results are obtained for the setup with transformation of the polarization from horizontal to vertical and vice versa confirming the success of the transformation.

Chapter 4

Structural characterization

X-ray reflectometry and diffraction were employed to characterize the structure of the samples regarding their chemical depth profile and their out-of-plane texture, respectively.

The series of NiO single layers are produced with the purpose to find adequate conditions for the reactive sputtering of highly (111) textured NiO layers. The stoichiometry of the NiO films was measured using X-ray reflectometry and their texture was analyzed from X-ray diffraction patterns. Results of these experiments are presented and discussed in the first section of this chapter. The settings for the total pressure and the $Ar:O_2$ ratio of the sputter gas were deduced from these results and were then applied for the preparation of NiO-FeCoV multilayers.

FeCoV single layers, NiO-FeCoV bilayers and FeCoV/NiO/FeCoV trilayers are compared in the second section regarding their crystalline orientation of the NiO and FeCoV layers along the direction of growth. A dependence of the texture on the underlying material is found for the NiO layers whereas FeCoV layers grow always with identical texture.

The results of X-ray reflectometry on FeCoV single layers, bilayers and trilayers are shown and discussed in section four of this chapter. A detailed layer structure of the samples has been deduced from the refinement of models of the chemical depth profile. The models have been developed systematically from FeCoV single layers to trilayers via NiO-FeCoV bilayers. Due to this systematic procedure, fine details about layer thickness, interface roughness, interfacial layers and surface oxidation have been unraveled.

The last section of this chapter summarizes the information obtained from the structural characterization of all the series prepared within this project.

4.1 Chemical composition and crystalline structure of NiO single layers

In this project, we prepared NiO layers by reactive DC magnetron sputtering. Their stoichiometry and their crystalline structure depend on the preparation conditions. It

is even possible to tune the growth orientation by varying the combination of pressure and mixture of the Ar:O_2 sputter gas[1]. In order to find proper preparation conditions for stoichiometric and highly (111) textured NiO layers, we deposited a series of single layers at different total pressures and different Ar:O_2 ratios of the sputter gas (see section 2.3). We investigated their stoichiometry and crystalline structure by X-ray reflectometry and diffraction. In addition, a comparison of the color of the films provides a first qualitative information about the stoichiometry of the NiO layers. The color of Ni is metallic silver while it is green for NiO. Another oxidation state of Ni is Ni_2O_3, which has a color of dark grey to black. In the following, first, the results of these experiments are presented and second, they are discussed regarding the desired structure for NiO layers in this work. On the basis of these results, we deduced proper conditions for the preparation of NiO-FeCoV multilayers.

Figure 4.1 shows the reflectivity data of NiO single layers in a narrow range of the incident angle θ around the critical angle for total reflection. The plateau of total reflection is not very pronounced because of absorption of the X-rays. Absorption is highest at the critical edge since the penetration of the X-ray beam into the material is deepest there while the beam is still totally reflected leading to a rather smooth transition from the regime of total reflection to the regime of propagation in the material. As the edge at the critical angle is not sharp, its value is usually determined from the position where the reflectivity has value of 0.5 [65]. A clear dependence of the critical angle for total reflection on the sputter conditions is observed. At higher angles oscillations are visible, which originate from the total thickness of the film (Kiessig fringes).

The diffraction patterns of the NiO single layers are depicted in figure 4.2. Bragg peaks according the crystal structure of NiO are present but no peaks exist corresponding to crystalline Ni. The positions of the Bragg peaks are in rather good agreement with the positions of bulk NiO. Small deviations indicate a weak distortion of the crystal lattice. The intensity of the peaks depends significantly on the conditions of preparation. The relative intensities of the [111], [200] and [220] peaks of polycrystalline NiO are 75%, 100% and 57%, respectively [80]. In general, we observe that the relative intensities of the NiO single layers deviate from this distribution indicating preferred crystalline orientations in the NiO films induced by the growth process.

The critical angle for total reflection is related to the average X-ray scattering length density $\langle b_{at}\rho \rangle$, which decreases with increasing content of oxygen in the NiO_x layers (equation 3.2 and 3.10). The degree of oxidation of Ni during layer growth is expected to increase with the amount of oxygen available for the oxidation process, i.e. with increasing partial pressure p_{O_2} of oxygen in the sputter gas. Values of $\langle b_{at}\rho \rangle$ are calculated from the critical angles (figure 4.1) and plotted in figure 4.3 versus p_{O_2}. It shows that at low p_{O_2} the average scattering length density $\langle b_{at}\rho \rangle$ is the highest while at low p_{O_2} it is the lowest. A comparison of the two extreme cases regarding the color of the films shows that at low p_{O_2}, the color is metallic silver while at high p_{O_2} the color of the films turns grey. The results indicate the presence of residual but disordered Ni (no Bragg peaks) at low p_{O_2} and an excess of oxygen forming Ni_2O_3 at high p_{O_2}.

[1] In sputtering, the growth of films can be influenced by the variation of various other parameters e.g. substrate temperature, deposition rate, particle bombardment etc..

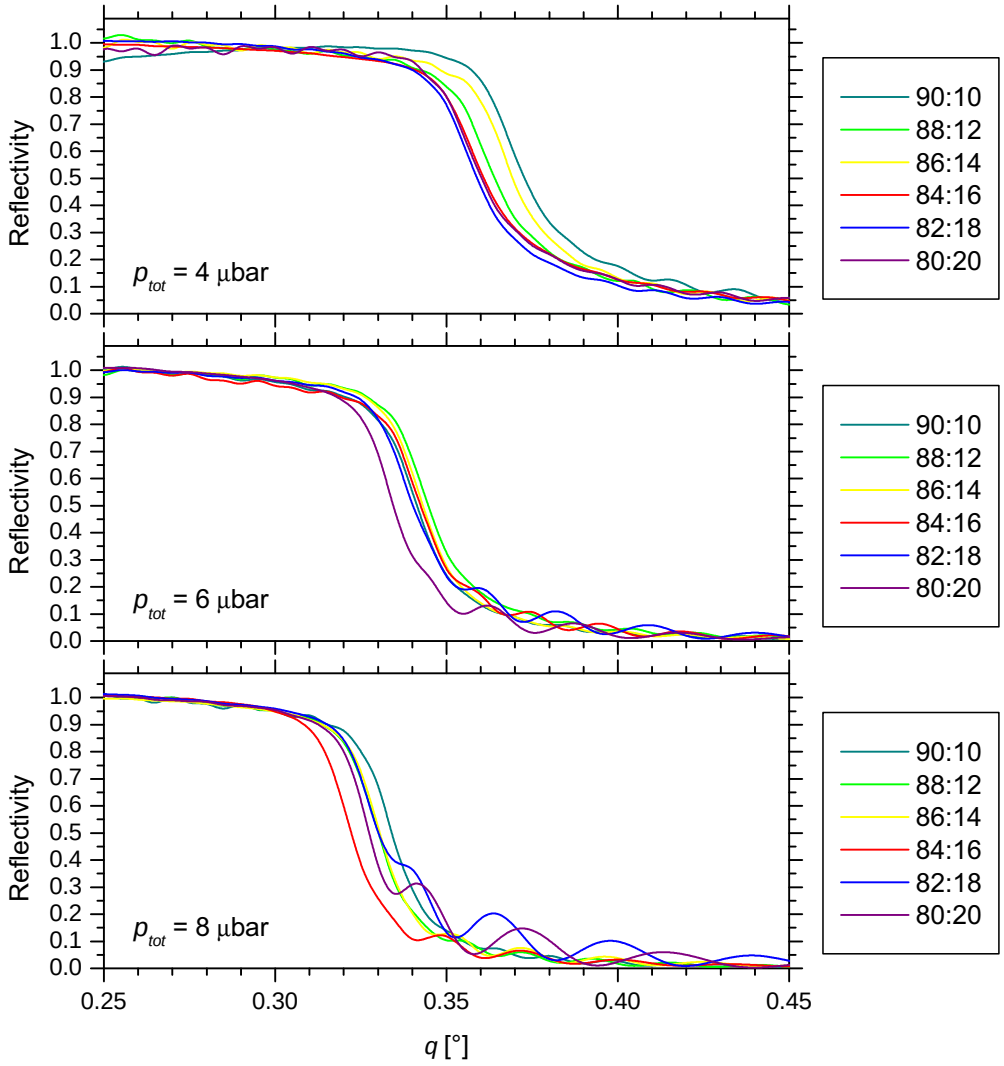

Figure 4.1: X-ray reflectivity data of NiO single layers on glass prepared at different total pressures p_{tot} and different $Ar{:}O_2$ ratios of the sputter atmosphere. The critical angle contains the information about the average scattering length density of the films.

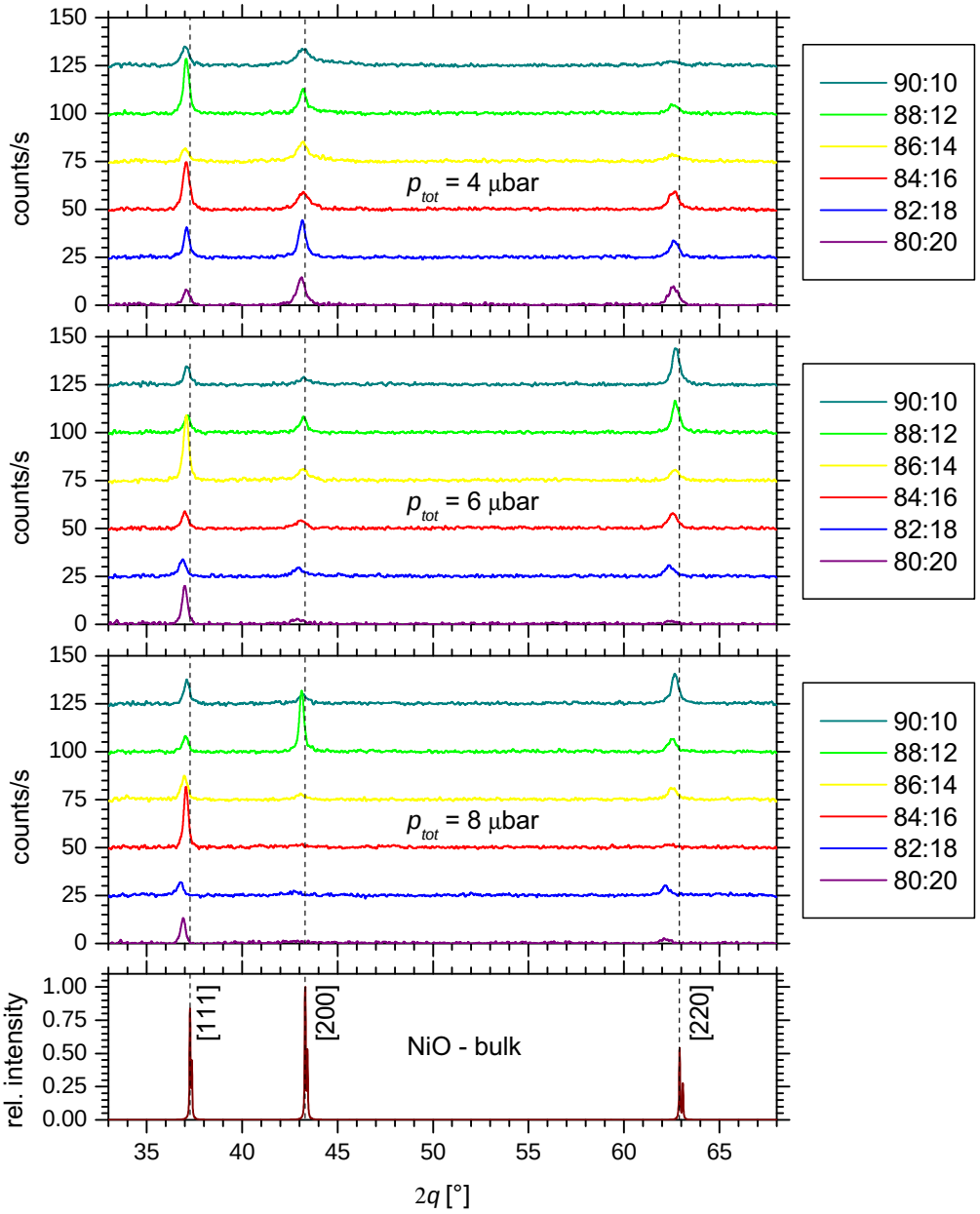

Figure 4.2: X-ray diffraction pattern of NiO single layers on glass prepared at different sputter conditions (p_{tot}, $Ar{:}O_2$ ratio). The diffraction patterns are vertically displaced for clarity. For comparison, the bottom diagram shows a calculated diffraction pattern [80] of bulk NiO indicating the relative intensities of the Bragg peaks for a polycrystalline material.

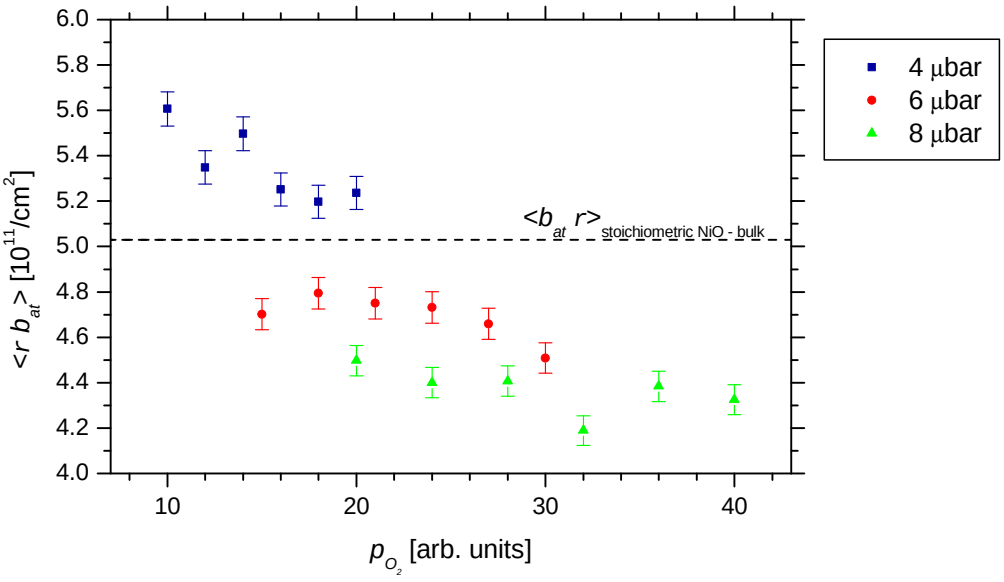

Figure 4.3: Average scattering length density $\langle \rho b_{at} \rangle$ for X-rays ($Cu_{K\alpha}$) of NiO single layers dependent on the O_2 partial pressure p_{O_2} of the Ar:O_2 sputter atmosphere. $\langle \rho b_{at} \rangle$ is calculated from the critical angle θ_c for total reflection (equation 3.10). The errors are deduced from the uncertainty of the alignment of the sample angle, which is estimated to be 0.005°.

Between low and high p_{O_2}, the dependence of the process of oxidation on the conditions of preparation appears more complex because no systematic variation with p_{O_2}, p_{tot} or Ar:O_2 is observed. Nevertheless, we find that at p_{tot} = 6 μbar the process of oxidation is rather stable for Ar:O_2 90:10 to 82:18 since $\langle \rho b_{at} \rangle$ is almost independent of the Ar:O_2 ratio. The stability in this regime suggests that the oxidation of Ni occurs via an equilibrium process, thus forming stoichiometric NiO. However, $\langle \rho b_{at} \rangle$ of these stoichiometric NiO layers is $\approx$ 6% smaller than for bulk NiO indicating a reduced density of the films. It has to be considered that X-ray reflectometry averages laterally over the in-plane coherence length of the X-ray beam, which is typically about 10 microns for the resolution of the X-ray beam used here [65]. Thus, it is sensitive to macroscopic defects like pores, which effectively reduce the scattering length density, consequently the critical angle.

Another possibility for a reduced density is an expanded crystal lattice. This may happen when oxygen atoms go to the interstitial sites of the lattice due to an excess compared to stoichiometric NiO. As a result the crystal lattice becomes expanded. In fact, we observe a small shift of the Bragg peaks, which is possibly a result of an expanded lattice. In order to test this possibility for NiO single layers prepared at p_{tot} = 6 μbar, the positions of the Bragg peaks (figure 4.2) were analyzed and the lattice constant is deduced. The calculated values are normalized by the lattice constant for bulk NiO and plotted in figure 4.4. In all NiO films, the lattice constant is very close to the bulk value confirming an almost undistorted NiO crystal lattice. Further, assuming a three dimensional expansion the volume of the unit cell will be increased by 2-3 %, which does not account for the reduced X-ray scattering length density of $\approx$ 6 %.

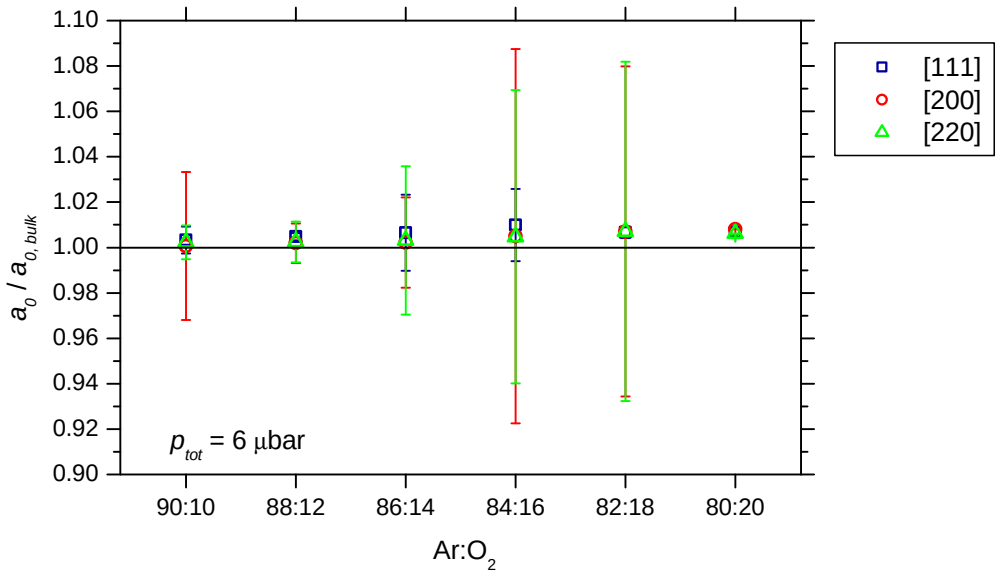

Figure 4.4: Normalized lattice constant a_0 of NiO single layers prepared at 6 µbar and various Ar:O_2 ratios. The values are calculated from the positions of the Bragg peaks (figure 4.2) and normalized by the lattice constant of bulk NiO $a_{0,bulk}$ = 0.4175 nm [81]. The error bars of some values are rather large since the intensity of the respective Bragg peaks is low allowing only a reduced accuracy in the determination of their position.

Finally, from the analysis of X-ray reflectivity and diffraction measurements, we concluded that NiO layers prepared at 6 μbar consist of stoichiometric NiO grains with bulk crystallinity but also contain some defects, which reduce the density when averaged on a macroscopic scale.

Obviously the density of the NiO films is even less at 8 μbar since $\langle \rho b_{at} \rangle$ is further reduced. The dependence of the density on the sputter pressure is known for sputter deposited films and is discussed in [82]. An increase of the pressure of the sputter gas increases the probability that target atoms collide with gas atoms. Consequently, their average kinetic energy decreases resulting in a reduced mobility of the atoms, which condense on the surface of the growing layer. When the mobility is low, grains grow preferentially in three dimensional islands leading to a reduced density of the film as probed in reflectometry.

In summary, the results from X-ray reflectivity show that at $p_{tot} = 6$ μbar, the formation of stoichiometric NiO takes place properly. In addition, the crystallinity depends on the Ar:O_2 ratio. The desired high (111) texture is obtained at a ratio of 86:14. Therefore, we prepared NiO layers in bilayer and trilayer samples by reactive sputtering at a total pressure of $p_{tot} = 6$ μbar and an Ar:O_2 ratio of 86:14.

4.2 Crystalline structure of FeCoV single layers and NiO-FeCoV multilayers

We measured the crystalline orientation of FeCoV single layers and NiO-FeCoV multilayers along the growth direction using symmetric X-ray diffraction. In this section, the experimental results are presented and the different series are compared regarding the dependence of the growth on the sequence of deposition of the materials. First, the diffraction patterns of FeCoV single layers represent the basic growth of FeCoV films. Second, the bilayer series allow a separate analysis of the texture of NiO and FeCoV layers depending on the underlying material. Finally the texture of the trilayers is compared with the results from single layer and bilayer series.

FeCoV single layers

Figure 4.5 shows the diffraction patterns for FeCoV single layers with $t_{FeCoV} = 20$ and 40 nm. The Bragg peaks for $t_{FeCoV} = 5$ nm cannot be measured because of the small thickness of the FeCoV layer. Hence, the number of coherent planes of the crystal lattice is very small and the intensities of the peaks are only of the order of the background. Peaks of the Ti buffer and capping layers are not visible because of the same reason. In addition, we measured the diffraction pattern of the target material, which is plotted in figure 4.5 for comparison. The target material can be considered to be almost polycrystalline showing peaks of [110] and [200] orientations. Due to the high symmetry of the crystal structure no other peaks are expected in the measured range. The high intensity of the Bragg peaks from the target material is due to the larger fraction of volume, which scatters coherently in bulk than in thin films. In case of FeCoV single layers only [110] peaks are present in the diffraction pattern indicating a pronounced (110) out-of-plane texture of the films.

The texture is a consequence of the condition that thin films usually tend to grow with lattice planes of highest area density [83] parallel to the film plane. Therefore, materials with a bcc crystal structure, e.g. FeCoV, exhibit a (110) out-of-plane texture in thin films. Furthermore, FeCoV layers are expected to grow preferentially with (110) texture because of the distribution of Fe and Co atoms in the lattice of the bulk material. For temperatures below 1000 K, like during the sample preparation here, Fe and Co atoms order in a bcc B2-phase (see section 2.1.1) occupying different sublattices. In sputtering from an alloy target, the sputtering yields of all constituents of the alloy are usually very similar leading to the same number of atoms arriving per unit time at the surface of the sample. As a result, during the growth of FeCoV an equal number of Fe and Co atoms (neglecting V) must be accommodated at the same time. Therefore, the atoms prefer to arrange in a lateral order of lattice planes with an equal distribution of Fe and Co. This condition is fulfilled for (110) planes of FeCoV leading to a (110) texture out-of-plane. The amount of vanadium is very small and the V atoms are expected to be arbitrarily distributed but do not affect the basic growth regarding the crystalline orientation. However, films deposited by sputtering typically consist of grains of single crystals with out-of-plane texture but their in-plane orientations are randomly distributed. This can also be assumed for FeCoV layers in this work, as neither the amorphous substrate promotes a growth of the films with a preferred

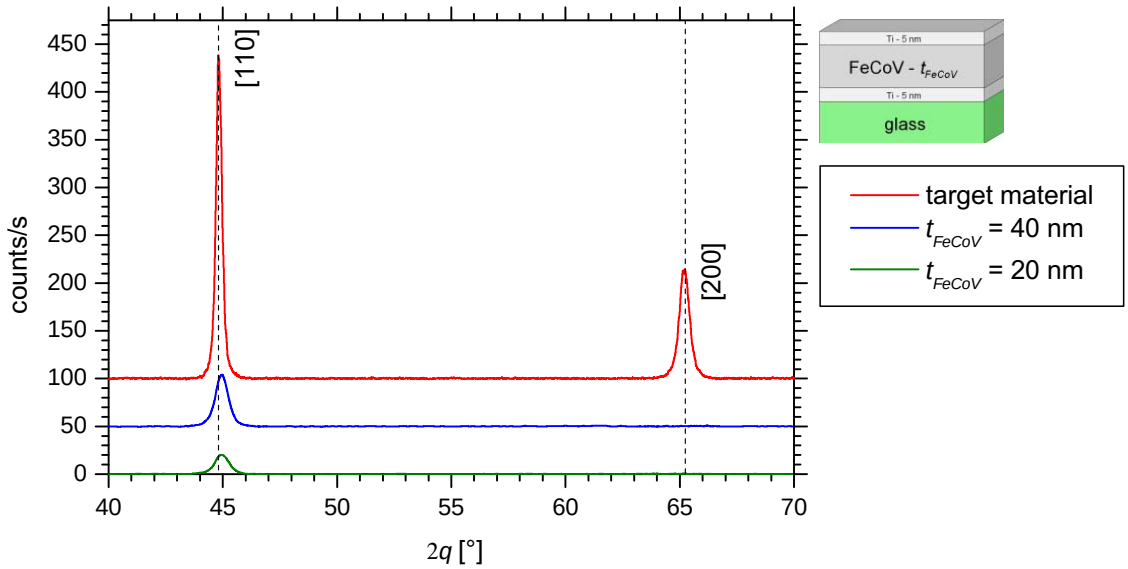

Figure 4.5: X-ray diffraction patterns of samples Ti (5 nm)/FeCoV (t_{FeCoV})/Ti (5 nm) and of the FeCoV target material. The diffraction patterns are vertically displaced for clarity. The vertical, dashed lines represent the positions of the peaks for bulk FeCoV, plotted for comparison.

in-plane orientation nor the preparation conditions are optimized for epitaxial growth in particular.

We determined the positions of the Bragg peaks from fitting a Gaussian function[2] to the experimental data and calculated the lattice parameter a_0. For FeCoV thin films (TF) $a_{0,TF} = (0.2849 \pm 0.001)$ nm and for the FeCoV target material $a_{0,bulk} = (0.2857 \pm 0.0002)$ nm. A detailed investigation of the dependence of lattice parameters of Fe-Co binary systems on the concentration of Fe and Co and the ordering phase is reported in [84]. There, a_0 is found to be 0.2857 nm for an equal content of Fe and Co in the ordered B2-phase which is in accordance with the value of $a_{0,bulk}$ measured on the target material. Although the lattice parameters obtained for FeCoV thin films and bulk are identical within the errors, the smaller value for $a_{0,TF}$ might be real as it is consistent for both thicknesses of the FeCoV layers. In [84], it is also reported that a_0 in the disordered A2-phase is 0.05 % smaller than that in the ordered phase. Assuming absolute accuracy for the deduced lattice parameters this would not account for the reduced value observed in FeCoV thin films. Additionally the ordered B2-phase is expected because of the course of growth as described above. Therefore the deviation of a_0 in FeCoV layers from bulk is more likely associated to a small distortion of the crystal lattice because of strain. Since $a_{0,TF}$ is deduced from the vertically stacked (110) planes, it suggests compressive stress out-of-plane. Hence, assuming conservation

[2]Usually, to account for the influence of grain size, strain etc. on the line shape of the Bragg peaks, more complex functions like Voight function are necessary. However, the Gaussian function provides sufficient accuracy for the determination of the position of the Bragg peaks as long as these have a symmetric shape.

of the unit cell volume tensile stress would be present in the plane of the layers.

FeCoV/NiO and NiO/FeCoV bilayers

The diffraction patterns of FeCoV/NiO and NiO/FeCoV bilayers are depicted for various t_{NiO} in figure 4.6. Several peaks appear corresponding to NiO and FeCoV Bragg peaks. As discussed above for the cases of thin FeCoV and Ti layers, the intensity of the NiO peaks decreases with decreasing t_{NiO} becoming comparable to the background for $t_{NiO} < 20$ nm.

In all samples FeCoV peaks are only present at the [110] position as a result of the textured growth as observed in FeCoV single layers as well. However, the intensities of the FeCoV Bragg peaks of NiO/FeCoV bilayers are significantly lower than in the case of FeCoV single layers and FeCoV/NiO bilayers. The lower intensity is due to a lower number of scattering planes contributing to the Bragg peak, which either can be caused by a smaller vertical grain size, or by an imperfect stacking of the lattice planes. We estimated the vertical grain size using the Scherrer formula [85]. The results show that the grain size is approximately equal to the layer thickness in all cases excluding the first possibility mentioned before. Consequently, when FeCoV is grown on NiO layers the stacking of the (110) lattice planes appears to have a larger distribution with respect to being parallel to the film plane but still maintaining a preferential growth with highest atomic area density in the plane of the layers. The intensities of FeCoV [110] peaks are almost identical for all NiO/FeCoV bilayers. Considering that the thicknesses of the FeCoV layers are identical, it suggests that the growth of FeCoV is independent of the thickness of the underlying NiO layer. In all samples of the bilayer series the Bragg peaks of FeCoV are slightly displaced from their bulk position as observed in the series of FeCoV single layers as well indicating a small distortion of the crystal lattice.

NiO/FeCoV bilayers exhibit strong [111] and [200] peaks as well as weak [220] peaks of NiO. The intensities of [111] peaks relative to [200] peaks are approximately two times higher than expected for a polycrystalline distribution and indicates that NiO layers consist predominately of grains with a (111) out-of-plane texture. This is in accordance with the structure observed in NiO single layers prepared at the same sputter conditions. In contrast to that, the diffraction pattern of the FeCoV/NiO bilayer with $t_{NiO} = 60$ nm exhibits strong peaks corresponding to the [111] and [200] orientations of NiO. Only a weak [220] peak is observed whose intensity is approximately a factor three lower than that expected in polycrystalline NiO. As a result, the NiO layers on top of FeCoV are not completely polycrystalline but contain two types of grains with different out-of-plane textures. In the case of grains with (111) texture out-of-plane, a small shift of the Bragg peak from the position in bulk is identified showing that the (111) planes have a slightly increased distance. A detailed discussion regarding the dependence of the textured growth on the underlying surface is given below following the results on FeCoV/NiO/FeCoV trilayers.

FeCoV/NiO/FeCoV trilayers

Figure 4.7 shows the diffraction patterns of FeCoV/NiO/FeCoV trilayers for various t_{NiO}. The intensities of FeCoV [110] peaks are almost identical for all samples of the

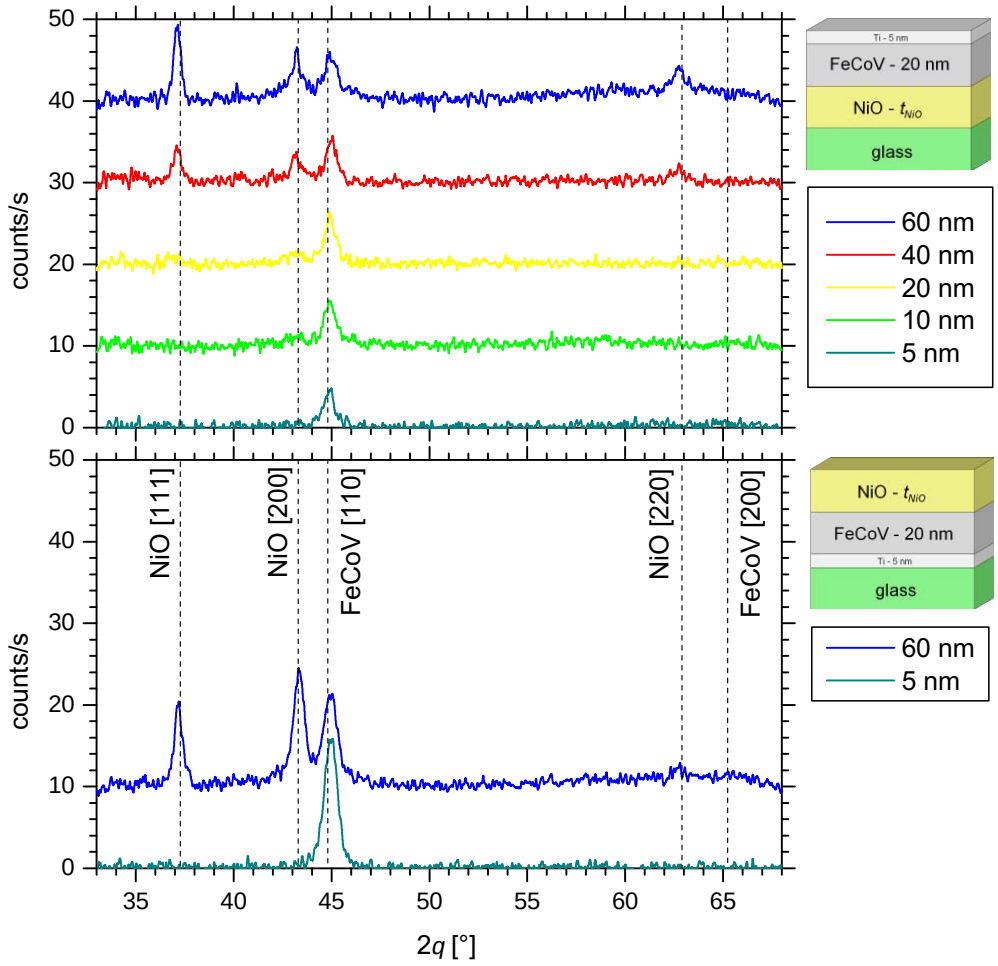

Figure 4.6: X-ray diffraction patterns of NiO/FeCoV (20 nm) and FeCoV (20 nm)/NiO bilayers with different t_{NiO}. The diffraction patterns are vertically displaced for clarity. The vertical, dashed lines represent the positions of FeCoV and NiO peaks for bulk.

trilayer series. A comparison with the bilayers shows that the intensity of the trilayers is the sum of the intensities of FeCoV/NiO and NiO/FeCoV bilayers. Again a small distortion of the crystal lattice of FeCoV is evident because of the small shift of the positions of the Bragg peaks compared to the position in bulk FeCoV.

The intensity of the NiO peaks decreases with decreasing t_{NiO} unless it is only of the order of the background for $t_{NiO} < 10$ nm. The distribution of intensity of the NiO Bragg peaks resembles the pattern of the FeCoV/NiO (60 nm) bilayer (figure 4.6), hence indicating the existence of two types of grains with out-of-plane textures of (111) and (200), respectively. The relative intensities of [111] and [200] peaks are approximately constant for all NiO thicknesses below 80 nm. For $t_{NiO} = 100$ nm the intensity of the [111] peak is significantly higher than the intensity of the [200] peak. As the underlying FeCoV surface, on which NiO is grown, is identical for all samples, we can assume that the growth of NiO also starts always in an identical way. Consequently, the concurrent evolution of the NiO Bragg peaks suggests that, for $t_{NiO} < 80$ nm

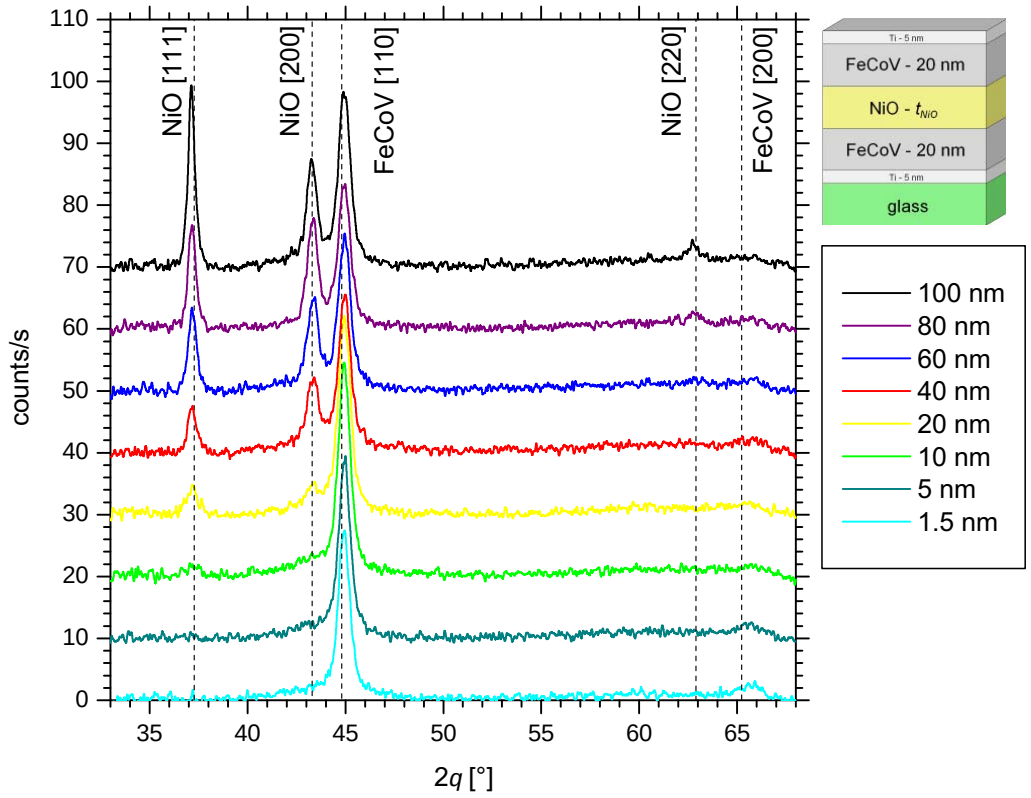

Figure 4.7: X-ray diffraction patterns of FeCoV (20 nm)/NiO (t_{NiO})/FeCoV (20 nm) trilayers. The diffraction patterns are vertically displaced for clarity. The vertical, dashed lines represent the positions of FeCoV and NiO peaks for bulk samples, plotted for comparison.

both textures grow simultaneously within individual grains. Furthermore, the ratio of the intensities between the two NiO Bragg peaks is approximately the same as for a polycrystalline structure [81] suggesting an equal distribution of grains with (200) and (111) textures. For $t_{NiO} = 100$ nm it is possible that the structure of grains, originally growing with (200) texture, collapses around $t_{NiO} = 80$ nm and the growth continues with a [111] texture favored at the conditions of preparation. Like in FeCoV/NiO bilayers, the NiO grains with (111) texture exhibit a small out-of-plane expansion of the crystal lattice as indicated by the displacement of the position of the [111] Bragg peaks.

Discussion of the texture of NiO layers

Finally, we discuss the different textures of NiO layers in FeCoV/NiO, NiO/FeCoV bilayers and in trilayers. We find that the growth of NiO in NiO/FeCoV bilayers is according to the NiO single layer counterpart. In both cases NiO is deposited directly on glass and exhibits a predominate (111) texture. Since the amorphous surface of the glass substrate does not assist any particular crystalline orientation of the NiO layer, the growth is determined by the sputtering conditions, which are tuned to achieve (111) texture out-of-plane.

It appears that the crystalline orientation is different when NiO grows on FeCoV as in the case of FeCoV/NiO bilayers and trilayers. Here, the diffraction patterns reveal the existence of two types of grains, i.e. with (111) and (200) textures, respectively. The (111) texture is expected since it is the preferred growth of NiO at the chosen conditions of preparation. In addition, the (111) texture satisfies the condition of highest atomic area density in the plane of the layer and is therefore favored in the growth of materials with fcc crystal structure [56]. The (200) texture is obviously promoted by the underlying FeCoV layer.

Usually for two materials with different equilibrium lattice constants, e.g. NiO and FeCoV, a mismatch between the lattices of the two materials exists at the interface. In that case, the next layer is initially forced to grow in registry with the underlying lattice causing strain and an extra contribution to the free energy [83]. Therefore, the minimization of the lattice mismatch is a decisive factor for the crystalline orientation of the growing layer. The mismatch is characterized by the lateral nearest neighbor distance of atoms of the two materials [56]. Within the (110) planes of FeCoV the nearest neighbor distance $d_{NN,FeCoV(110)}$ is 0.2474 nm. The according planes of the predominately observed (111) and (200) textures of NiO have nearest neighbor distances of $d_{NN,NiO(111)} = 0.2955$ nm and $d_{NN,NiO(200)} = 0.2090$ nm, respectively. As a result, the mismatch f:

$$f = \frac{d_{NN,NiO}}{d_{NN,FeCoV(110)}} - 1 \tag{4.1}$$

is +19 % for FeCoV (110)/NiO (111) and -16 % for FeCoV (110)/NiO (200), thus, the latter combination appears to be slightly favorable. However, additional complexity arises due to roughness and the reactive sputtering which involves oxidation processes of the growing NiO layer as well as of the underlying FeCoV surface in the growth mechanism. Apparently, local details at the interface, which have obviously a random distribution here, decide whether NiO grains grow with (200) or (111) texture.

4.3 Chemical depth profile of FeCoV single layers and NiO-FeCoV multilayers

The chemical depth profiles of the samples were probed measuring specular X-ray reflectivity (see sections 3.2.1 and 3.3). We compared the experimental data with reflectivity profiles computed from models of the vertical layer structure. The model parameters were refined through a fitting procedure using the software tool '*SimulReflec*' [71]. In particular, we obtained the scattering length density and the thickness of the layers as well as the roughness at the interfaces. A systematic development of the models from the FeCoV single layers via the bilayers to the trilayers enabled us to deduce fine details of the layer structure. Accordingly, the results of specular reflectometry are presented and discussed in the following. This section is completed with results of initial X-ray off-specular reflectivity measurements on selected trilayer samples, which provide a qualitative information about the vertical conformity of the profile of the interfaces.

FeCoV single layers

Figure 4.8 shows the reflectivity profiles of Ti/FeCoV/Ti samples with different thicknesses of FeCoV. Below $Q_z \approx 0.5$ nm^{-1} a plateau of almost constant reflectivity exists corresponding to the regime of total reflection of the X-ray beam. The small slope in this range and a rather smooth variation around the critical edge for total reflection are a consequence of the finite penetration of the X-ray beam into the film, accompanied by absorption. Beyond the critical edge, the reflectivity shows oscillations because of the interference of partial waves reflected from different interfaces of the samples. The interference patterns contain the information about the vertical layer structure.

Since the samples are not composed of a periodic motif, no superlattice Bragg peaks are present. The basic oscillations arise from the interference of partial waves reflected at the surface and at the interface between the film and the substrate. These oscillations are known as Kiessig fringes and contain the information about the total thickness of the films. Therefore, their periodicity decreases with increasing thickness of the FeCoV layer according to the inverse relation of reciprocal and real space. The original, regular Kiessig fringes are distorted due to the contribution from partial waves originating from the interfaces between FeCoV layers and the Ti buffer/capping layers. The region right beyond the critical edge ($Q_z \approx 0.7$ nm^{-1}) is very sensitive to the surface oxidation of the Ti capping layer, which is identified in all samples. Thus, it allows a precise determination of the variation of the refractive index at the surface of the samples. The complete reflectivity profiles are used to refine the parameters of the layer models.

We find that simple models of Ti/FeCoV/Ti layers with proper layer thicknesses and interface roughnesses do not provide good agreement between experimental and computed data. Additional thin layers at the interfaces are required in the models to reproduce the experimental reflectivities satisfactorily. Table 4.1 summarizes the parameters of the final models. The computed reflectivities based on these models are included in figure 4.8.

Extra thin layers are introduced at the interfaces between the glass substrates and the Ti buffer layers in order to account for the gradual distribution of the refractive index. The smooth transition is presumably a consequence of the depth profile of the scattering length density at the glass surface and that titanium reacts chemically with the surface of the glass due to its high affinity. As a result a mixed region forms with a scattering length density intermediate between the values for glass and Ti. The situation is similar at the interface between the Ti buffer layers and the FeCoV layers. Here, the interfacial layers of intermediate scattering length density indicate a region where the two materials are interdiffused. The Ti capping layers are enormously affected by surface oxidation forming layers of TiO_2 with a thickness of ≈ 4 nm when the samples are exposed to air after preparation. The residual Ti layers exhibit a scattering length density slightly higher than that for bulk. Most likely, it reflects an interdiffusion of FeCoV and Ti at their common interface as it is observed between the Ti buffer layer and the FeCoV layer as well. Finally, the introduction of a terminating layer of rather low density on the top of the layer sequence improves the agreement between experi-

t_{FeCoV}	5 nm				20 nm				40 nm			
	t [nm]	ρb_{at} [10^{11} cm^{-2}]	Σ_a [10^{10} cm^{-2}]	σ_{rms} [nm]	t [nm]	ρb_{at} [10^{11} cm^{-2}]	Σ_a [10^{10} cm^{-2}]	σ_{rms} [nm]	t [nm]	ρb_{at} [10^{11} cm^{-2}]	Σ_a [10^{10} cm^{-2}]	σ_{rms} [nm]
glass	-	1.96	0.17	0.21	-	1.96	0.17	0.29	-	1.96	0.17	0.25
glass-Ti	0.74	2.41	1.61	0.01	0.81	2.54	1.70	0.06	0.75	2.64	1.77	0.04
Ti	4.37	3.55	2.98	0.60	4.20	3.55	2.98	0.91	4.39	3.55	2.98	0.52
Ti-FeCoV	0.56	4.01	1.77	0.27	0.55	4.78	2.11	0.21	0.50	4.53	1.99	0.31
FeCoV	4.38	5.95	8.08	0.40	17.7	5.95	8.08	0.45	33.0	5.95	8.08	0.57
Ti	2.79	3.72	3.13	0.56	2.51	3.76	3.16	0.75	2.42	3.76	3.16	0.71
TiO_2	3.88	3.19	1.60	0.51	3.92	3.19	1.60	0.53	4.08	3.19	1.60	0.55
TiO_xX	0.83	0.26	0	0.08	1.35	0.61	0	0.24	0.85	0.41	0	0.27

Table 4.1: Model parameters for samples glass/Ti (5 nm)/FeCoV (t_{FeCoV})/Ti (5 nm) with nominal thicknesses t_{FeCoV} = 5, 20, 40 nm. The parameters of individual layers are the thickness t, the scattering length density ρb_{at} and the absorption cross-section $\Sigma_a = r_0 \rho f''$ for X-rays ($\lambda = 0.154$ nm) and the RMS value of the interfacial roughness σ_{rms}. The errors of the given values are of the order of 5 %. This is estimated from the Q-resolution of the experiment and the relation between the critical angle and the scattering length density (equation 3.10). Additionally, the estimated error is supported testing the stability of the set of parameters by modifying parameters purposefully and repeating the refinement procedure again.

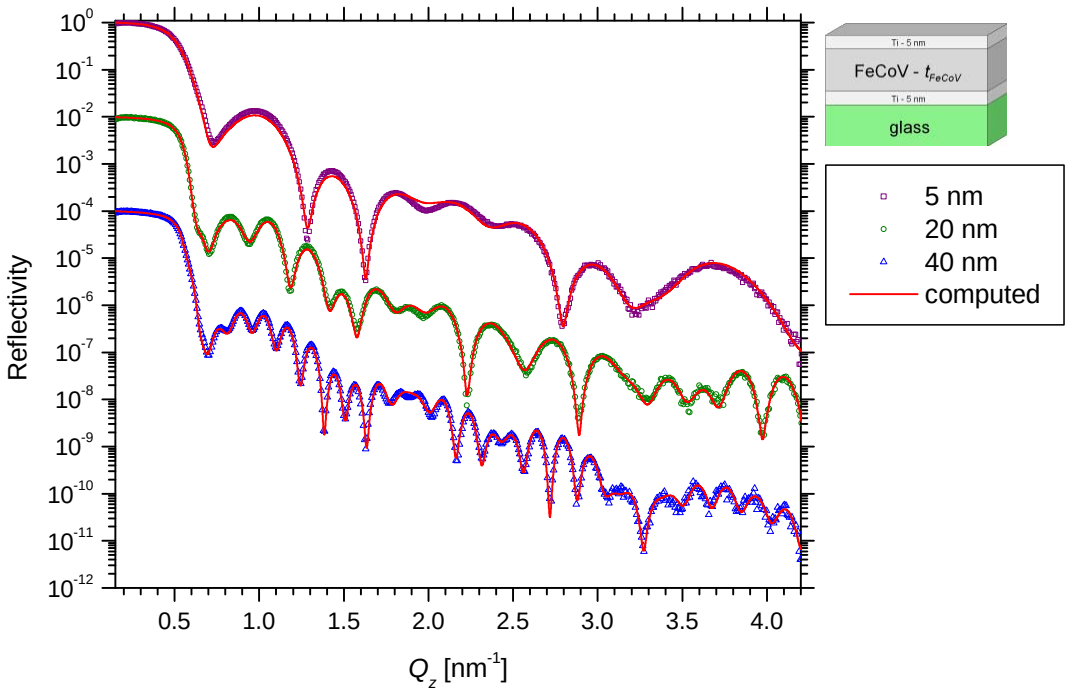

Figure 4.8: X-ray reflectivity profiles of samples Ti (5 nm)/FeCoV (t_{FeCoV})/Ti (5 nm). Experimental data (symbols) are shown together with computed reflectivities (lines) from proper layer models (see table 4.1). The profiles are vertically shifted for clarity.

mental and computed reflectivities. This is understood as an adsorption on the surface of the sample. In general, we find that within the first few nm the scattering length density varies strongly because of oxidation and adsorption as mentioned before. Nevertheless, the deduced combination of layer thicknesses, scattering length densities and roughnesses accounts for this variation properly.

The complete depth profiles of the scattering length density are computed from the parameters in table 4.1 and are depicted in figure 4.9. The sequence of the plateaus in the scattering length density, starting from the substrate, is according the sequence of the basic layers: Ti/FeCoV/Ti/TiO_2. The smooth transitions at the interfaces and at the surface represent the gradual variation of the scattering length density including interfacial roughness and additional layers as discussed above. The scattering length densities of the FeCoV and Ti buffer layers correspond to their bulk values.

The actual thicknesses of the FeCoV layers deviate from the nominal values because the calibration was optimized in detail for the particular sputter conditions used in this project. A relative variation of the layer thicknesses was aimed by adjusting the velocity of the substrate translation during deposition. The velocities of the substrate translation was set to 0.74, 0.19 and 0.1 m/min resulting in actual thicknesses t_{FeCoV} = 4.38, 17.65 and 33.00 nm, respectively. According to the relative variation of velocity, the thicknesses of the FeCoV layers were obtained precisely. This suggests that only a relatively small amount of the FeCoV material diffuses into the adjacent

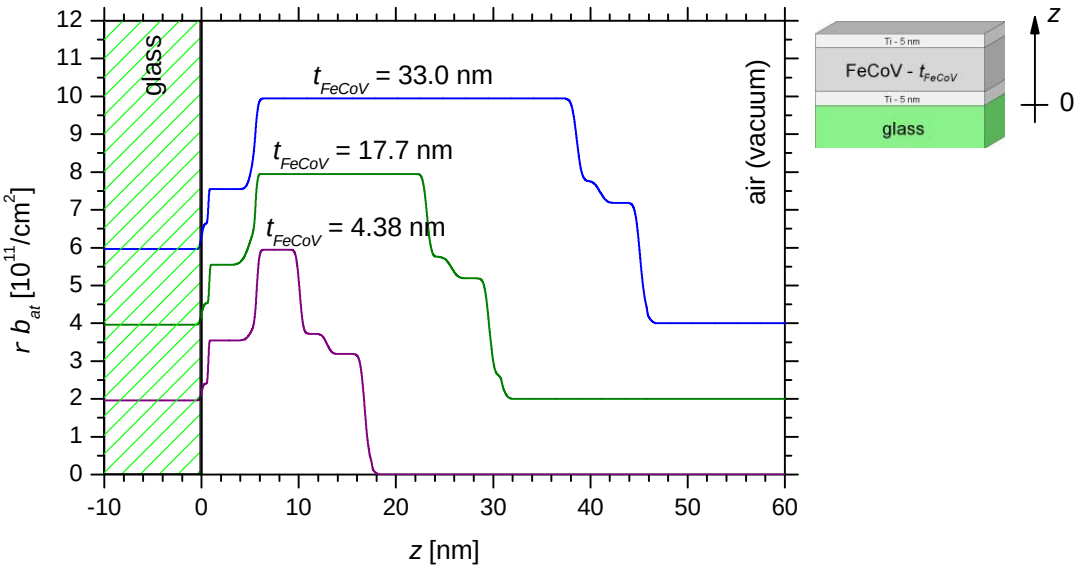

Figure 4.9: Profiles of the scattering length density of Ti (5 nm)/FeCoV (t_{FeCoV})/Ti (5 nm) samples computed from the parameters of the layer models (table 4.1) [71]. z is the distance form the surface of the substrate. The plateau belonging to FeCoV increases with increasing t_{FeCoV}. Corresponding actual values are included. The profiles are vertically shifted for clarity.

layers as discussed above. This is supported by the fact that the scattering length densities of the intermediate layers on either side of the FeCoV layer are significantly closer to the values for Ti than for FeCoV (see table 4.1).

FeCoV/NiO and NiO/FeCoV bilayers

The experimental reflectivities of FeCoV/NiO and NiO/FeCoV bilayers are presented in figure 4.10 together with computed profiles. As discussed above in the case of FeCoV single layers, the regimes of total reflection and Kiessig fringes can be identified. Regarding the critical edge of total reflection, the FeCoV/NiO bilayer with $t_{NiO} = 60$ nm represents an exception. Here, the critical edge appears rather sharp compared to all other samples, which is a consequence of only little absorption in the NiO layer while the X-ray beam is totally reflected. This does not account for the FeCoV/NiO bilayer with $t_{NiO} = 5$ nm because the penetration of the X-ray beam in the regime of total reflection is up to ≈ 10 nm [64] and therefore, the beam still "sees" the underlying FeCoV layer, which has higher absorption. The periodicity of the Kiessig fringes decreases with increasing total thickness of the samples as discussed above for the case of FeCoV single layers. A deviation of this behavior occurs in the case of FeCoV/NiO bilayers for approximately $Q_z > 1.5$ nm^{-1}. There, the periodicity ΔQ_z appears to be independent of the total thickness of the films. An estimation of the according dimension in real space using $t = 2\pi/\Delta Q_z$ results in $t \approx 23$ nm, which matches very well with the sum of the thicknesses of the Ti buffer layer and the FeCoV layer (see appendix A). It indicates that the reflectivity profile in this range is dominated by the interference of partial waves originating from the glass/film interface and the FeCoV/NiO interface.

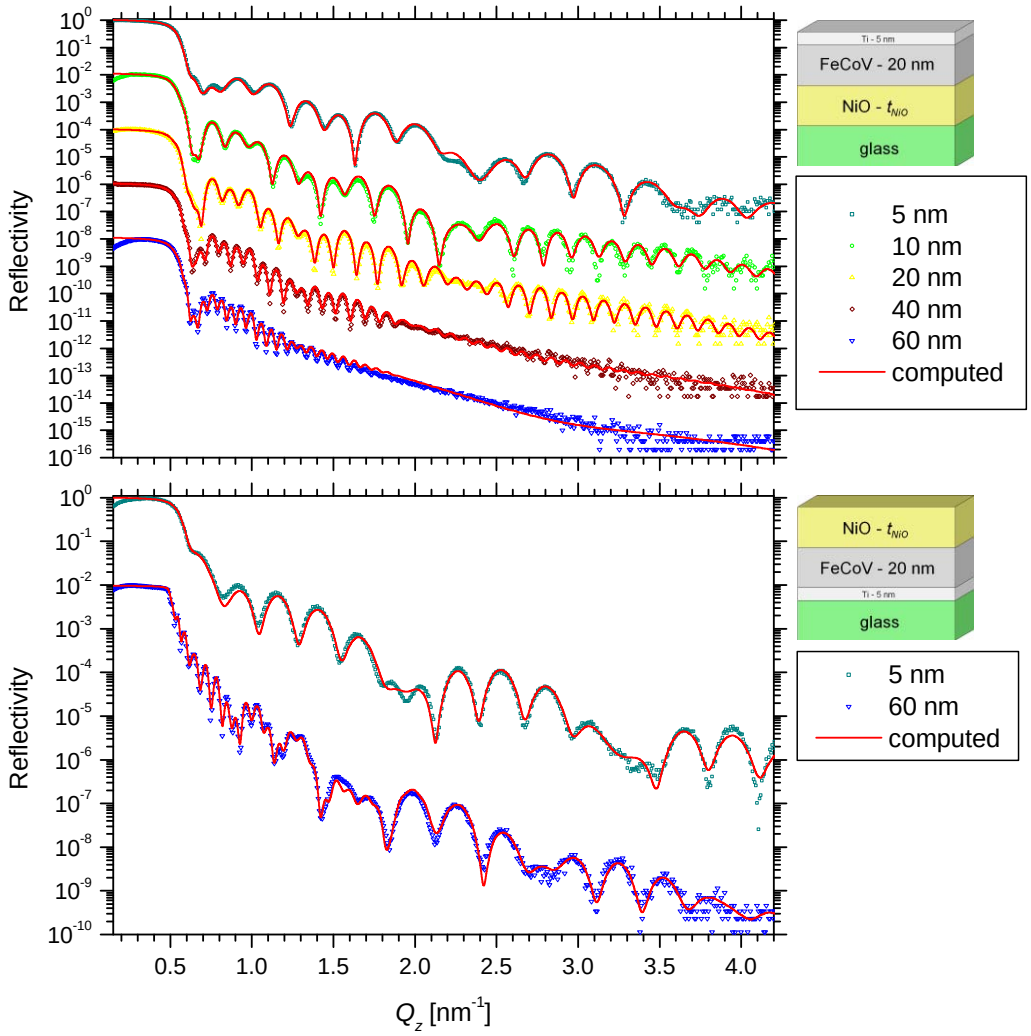

Figure 4.10: X-ray reflectivity profiles of samples NiO (t_{NiO})/FeCoV (20 nm) and FeCoV (20 nm)/NiO (t_{NiO}). Experimental data are shown as symbols whereas computed reflectivities are represented by lines. The profiles are vertically shifted for clarity.

The Kiessig fringes are suppressed at high Q_z because of relatively high roughness at the surface of the sample. The situation is similar in the case of NiO/FeCoV bilayers where the decreasing amplitude of the Kiessig fringes suggests an increase of the interfacial roughness with increasing t_{NiO}.

We refined models of the layer structure in order to reproduce the measured reflectivity data with computed profiles (figure 4.10). The parameters of the final models are summarized in tables A.1 and A.2 (appendix A). Depth profiles of the respective scattering length density are depicted in figure 4.11 for selected samples. The sequences of the plateaus in the profiles of the scattering length density are according the layer structure illustrated in the schematics of figure 4.11.

The models for NiO/FeCoV bilayers consist of the nominal layer structure with proper

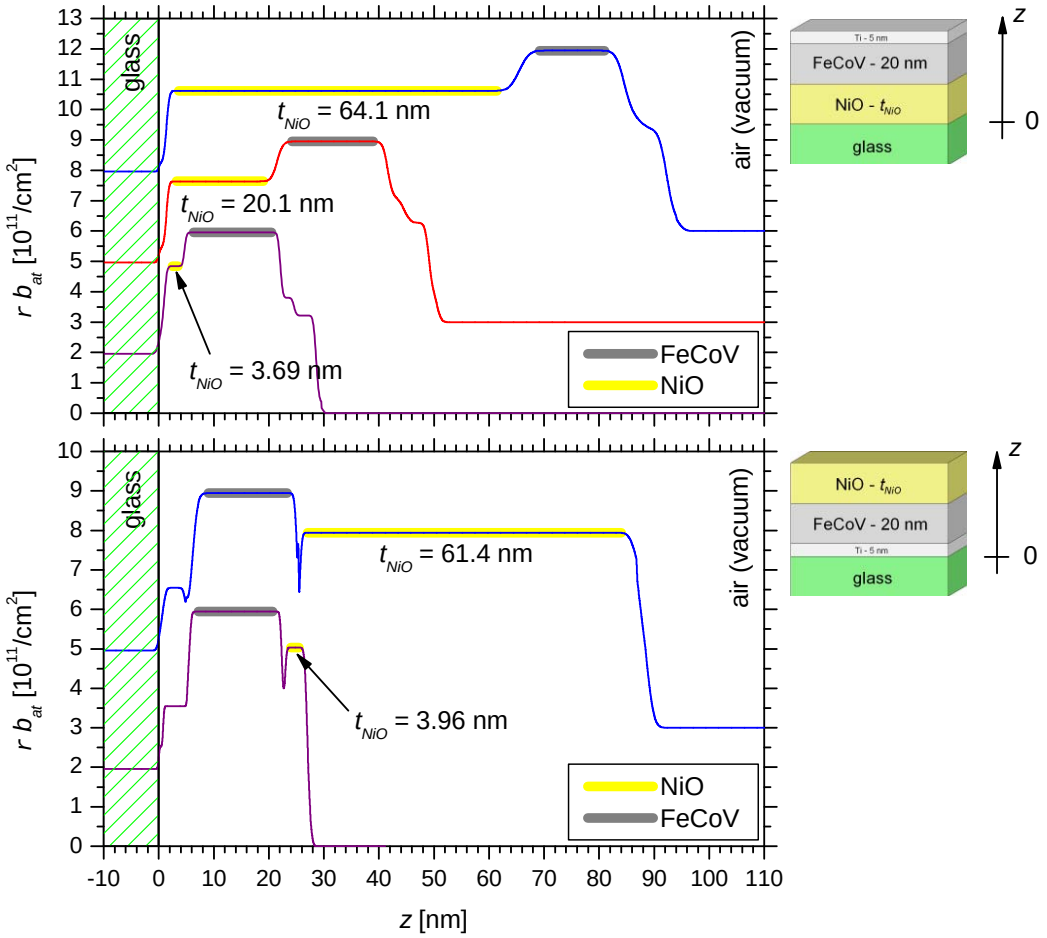

Figure 4.11: Profiles of the scattering length density of NiO (t_{NiO})/FeCoV (20 nm) and FeCoV (20 nm)/NiO (t_{NiO}) bilayers computed from the parameters of the layer models (table A.2) [71]. z is the distance form the surface of the substrate. The plateau belonging to NiO increases with increasing t_{NiO}. Corresponding actual values are included. The ranges of NiO and FeCoV layers are highlighted with bars of individual colors. The profiles are vertically shifted for clarity.

thicknesses and roughnesses of the NiO and FeCoV layers. The oxidation of the Ti capping layer is included the same way as discussed above for FeCoV single layers. We find a scattering length density of $(4.7 \pm 0.1) \cdot 10^{11}$ cm^{-2} for NiO, consistently for all NiO/FeCoV bilayers. This is ≈ 7 % lower than for bulk NiO but it is consistent with the value measured on the NiO single layer prepared under identical sputter conditions (see section 4.1). Apparently, this is a general feature at the chosen sputter conditions when NiO is grown directly on glass. The scattering length densities of the other layers are identical to their counterparts in the series of FeCoV single layers. The roughness of the NiO layer increases from ≈ 0.4 to 1.8 nm for $t_{NiO} = 5$ to 60 nm, respectively. This is accompanied by a very similar evolution of roughness of the subsequent interfaces. The increase of the interfacial roughness manifests itself in the profiles of the scattering length density as an increasingly gradual transition between the plateaus of constant scattering length density of adjacent layers.

The scattering length density profiles of the FeCoV/NiO bilayers (figure 4.11) show significant dips at the interfaces between the FeCoV and NiO layers, which are related to very thin layers ($\approx$ 0.3 - 0.5 nm) of rather low scattering length density. We suppose that these layers evolve from oxidation of the surfaces of the FeCoV layers when the process is paused in order to stabilize the Ar:O_2 atmosphere for the deposition of the following NiO layers. During that time, the surface of the FeCoV layers is exposed to the reactive Ar:O_2 atmosphere. A small dip can also be identified at the Ti-FeCoV interface of the FeCoV/NiO bilayer with $t_{NiO} = 60$ nm. In general, an additional layer is included at the interface between the Ti buffer and the FeCoV layer (see e.g. FeCoV single layers) to account for the gradual variation of the scattering length density because of interdiffusion of Ti and FeCoV. In contrast, the scattering length density of this additional layer in the FeCoV/NiO (60 nm) bilayer is lower and its thickness higher than in other samples. We assume that this is related to an oxidation of the Ti surface, which presumably originates from residual reactive gas in the sputter chamber during the preparation of that particular sample. All layers of pure materials exhibit scattering length densities which are identical to their bulk counterparts. In particular, for the NiO layers, deposited on top of FeCoV, a scattering length density of $(5.0 \pm 0.1) \cdot 10^{11}$ cm^{-2} is found, which corresponds to NiO bulk but is in contrast to the reduced scattering length density when NiO is deposited directly on glass.

FeCoV/NiO/FeCoV trilayers

The reflectivity profiles of FeCoV/NiO/FeCoV trilayers (figure 4.12) exhibit all features like observed and already discussed for the FeCoV single layers and the bilayers, previously. The periodicity of the Kiessig fringes decreases with increasing t_{NiO} as a consequence of increasing total thickness. They become masked for $t_{NiO} \geq 40$ nm at large Q_z, which is related to the increasing roughness as discussed in the following. The refinement of the layer models is based on the results from the FeCoV single layers and the bilayers. Only minor adjustments are necessary to reproduce the measured reflectivities by the computations (figure 4.12). A compilation of the model parameters for all trilayer samples is given in table A.3 (appendix A) and a selection of respective profiles of the scattering length density is depicted in figure 4.13.

The profiles of the scattering length density of the FeCoV/NiO/FeCoV trilayers show consistently a significant dip between the FeCoV layer at the bottom and the NiO on top of it. This dip is also observed in the case of FeCoV/NiO bilayers and originates from a thin interfacial layer because of surface oxidation of the FeCoV layer as discussed before. The scattering length densities of the various layers are identical with their bulk counterparts. In particular the NiO layers show a scattering length density of $(5.0 \pm 0.1) \cdot 10^{11}$ cm^{-2}, which is also in accordance with the FeCoV/NiO bilayers. The roughness of the NiO/FeCoV interface increases from 0.26 to 3.24 nm for $t_{NiO} = 1.5$ to 100 nm, respectively. This affects also the subsequent interfaces between the layers on top of NiO and shows up in the profiles of the scattering length density by the increasingly gradual transition between adjacent layers similarly to that observed in NiO/FeCoV bilayers.

The increasing roughness leads to the fact that for samples with $t_{NiO} \geq 40$ nm the

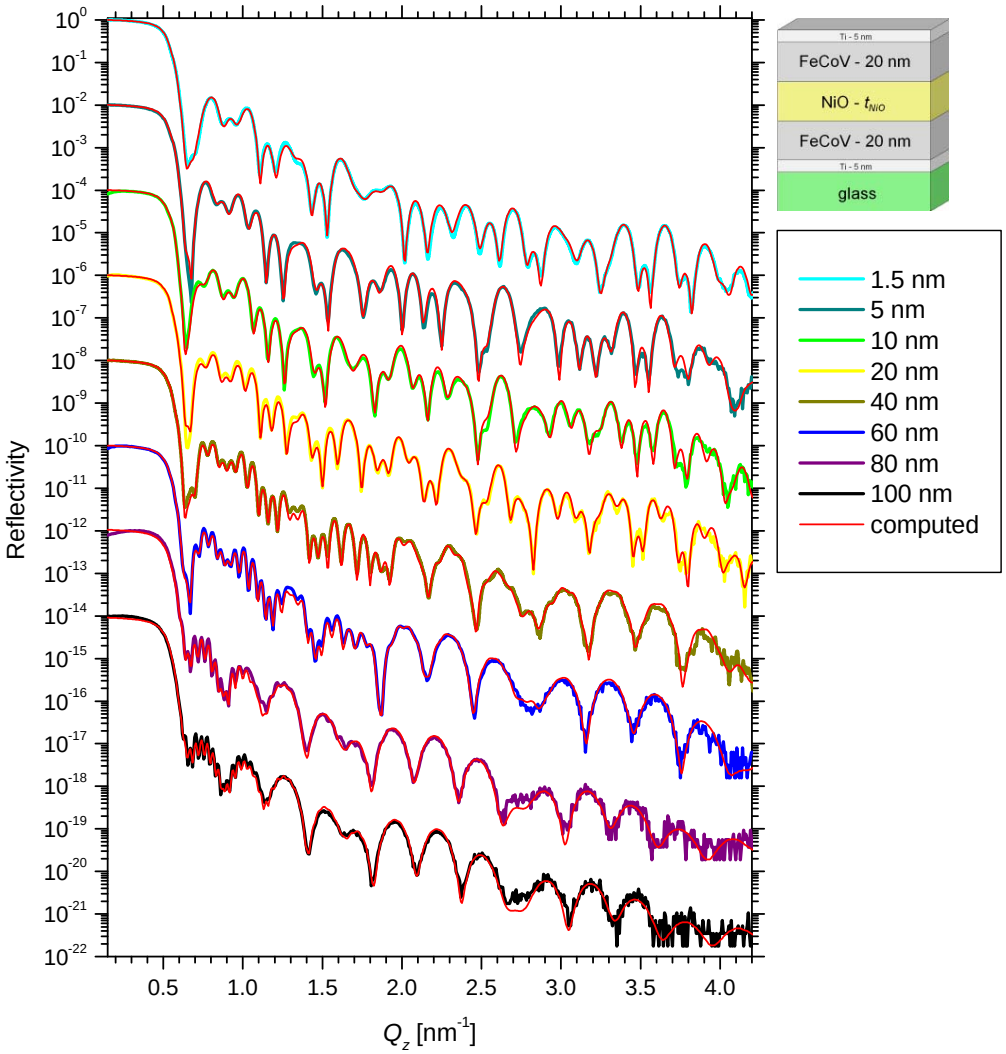

Figure 4.12: X-ray reflectivity profiles of FeCoV (20 nm)/NiO (t_{NiO})/FeCoV (20 nm) trilayers. Experimental data are shown as lines with individual colors whereas computed reflectivities are represented by red lines. The profiles are vertically shifted for clarity.

Kiessig fringes vanish at large Q_z. In this range the period ΔQ_z of the oscillations corresponds to a dimension in real space of $t = 2\pi/\Delta Q_z \approx 23$ nm. Like in the bilayer FeCoV/NiO (60 nm), it accounts for the total thickness of the Ti buffer layer and the adjacent FeCoV layer. It shows that the reflectivity profile in this range is dominated by the intensity of partial waves originating from the interfaces glass/film and FeCoV/NiO and Kiessig fringes are not present because the contribution of the rough surface of the samples to the reflectivity is only little.

Additional qualitative information about the interfaces in trilayers has been obtained from initial off-specular X-ray reflectometry measuring the intensity of diffuse scattering. The off-specular intensity is recorded at incident and exit angles being unequal with respect to the plane of the films (see section 3.3). The distribution of diffuse scattering contains information about lateral structures of interfaces and their vertical

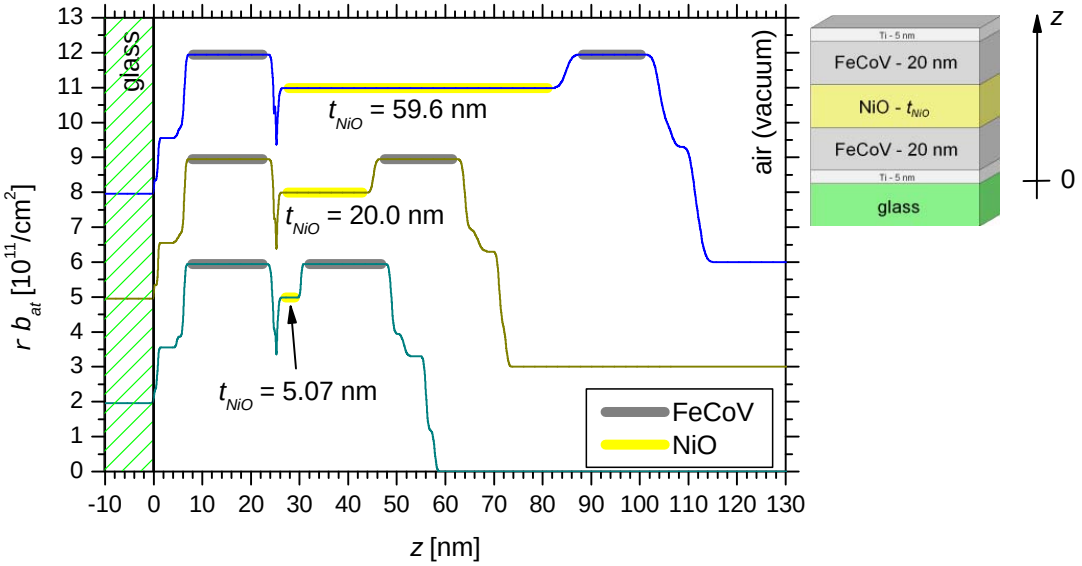

Figure 4.13: Profiles of the scattering length density (SLD) of FeCoV (20 nm)/NiO (t_{NiO})/FeCoV (20 nm) trilayers computed from the parameters of the layer models (table A.3) [71]. z is the distance form the surface of the substrate. The plateau belonging to NiO increases with increasing t_{NiO}. Corresponding actual values are included. The ranges of NiO and FeCoV layers are highlighted with bars of individual colors. The profiles are vertically shifted for clarity.

correlation [64, 65]. Figure 4.14 shows off-specular intensity maps of two samples representative for thin and thick NiO layers. The measured intensities are plotted in Q_x, Q_z reciprocal space maps. The accessible reciprocal space is limited by the horizon of the sample, which is the lower limit for incident and reflected X-rays. Therefore, the white areas are not accessible for the measurement. The variation of intensity along the vertical rod at $Q_x = 0$ is the specular reflectivity profile as plotted in figure 4.12.

The reciprocal space map for $t_{NiO} = 5$ nm (figure 4.14a)shows a concentration of the intensity from diffuse scattering at positions of Q_z where the oscillations in the specular reflectivity profile exhibit maxima, too. In general, such a pattern results from a partial coherence of diffuse scattered X-rays and indicates that the profiles of the interfaces are vertically replicated (see figure 4.15). The partial coherence can also be understood as a kind of resonant scattering (RDS) and is therefore known as Resonant-Diffuse-Scattering, which is localized within so called RDS-sheets [64, 65]. The bent shape of these sheets is due to refraction of the X-ray beam. Since the angles of either incident or reflected beams decrease towards the borders of the accessible reciprocal space and since the effect of refraction is strongest at low angles, the bending of the RDS-sheets is pronounced there.

Generally, superlattice structures with vertically correlated interfaces show diffuse scattering, which extends from the Bragg peaks of the superlattice into the off-specular reciprocal space. The distribution of the intensity is related to the coherence of the

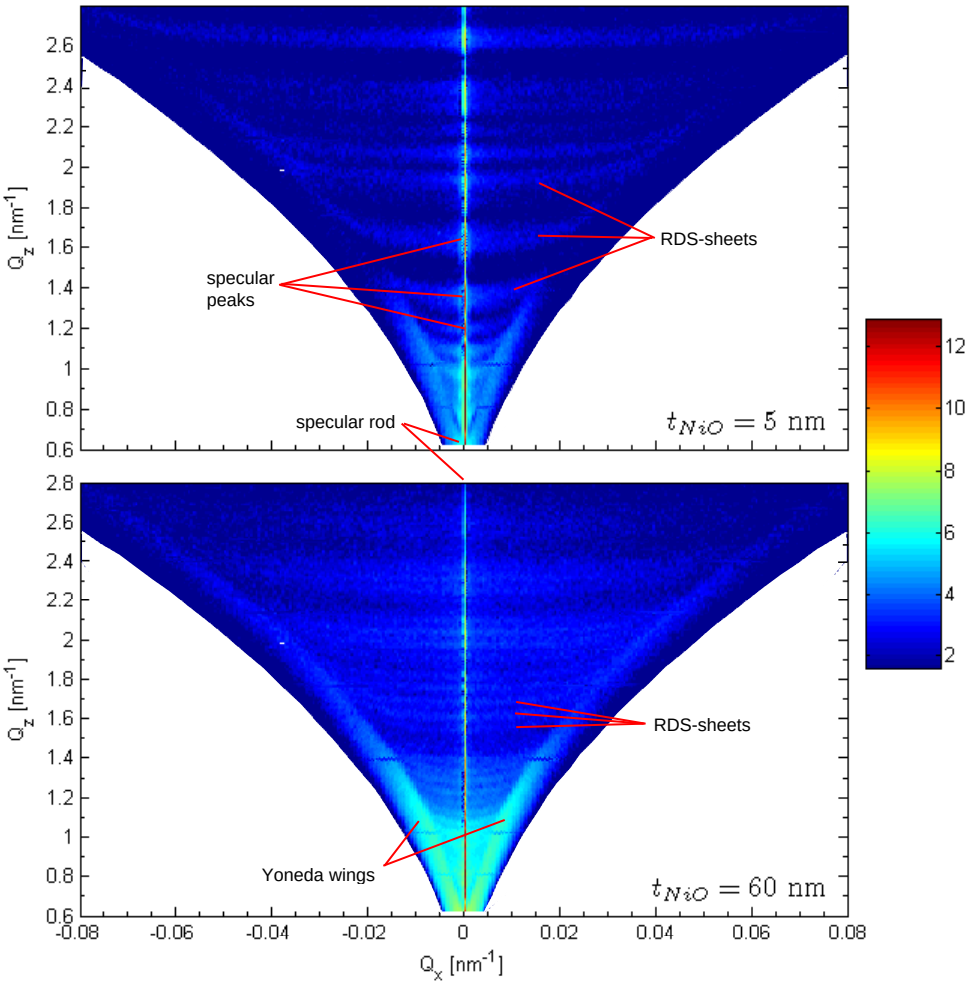

Figure 4.14: Reciprocal space maps of representative trilayers Ti (5 nm)/FeCoV (20 nm)/NiO (t_{NiO})/FeCoV (20 nm)/Ti (5 nm). The intensity is color coded in a logarithmic scale. The white areas represent a part of the reciprocal space, which is not accessible because of the limitation for incident and reflected beam caused by the horizon of the sample. Particular features of the scattering pattern are exemplary marked.

interfaces throughout the superlattice stack. In case of the trilayers of the present work, the specular oscillations originate from the interference of partial waves which are reflected from the substrate/film interface and from the surface of the film, respectively. This suggests that the observed diffuse scattering represents the correlation of these two particular interfaces. However, these interfaces will be conformal only if the interfaces in between have the same lateral profile.

Another prominent feature in the off-specular map in figure 4.14a) is the intensity starting at low Q_z and following the borders of the accessible reciprocal space at either side of the specular rod. This kind of diffuse scattering is known as Yoneda wings and originates from uncorrelated roughness. It arises when either the incident or the reflected beam is below the critical angle of total reflection. The simultaneous existence of RDS-sheets and Yoneda wings indicates that the interfaces are essentially vertically

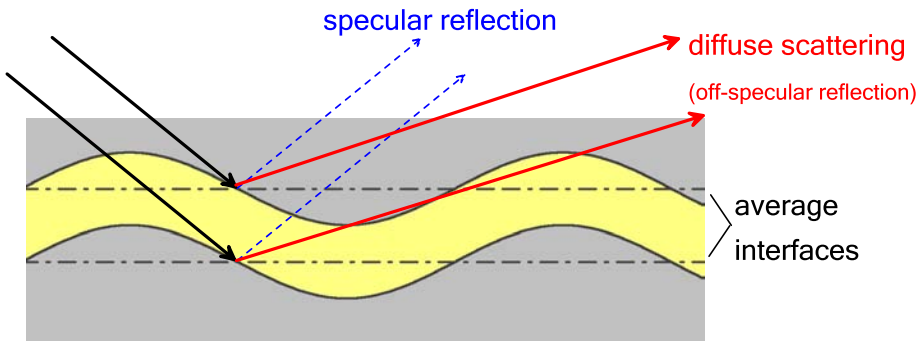

Figure 4.15: Illustration of specular reflection and diffuse scattering from vertically correlated interfaces. The specular reflectivity probes the average position of the interfaces. The phase relation of diffuse scattered X-rays from conformal interfaces is identical to the phase relation of specular reflected X-rays. Thus, the pattern of the diffuse intensity reproduces along the Q_z direction the features of the specular reflectivity profile.

correlated but contain a random component in addition.

The off-specular map for $t_{NiO} = 60$ nm (figure 4.14b) displays the same features as observed for $t_{NiO} = 5$ nm. Below $Q_z \approx 2$ nm^{-1} RDS-sheets starting from the specular Kiessig fringes can be identified. The diffuse intensity above $Q_z \approx 2$ nm^{-1} concentrates around the specular maxima which results from the interference of partial waves reflected from the substrate/film and FeCoV/NiO interfaces, as discussed above. Therefore, we suppose that the RDS-sheets in this range arise because of partial coherence of X-rays, which are diffuse scattered at these interfaces. In general, the RDS-sheets are less localized for $t_{NiO} = 60$ nm than for $t_{NiO} = 5$ nm. Additionally, the Yoneda wings have higher intensities in the case of $t_{NiO} = 60$ nm. Both features indicate that in the case of the thick NiO layers, the correlation of the interfaces decreases towards the surface and the random component in the interfacial roughness increases. The observation of uncorrelated roughness at the interfaces on top of the NiO layers which increases with t_{NiO} is in accordance with the increasing RMS roughness as deduced from the specular reflectivity profile. Nevertheless a certain degree of correlation exists giving rise for RDS-sheets as observed for even thick NiO spacer layers.

In summary, the off-specular intensity patterns indicate mostly conformal interfaces in the trilayer samples. In other words, although the interfaces show vertical fluctuations, due to their correlation, the layer thicknesses are supposed to be laterally homogeneous. This is of particular interest for the NiO spacer layers because random profiles of the interfaces would be accompanied by fluctuations of the layer thickness leading to a lateral variation of the vertical antiferromagnetic spin structure.

4.4 Summary of structural characterization

This section summarizes the information, which has been obtained from the structural characterization using X-ray diffraction and reflectometry, in particular regarding the

comparison of the FeCoV/NiO/FeCoV trilayers with NiO-FeCoV bilayers.

Proper conditions for the reactive sputtering of the desired NiO layers were deduced from X-ray diffraction and reflectivity measurements on the series of NiO single layers. We found that using a sputter gas with an $Ar:O_2$ ratio of 86:14 at a total pressure of 6 μbar would result in stoichiometric NiO layers with a pronounced (111) out-of-plane texture. We applied these settings for the deposition of NiO layers in the NiO-FeCoV multilayers.

Regarding the crystalline structure and orientation of FeCoV and NiO layers we deduce the following information and respective conclusions from the X-ray diffraction patterns:

- FeCoV layers, which are grown on top of Ti buffer layers exhibit a pronounced (110) texture out-of-plane. This is verified by the results from the series of glass/Ti/FeCoV/Ti and glass/Ti/FeCoV/NiO films. Respective Bragg peaks have identical positions, intensities and shapes.

- FeCoV layers, which are grown on top of NiO layers (series glass/NiO/FeCoV/Ti) are still (110) textured out-of-plane but the lower intensity of their Bragg peaks suggests a small random inclination of the (110) planes with respect to the plane of the films. However, position and intensity of the Bragg peaks and therefore the growth of FeCoV on top of NiO are independent of the thickness of the underlying NiO layer.

- Both previous conclusions are supported by the results of the diffraction experiments on the trilayer series (glass/Ti/FeCoV/NiO/FeCoV/Ti). There, the intensities of the FeCoV Bragg peaks are again independent of the NiO thickness. Moreover, the observed intensities in the trilayers are the sum of the intensities measured on FeCoV/NiO and NiO/FeCoV bilayers indicating that FeCoV layers of the bilayers are representatives of the respective counterparts in the trilayers regarding their crystallinity.

- In all series the vertical atomic distance in the FeCoV layers appears slightly reduced. Assuming a conservation of the volume of the unit cell, it indicates a small tensile strain in the plane of the layers.

- The texture of NiO layers depends on the underlying material. When NiO is directly grown on glass like in the series of glass/NiO and glass/NiO/FeCoV/Ti films, predominately (111) out-of-plane texture is observed. NiO layers, which are deposited on FeCoV consist apparently of a nearly equal distribution of two types of grains with (200) and (111) textures. This is consistently observed in samples of glass/Ti/FeCoV/NiO and glass/Ti/FeCoV/NiO/FeCoV/Ti.

- The distribution of the two types of NiO grains in FeCoV/NiO/FeCoV trilayers is independent of the thickness of the NiO layers for $t_{NiO} \lesssim 80$ nm.

The chemical depth profile was probed by X-reflectivity measurements. From the analysis the layer structure including layer thickness, X-ray scattering length density and interface roughness has been obtained. The most significant results are summarized

below including the discussion on the roughnesses of ferro- and antiferromagnetic layers in bilayers and trilayers. The values are compiled in table 4.2:

- All FeCoV layers have a scattering length density of the bulk material independent of the underlying material/surface. Their thicknesses are very consistent, e.g. the average thickness in the trilayers is 18.8 nm with a maximum deviation of 5 % from the average value.

- The scattering length density of NiO layers depends on the underlying material. NiO layers deposited on top of FeCoV (glass/Ti/FeCoV/NiO and glass/Ti/FeCoV/NiO/FeCoV/Ti) have a scattering length density of the bulk material whereas it is reduced by $\approx$ 7 % when NiO is grown directly on glass (glass/NiO and glass/NiO/FeCoV/Ti. The reduced density is presumably due to pores between the grains of bulk NiO. The accuracy of the thickness of the NiO layers is better than 6 %.

- Consistently, in samples with NiO deposited on top of FeCoV, thin interfacial layers are identified between the two layers. It is supposed that these layers result from an oxidation of FeCoV before NiO is deposited. Recently, the magnetic properties of native oxides of FeCo layers have been investigated. It has been found that oxidized FeCo is a medium for interfacial exchange [86, 87, 88]. The magnetic properties of the interfaces between FeCoV and NiO in the present work are discussed in section 5.2.2, in detail.

- The roughness of FeCoV layers grown on Ti (e.g. at the bottom of the trilayers) is consistently $\sigma_{rms} \approx 0.6$ nm. An identical roughness is observed for FeCoV layers on top of NiO unless the roughness of the underlying NiO layer exceeds 0.6 nm. Interestingly, below this limit the roughness of the FeCoV layers is independent of the roughness of the NiO layer. In general, the NiO roughness increases with increasing t_{NiO}. Once it is higher than 0.6 nm the roughness of FeCoV layers on top of NiO also increases, according the evolution of the NiO roughness. This occurs in the trilayers for $t_{NiO} > 20$ nm while it starts already for $t_{NiO} \geq 10$ nm in the case of NiO/FeCoV bilayers. In the latter, the roughness of FeCoV layers and underlying NiO layers is in general higher compared with their trilayer counterparts. This is presumably a consequence of pores in the NiO layers grown on glass as concluded from the reduced scattering length density.

- Off-specular X-ray reflectivity measurements indicate conformal interface profiles in FeCoV/NiO/FeCoV trilayers. As a result, e.g. NiO have laterally a very homogeneous thickness although the interfaces are not ideally flat. Thus it is assumed that the antiferromagnetic spin structure is reproduced at every position in the plane of the samples.

In summary, the structural analysis using X-ray diffraction and reflectometry shows consistent results for all samples prepared within this project. This fact confirms the consistent and high quality of the samples prepared by DC magnetron sputtering. Therefore, a separate investigation of FeCoV single layers and NiO-FeCoV bilayers enables to retrieve additional information about the magnetic properties of their counterparts in the trilayers.

		RMS roughness σ_{rms} [nm]		
t_{NiO}	layer	trilayer	NiO/FeCoV bilayer	FeCoV/NiO bilayer
5 nm	FeCoV bottom	0.64	-	0.37
	NiO	0.27	0.42	0.48
	FeCoV top	0.53	0.51	-
10 nm	FeCoV bottom	0.57	-	-
	NiO	0.41	0.90	-
	FeCoV top	0.54	0.90	-
20 nm	FeCoV bottom	0.52	-	-
	NiO	0.60	1.09	-
	FeCoV top	0.66	1.01	-
40 nm	FeCoV bottom	0.59	-	-
	NiO	1.04	1.37	-
	FeCoV top	0.97	1.30	-
60 nm	FeCoV bottom	0.56	-	0.60
	NiO	1.43	1.67	1.48
	FeCoV top	1.36	1.71	-

Table 4.2: Summary of RMS roughnesses of ferro- and antiferromagnetic layers - a comparison of trilayers and bilayers. The errors of the roughnesses are estimated to be in the order of 10 %.

In particular, detailed chemical depth profiles are obtained for the trilayers, which establish a well defined basis for the depth profile of the nuclear scattering length density for the analysis of polarized neutron reflectivity measurements. The consistency of the obtained layer models of the various samples confirms a high reliability of the fitting process.

Chapter 5

Bulk and layer resolved magnetic properties

In the present chapter, the measurements of the magnetic properties of FeCoV single layers, bilayers and trilayers are presented. We probed bulk magnetic properties using DC magnetometry. In particular, the magnetization reversal was studied with the external field applied in the plane of the samples. The hysteresis loops were recorded along different directions in order to test the samples for a net magnetic in-plane anisotropy and to determine coercive fields. In addition to the experiments at room temperature, we measured hysteresis loops also at various temperatures below and above $T = 300$ K to examine the temperature dependence of the magnetization reversal. At low temperatures the onset of a net exchange bias is observed in bilayer and trilayer samples with an interesting dependence on the orientation of the ferromagnetic magnetization at room temperature. Magnetization measurements on selected samples are also performed above the Néel temperature of NiO. The idea of these experiments is to "switch off" the antiferromagnetism. When NiO is in the paramagnetic state, the magnetic properties of the bilayers and trilayers are expected to differ from the behavior when antiferromagnetic NiO is exchange coupled to the FeCoV layers. In fact, a drastic change of the magnetization reversal is observed at $T = 530$ K.

We employed polarized neutron reflectometry with polarization analysis on the trilayers in order to obtain a layer resolved profile of the magnetization vector. The saturation magnetization of the individual FeCoV layers on an absolute scale was deduced from the reflectivity profiles of magnetically saturated samples. Of particular interest were the configurations of the magnetization vectors during the magnetization reversal. Therefore, the polarization dependent reflectivity profiles were measured at selected fields during the magnetization reversal. Here, the evolution of the magnetization vectors of individual FeCoV shows a significant dependence on the thickness of the NiO spacer layer. Additionally, we realized a special setup for polarized neutron reflectometry (see section 3.4.2), which in principle, is directly sensitive to the relative orientation of magnetic moments, i.e. the relative orientation of the magnetization vectors in the ferromagnetic layers of the trilayer samples. First results from initial experiments of this type support the results obtained from conventional polarized neutron reflectometry.

In the following, the results of the experiments on the magnetic properties are shown

in separate sections for the series of FeCoV single layers, bilayers and trilayers. The first section is dedicated to the series of FeCoV single layers from which the properties of FeCoV as free thin layers are obtained. These will serve for the comparison with the properties of FeCoV layers, which are in contact with antiferromagnetic NiO layers. In sections two and three the results from DC magnetometry on the FeCoV/NiO and NiO/FeCoV bilayers are presented. These series represent constituents of the FeCoV/NiO/FeCoV trilayer motif and allow a separate investigation of the individual properties of the top and bottom FeCoV layers of the trilayers. The final section of this chapter is dedicated to the experiments on the FeCoV/NiO/FeCoV trilayers in order to investigate the role of NiO in mediating an exchange coupling between the FeCoV layers. Each section includes the discussion of the particular features observed in the experiments. The complete discussion concerning exchange coupling between the FeCoV layers mediated by the NiO spacer layer is presented in chapter 6.

5.1 FeCoV single layers

We study bulk magnetic properties of Ti/FeCoV (t_{FeCoV})/Ti layers in order to obtain intrinsic properties of free FeCoV layers without contact to other magnetic layers. The properties for $t_{FeCoV} = 20$ nm are of particular interest because this thickness has been chosen for the FeCoV layers in the series of bilayers and trilayers. Single layers of FeCoV in our project show isotropic magnetic properties in the plane of the films with a relatively high coercivity compared to bulk. We infer that these properties are a consequence of a random distribution of local stress causing high local magnetic anisotropies of magneto-elastic origin. In addition, FeCoV layers with $t_{FeCoV} = 5$ and 40 nm have been investigated to test the sensitivity of the magnetic properties on the layer thickness. We find a dependence of the coercivity, which can be properly explained in terms of the random anisotropy model. Measurements of the MH-loop at low temperature show that the barrier for the reversal of magnetization is enhanced resulting in an increased coercivity. In the following, experimental results and their discussion are presented in separate subsections.

5.1.1 Experiments

This section compiles the measurements of the MH-loops of FeCoV single layers partitioned according the temperatures of the measurements.

MH-dependence at $T = 300$ K

The MH-loops along the x and y axes of the sample measured at room temperature are depicted in figure 5.1. The identical MH-dependencies along both directions for $t_{FeCoV} = 20$ and 40 nm indicate that their net magnetic properties are isotropic in the plane of the films. This is also valid for $t_{FeCoV} = 5$ nm except a small difference in the squareness of the hysteresis suggesting a very weak in-plane anisotropy. The coercivity is found to depend on the thickness of the FeCoV layer. For $t_{FeCoV} = 5$ nm the coercive field is $H_c = (60 \pm 3)$ Oe. It increases for $t_{FeCoV} = 20$ nm to $H_c = (185 \pm 3)$ Oe and decreases again to $H_c = (165 \pm 3)$ Oe for $t_{FeCoV} = 40$ nm.

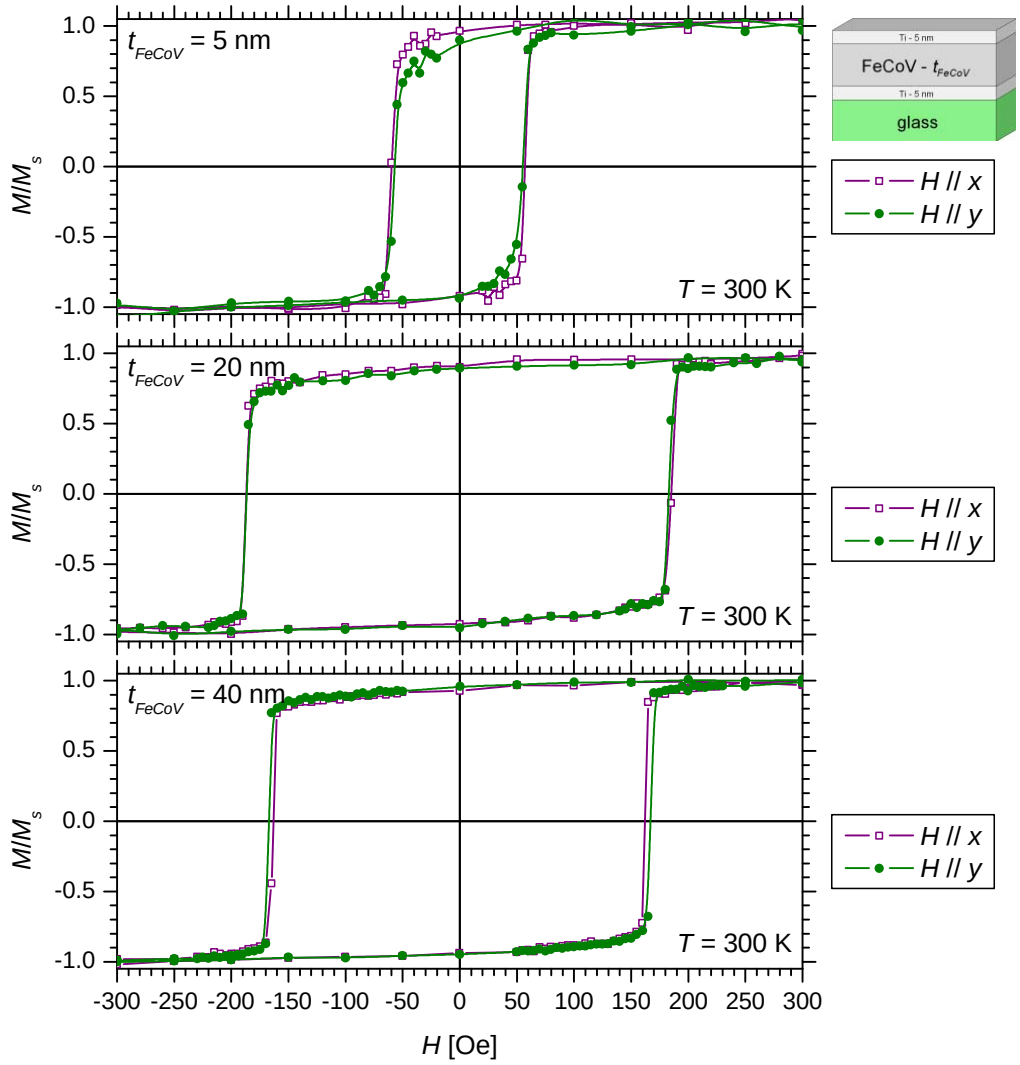

Figure 5.1: MH-loops of FeCoV (t_{FeCoV}) single layers measured with the external field applied in-plane along the orthogonal directions x and y of the samples.

MH-dependence at $T = 2$ K

The hysteresis loop for $t_{FeCoV} = 20$ nm was measured at $T = 2$ K as well and is plotted in figure 5.2. The coercivity is (225 ± 3) Oe, which is a factor of ≈ 1.2 higher than at room temperature. This indicates that the barrier for the reversal of magnetization increases at low temperature.

5.1.2 Discussion

The coercive fields of FeCoV single layers are significantly higher than H_c of bulk FeCoV, which is ≈ 2 Oe [47]. The high coercivity of FeCoV thin films is presumably of magneto-elastic origin, since FeCo alloys have a very high positive magnetostriction coefficient λ_s. For bulk $Fe_{50}Co_{50}$, which is close to the composition of FeCoV being investigated here, $\lambda_s = 8.34 \cdot 10^{-5}$ [42]. Thus, a small strain causes already a significant

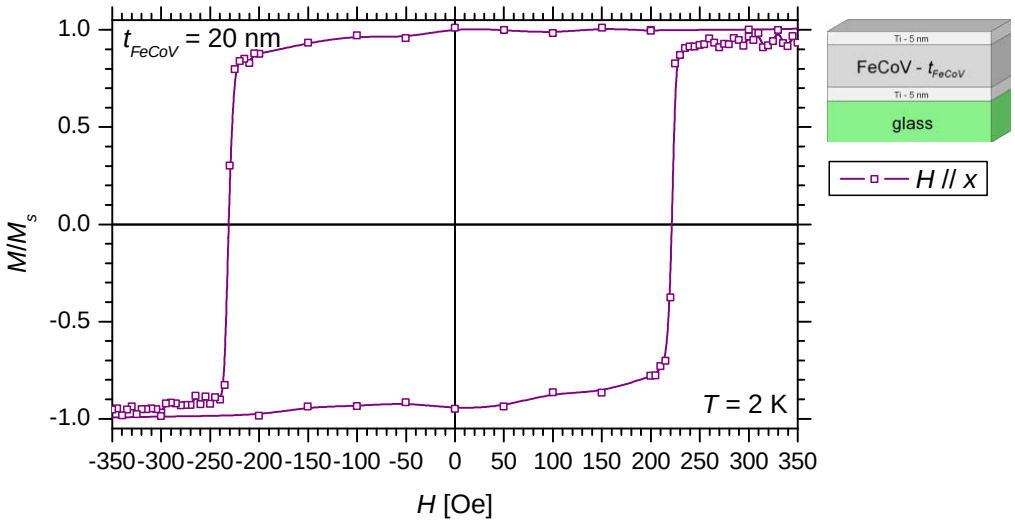

Figure 5.2: MH-loop of FeCoV (20 nm) single layer measured at $T = 2$ K. The coercivity is increased compared to room temperature by a factor of ≈ 1.2.

anisotropy.

Investigations of Kumar et al. [48, 76] on FeCoV/TiN$_x$ multilayers with varying t_{FeCoV} and t_{TiN_x} show a correlation between a net strain anisotropy and an in-plane magnetic anisotropy of the FeCoV layers. We obtained very similar results in a preliminary study to this project on multilayers of [Ti (t_{Ti})/FeCoV (10 nm)/Ti (t_{Ti})/FeCoV (3 nm)]$_{20}$ with $t_{Ti} = 3$, 5, 8, 10 and 15 nm [50]. The stress in the films is determined from the difference of curvature of Si wafers before and after the coating. Figure 5.3a shows the dependence of stress σ on t_{Ti} measured along two orthogonal orientations of the sample. Constantly, a difference exists between the directions indicating an anisotropy in the distribution of stress in the plane of the films. The difference $\Delta\sigma$ in stress between the two orientations results in a tensile stress along the y axis, relative to the x axis. As reported in [48], we compare the magneto-elastic energy with the magnetic anisotropy energy as obtained from the measurement of the hysteresis loop. In general, the magneto-elastic energy density E_{me} due to magnetostriction is calculated to be

$$E_{me} = 3/2 \cdot \lambda_s \cdot \sigma \tag{5.1}$$

with σ being the stress in the films, which here is the difference $\Delta\sigma$ in stress between x and y axis. The density of the anisotropy energy is calculated from the difference between the integrals $\int MdH$ for magnetically easy and hard axes in the first quadrant of the MH-loop [89]. The comparison in figure 5.3b shows a very similar variation with t_{Ti} indicating clearly the correlation of the magnetic and the strain anisotropy. These studies show the dominant role of magnetostrictive effects on the magnetic properties of FeCoV thin films.

Both cases discussed above exhibit a net magnetic anisotropy due to magnetostrictive effects from a net anisotropy of the strain distribution. It is supposed that the

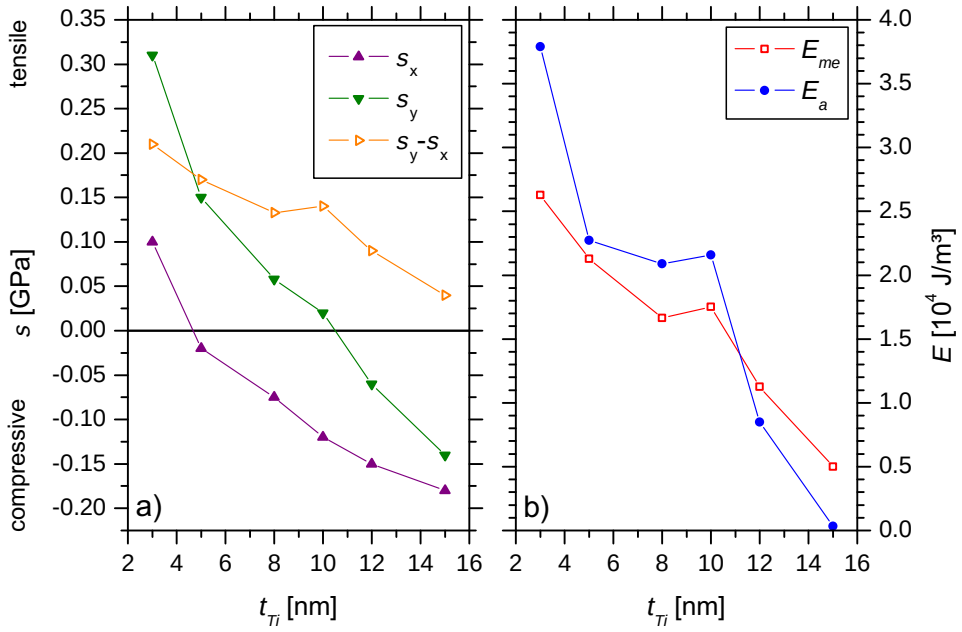

Figure 5.3: Magnetostriction in [Ti (t_{Ti})/FeCoV (10 nm)/Ti (t_{Ti})/FeCoV (3 nm)]$_{20}$ multilayers. a) in-plane distribution of stress σ dependent on t_{Ti} measured along the orthogonal x and y axes of the sample. b) comparison of the magneto-elastic energy density E_{me} as calculated from $\Delta\sigma = \sigma_y - \sigma_x$ (equation 5.1) and the anisotropy energy density E_a, determined from the hysteresis loops along the easy and hard axes.

anisotropy is induced by the asymmetric sputter geometry because of a rather elongated target (75 x 500 mm^2) and aperture of the facility being used for the preparation of these samples [90]. We observe isotropic properties for the FeCoV single layers in the present work, presumably because of the rather symmetric sputter geometry of the facility being used here (section 2.2), would not lead to an anisotropic distribution of stress, therefore. However, local strain and magnetostriction may exist creating regions of high magnetic anisotropy with a random distribution. These regions may form pinning centers for domain wall motion resulting in a high coercivity, as it is proposed by Cohen to be the reason for the unusually large coercivity of NiFe films [91]. Platt et al. [92] and Jung et al. [93] measured the angular dependence of the in-plane torque of FeCo alloy thin films and determined the rotational hysteresis loss as a function of applied field. Both observe a substantial hysteresis loss, even in the range of kOe, indicating a wide distribution of the strength of local anisotropies up to very high values. The distribution (homogeneity) of magnetic anisotropy is presumably related to a distribution in magnetostriction.

We find a contraction of the lattice in the out-of-plane direction from the diffraction patterns of the FeCoV single (section 4.2). This results in an expanded in-plane lattice when a conservation of the unit cell volume is assumed. The contraction $(\Delta l/l)_{out-of-plane}$ out-of-plane is ≈ -0.0028, which translates to an in-plane expansion of $(\Delta l/l)_{in-plane} \approx 0.0028$ assuming a compensation in one direction as the maximum.

The associated in-plane stress σ is calculated to be

$$\sigma = \varepsilon \cdot (\Delta l/l)_{in-plane} \tag{5.2}$$

with $\varepsilon = 2.1 \cdot 10^{11}$ N/m^2 the modulus of elasticity for FeCoV [47]. This results in a stress of $\sigma = 0.59$ GPa and a magneto-elastic energy density of $E_{me} = 7.4 \cdot 10^4$ J/m^3 using equation 5.1. The coercive field H_c can be calculated applying the Stoner-Wohlfarth model assuming a single domain particle with a uniaxial anisotropy [55] which is here of magneto-elastic origin:

$$H_c = \frac{2K}{M_s}. \tag{5.3}$$

K is the anisotropy constant, i.e. the energy density associated with the uniaxial anisotropy, which is equal to E_{me} in the present case of magnetostriction. The saturation magnetization M_s is 2.3 T for FeCoV [47]. As a result, the coercive field is estimated to be ≈ 800 Oe. The obtained value is significantly larger than the coercive fields deduced from the hysteresis loops. This is presumably because i) the estimation of the in-plane stress is maximum since it is based on a one dimensional in-plane expansion of the lattice to compensate the out-of-plane contraction and ii) an averaging over interacting domains with a random distribution of the magnetostrictive anisotropies, which effectively reduces the coercivity and is not considered in the estimation (see the discussion below about the thickness dependence of the coercivity). However, it has the same order of magnitude and is consistent with the observations of Platt [92] and Jung [93] demonstrating the impact of magnetostriction on the magnetic properties of FeCoV thin films in this project.

The hysteresis loops of the FeCoV single layers exhibit a dependence of the coercive field on the thickness of the layers. Our results for the three different thicknesses of FeCoV are consistent with a more detailed study on the thickness dependence [48, 92]. There it is reported, that in the regime of a few nm of the FeCoV thickness, the coercivity increases with t_{FeCoV} reaching a maximum in the range of $\approx$ 10 to 20 nm. At higher thicknesses ($>$ 30 nm) the coercivity gradually decreases again. The thickness dependence in FeCoV layers is presumably related to the lateral grain size. Platt et al. measured the lateral grain size using cross-sectional TEM and found a correlation of the thickness and the lateral grain size [92]. In their case, the grain size increased from $\approx$ 15 nm to 30 nm when the FeCo thickness increased from 5 to 10 nm, respectively. This was accompanied by a drastic increase of coercivity from $\approx$ 20 Oe to 120 Oe.

In particular, the relative size of the grains compared to the domain wall width is apparently decisive for the coercivity. The domain wall width estimated by Platt et al. for $Fe_{50}Co_{50}$ is $\approx$ few 10 nm [92]. This is comparable with the grain size up to which the coercivity of thin films of FeCo alloys increases with increasing grain size, i.e. layer thickness. The thickness dependence of coercivity in this regime is properly explained within the random-anisotropy model [94, 95, 96, 97]. It describes the magnetic properties of magnetically coupled small particles (grains) with a random distribution of their individual uniaxial anisotropy. Due to the intergrain interaction and when the size of the grains is comparable or smaller than the domain wall width

in bulk, the magnetization of single grains does not follow their individual anisotropy, rather a common orientation within correlated grains establishes. The magnetization is controlled by an effective anisotropy averaged over correlated grains and reduced by a factor of $1/\sqrt{N}$ for a random orientation of the anisotropy axes of the grains, where N is the number of the magnetically correlated grains. When the grain size decreases, as for decreasing layer thickness in the present case, N increases leading to the observed decrease of coercivity. The reduced effective anisotropy of correlated grains is also supposed to explain partly the difference between the measured coercivity and the coercivity estimated from the stress in the films, as discussed above.

For larger grains, a domain wall can be completely accommodated in one grain avoiding grain boundaries, which are presumably local pinning centers. As a result, the coercivity is expected to decrease like it is observed for FeCoV layers with thicknesses beyond ≈ 30 nm.

At low temperature, we observe an increase in coercivity, which is presumably caused by the reduction of thermal fluctuations assisting the magnetization reversal [55]. Consequently, the applied field has to be larger to overcome the potential barrier for the reversal of the magnetization. In particular, for $t_{FeCoV} = 20$ nm the coercive field at $T = 2$ K is (225 ± 3) Oe, which is a factor of ≈ 1.2 higher than at room temperature.

In summary, we find that free FeCoV single layers of the present work have isotropic magnetic properties in the plane of the films. Furthermore, they show relatively high coercivity compared to bulk FeCoV, which is related to high local anisotropies of magneto-elastic origin. In particular, the FeCoV single layer with $t_{FeCoV} = 20$ nm has a coercivity of $H_c = (185 \pm 3)$ Oe. This can be considered as an intrinsic feature of the FeCoV layer and will be the reference in the discussion of the magnetic properties of NiO-FeCoV multilayers.

5.2 FeCoV/NiO bilayers

We investigate the magnetic properties of FeCoV/NiO (t_{NiO}) bilayers since they provide separate information about the bottom FeCoV layer in the trilayers including the influence from antiferromagnetic NiO on top. At room temperature, the hysteresis loops of the bilayers are very similar to that of the FeCoV single layers indicating that the magnetic properties are governed by the intrinsic properties of the ferromagnetic layer. Only a weak influence of the antiferromagnetic is observed in the case of a thick NiO layer, which manifests itself as small exchange bias. The influence of NiO becomes prominent at low temperature as we observe from the significant shift of the hysteresis loop along the field axis. We find that the direction of exchange bias is defined by the orientation of the magnetization of the ferromagnet. This suggests that the ferromagnet causes a reorientation of the antiferromagnetic spins, which are stabilized at low temperatures. The hysteresis loop measured at temperatures above T_N of bulk NiO provides information about the properties of the bilayers when NiO is in the paramagnetic phase. In the following, first, the experimental results are shown and second, they are discussed regarding the contribution of antiferromagnetic NiO to the magnetic properties.

5.2.1 Experiments

We measured hysteresis loops of FeCoV/NiO bilayers at various temperatures. In addition to room temperature, experiments were performed at $T = 2$ K since we observe enhanced exchange bias at low temperatures. At $T = 530$ K ($> T_N$ of bulk NiO), NiO is expected to be paramagnetic simulating the absence of the antiferromagnet. This enables to differentiate the magnetic properties of FeCoV/NiO bilayers with and without a possible exchange coupling between antiferro- and ferromagnetic layers. The presentation of the results is structured according the temperature during the experiments.

MH-dependence at $T = 300$ K

Hysteresis loops of FeCoV/NiO bilayers are depicted in figure 5.4 measured along the x and y axes at room temperature. The MH-loops for $t_{NiO} = 5$ nm are independent of the orientation, indicating isotropic magnetic properties in the plane of the FeCoV layer with a coercivity of $H_c = (169 \pm 3)$ Oe. For $t_{NiO} = 60$ nm, a small difference of the hysteresis loops appears between the two orientations. Along the y axis the hysteresis is more square like than along the x axis suggesting the existence of a weak in-plane anisotropy. The coercivities along the two directions are (168 ± 3) Oe and (162 ± 3) Oe, respectively. In addition, the hysteresis loops are slightly displaced along the field axis indicating exchange bias with a very small bias field of $H_{eb} = (6 \pm 3)$ Oe. Except the observed small exchange bias, the properties are very similar to the single layer of FeCoV (20 nm) and almost independent of t_{NiO} suggesting that the ferromagnetic layer dominates the properties of the bilayers.

MH-dependence at $T = 2$ K

Hysteresis loops of the bilayer with $t_{NiO} = 60$ nm were measured along its x and y axis. Prior to the experiments, the sample was prepared in particular (see figure 5.5):

i) (a) at room temperature a field of $H = +1000$ Oe was applied to achieve magnetic saturation $\vec{M}_{s,300K}$ along the x axis. (b) the sample was cooled down to 2 K in $H = +1000$ Oe maintaining the orientation of the magnetization. (c) at 2 K the MH-loop was measured along the x axis, i.e. parallel to the orientation of the magnetization $\vec{M}_{s,300K}$ before cooling.

ii) (a) at room temperature a field of +1000 Oe was applied to align and saturate the magnetization of the sample along the x axis ($\vec{M}_{s,300K}$). (b) the external field was then removed but the orientation of the magnetization was almost preserved due to its high remanence. (c) the sample, respective its magnetization, was rotated by 90°. (d) the sample was cooled down to 2 K in zero field. (e) at 2 K the MH-loop was subsequently measured along the y axis, i.e. perpendicular to the orientation of the magnetization $\vec{M}_{s,300K}$ before cooling.

The procedure in ii) enables to measure the MH-dependence perpendicular to the unidirectional anisotropy, which is induced along the x axis, as the results will show.

Figure 5.6 shows the hysteresis loops, measured at $T = 2$ K, of the first and 6th

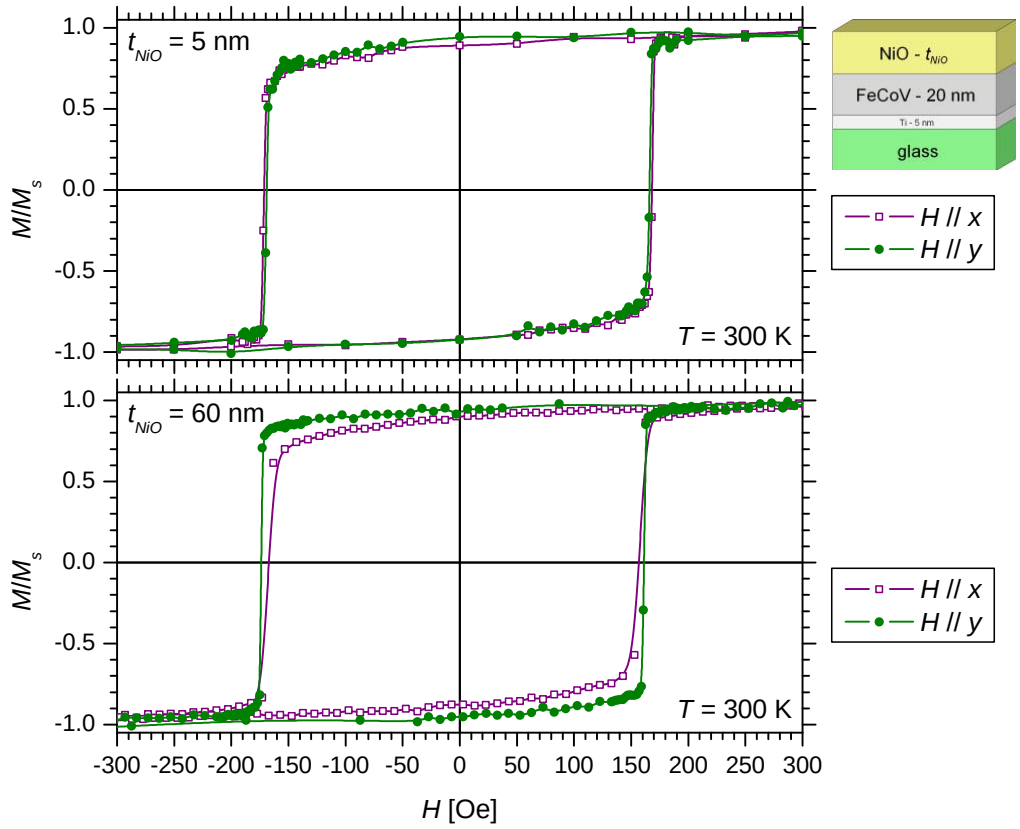

Figure 5.4: Hysteresis loops of FeCoV (20 nm)/NiO (t_{NiO}) bilayers measured with the external field applied in-plane along the orthogonal directions x and y of the samples.

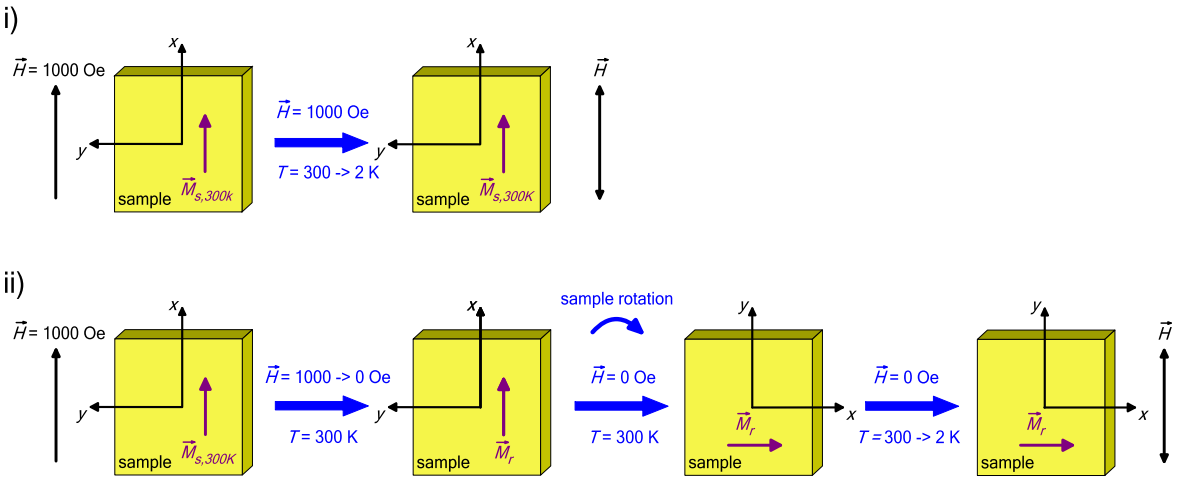

Figure 5.5: Illustration of the preparation of the sample prior to the experiments at $T = 2$ K. Finally, MH-loops were measured along the x (i) and y (ii) axes of the sample. $\vec{M}_s$, $\vec{M}_r$ and $\vec{M}_{s,300K}$ denote the state of the layer magnetization at the individual steps of the sample preparation representative for the saturation magnetization, the remanent magnetization and the state of magnetization during cooling, respectively. Details of the sample preparation are described in the text.

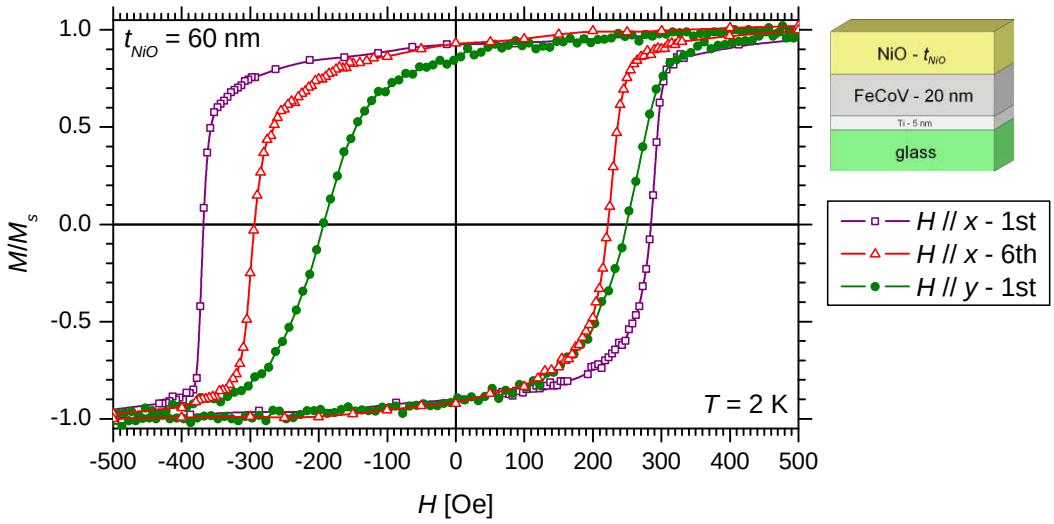

Figure 5.6: MH-loops of FeCoV (20 nm)/NiO (60 nm) bilayer at 2K. After cooling, hysteresis during the first cycle of field were measured along the x and y axes. In addition, the MH-loop of the 6th cycle of field along the x axis was recorded showing the training of the sample. The preparations of the sample prior to the measurements are illustrated in figure 5.5.

cycle of the external field for i) and of the first cycle for ii). In case of i), the MH-loops are shifted towards negative fields, i.e. opposite to $\vec{M}_{s,300K}$, showing that a net unidirectional anisotropy (exchange bias) establishes itself during the cooling process. The exchange bias field and the coercivity of the first cycle of the external field are $H_{eb} = (42 \pm 3)$ Oe and $H_c = (328 \pm 3)$ Oe, while they are reduced to $H_{eb} = (36 \pm 3)$ Oe and $H_c = (258 \pm 3$ Oe) in the 6th loop. The reduction indicates the training of the sample, which is typically observed in exchange biased systems [13, 98]. For comparison, the coercivity at 2 K of the FeCoV (20 nm) single layer is (225 ± 3) Oe. As a result, the FeCoV/NiO (60 nm) bilayer has a coercivity, which is enhanced by ≈ 45 % (≈ 15 %) in the first (6th) MH-loop after cooling, compared to the single layer counterpart. The increase in coercivity is also a typical feature arising when exchange bias sets in.

The hysteresis loop measured along the y axis, i.e. perpendicular to $\vec{M}_{s,300K}$ (ii), shows a gradual reversal of the magnetization resembling the MH-dependence along a magnetically hard axis. This is a feature, which is expected to exist perpendicular to a unidirectional anisotropy axis [99] and therefore consistent with the observation of exchange bias along the x axis. However, the hysteresis loop is also not centered around zero field but it is shifted by $H_{eb} = (28 \pm 3)$ Oe towards positive fields suggesting the existence of another unidirectional anisotropy, which is perpendicular to $\vec{M}_{s,300K}$. Here, it has to be considered that in case (ii) the sample was cooled in its remanent state. Therefore, the magnetization within some domains presumably deviated from $\vec{M}_{s,300K}$ during the cooling process. Obviously, these domains induced the exchange bias along the y axis. The hysteresis of the MH-loop along the y axis is another indication for the formation of domains, which is not expected perpendicular to the unidirectional anisotropy axis of a single domain.

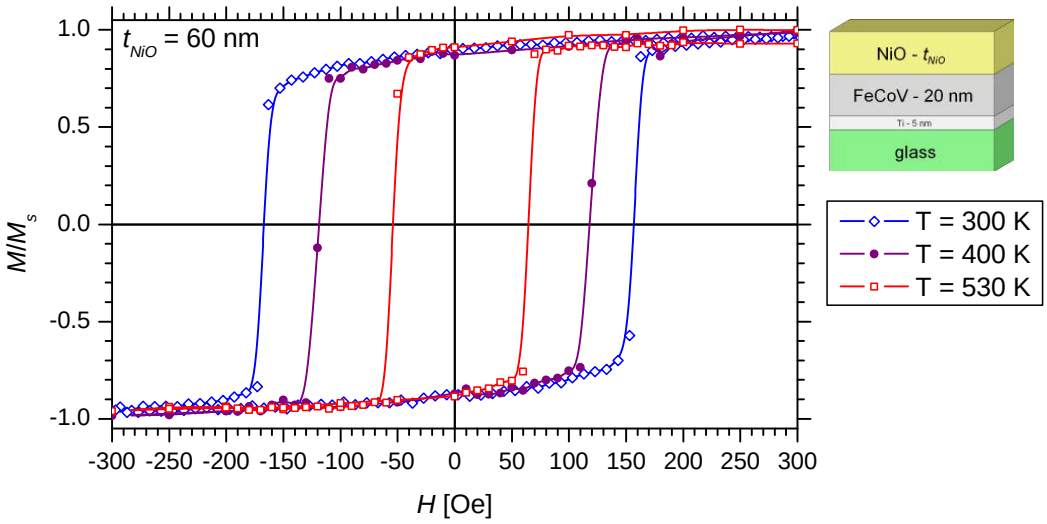

Figure 5.7: MH-loops of FeCoV (20 nm)/NiO (60 nm) bilayer measured between room temperature and T = 530 K. The MH-loops were measured along the x axis of the sample.

MH-dependence at $T > 300$ K

Figure 5.7 shows MH-loops along the x direction of the FeCoV/NiO bilayer with $t_{NiO} = 60$ nm measured at $T = 300$, 400 and 530 K. At $T = 530$ K, the NiO layer is supposed to be paramagnetic since the temperature is above T_N of bulk NiO. The coercivity decreases with increasing temperature because the energy barrier for the magnetization reversal is reduced presumably due to thermal activation. In particular, the coercivity is reduced to $H_c = (60 \pm 3)$ Oe at $T = 530$ K, which is ≈ 35 % of the coercivity at room temperature. It is important to notice that the MH-loop is open at positive saturation indicating that during the experiment the saturation magnetization decreases. Presumably interdiffusion at the FeCoV interfaces reduces or even removes the magnetization in the volume of interdiffusion. However, the shape of the hysteresis is almost unchanged indicating that the process during the magnetization reversal is the same, even above T_N of bulk NiO.

5.2.2 Discussion

In general, FeCoV/NiO bilayers and FeCoV single layers show rather similar MH-loops, e.g. they have similar coercivities. Considering that the underlying surface is identical in both series, the growth and therefore the intrinsic magnetic properties of the FeCoV layers are expected to be identical, too. The difference between the two series is at the upper interface of the FeCoV. The proximity of an antiferromagnet usually affects the magnetization reversal of the ferromagnetic layer because of interfacial exchange. The hysteresis loops of $t_{NiO} = 5$ nm indicate in-plane isotropic magnetic properties with coercive fields almost identical to the corresponding FeCoV single layer. Obviously the intrinsic properties of the FeCoV layer control the magnetization reversal. In the case of $t_{NiO} = 60$ nm, a weak influence of the NiO layer can be inferred from the weak anisotropy and small exchange bias. Nevertheless, the magnetization reversal is

mainly determined by the FeCoV layer. The lack of anisotropy and exchange bias for $t_{NiO} = 5$ nm might be understood because the contribution of the antiferromagnetic anisotropy to the free energy per unit area $E_{AF,aniso}$ is proportional to the thickness t_{AF} of the antiferromagnet, i.e. $E_{AF,aniso} = K_{AF} \cdot t_{AF}$, with K_{AF} the anisotropy constant of the antiferromagnet. Thus the contribution is less significant for low NiO thickness.

At low temperature ($T = 2$ K), we observe significant exchange bias as a consequence of a pronounced influence of antiferromagnetic NiO. Interestingly, we find a distribution of the direction of exchange bias from the MH-loops along orthogonal directions. This observation suggests that the direction of exchange bias is not related to a particular, common direction in the sample but the local magnetization within domains of the ferromagnetic layer determines the creation of unidirectional anisotropy. In [100], using XMLD, the arrangement of lateral domains in the antiferromagnetic layer was studied. There, it was shown that the ferromagnetic magnetization provokes a repopulation of antiferromagnet domains having their anisotropy axis parallel or close to the ferromagnetic magnetization. These antiferromagnetic domains contribute to the exchange bias and, as a consequence, the direction of exchange bias is induced locally depending on the alignment of the ferromagnetic moments. This appears to be in agreement with our experimental observations. We suspect that the ferromagnet manipulates via interfacial exchange the orientation of the antiferromagnetic spins at room temperature, i.e. it can drag the antiferromagnetic spins. When the temperature is reduced the antiferromagnetic spins become rigid. Hence, they are not completely free to follow the ferromagnet leading to the observed exchange bias and increase of coercivity, which higher than for the FeCoV single layer at $T = 2$ K. In particular for the case ii), the unidirectional anisotropy perpendicular to $\vec{M}_{s,300K}$ results from local ferromagnetic domains with orientations slightly off from $\vec{M}_{s,300K}$. The reduced bias field is presumably a consequence that in the experiment only projections of the local unidirectional anisotropies onto the direction of the applied field are probed. For i), the magnetization of the FeCoV layer is completely aligned and the shift of the loop is opposite to $\vec{M}_{s,300K}$. However, during cycling of the field, antiferromagnetic domains may regain their original orientation leading to the training of the sample.

Above T_N of bulk NiO, we do not observe a particular difference of the magnetization reversal compared to room temperature. Only, the coercivity is reduced, presumably because of thermal activation. The similarity of the mechanism of the magnetization reversal must be expected because the magnetic properties of FeCoV/NiO bilayers are anyway determined by the intrinsic properties of the FeCoV layer, even in the presence of antiferromagnetic NiO.

At this point, the properties of the thin oxide layers shall be discussed, which are identified between the FeCoV and the NiO layer in the FeCoV/NiO bilayers as well as in the trilayers. Beach et al. investigated the structural and magnetic properties of [Co_xFe_{1-x}/native oxide] multilayers [86, 87, 88]. In their experiments, each layer of CoFe was exposed to an oxygen atmosphere for ten seconds after sputter deposition. They found that for $x = 0.5$ an oxide layer of ≈ 1.4 nm was formed with equal amount of Co and Fe being oxidized. Regarding the magnetic properties, it was observed that for $x < 0.9$ magnetism was established with a saturation magnetization roughly 1/3 of

the saturation magnetization of FeCoV for $x = 0.5$. Thus, the oxide layers in the samples investigated here are supposed to mediate magnetic coupling between the ferro- and antiferromagnetic layers.

In summary, the magnetic properties of the series of FeCoV layers with a NiO layer on top are very similar to free FeCoV single layers at room temperature. As a result, the magnetism of the FeCoV/NiO bilayers is apparently governed by the intrinsic properties of the FeCoV layer. A distinct contribution of the antiferromagnetic NiO layer via interfacial exchange does not show up while probing the net magnetic properties at room temperature, presumably because the antiferromagnetic spins rotate irreversibly with the ferromagnet during the magnetization reversal. They may follow the ferromagnetic spins during the magnetization reversal due to interfacial exchange. The magnetization behavior for $t_{NiO} = 60$ nm, which is slightly different from the FeCoV single layer counterpart, hints towards a weak influence of the NiO layer. At low temperature, the influence of the antiferromagnet becomes prominent, which manifests in the form of a net shift of the hysteresis loop due to exchange bias and an enhanced coercivity.

5.3 NiO/FeCoV bilayers

NiO (t_{NiO})/FeCoV bilayers represent the upper part of the trilayer motif. We measured MH-loops of the series to obtain separate information about the properties of FeCoV layers deposited on top of NiO. The most significant difference to FeCoV single layers and FeCoV/NiO bilayers is a distinct magnetic anisotropy and rather low coercivity at room temperature. Weak exchange bias is observed for thick NiO layers. At low temperature, exchange bias becomes significant for all thicknesses of NiO within this work. The unidirectional anisotropy can be tuned along either direction of the anisotropy axis dependent on the orientation of the ferromagnet, which is similar to the series of FeCoV/NiO bilayers. We infer that at room temperature the antiferromagnetic spins are flipped between the two possible orientations of the anisotropy axis initiated through interfacial coupling by the reversal of the ferromagnet. At low temperature, the antiferromagnetic spins become stabilized, which establishes exchange bias. The results of experiments above T_N of NiO reveal that the anisotropy is induced by the NiO layer and transferred to the FeCoV layer via exchange coupling across their common interface. This section contains the experimental results followed by the discussion of these.

5.3.1 Experiments

This section presents the hysteresis loops measured at room temperature at temperatures below and above as well. At $T = 2$ K, we study exchange bias and at $T = 530$ K ($> T_N$) of bulk NiO the properties of the bilayers when NiO is paramagnetic. In the following, the results are structured according the temperature during the experiments.

MH-dependence at $T = 300$ K

We measured hysteresis loops of NiO/FeCoV bilayers at room temperature along orthogonal x and y directions in the plane of the films. The experimental results are depicted in figure 5.8. All samples have rather low coercivity and an in-plane net magnetic anisotropy exhibiting magnetically easy and hard axis along the x and y directions, respectively. Only for $t_{NiO} = 60$ nm, do the hysteresis loops along x and y axes not show pronounced easy/hard axis behavior but still suggest an in-plane net magnetic anisotropy. The features are distinctively different from the properties of FeCoV single layers and FeCoV/NiO bilayers.

The coercivity of NiO/FeCoV bilayers along the easy axis increases from (8 ± 3) to (37 ± 3) Oe for $t_{NiO} = 5$ to 60 nm, respectively. Hence, the coercivity of FeCoV layers deposited on top of NiO is significantly reduced by a factor of ≈ 5 to 20 compared to the bilayers with NiO on top of FeCoV. Additionally, samples with $t_{NiO} \geq 40$ nm display weak exchange bias with a small bias field of $H_{eb} = (6 \pm 3)$ Oe. The shape of the MH-loop along the hard axis varies gradually with increasing t_{NiO}. At $t_{NiO} = 5$ nm, the linear MH-dependence with almost no hysteresis has the typical characteristics of a single domain with uniaxial anisotropy. With increasing t_{NiO} a kind of two step process for the reversal of magnetization is established accompanied by formation of hysteresis. Although the MH-loops for $t_{NiO} = 60$ nm appear different compared to the other samples, still a step in the magnetization reversal can be noted along the y axis being consistent with the gradual variation of the magnetic properties with the thickness of the NiO layer.

Since the shapes of the hysteresis loops for $t_{NiO} = 60$ nm differ significantly from typical loops along magnetically easy and hard axes, additional experiments were performed on this sample. Ferromagnetic resonance (FMR) was employed to investigate the in-plane anisotropy in detail. The dependence of the resonance field H_{res} on the direction α in the plane of the sample is shown in figure 5.9a), with $\alpha = 0°$ being parallel to the x axis. The profile of H_{res} shows a periodicity of 180° with a phase shift of $\approx 32°$ indicating a uniaxial anisotropy with the anisotropy axis at an angle of $\alpha \approx 32°$ to the x axis. In addition, the anisotropy field H_{ani} is determined to be ≈ 35 Oe. Based on these results, the MH-loop was measured along the anisotropy axis and the result is shown in figure 5.9b. It resembles the MH-loop along an easy axis of magnetization with a coercivity of $H_c = (30 \pm 3)$ Oe, which is in rather good agreement with the results from FMR. In addition, the loop is slightly shifted by (10 ± 3) Oe along the field axis reflecting a weak net exchange bias.

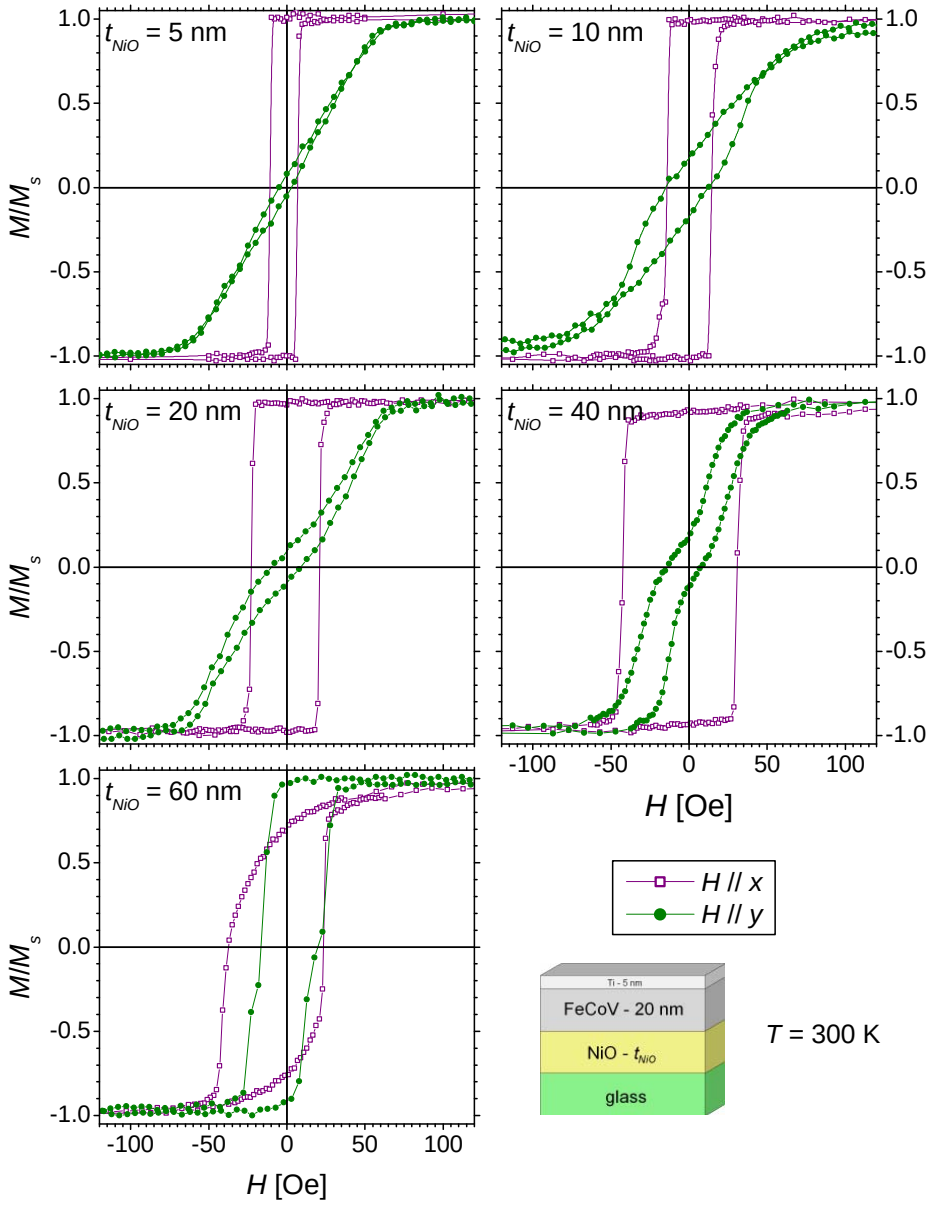

Figure 5.8: MH-loop of NiO (t_{NiO})/FeCoV (20 nm) bilayers measured with the external field applied in-plane along the orthogonal directions x and y of the samples.

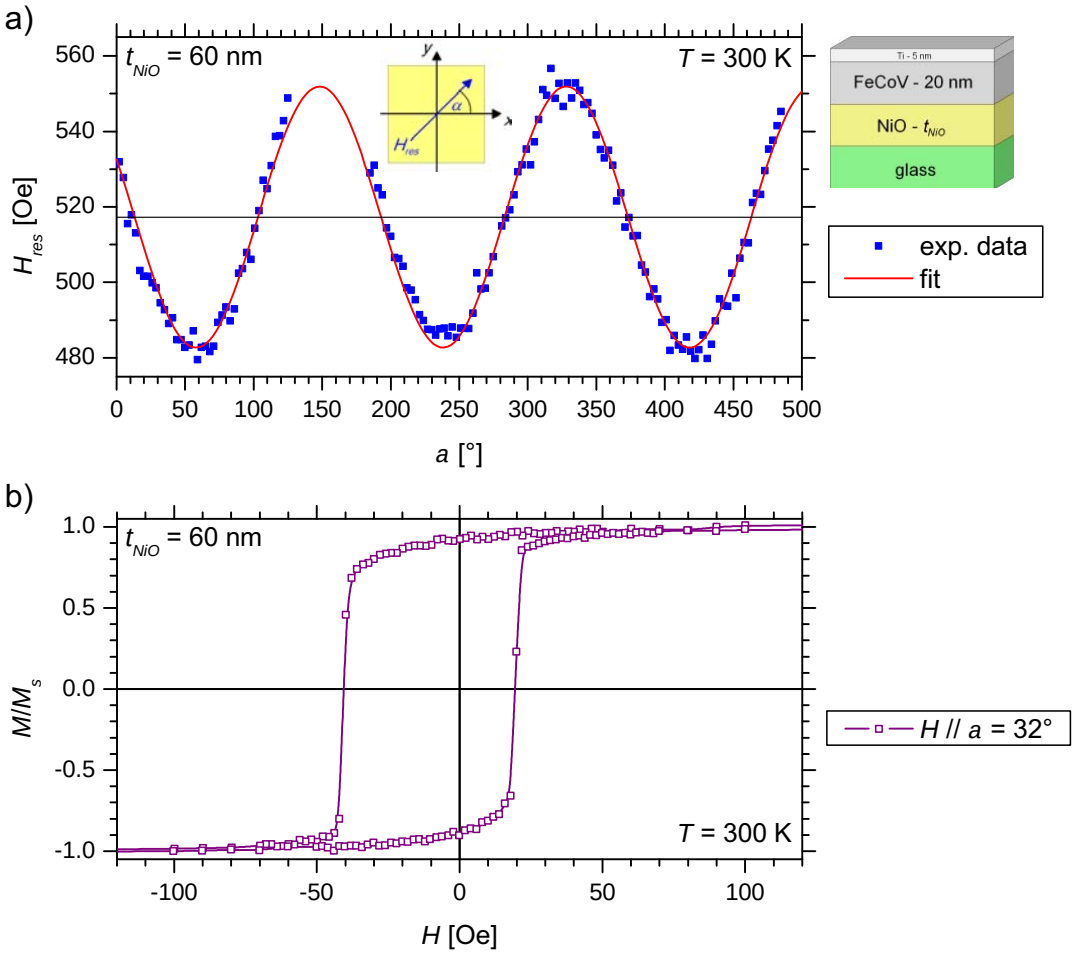

Figure 5.9: a) FMR of NiO (60 nm)/FeCoV (20 nm) bilayer. The resonance field H_{res} is plotted versus the sample orientation α. b) MH-loop measured along the anisotropy axis as deduced from the FMR experiment.

MH-dependence at $T = 2$ K

Figure 5.10 shows a compilation of MH-loops of NiO (t_{NiO})/FeCoV bilayers measured at $T = 2$ K along the anisotropy axis, i.e. easy axis of magnetization. The samples were cooled from room temperature to 2 K in a magnetic field of $H = 1000$ Oe, which was enough to saturate the magnetization of the samples. The plots contain the 1st and 6th loop after cooling having a difference due to training of the samples. All samples exhibit enhanced coercivities and exchange bias. Table 5.1 summarizes coercive H_c and bias H_{eb} fields deduced from the width of the hysteresis and the shift of the loop, respectively. It shows that both are increasing with increasing t_{NiO} first but then gradually decrease beyond $t_{NiO} = 20$ nm.

In further experiments, we cooled in zero magnetic field samples with NiO (40 nm)/FeCoV in their as-prepared state and measured MH-loops along x and y axes at $T = 2$ K. For this experiment, two different pieces were used, cut from adjacent

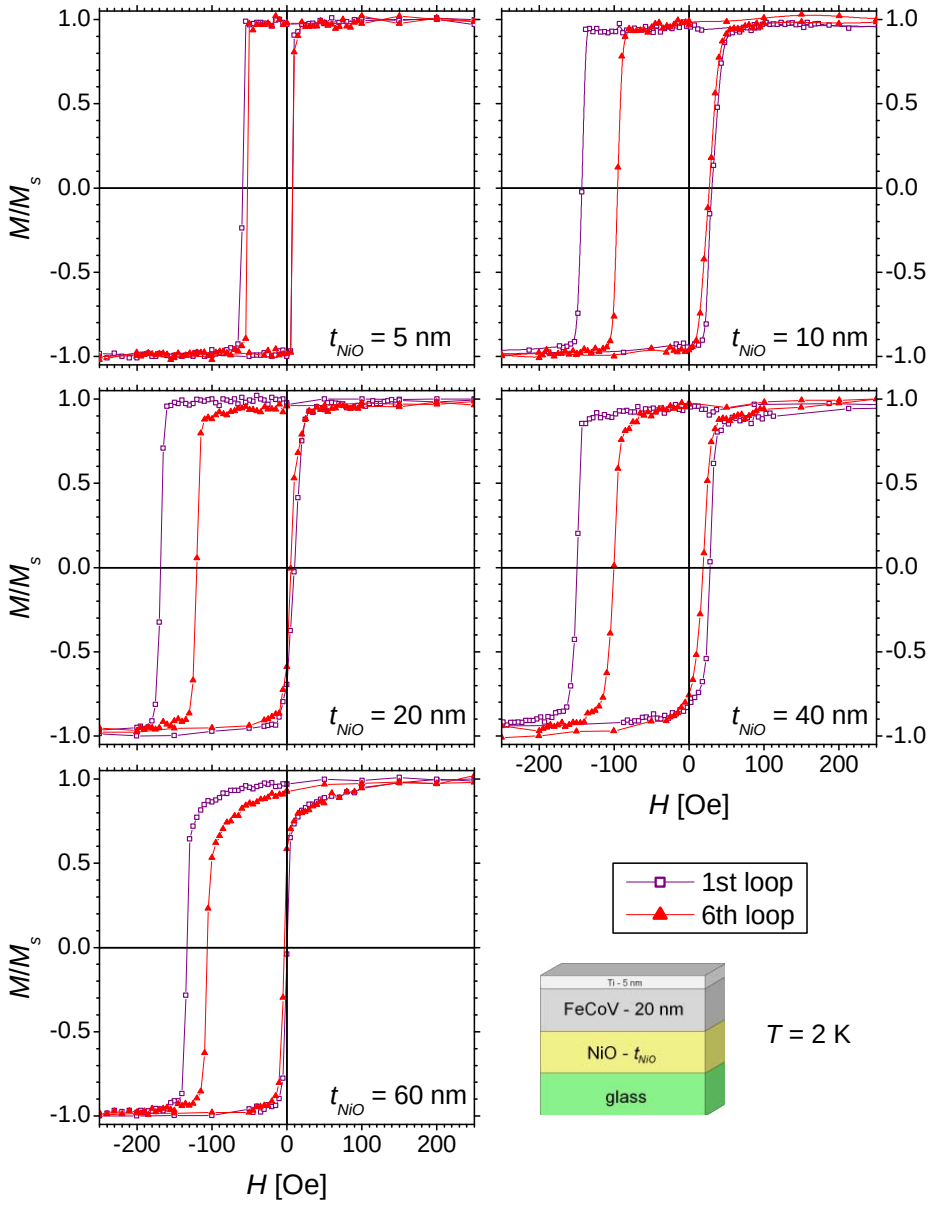

Figure 5.10: MH-loops of NiO (t_{NiO})/FeCoV (20 nm) bilayers measured at $T = 2$ K along the x axis of the samples, except $t_{NiO} = 60$ nm, which was measured along the anisotropy axis as deduced from the FMR experiment. The samples were cooled from room temperature to $T = 2$ K in a magnetic field of 1000 Oe. In addition to the first loops after cooling, the sixth loop is plotted showing the training of the samples.

t_{NiO}	1st loop		6th loop	
	H_c [Oe]	H_{eb} [Oe]	H_c [Oe]	H_{eb} [Oe]
5 nm	33	26	30	23
10 nm	87	56	61	34
20 nm	89	79	63	58
40 nm	89	61	59	41
60 nm	67	67	51	55

Table 5.1: Compilation of coercive H_c and bias H_{eb} fields of NiO (t_{NiO})/FeCoV (20 nm) bilayers at $T = 2$ K after field cooling in a magnetic field of 1000 Oe. The errors are ± 3 Oe.

locations in the original large sample. In both cases, first, the field was increased from 0 Oe to +1000 Oe (virgin loop). Second, the field was swept from +1000 to -1000 Oe and vice versa in order to record the hysteresis loop. Figure 5.11 shows the results of these experiments.

The virgin loop along the x axis, i.e. anisotropy axis, starts with a magnetization of $\approx -0.15 M_s$ at 0 Oe. While increasing the field, the magnetization is preserved until a field of $\approx +150$ Oe is reached. There, the magnetization jumps abruptly to positive saturation. While reducing the field to -1000 Oe, the reversal of magnetization occurs in two steps at fields of -25 Oe and -140 Oe, respectively. In between, the magnetization has a value of $\approx -0.15 M_s$. The variation of magnetization along the ascending branch is very similar to the descending branch as described before. The steps are at +35 Oe and +120 Oe. One important detail is that the magnetization at the intermediate plateaus in both branches of the hysteresis loop and at the beginning of the virgin loop are identical. Thus, the individual steps in the MH-loop can be attributed unambiguously to the magnetization reversal of two types (A and B) of domains, which are exchange biased in opposite direction.

In order to quantify the associated coercive and bias fields, it is necessary to consider the individual history before the reversal of a respective type of domain. Let us say, the magnetization of domains of type A (B) in the as prepared state is opposite (along) the positive field direction. When the field is increased during the virgin loop, domains A experience the reversal opposite to their bias field. For domains B nothing happens as they are already aligned along the direction of the external field. In the descending branch the first step corresponds to the first reversal of domains A towards their bias field. As a result, the bias field of domains A is $H_{eb} = (63 \pm 3)$ Oe (shifted to $+H$) and their coercivity is $H_c = (88 \pm 3)$ Oe. During the virgin loop, domains of type B are not affected, thus the second step in the descending branch and the first step in the ascending branch correspond to first reversals opposite and towards their local exchange bias field, respectively. The deduced bias field and coercivity of domains B are $H_{eb} = (53 \pm 3)$ Oe (shifted to $-H$) and $H_c = (88 \pm 3)$ Oe, respectively. The values are in good agreement with the values deduced from the first MH-loop after field cooling (see table 5.1). The magnetization of $\approx -0.15 M_s$ at the beginning of the virgin loop and during the intermediate plateaus suggests that the distribution of domains of type A and B is $\approx 57 : 43$.

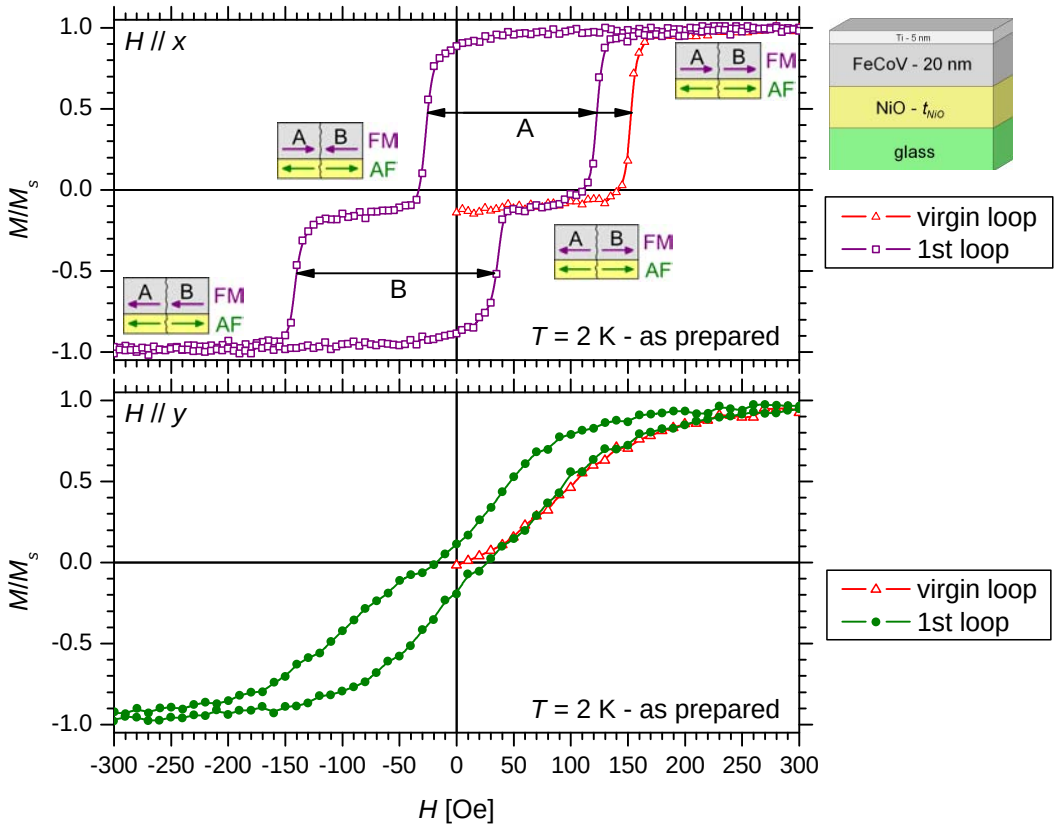

Figure 5.11: MH-loops of NiO (40 nm)/FeCoV(20 nm) bilayer measured at $T = 2$ K. The cooling was performed in the as-prepared state and zero magnetic field. The pictograms show the orientation of the two types of domains (FM) at particular states of the hysteresis loop. The direction of the pinning is marked by the arrows in the antiferromagnet (AF). The experiments are performed on two different pieces being next to each other in the original large sample.

The MH-loop measured along the y axis, i.e. perpendicular to the anisotropy axis, shows the expected reversal of a magnetically hard axis. The loop is centered around zero field supporting the assumption that no domains exist in the as-prepared state with a component of magnetization parallel to the y axis.

MH-dependence at $T > 300$ K

Additionally, we measured MH-loops of the NiO (10 nm)/FeCoV (20 nm) bilayer at temperatures of $T = 400$ and 530 K with the latter being above T_N of bulk NiO. Due to the specifications of the SQUID magnetometer for the sample size and the mounting of the sample (see section 3.1.2) two pieces had to be used to perform the measurements along the x and y axes, respectively. The measurements are plotted in figure 5.12 including the results at $T = 300$ K for comparison.

At $T = 400$ K, the type of the magnetization reversal is unaltered compared to $T = 300$ K representing a magnetically easy axis along x and a hard axis along y.

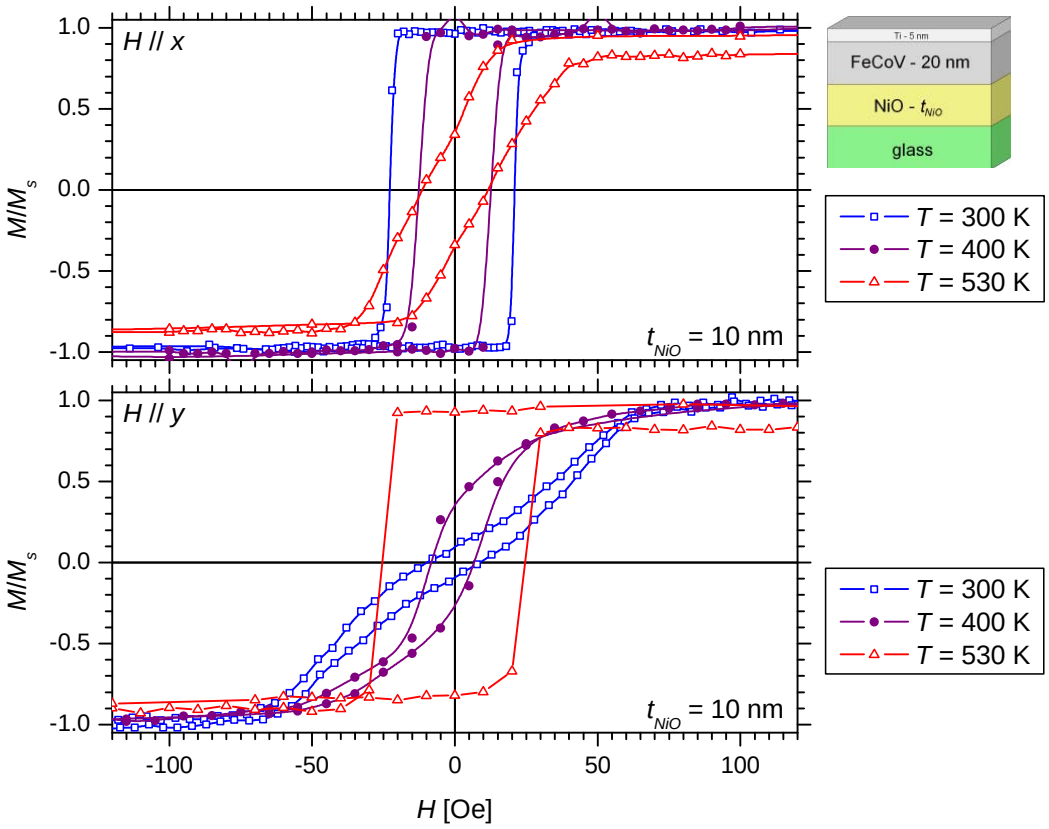

Figure 5.12: MH-loops of NiO (10 nm)/FeCoV(20 nm) bilayer measured at various temperature.

The coercivity along the x axis is slightly reduced to (12 ± 3) Oe. The MH-loop at $T = 400$ K along the y axis deviates from the loop at 300 K but still resembles the shape of a magnetically hard axis. The situation becomes different at $T = 530$ K, which is above the Néel temperature of bulk NiO ($T_N = 523$ K). Here, the MH-dependence along the x axis is linear during the magnetization reversal indicating a magnetically hard axis. Along the y axis the hysteresis has the square shape of a magnetically easy axis. Hence, the anisotropy has changed its orientation above T_N.

As already observed in FeCoV/NiO bilayers the saturation magnetization is reduced at negative saturation and at positive saturation of the ascending branch, compared to its initial value at the beginning of the measurement at $T = 530$ K. Obviously, the sample undergoes a modification during the measurement of the hysteresis. Presumably, interdiffusion reduces the magnetization at the interfaces of the FeCoV layer. However, the results show a significant difference of the magnetic properties below and above T_N of bulk NiO, i.e. between the antiferromagnetic and the paramagnetic phase of the NiO layer. This confirms that below T_N the magnetic properties of the FeCoV layer are influenced by the antiferromagnetic NiO because of interfacial coupling between the two layers.

5.3.2 Discussion

We observe that NiO (t_{NiO})/FeCoV bilayers have low coercivity and magnetic anisotropy in the plane of the films, which is in contrast to FeCoV single layers and FeCoV/NiO bilayers. The net magnetic anisotropy in the plane of the films presumably arises from an anisotropic strain distribution in the NiO layers. We measured the stress of the NiO (5 nm)/FeCoV (20 nm) bilayer along the x and y axis by comparing the radius of curvature of a thin silicon wafer before and after the deposition of the film. It shows an anisotropy with the stress along the y axis being tensile relative to the x axis. Hence, it is expected that the magnetically easy axis is parallel to the y direction since FeCoV has a positive magnetostriction coefficient (see section 5.1). In contrast, the MH-measurements show the easy axis parallel to the x axis suggesting that the magnetic anisotropy is established by the NiO layer and transferred to the FeCoV layer via interfacial coupling. In fact, NiO has a negative magnetostriction coefficient [101], thus, an anisotropy based on magnetostriction is expected to be along the direction of compressive stress, i.e. along the x axis in the present case. The conclusion is supported by the MH-loops of the NiO (10 nm)/FeCoV (20 nm) bilayer at $T = 530$ K. There, the orientations of magnetically easy and hard axes are interchanged compared to $T \leq 400$ K. At $T = 530$ K, the NiO layer is in the paramagnetic phase ($T_N = 523$ K), i.e. the magnetic moments of Ni are not exchange coupled to each other. Consequently, since the antiferromagnetic state is not present, the magnetism of the FeCoV layer is solely determined by its intrinsic properties. Since the stress distribution is not expected to be significantly altered at $T = 530$ K the magnetically easy axis should be therefore parallel to the direction with tensile stress, which is according to the observations.

The low coercivity might be also a consequence of the anisotropy of the NiO layer. As discussed above, the stress distribution leads to anisotropies in FeCoV and NiO layers, which are perpendicular to each other. Due to interfacial coupling these are in competition but with the anisotropy of the NiO layer governing the magnetic properties. Nevertheless the competition reduces the barrier to execute the magnetization reversal resulting in the observed low coercivity. However, the microstructure, in particular the lateral grain size of the films may also influence the coercivity.

The shape of the hysteresis loops of NiO/FeCoV bilayers gradually varies with t_{NiO} at room temperature. This can be understood in terms of the ripple theory that describes the magnetization reversal in ferromagnetic thin films [102]. Irrespective of the existence of a net magnetic anisotropy, the magnetization reversal will never occur by a coherent rotation as predicted by the Stoner-Wohlfarth model. Lateral inhomogeneities create a distribution of local anisotropies with orientations deviating from the average anisotropy axis and intrinsic demagnetizing fields arise because of the fluctuations of the local anisotropy (figure 5.13). In order to minimize the demagnetizing fields, nucleation of domains takes place affecting the magnetization reversal.

During the magnetization reversal along the easy axis, i.e. parallel to the anisotropy axis, domains nucleate when the applied field is decreased from saturation reducing the intrinsic demagnetizing fields. In the following, domains with magnetization opposite to the direction of previous saturation grow and the magnetization reversal is

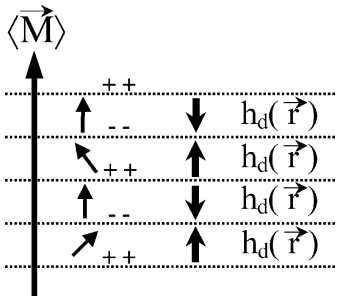

Figure 5.13: Illustration of magnetization ripples: local anisotropies deviate from the net anisotropy axis. The average magnetization $\langle\vec{M}\rangle$ aligns parallel to the net anisotropy axis. Local fluctuations of the magnetization (ripples) create intrinsic demagnetizing fields $h_d(\vec{r})$.

finished by domain wall motion. Dependent on the energy which is necessary to initiate the individual processes, the MH-loop has a different shape. For $t_{NiO} = 5$ nm, the magnetization reversal occurs as a sharp transition similar to the coherent rotation in a single domain particle described by the Stoner-Wohlfarth model indicating a well defined anisotropy axis. Nevertheless, the sequence of nucleation of reversed domains, domain growth and wall motion is involved but the processes occur immediately after each other since the energy to nucleate domains is the highest, blocking the others. The shape of the hysteresis loop suggests that the intrinsic demagnetizing fields are low. For larger t_{NiO}, a small but gradual decrease of the magnetization appears when the external field is reduced from saturation and applied in the opposite direction. This indicates that the energy for domain nucleation is lower and nucleation, growth and wall motion occur in this sequence step by step at distinct applied fields. Obviously the intrinsic demagnetizing fields increase when t_{NiO} is larger due to a larger distribution of the orientation of local anisotropies. The increase of local fluctuations is presumably associated with relaxation of the strain anisotropy with in increasing t_{NiO}.

The evolution of the MH-loops along the hard axis is consistent with the observations along the easy axis as discussed above. For small t_{NiO}, the low intrinsic demagnetizing fields allow the formation of large domains. Each domain behaves like a Stoner-Wohlfarth single domain and the magnetization within it rotates coherently towards the external field during the magnetization reversal. Therefore, the MH-loop is linear between opposite saturation for $t_{NiO} = 5$ nm with a remanence being almost zero. The saturation field is determined by the magnetic anisotropy of the system. At larger t_{NiO}, the stronger demagnetizing fields affect the magnetization reversal leading to the observed hysteresis and remanence larger than zero.

In addition, we find the evolution of a two step process along the hard axis of the MH-loops with increasing t_{NiO}. Liu and Adenwalla observed a very similar property in an exchange biased NiO (45 nm)/NiFe (15 nm) bilayer [103]. They imaged the magnetization reversal using magnetic force microscopy and found the formation of domain walls as a consequence of the distribution of the orientation of local anisotropies. In their case,when the applied field was reduced from saturation along the hard axis, the magnetization rotated towards the local anisotropies rather easily. At some stage, the

magnetization of neighboring areas pointed towards different directions according to the axis of the local anisotropy, thus domain walls were formed between them. Further, they observed that while decreasing the applied field towards opposite saturation the domain walls were pinned. Consequently, the magnetization within the domains coherently rotates as also expected within the ripple theory. Only when the applied field is strong enough the domain walls could untwist because all domains align along the external field. They conclude that, at fields where the domain walls are formed, interfacial exchange apparently governs the magnetization reversal and blocks the rotation of the magnetization. The blocking is not uniform because of the distribution of local anisotropy axes causing a step in the MH-loop.

In terms of the ripple theory, a distribution of local uniaxial anisotropies causes hysteresis along the magnetically hard axis but not a step in the MH-loop. The step arises from a distribution of unidirectional anisotropy axes, which originate from the interface coupling between the ferro- and antiferromagnet. This is consistent with our observation that the evolution of the step along the hard axis is accompanied by weak exchange bias along the easy axis. Although the hard axis for $t_{NiO} = 20$ nm shows a step, exchange bias along the easy axis cannot be identified, presumably because of the finite resolution of the measurement.

At room temperature, we find only small exchange bias for samples with $t_{NiO} \geq 40$ nm but exchange bias becomes significant at low temperature for all thicknesses of the NiO layer. This is contrast to the results of Liu and Adenwalla who observed exchange bias with a bias field of $H_{eb} \approx 40$ Oe along the easy axis at room temperature. Additionally, they find that with increasing temperature, exchange bias decreases and vanishes around $T = 450$ K. They claim that this is a consequence of thermal activation making the antiferromagnet spin structure unstable and the ferromagnet drags the antiferromagnetic spins. Except the range of temperature, our observations are consistent with the results of Liu and Adenwalla.

Therefore, we infer that in our case the antiferromagnetic spin structure is not stable at room temperature and rotates with the ferromagnetic layer. Presumably because of a net anisotropy in the antiferromagnet, its spins can be only flipped between two orientations determining also the stable orientations of the ferromagnetic magnetization via interfacial coupling. At low temperature, the spin structure of the antiferromagnet becomes rigid and it controls the magnetization reversal. The rotation of antiferromagnetic spins at room temperature and their stabilization at low temperature are supported by the comparison of the results at $T = 2$ K between field cooled and as-prepared zero field cooled samples. The latter shows that local interfacial coupling leads to a corresponding exchange bias, which depends on the orientation of the ferromagnetic domains (figure 5.11). When the ferromagnet is saturated, it drags the antiferromagnetic spin structure towards a common orientation. As a result, the field cooling experiment shows a uniform net exchange bias.

In summary, the magnetic properties of NiO/FeCoV bilayers are strongly determined by the antiferromagnetic NiO layer. Due to interfacial exchange between antiferromagnetic and ferromagnetic layers, the anisotropy in the NiO layer, based on the anisotropy

in the distribution of strain, is transferred to the FeCoV layer. Apparently, the strain anisotropy relaxes with increasing thickness of the NiO layer giving rise to fluctuations of local anisotropies. Although interfacial coupling is supposed to exist at room temperature, exchange bias is not observed, which is a consequence that the antiferromagnetic spins are not stable and follow the ferromagnetic magnetization during the magnetization reversal. At low temperature, the antiferromagnetic spins are stabilized leading to exchange bias and an increase in coercivity. In general, FeCoV layers deposited on top of NiO have rather low coercivity compared to the single layers and the FeCoV/NiO bilayers.

5.4 FeCoV/NiO/FeCoV trilayers

This section is dedicated to the measurements of the magnetic properties of the FeCoV (20 nm)/NiO(t_{NiO})/FeCoV(20 nm) trilayers using DC magnetometry and specular polarized neutron reflectometry with polarization analysis. The MH-loops show a strong dependence of the magnetization reversal on the thickness of the NiO spacer layer. From the layer resolved information about the magnetization, obtained from polarized neutron reflectivity measurements, we find that at small NiO thicknesses the magnetization of the FeCoV layers reverse simultaneously. For thicker NiO spacer layers the top FeCoV layer reverses first at a low field ($\approx H_c$ of NiO/FeCoV bilayers), followed by the bottom layer at a higher field, which is almost equal to the coercivity of the FeCoV/NiO bilayers. Between these two switching fields, the magnetization of top and bottom FeCoV layers are aligned antiparallel to each other. In addition, we measured hysteresis loops at low temperature and above T_N of NiO to test the influence of the antiferromagnet on the properties of the trilayer. The experimental results are presented in the following sections. A detailed discussion of these and regarding the role of NiO in mediating an exchange coupling between the ferromagnetic layers is given in section 6.

5.4.1 Bulk magnetization

MH-loops of FeCoV (20 nm)/NiO (t_{NiO})/FeCoV (20 nm) trilayers are presented in this sections. In addition to experiments at room temperature, the results at $T = 2$ to 530 K ($> T_N$ of NiO) provide information about the contribution of antiferromagnetic NiO to the magnetic properties of the trilayers. In the following, the results are partitioned according the temperature during the measurements.

MH-dependence at $T = 300$ K

Figure 5.14 shows the hysteresis loops of FeCoV/NiO/FeCoV trilayers for various NiO thicknesses measured at room temperature. The hysteresis reveals a strong dependence of the magnetization reversal on the thickness of the NiO layer. A single and gradual reversal process for $t_{NiO} \leq 10$ nm is observed with a coercivity of ≈ 165 Oe. For $t_{NiO} \geq 20$ nm, the reversal occurs in two steps, respectively at two different fields. The field of the first step decreases with increasing t_{NiO} until it remains constant at ≈ 70 Oe for $t_{NiO} \geq 60$ nm. The second step of the reversal occurs at ≈ 180 Oe independent of t_{NiO}. The net magnetization within the plateau separating the two steps in the

magnetization reversal, shows also a weak dependence on t_{NiO}. For $t_{NiO} = 20$ nm, the average net magnetization in the plateau is $\approx 0.2M_s$ opposite to the direction of magnetization prior to the reversal. This value decreases with increasing t_{NiO} and becomes $\approx 0.1M_s$ for thickest NiO layers.

The MH-loops along x and y directions are almost identical indicating that the magnetic properties are isotropic in the plane of the samples. Only the trilayers with $t_{NiO} \geq 60$ nm exhibit a weak anisotropy as suggested by the difference between the two orientations in the shape of the hysteresis loop at the edge of the first step in the magnetization reversal.

MH-dependence at $T = 2$ K

Selected trilayers, representative for a single transition ($t_{NiO} = 5$, 10 nm) and a two step process ($t_{NiO} = 40$ nm) of the magnetization reversal at $T = 300$ K, are measured at $T = 2$ K as well. These sample were cooled in a field of $H = 1000$ Oe and their hysteresis loops of the first and sixth cycle of field after cooling are plotted in figure 5.15. A compilation of coercive and exchange bias fields is provided in table 5.2. For $t_{NiO} = 40$ nm, it is assumed that first and second step of ascending and descending branches correspond to top and bottom FeCoV layers (as it will be proven by polarized neutron reflectivity section 5.4.2).

Trilayers with $t_{NiO} = 5$ and 10 nm show increased coercivity compared to room temperature but only weak exchange bias. The hysteresis loops of the sixth cycles are almost unaltered compared to the first indicating that almost no training of the samples occurs. Apparently, the typical properties associated with exchange bias are suppressed. This is in contrast to NiO/FeCoV bilayers with respective thicknesses, which show significant exchange bias of $H_{eb} = 26$ and 56 Oe in the untrained case for $t_{NiO} = 5$ and 10 nm, respectively. This suggests that the FeCoV layer at the bottom affects the antiferromagnet and therefore the origin for exchange bias of FeCoV layers on top of NiO.

For $t_{NiO} = 40$ nm, a shift of the complete hysteresis loop and a training of the sample is observed. The coercivity of the top FeCoV layer is enhanced by ≈ 70 % compared to the bilayer counterpart whereas exchange bias is almost identical. A similar evolution is observed for the bottom layer but the enhancement in coercivity relative to FeCoV/NiO bilayers at $T = 2$ K, is only ≈ 10 and 30 % of the untrained and trained sample, respectively.

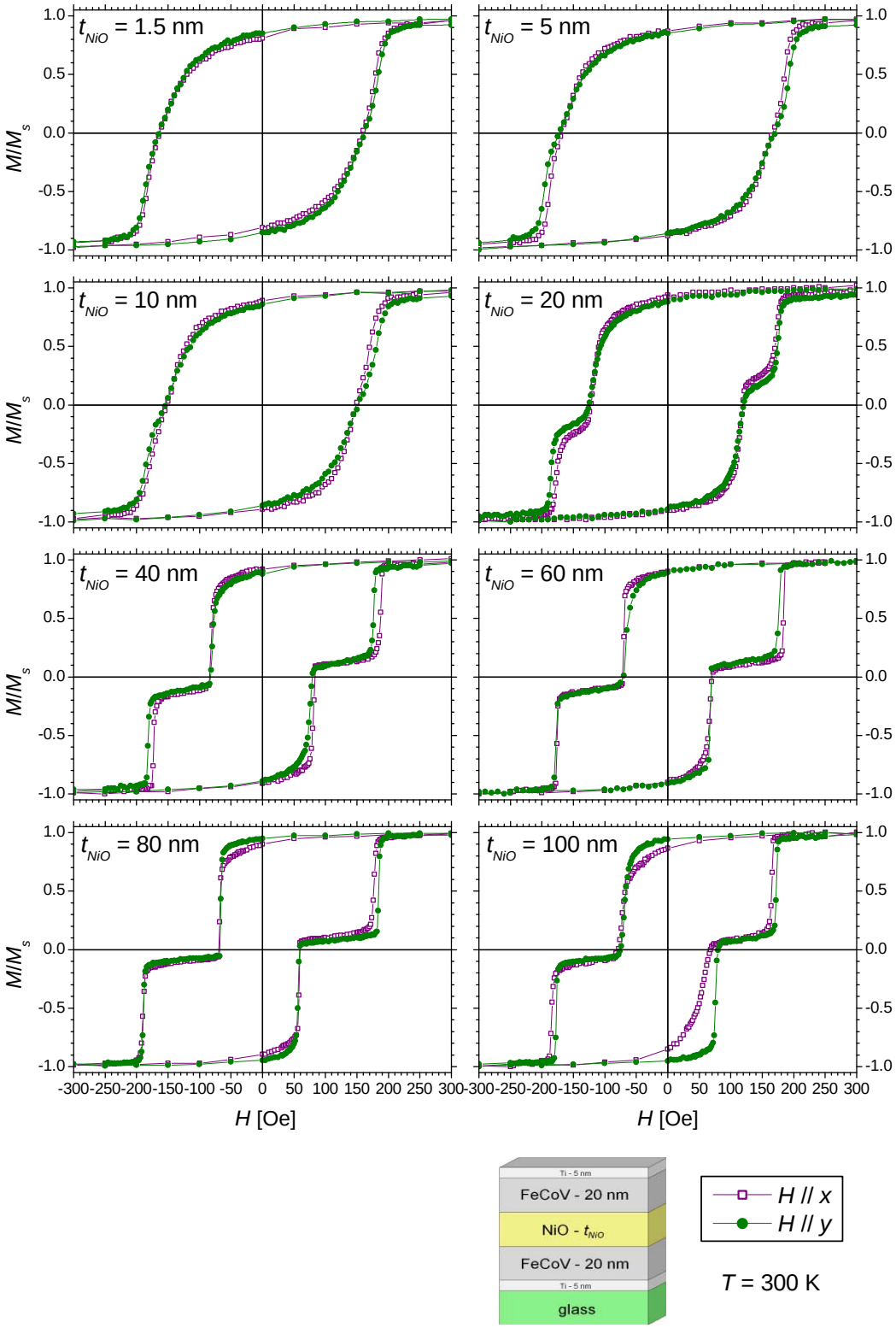

Figure 5.14: MH-loops of FeCoV (20 nm)/NiO (t_{NiO})/FeCoV (20 nm) trilayers measured with the external field applied in-plane along the orthogonal directions x and y of the samples.

t_{NiO}	1st loop		6th loop	
	H_c [Oe]	H_{eb} [Oe]	H_c [Oe]	H_{eb} [Oe]
5 nm	305	11	305	7
10 nm	290	11	290	7
40 nm (top FeCoV)	154	67	107	42
40 nm (bottom FeCoV)	369	47	331	27

Table 5.2: Compilation of coercive H_c and exchange H_{eb} fields of FeCoV (20 nm)/NiO (t_{NiO})/FeCoV (20 nm) trilayers at $T = 2$ K after field cooling in a magnetic field of 1000 Oe. The errors are ±3 Oe.

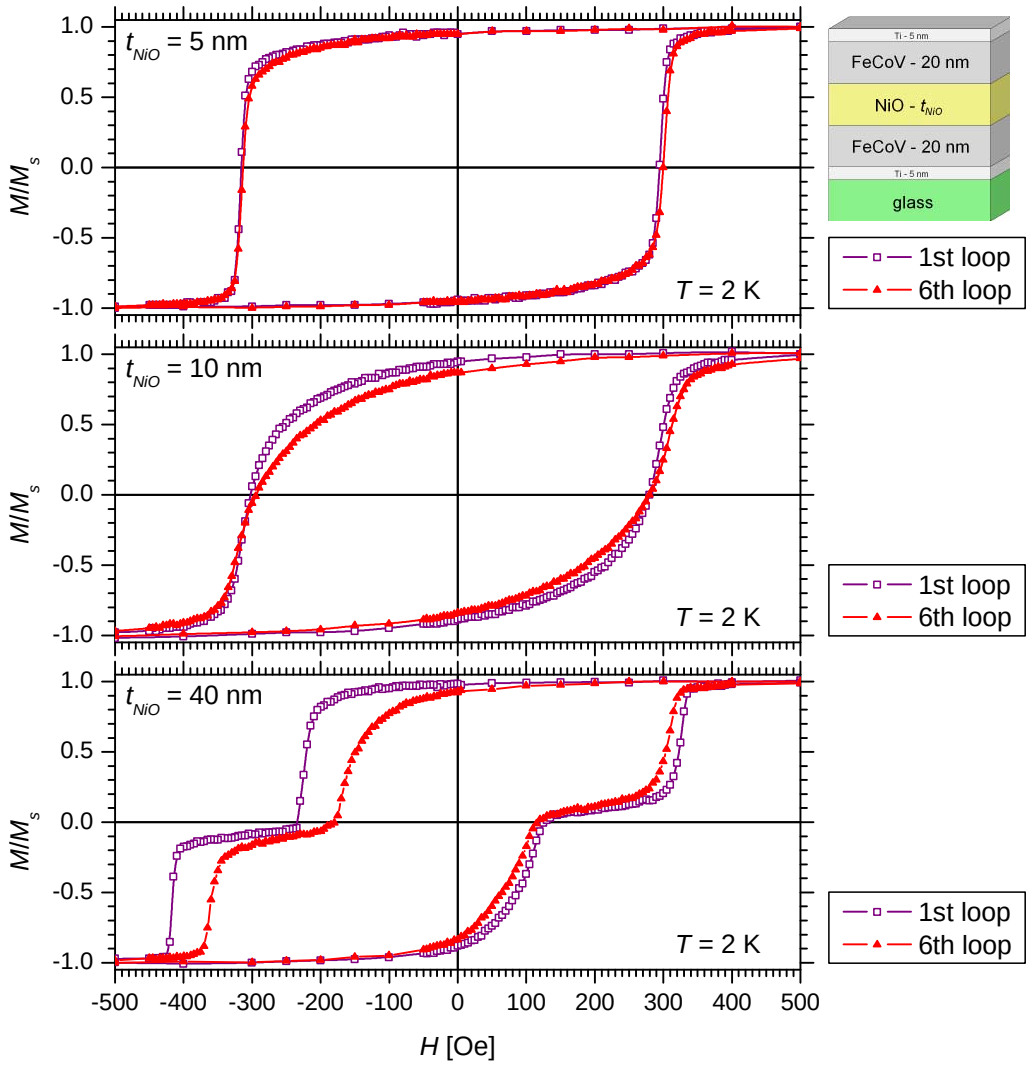

Figure 5.15: MH-loops of FeCoV (20 nm)/NiO (t_{NiO})/FeCoV (20 nm) trilayers measured at $T = 2$ K along the x axis of the samples. The samples were cooled from room temperature to $T = 2$ K in a magnetic field of 1000 Oe. In addition to the first loops after cooling, the sixth loop was measured to test the training of the samples.

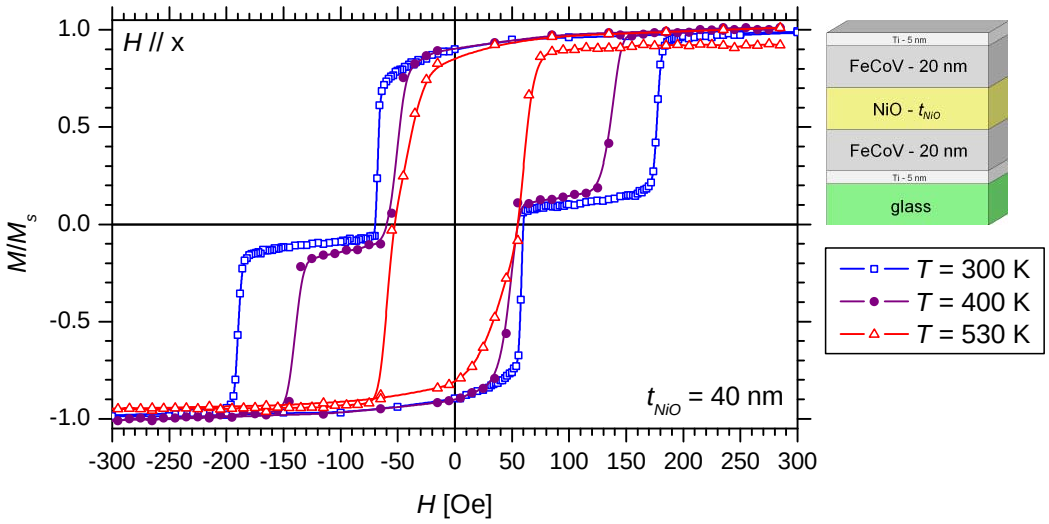

Figure 5.16: MH-loop of FeCoV(20 nm)/NiO (40 nm)/FeCoV(20 nm) trilayer measured at various temperature.

MH-dependence at $T > 300$ K

To test the evolution of the intermediate plateau in the magnetization reversal with increasing temperature, we measured MH-loops of the FeCoV/NiO/FeCoV trilayer with $t_{NiO} = 40$ nm at $T = 400$ and 530 K. The experimental results are plotted in figure 5.16 including the MH-loop at room temperature for comparison. At $T = 400$ K the magnetization reversal occurs in two steps similar as at $T = 300$ K. Only the fields corresponding to the steps are reduced since thermal activation supports the reversal of magnetization towards the applied magnetic field. The magnetization reversal becomes a single and gradual process at $T = 530$ K with a coercivity of (60 ± 3) Oe. Again, like in bilayers at $T = 530$ K, the saturation magnetization decreases during the experiment which manifests in an open loop at positive saturation, in particular.

5.4.2 Polarized neutron reflectivity

Polarized neutron reflectivity with polarization analysis (PNR) was performed on representative samples in order to retrieve the magnetization vectors layer resolved at various states of the hysteresis loop. All four cross-sections (R^{++}, R^{--}, R^{+-}, R^{-+}) were measured and their reflectivity profiles were modeled using the structural parameters obtained from the refinement of the X-ray reflectivity data (section 4.3) and adjusting the magnetic state of the ferromagnetic layers. The results are presented in the following order: (1) measurements at magnetic saturation, (2) measurements at magnetic states during magnetization reversal and (3) measurements with neutron polarization perpendicular to the sample.

Polarized neutron reflectivity at magnetic saturation

First measurements of the PNR profiles were conducted in a field of $H = +5000$ Oe applied to the samples. The results of these experiments are shown in figure 5.17. The intensities in the spin flip channels (R^{+-}, R^{-+}) are of the order of the background after correcting the experimental data for the finite efficiency of the polarizer/analyzer supermirrors (section 3.4.3). Therefore, they are not included in the plots. The reflectivity profiles show at low Q_z the regime of total reflection. For trilayers with $t_{NiO} = 1.5$ and 5 nm a distinct difference between the critical edges of R^{++} and R^{--} can be identified, which decreases with increasing t_{NiO}. It has to be considered that the neutrons have a finite penetration into the film even in the regime of total reflection, thus, probing an average of the scattering length density within this depth. In the case of the trilayers the average scattering length density $\langle \rho b \rangle$ can be formulated as

$$\langle \rho b \rangle = \frac{t_{FeCoV}}{t_{total}} \rho_{FeCoV} (2 b_{coh,FeCoV} \pm p_{m,FeCoVtop} \pm p_{m,FeCoVbottom}) + \frac{t_{NiO}}{t_{total}} \rho_{NiO} b_{coh,NiO} \tag{5.4}$$

assuming identical thicknesses t_{FeCoV} of top and bottom FeCoV layers and neglecting the thin Ti layers. The thicknesses t, number densities ρ and the coherent scattering lengths b_{coh} denote the parameters of the materials as given in the indices. t_{total} is the total thickness of the FeCoV/NiO/FeCoV trilayer and $p_{m,FeCoVtop(bottom)}$ is the magnetic scattering length of the top (bottom) FeCoV layer. Since the net magnetic moment of the antiferromagnetic NiO layer cancels in neutron reflectivity there is no magnetic contribution to the scattering.

In case of saturation, both magnetization vectors of top and bottom FeCoV layers are aligned parallel and equation 5.4 reduces to

$$\langle \rho b \rangle = 2 \frac{t_{FeCoV}}{t_{total}} \rho_{FeCoV} (b_{coh,FeCoV} \pm p_{m,FeCoV}) + \frac{t_{NiO}}{t_{total}} \rho_{NiO} b_{coh,NiO}. \tag{5.5}$$

At small t_{NiO} the average scattering length density is dominated by the contribution from the ferromagnetic layers, which depends on the neutron polarization, in addition. Therefore, the critical edge splits up (see equation 3.24 for comparison). In fact, the critical edge in the reflectivity profile R^{--} for $t_{NiO} \leq 5$ nm is determined by the

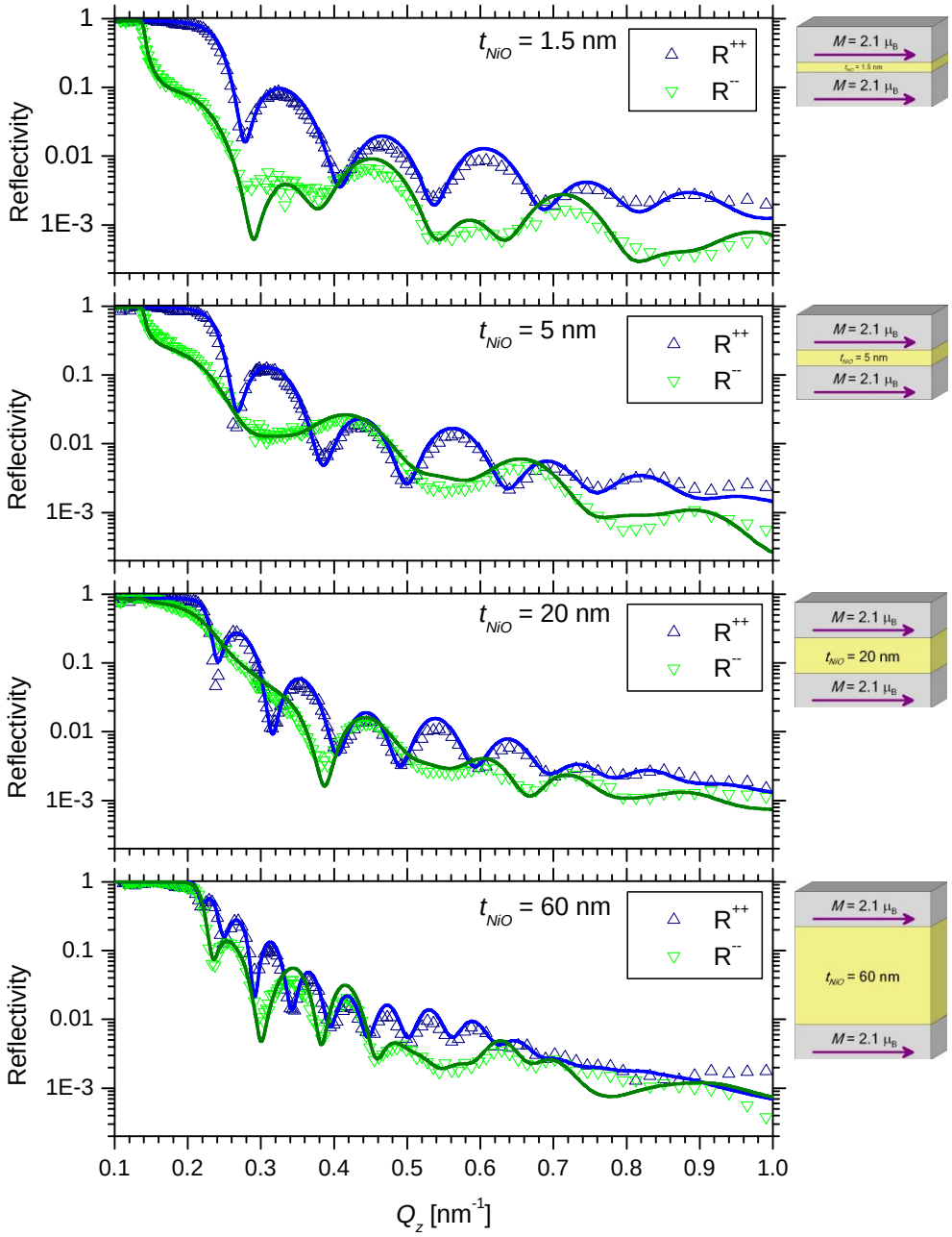

Figure 5.17: Polarized neutron reflectivity of FeCoV (20 nm)/NiO (t_{NiO})/FeCoV (20 nm) trilayers measured at $H = +5000$ Oe. Experimental data are represented by symbols and computed reflectivities by lines. The computation is based on the configuration of the magnetization vectors as illustrated by the schematics.

substrate since the scattering length ($b_{coh} - p_m$) is almost zero for the prominent contribution of FeCoV and therefore smaller than the scattering length of the glass substrate.

When t_{NiO} increases, the contribution of NiO becomes prominent and dominates $\langle \rho b \rangle$ at large NiO thicknesses. As a result, the polarization dependent part decreases relatively with increasing t_{NiO} and the splitting between the critical edge of the two neutron spin states decreases becoming almost zero at $t_{NiO} = 60$ nm. Additionally, the evolution of the critical edge for both neutron polarizations, i.e. the vanishing of the splitting, confirms qualitatively that the NiO layers do not contain residual ferromagnetic Ni. In such a case, this contribution would increase with increasing t_{NiO} and a splitting of the critical edge would remain.

Beyond the critical edge, the reflectivity profiles exhibit oscillations, which are related to the total thickness of the films. Therefore, their period decreases with increasing t_{NiO} as also observed and discussed in the case of the X-ray reflectivity measurements (section 4.3). The maxima in the reflectivity profiles R^{++} and R^{--} are shifted with respect to each other, which is a consequence of the difference in refractive index for the two spin states of the neutrons (equation 3.22).

The best agreement of the computed reflectivities with the experimental data is found consistently for a magnetic moment of $2.1\mu_B$ per f.u. for the ferromagnetic layers and full alignment along the applied field. The magnetic moment is ≈ 10 % lower than in bulk FeCoV ($2.3\mu_B$/f.u) [47] but consistent with previous investigations of Kentzinger et al. on the magnetization profile of a FeCoV/TiN_x polarizing supermirror [104]. The results from modeling and the absence of spin flip scattering confirm the existence of a magnetically saturated state present at a field of +5000 Oe.

Polarized neutron reflectivity during magnetization reversal

In order to unravel the evolution of the magnetization vectors during the magnetization reversal polarized neutron reflectivity profiles were measured at selected magnetic fields. Trilayers of various t_{NiO} were examined representing the different regimes from a gradual single reversal at thin NiO spacer layers to the two step process at thick NiO layers. Prior to the measurements all samples were subjected to $H = -5000$ Oe followed by the application of an appropriate positive field to prepare the desired magnetic state.

Figure 5.18 shows the results for $t_{NiO} = 1.5$ and 5 nm, measured at +150 Oe. Both cases exhibit a difference in the critical edge for R^{++} and R^{--}. Since the regime of total reflection is more extended for R^{--} than for R^{++} the magnetization vectors of the FeCoV layers have still a significant component antiparallel to the applied field. Significant spin flip scattering (R^{+-}, R^{-+}) is present resulting from components of the magnetization vectors perpendicular to the neutron polarization. Further analysis of the experimental reflectivities was done by modeling. It appears that the reflectivity profile is more sensitive to the magnetization of the top layer. The estimated error of the parameters of the magnetization vectors are $\pm 0.1\mu_B$ ($\pm 0.1\mu_B$) and $\pm 5°$ ($\pm 10°$) for the modulus and direction in the top (bottom) FeCoV layer, respectively. The

t_{NiO} [nm]	1.5	5	20			40	60
H [Oe]	150	150	100	135	165	110	110
M_t [μ_B]	0.8	0.8	1.0	1.0	0.8	1.8	2.0
α_t [°]	155	160	158	153	20	0	0
$M_{t,\parallel}$ [μ_B]	-0.73(9)	-0.75(9)	-0.93(9)	-0.89(9)	0.75(9)	1.80(9)	2.00(9)
$M_{t,\perp}$ [μ_B]	0.34(8)	0.27(8)	0.37(10)	0.45(10)	0.27(8)	0.0(2)	0.0(2)
M_b [μ_B]	1.2	1.0	1.2	1.4	1.2	1.7	1.5
α_b [°]	155	160	160	160	20	180	180
$M_{b,\parallel}$ [μ_B]	-1.1(2)	-0.9(2)	-1.1(2)	-1.3(2)	1.1(2)	-1.7(2)	-1.5(2)
$M_{b,\perp}$ [μ_B]	0.5(1)	0.3(1)	0.4(1)	0.5(1)	0.4(1)	0.0(2)	0.0(2)
$M_{net,\parallel}/M_s$	-0.43(4)	-0.40(4)	-0.49(5)	-0.53(5)	0.45(5)	0.02(5)	0.12(5)
M_{DCM}/M_s	-0.20	-0.29	-0.58	0.15	0.23	0.11	0.12

Table 5.3: Compilation of the parameters of the magnetization vectors deduced from modeling the PNR data. $M_{t(b)}$, $\alpha_{t(b)}$ are the modulus and the direction of the magnetization vector of the top (bottom) FeCoV layer, respectively. The reduction into parallel $M_{t(b),\parallel}$ and perpendicular $M_{t(b),\perp}$ components is also included. Finally, the net magnetization parallel to the applied field $M_{net,\parallel}$ is compared with the corresponding data M_{DCM} obtained from the hysteresis loop.

schematics in figure 5.18 depict the configurations of the magnetization vectors being used for the computed reflectivities. The deduced parameters of the magnetization vectors are summarized in table 5.3.

As the spin flip cross-sections (R^{+-}, R^{-+}) in PNR are sensitive only to the absolute value of the component of the magnetization perpendicular to the polarization of the neutron, the computed reflectivities are identical when both magnetization vectors are mirrored at the axis of the applied field. The profiles of the spin flip reflectivities (R^{+-}, R^{-+}) are different when the magnetization vector of only one layer is mirrored suggesting that the magnetization reversal of the two ferromagnetic layers occurs in unison with the applied field.

A comparison of the net magnetization parallel to the applied field calculated from the magnetization vectors and that from the corresponding bulk magnetization shows fairly good agreement. Deviations originate partly from the finite tolerance (±10 Oe) of the magnetic field applied to the sample during the PNR measurement, which is in particular crucial when the MH-loop has a steep slope at the point of interest. Moreover, the magnetic state of the sample, e.g. domain formation, can limit the information available from specular PNR, as discussed in the following including the results of all samples measured during the magnetization reversal.

The magnetization reversal of the trilayer with t_{NiO} = 20 nm is traced measuring polarized neutron reflectivity profiles at H = +100, +135 and +165 Oe. Figure 5.19 depicts the experimental data including the computed PNR profiles and the corresponding configurations of the magnetization vectors. The non-spin flip reflectivity profiles (R^{++}, R^{--}) become interchanged when the applied field is increased from H = +100 to +165 Oe in accordance with the reversal of the net magnetization. In addition, the spin flip reflectivities (R^{+-}, R^{-+}) increase initially from H = +100 to +135 Oe

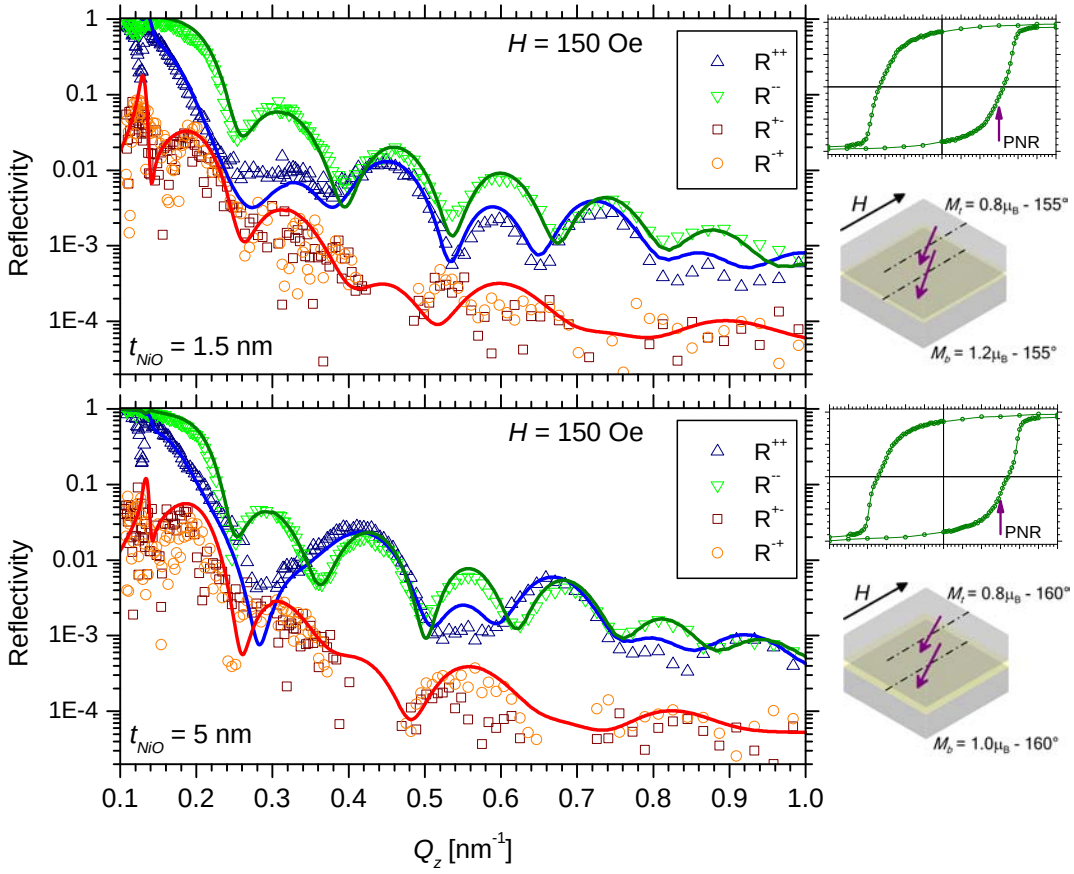

Figure 5.18: Polarized neutron reflectivity of Ti (5 nm)/FeCoV (20 nm)/NiO (t_{NiO})/FeCoV (20 nm)/Ti (5 nm) trilayers with t_{NiO} = 1.5 and 5 nm, measured at +150 Oe (see pictogram of MH-loops). Experimental data are represented by symbols and computed reflectivities by lines. The computation is based on the configuration of the magnetization vectors as illustrated by the schematics.

but decrease when the applied field is increased further to $H = +165$ Oe. The evolution of the spin flip scattering suggests that magnetic moments of the FeCoV layers are deviated away from the axis of the applied field during the magnetization reversal.

The measured reflectivity profiles at $H = +100$ Oe are well reproduced by the computations. It shows that the average magnetization of the FeCoV layers is reduced compared to saturation and forms certain angles with respect to the applied field. At $H = +135$ and 165 Oe, the non-spin flip (R^{++}, R^{--}) reflectivity beyond the critical edge and the level of spin flip scattering are described reasonably well by the computations. Some details are not reproduced in detail by the computation of specular PNR, presumably due to the presence of magnetic domains, which influence the magnetic scattering (see discussion below). As a result, the deduced net magnetization parallel to the applied field shows also significant deviations from results of DC magnetometry (table 5.3). Nevertheless, the experiments show unambiguously that both layers participate in the magnetization reversal simultaneously.

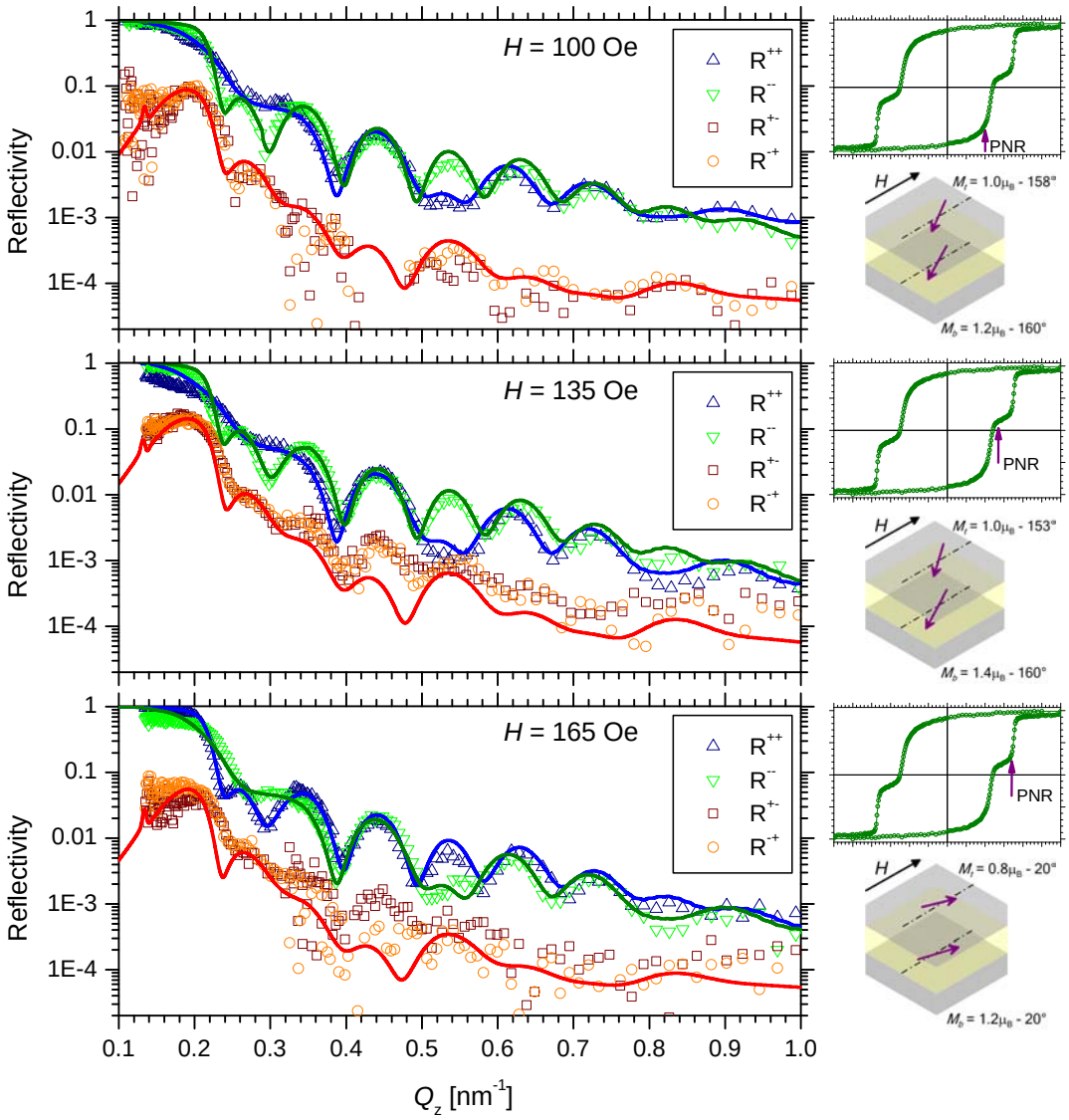

Figure 5.19: Polarized neutron reflectivity of Ti (5 nm)/FeCoV (20 nm)/NiO (20 nm)/FeCoV (20 nm)/Ti (5 nm) trilayer, measured at selected states of magnetization during the reversal (see pictogram of MH-loops). Experimental data are represented by symbols and computed reflectivities lines. The computation is based on the configuration of the magnetization vectors as illustrated by the schematics.

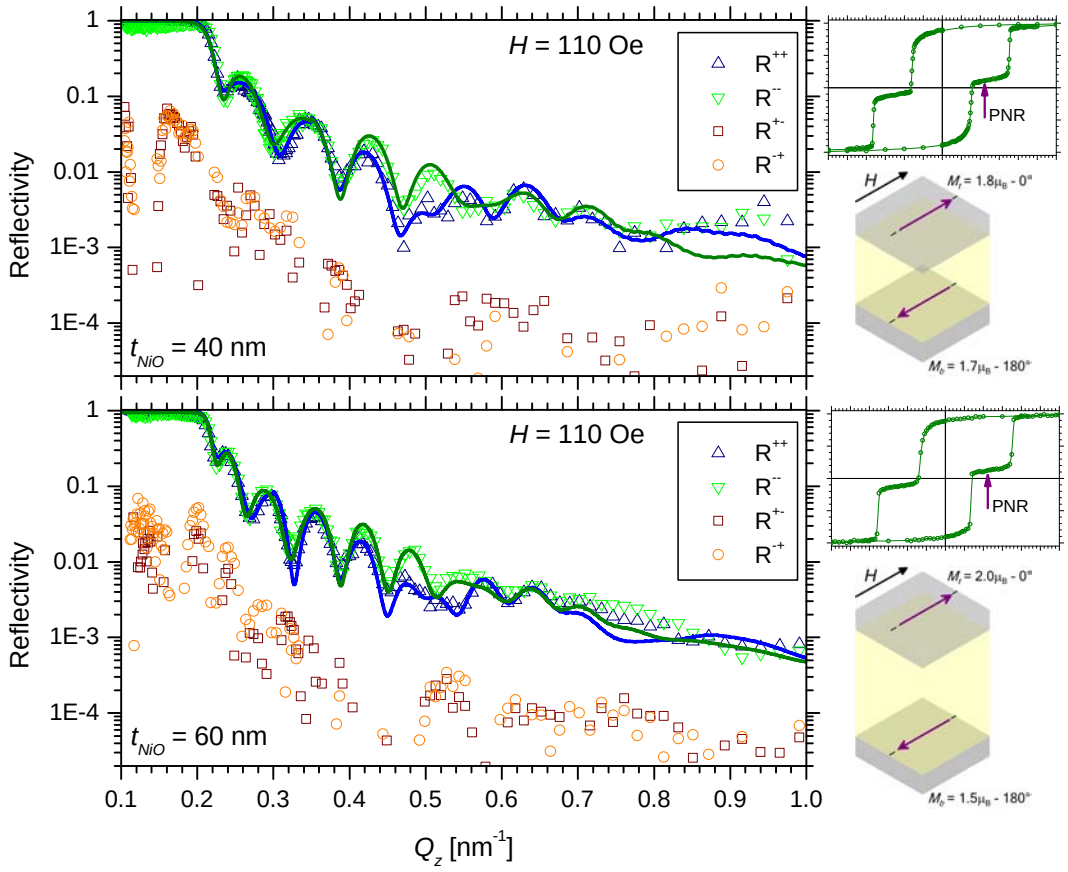

Figure 5.20: Polarized neutron reflectivity of Ti (5 nm)/FeCoV (20 nm)/NiO (t_{NiO})/FeCoV (20 nm)/Ti (5 nm) trilayers with t_{NiO} = 40 and 60 nm, measured at +110 Oe (see pictogram of MH-loops). Experimental data are represented by symbols and computed reflectivities by lines. The computation is based on the configuration of the magnetization vectors as illustrated by the schematics.

The polarized neutron reflectivity of the trilayers with t_{NiO} = 40 and 60 nm was measured at +110 Oe representing the region of the plateau separating the two steps of the reversal. In figure 5.20, experimental and computed reflectivities are plotted. The profiles of non-spin flip reflectivities (R^{++}, R^{--}) are almost identical suggesting that the refractive index is almost identical for both spin states of the neutrons. Considering equation 5.4, this is the case when either the magnetization of each FeCoV layer becomes zero ($p_m = 0$) or the magnetization vectors are oriented antiparallel. A third possibility is that the magnetization vectors are perpendicular to the neutron polarization which is incompatible with the observed low spin flip scattering.

The modeling shows that the experimental non-spin flip reflectivity profiles (R^{++}, R^{--}) can be reproduced with the magnetization vector of the top FeCoV layer aligned parallel and the magnetization of the bottom FeCoV layer antiparallel to the applied field (see schematics in figure 5.20). The magnetization in the top FeCoV layer is almost equal to the value at saturation while it is slightly reduced in the bottom layer

(table 5.3). The low level of spin flip scattering indicates that only small components of the magnetization vectors perpendicular to the applied field are present. The results unambiguously show that the ferromagnetic layers are magnetized opposite to each other. In detail, the magnetization of the top FeCoV layer reverses at the first step in the MH-loop while in the bottom layer the magnetization is still pinned in a direction opposite to the applied field until its switching field is reached.

In general, the total magnetic moments of the FeCoV layers are reduced during the magnetization reversal compared to their saturation moment. The reduction indicates that the ferromagnetic layers break up into lateral domains, which are smaller than the in-plane coherence length of the neutron beam (few 10 μm). Therefore, the coherent neutron beam probes an average over many domains with different orientations causing additional complexity in the scattering of the neutrons. Domains are lateral fluctuations of the local magnetization giving rise to off-specular scattering. Due to the finite instrumental resolution, the intensity measured in specular reflectometry contains also a contribution from diffuse scattering. This might adulterate the specular reflectivity profile and therefore the information about the depth profile of the multilayer. In particular, the complexity due to a multi-domain state is observed for $t_{NiO} = 20$ nm at $H = 135$ and 165 Oe limiting the available information from the modeling of the specular PNR. Nevertheless, the reduced total magnetic moment is unambiguous and indicates that for $t_{NiO} \leq 20$ nm the magnetization reversal occurs for both FeCoV layers within the same range of the applied field. Off-specular PNR measurements are envisaged to distinguish specular and diffuse scattering and will provide additional information about the lateral distribution of magnetic domains.

Polarized neutron reflectivity with out-of-plane polarization

Additional experiments were performed with the polarization of neutrons held perpendicular to the sample surface (see section 3.4.2). The magnetic states of the samples were obtained using a separate electromagnet with the magnetic field applied in the plane of the sample by the following steps: i) the samples were saturated in a field of $H = -5000$ Oe in order to start from defined conditions, ii) the field is increased to the desired positive field, iii) third, the magnetic field was removed and the sample is transferred to the reflectometer. When the field was removed the original magnetic state was almost retained as proven by the MH-measurements. After the installation of the sample a guide field of $H \approx 30$ Oe is switched on to define the polarization of the neutrons perpendicular to the surface of the sample. It is to mention that DC magnetization measurements perpendicular to the surface show a hard axis of magnetization where saturation is achieved only beyond 20 kOe. Thus the guide field did not affect the in-plane layer magnetization at all. A Q-range of 0.1 - 0.5 nm^{-1}, covered with one angle of incidence (0.6°) was sufficient to observe the particular features of the experiment.

Figure 5.21 shows the experimental results of representative samples with $t_{NiO} = 5$, 20 and 60 nm. The applied fields in step ii) were $H = 150$ (figure 5.18), 135 (figure 5.19) and 110 Oe (figure 5.20), respectively. These fields correspond to those fields at which specular PNR with neutron polarization in the plane of the films were performed. For

each sample, a measurement with inverted guide field H_G at the sample was performed in order to exclude instrumental artifacts. The results for both orientations of H_G show the expected inversion of R^{+-} and R^{-+}. In all experiments, non-spin flip reflectivities (R^{++}, R^{--}) are identical since they are of pure nuclear origin. Small differences between R^{++} and R^{--} originate from a small inclination of the neutron polarization ($\leqslant 3°$) from being perpendicular to the sample surface. These tests demonstrate the authenticity of the experiments.

For $t_{NiO} = 5$ nm, no asymmetry of the spin flip reflectivities (R^{+-}, R^{-+}) is observed. It has to be considered that domains are present having a size smaller than the coherence length of the probing neutron beam. A random distribution of domains with arbitrary orientations in top and bottom FeCoV layers would also lead to identical spin flip reflectivities (R^{++}, R^{--}). However, such a configuration is not compatible with the PNR data with in-plane polarization. Therefore, the combined PNR results demonstrate that the magnetization vectors of the bottom and top FeCoV layers are collinear during the magnetization reversal.

A small asymmetry between R^{+-} and R^{-+} appears for $t_{NiO} = 20$ nm around $Q_z \approx 0.24$ nm^{-1}. The asymmetry suggests that the magnetic moments of top and bottom FeCoV layers are not collinear because they have some small freedom to respond to the applied field individually during the reversal. The asymmetry of the spin flip cross-sections (R^{+-}, R^{-+}) is pronounced for $t_{NiO} = 60$ nm and arises within a range of $0.22 < Q_z < 0.31$ nm^{-1}. It indicates that the magnetization vectors of top and bottom FeCoV layers are not exactly antiparallel between the two steps of the magnetization reversal. Apparently the magnetization of the top layer is aligned parallel to the applied but the orientation in the bottom layer has a small angle to the field axis giving rise to the observed weak spin flip scattering in the experiments with in-plane neutron polarization.

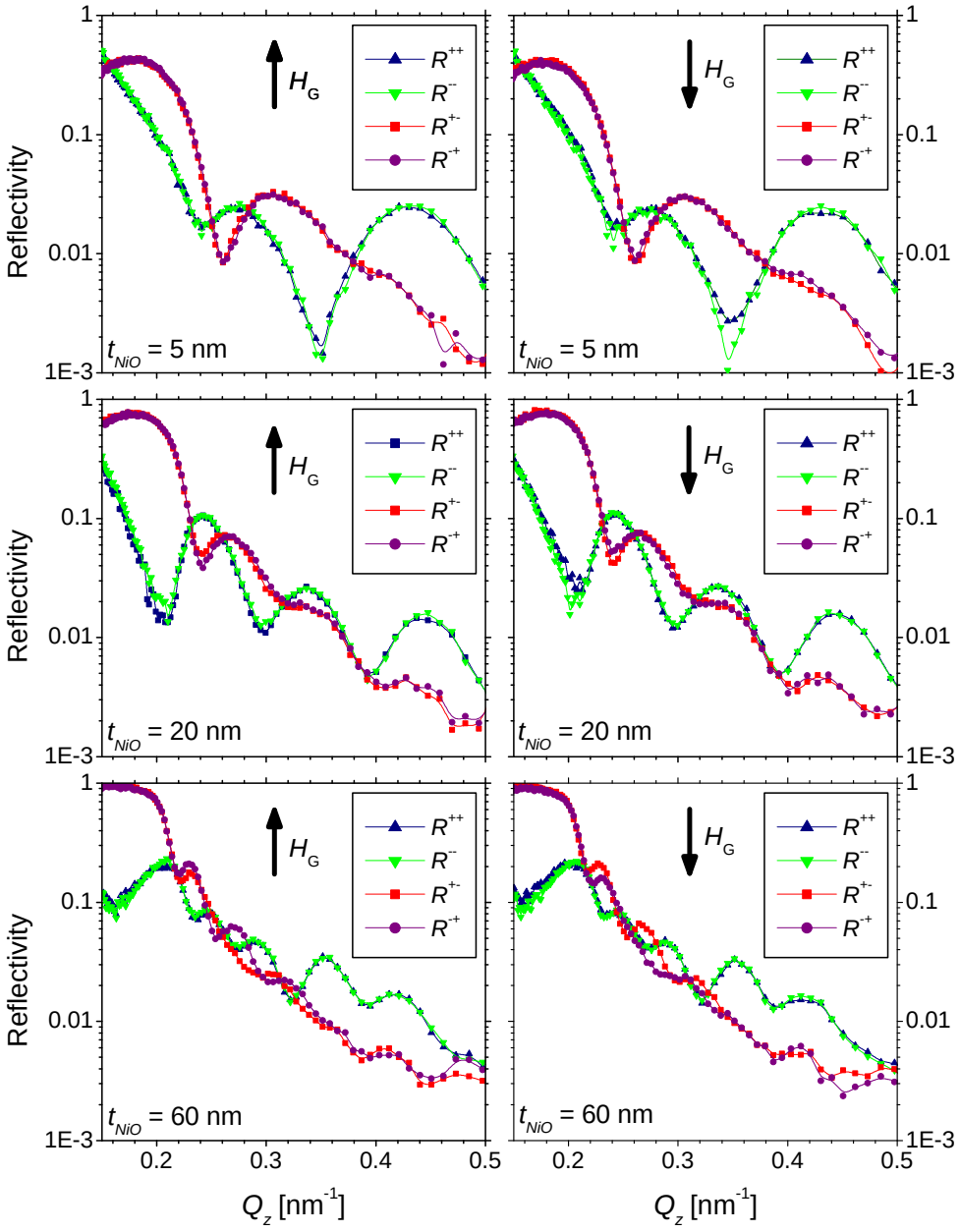

Figure 5.21: Polarized neutron reflectivity of trilayers Ti (5 nm)/FeCoV (20 nm)/NiO (t_{NiO})/FeCoV (20 nm)/Ti (5 nm) with neutron polarization perpendicular to the surface of the samples. Each sample is measured with the guide field H_G in either direction perpendicular to the sample to rule out instrumental artifacts. The size of the symbols represents approximately the size of the error bars.

Chapter 6

Discussion of the magnetization reversal of trilayers

This section discusses the observed magnetic properties of FeCoV/NiO (t_{NiO})/FeCoV trilayers regarding a possible exchange coupling of the ferromagnetic layers across the antiferromagnetic spacer. The discussion includes the separate information obtained from the systematic investigation of additional series of FeCoV single layers, FeCoV/NiO and NiO/FeCoV bilayers. The experiments, in particular polarized neutron reflectometry, reveal a coupling of the FeCoV layers, which depends on the thickness of the NiO spacer layer. Basic mechanism for interlayer exchange coupling are discussed focusing finally on the antiferromagnetic spins as the medium. The experimental observations are compared with scenarios demonstrated theoretically by Xi and White [26] for the magnetization reversal of exchange coupled ferromagnetic layers in ferro-/antiferro-/ferromagnetic trilayers involving the spins of the antiferromagnetic spacer.

The MH-loops of FeCoV/NiO (t_{NiO})/FeCoV trilayers show a dependence on the thickness of the NiO spacer layer. For $t_{NiO} \leq 10$ nm, the magnetization reverses via a single gradual process whereas for $t_{NiO} \geq 40$ nm the reversal occurs in two steps, which are clearly separated by a plateau of almost zero net magnetization. The width of the plateau remains nearly constant for $t_{NiO} \geq 40$ nm. Between the two regimes, the MH-loop for $t_{NiO} = 20$ nm reveals also two steps during the magnetization reversal but these are less separated than for $t_{NiO} \geq 40$ nm. It suggests that the range of 10 nm $< t_{NiO} <$ 40 nm corresponds to a transition from the single to the two step process of the magnetization reversal.

The bilayer series exhibit magnetic properties, which depend on the sequence of the layers. FeCoV (20 nm)/NiO bilayers show almost identical MH-loops like the FeCoV (20 nm) single layer at room temperature indicating that the intrinsic properties of FeCoV dominate the properties of the bilayer. Accordingly, it is expected that FeCoV layers at the bottom of the trilayers have the same intrinsic properties, in particular a relatively high coercivity ($H_c \approx 170$ Oe). Contrary to that, the series of NiO/FeCoV (20 nm) bilayers shows that FeCoV layers become magnetically soft when deposited on top of NiO with a small increase of H_c from ≈ 8 to 37 Oe for $t_{NiO} = 5$ to 60 nm, respectively. Hence, the results of the bilayer series suggest that in FeCoV/NiO/FeCoV trilayers the antiferromagnetic NiO layer is sandwiched between

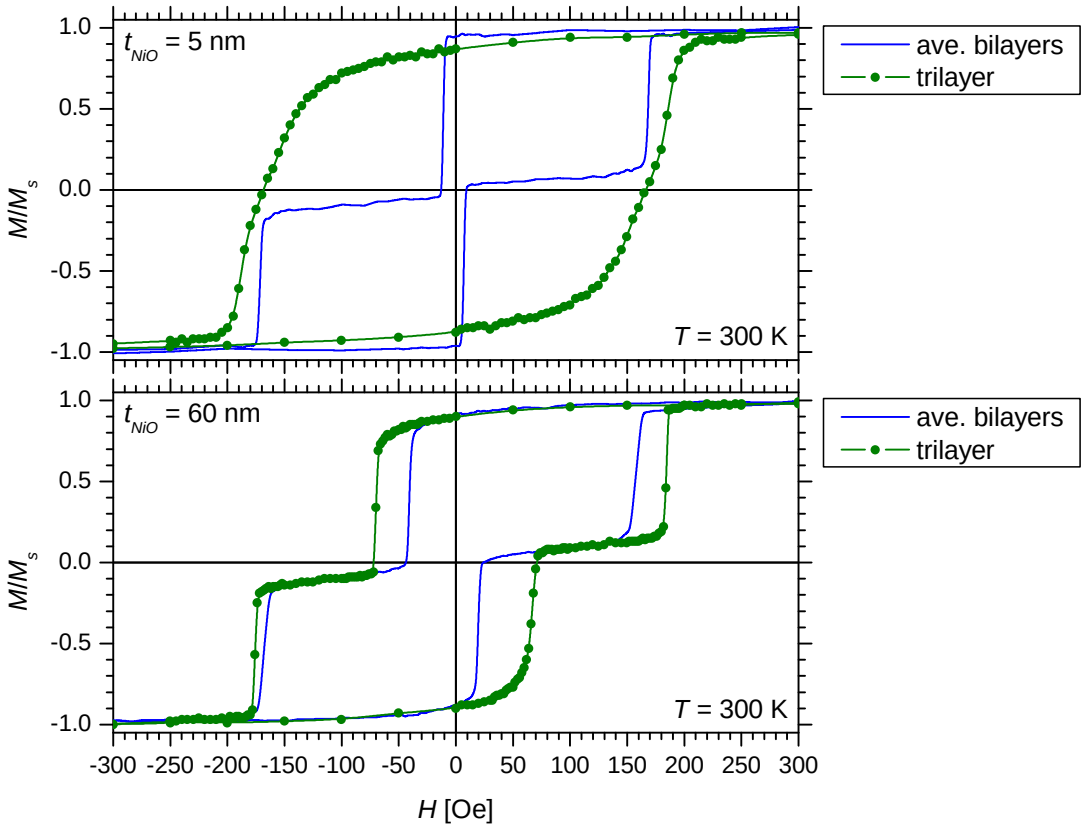

Figure 6.1: Comparison of MH-loops between trilayers and an average of corresponding FeCoV/NiO and NiO/FeCoV bilayers (blue lines).

a hard ferromagnetic layer at the bottom and a soft ferromagnetic layer at the top[1].

Averaged MH-loops of FeCoV/NiO and NiO/FeCoV bilayers are plotted together with MH-loops of respective trilayers in figure 6.1. The comparison shows that the simple averaging of the properties of the bilayers does not reproduce the features of the trilayers, neither for the thin nor for the thick regime of NiO spacer layers. In particular, for $t_{NiO} < 40$ nm the magnetization reversal of the soft top FeCoV layer is delayed compared to NiO/FeCoV bilayers. The increased reversal field is due to pinning, which originates via exchange coupling from the magnetically harder FeCoV layer at the bottom.

The coupling between FeCoV layers is evident from the analysis of polarized neutron reflectivities during the magnetization reversal. Table 6.1 summarizes the magnetization $M_{b,\|}$ (component parallel H) of the bottom FeCoV layer in the trilayers deduced from PNR. The data are compared with the magnetization M_{DCM} at corresponding fields from DC magnetometry on the FeCoV/NiO (60 nm) bilayer, which is representative for the series of FeCoV/NiO bilayers.

[1]The expressions soft/hard ferromagnetic layers denote in this present context ferromagnetic layers with low/high coercivity.

t_{NiO} [nm]	1.5	5	20			40	60
H [Oe]	150	150	100	135	165	110	110
$M_{b,\parallel}/M_s$	-0.5(1)	-0.4(1)	-0.5(1)	-0.6(1)	0.5(1)	-0.8(1)	-0.7(1)
M_{DCM}/M_s	-0.82	-0.82	-0.86	-0.83	0.79	-0.84	-0.84

Table 6.1: Magnetization of FeCoV layers at the bottom in trilayers and FeCoV/NiO bilayers. $M_{b,\parallel}$ is the component of magnetization vector in the trilayers parallel to the applied field deduced from PNR. It is compared with M_{DCM} from the hysteresis loop of the bilayer FeCoV/NiO (60 nm).

For $t_{NiO} < 40$ nm, $M_{b,\parallel}$ is significantly lower than M_{DCM} indicating that the magnetization reversal of the bottom FeCoV layer is further progressed in the trilayers than in the bilayer at identical applied fields. This is understood in terms of an exchange coupling between the ferromagnetic layers where magnetic moments of the magnetically soft top layer are not only pinned but some also drag magnetic moments of the originally hard bottom layer. This suggests that the magnetization reversal occurs simultaneously in both FeCoV layers via vertically correlated domains due to an exchange coupling between the ferromagnetic layers. Additionally, the results of polarized neutron reflectometry with neutron polarization perpendicular to the surface of the sample suggest that the magnetization vectors of top and bottom FeCoV layers for $t_{NiO} = 5$ nm are collinear during magnetization reversal (section 5.4.2). Polarized neutron reflectivity measurements for $t_{NiO} = 20$ nm indicate that the magnetization vectors of top and bottom FeCoV layers are not collinear (figure 5.21) and the magnetization reversal of the bottom FeCoV layer lags initially slightly behind the reversal of the top FeCoV layer but in the final stage of the magnetization reversal it is further progressed (figure 5.19).

For $t_{NiO} = 40$ and 60 nm the comparison in table 6.1 shows a good agreement between the results from PNR and DC magnetometry confirming the model of antiparallel magnetization vectors in the intermediate plateau for $t_{NiO} \geq 40$ nm.

From the above discussion, it follows that the dependence of the hysteresis loops of FeCoV/NiO/FeCoV trilayers on t_{NiO} is a consequence of an exchange coupling between the ferromagnetic layers, which depends on the thickness of the NiO spacer layers. The coupling is strong at small t_{NiO} connecting the magnetization reversal of top and bottom layer. It relaxes with increasing t_{NiO} allowing a separate reversal of top and bottom FeCoV layers.

In the introduction, various types of exchange coupling between ferromagnetic layers are addressed. The mechanism depends on the material of the layer separating the ferromagnetic layers. In the present work the spacer layer is an insulating antiferromagnet. Therefore, RKKY type of interlayer exchange coupling is excluded since it is mediated by metals via itinerant electrons. For insulating spacer layers, an exponential decay of interlayer exchange coupling with thickness is expected, a fact attributed to spin-polarized electron tunneling through the spacer layer [8]. Hence, it is only of short range (few atomic layers) and cannot be expected for the rather thick NiO spacer layers in this work.

The roughness of the layers may lead to pinholes that provide a direct contact and therefore a direct coupling of the ferromagnetic layers, in particular for very thin spacer layers. For a comparison of spacer layer thickness and roughness, the amplitude h of the surface profile of the bottom FeCoV layer is estimated assuming a sinusoidal varying roughness. In this case, h is related to the RMS roughness σ_{rms} by $h = \sqrt{2}\sigma_{rms}$. It results in a peak to peak distance of $2h \approx 1.4$ nm for the trilayer with thinnest NiO. This is close to the real layer thickness of $t_{NiO} = 1.77$ nm, but already in the trilayer with $t_{NiO} = 5$ nm the fluctuations of the interface profile are significantly smaller than the thickness of the NiO spacer layer. Additionally, from off-specular X-ray reflectivity measurements a vertically correlated roughness is identified, which implies that the interface profile is not smooth but the layer thickness of NiO is homogeneous (see illustration in figure 4.15). Therefore, adjacent FeCoV must be well separated. In summary, it can be excluded that the observed exchange coupling for $t_{NiO} \leq 20$ nm is due to a direct coupling of the FeCoV layers via pinholes.

A magnetostatic coupling can arise from magnetic roughness, which is known as Néels orange-peel effect [105]. Figure 6.2 illustrates the dipolar field originating from magnetic poles at the rough interfaces. The field created by the bottom layer, which is assumed to be magnetically hard, acts on the soft top layer pinning its magnetization. Therefore the magnetization reversal of the top layer is hindered resulting in a gain in coercivity. The 'orange-peel' field H_N is estimated assuming a sinusoidal interface roughness profile (vertically coherent), with amplitude h and wavelength λ_r [105]:

$$H_N = \frac{\pi^2 h^2}{\sqrt{2}\lambda_r t_f} M_s e^{-\frac{2\pi\sqrt{2}t_s}{\lambda_r}} \tag{6.1}$$

t_f is the thickness of the magnetically soft layer, t_s that of the non-magnetic spacer layer and M_s is the saturation magnetization of the magnetically hard layer at the bottom. The amplitude h is deduced from the RMS roughness of the bottom FeCoV layer. The wavelength of the roughness oscillation is ≈ 4 μm as obtained from a preliminary AFM analysis. Computed H_N is plotted in figure 6.3 as a function of t_{NiO} of the FeCoV/NiO/FeCoV trilayers. This is compared with $H_{ex} = H_{c1} - H_{c2}$, which is the gain in coercivity of FeCoV layers on top of NiO in trilayers (H_{c1}) compared to NiO/FeCoV bilayers (H_{c2}) with corresponding t_{NiO} (for $t_{NiO} = 80$ and 100 nm H_{c2} of NiO (60 nm)/FeCoV is used). In the case of the trilayers, H_{c1} is the average of the fields where $M = 0.5M_s$ and $-0.5M_s$ in the descending and ascending branches, respectively, assuming that the magnetization reversal of the top FeCoV layer is represented by the first half of the transition. H_{ex} can be considered as the exchange field, which pins the soft magnetic FeCoV layer on top of the trilayers. It shows that the dipolar contribution from 'orange-peel' field H_N is only a few Oe (< 3 Oe) and does not account for the observed gain in coercivity of the ferromagnetic layers, which is one to two orders of magnitude larger.

Finally, I like to focus the discussion on the antiferromagnetic spin structure of the NiO spacer layer as the medium to promote exchange coupling between the ferromagnetic layers. Xi and White discuss theoretically the role of the antiferromagnetic spins for the magnetization reversal of ferro-/antiferro-/ferromagnetic trilayers [26]. They

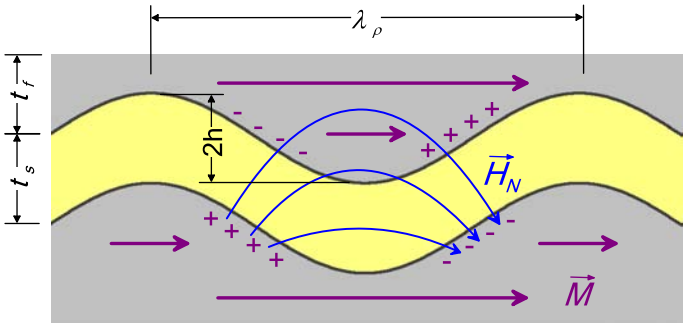

Figure 6.2: Illustration of the 'orange-peel' field H_N originating from magnetic roughness.

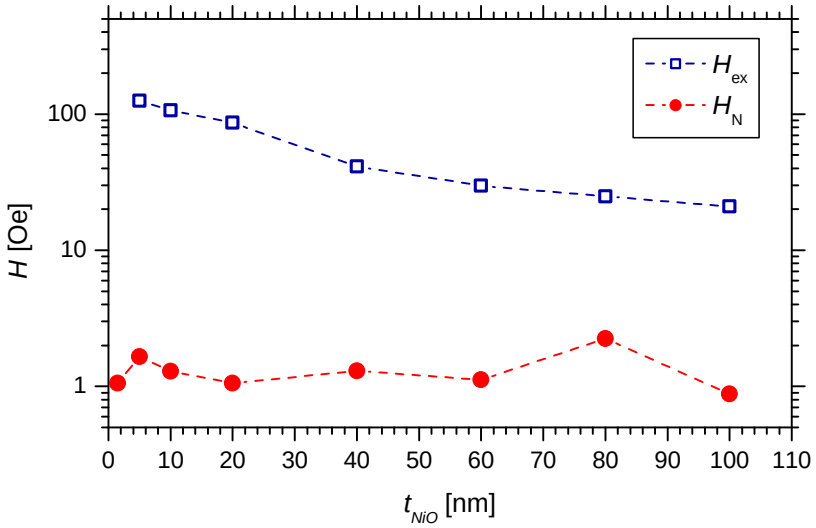

Figure 6.3: Comparison of the 'orange-peel' field H_N with the gain in coercivity H_{ex} of the top FeCoV layers deduced form MH-loops (see text).

demonstrate different scenarios of the evolution of the antiferromagnetic spin structure during the magnetization reversal of the ferromagnetic layers and emphasis the importance of the following parameters, in particular their relative values (see also figure 6.4):

- Interfacial coupling between the antiferromagnetic spacer and the ferromagnetic layers at either side, which is described by the area density of the interfacial coupling energies $J_{int(1)}$ and $J_{int(2)}$.

- Domain wall energy $\sigma_W = 2\sqrt{A_{AF} \cdot K_{AF}}$ of the antiferromagnet. A_{AF} and K_{AF} are the exchange coupling constant and the uniaxial anisotropy constant of the antiferromagnet.

- Domain wall width $\delta_W = \sqrt{A_{AF}/K_{AF}}$ and thickness t_{AF} of the antiferromagnetic spacer.

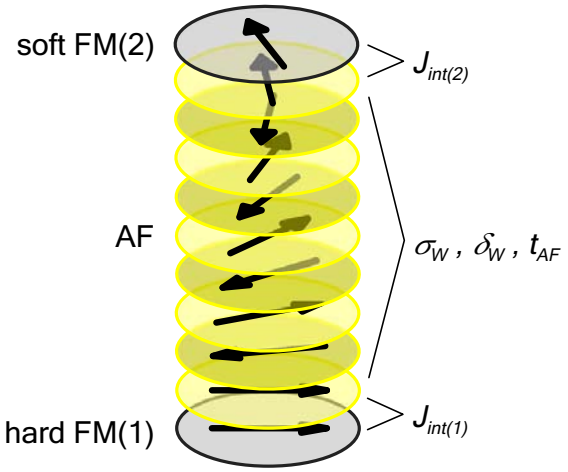

Figure 6.4: Illustration of a ferro-/antiferro-/ferromagnetic trilayer characterized by the interfacial exchange coupling constants $J_{int(i)}$, the antiferromagnetic domain wall energy σ_W and the domain wall width δ_W and thickness t_{AF} of the antiferromagnetic spacer.

Since interfacial coupling is an essential ingredient of the interlayer exchange coupling between the ferromagnetic layers, I like to summarize at this point the experimental results providing evidence for it in particular:

i) Exchange bias in FeCoV/NiO and NiO/FeCoV bilayers at $T = 2$ K (figures 5.6 and 5.10).

ii) Weak exchange bias in FeCoV/NiO and NiO/FeCoV bilayers with $t_{NiO} \gtrsim 40$ nm at $T = 300$ K (figures 5.4, 5.8 and 5.9b).

iii) Reorientation of the in-plane magnetic anisotropy in NiO/FeCoV bilayers at $T = 530$ K ($> T_N$), i.e. when NiO is paramagnetic (figure 5.12).

The observation of exchange bias at $T = 2$ K (i) demonstrates that an exchange interaction between ferro- and antiferromagnetic layers exists, which is valid for both interfaces of FeCoV/NiO and NiO/FeCoV. At room temperature, thermal activation surpasses exchange bias or it is only very weak as in bilayers with $t_{NiO} \gtrsim 40$ nm (ii). The absence of exchange bias must not necessarily imply an absence of interfacial coupling. In contrary, it might be an indication that the interfacial coupling is stronger than the anisotropy of the antiferromagnet, therefore the essential condition $K_{AF} \cdot t_{AF} \geq J_{int}$ for exchange bias is not fulfilled [106, 107, 108]. This is strongly supported by the experiments at $T = 530$ K (iii). As discussed in section 5.3.2, when NiO is paramagnetic ($T > 523$ K) the anisotropy of the NiO/FeCoV bilayer is defined by the intrinsic anisotropy of the FeCoV layer, which is apparently perpendicular to the anisotropy governing at room temperature. Hence, below T_N of the NiO layer its uniaxial anisotropy defines magnetically easy and hard axes of the NiO/FeCoV bilayer via interfacial coupling but the antiferromagnetic spins are rotated between the two directions of their uniaxial anisotropy. The rotation of the antiferromagnetic spins explains also the different behavior of the field cooled and zero field cooled as-prepared NiO/FeCoV bilayer at $T = 2$ K (figure 5.11). The as-prepared state contains two

types of domains, in which the magnetization points in opposite directions resulting also in opposite exchange bias. When the bilayer is saturated at room temperature the domains with originally opposite orientation drag the adjacent antiferromagnetic spins to the second equilibrium of their uniaxial anisotropy leading to uniform exchange bias at low temperature as observed for field cooled samples.

In conclusion, interfacial coupling is established between NiO and FeCoV layers but the spins of the antiferromagnet rotate irreversibly together with the magnetization of the ferromagnet during magnetization reversal of the bilayers at room temperature. Thus, exchange bias is not observed. This suggests further that the internal spin structure is destabilized by thermal activation at room temperature but becomes rigid at low temperatures promoting exchange bias.

Regarding the contribution of the internal spins of the antiferromagnet to magnetic properties the following experimental results provide distinct information:

iv) In FeCoV/NiO/FeCoV trilayers with $t_{NiO} \leq 10$ nm, only very weak exchange bias is observed at $T = 2$ K (figure 5.15), in contrast to the bilayer counterparts.

v) Polarized neutron reflectivity measurements in the range of the magnetization reversal of FeCoV/NiO/FeCoV trilayers with $t_{NiO} \leq 20$ nm reveal that in the bottom FeCoV layer the fraction of reversed domains is larger than in the single layer and bilayer counterparts at identical applied fields (table 6.1).

Trilayers with $t_{NiO} \leq 10$ nm show almost no exchange bias ($H_{eb} \lesssim 10$ Oe) when field cooled to $T = 2$ K (iv), which is in contrast to NiO/FeCoV bilayers with respective t_{NiO}, e.g. $H_{eb} = (56 \pm 3)$ Oe for untrained NiO (10 nm)/FeCoV bilayer. The comparison suggests that the effect of exchange bias is not only confined to the interfacial spins because in that case exchange bias must be expected also for the trilayers. Hence, the internal spins must be involved when exchange bias is observed. The different properties between bilayers and trilayers for $t_{NiO} \leq 10$ nm must originate from the difference at the bottom of the NiO layer and can be understood as follows. It is assumed that in the case of the NiO/FeCoV bilayer the end far from the antiferro-/ferromagnetic interface is rigid during the reversal of the FeCoV layer. The pinning of these antiferromagnetic spins is the origin for exchange bias, presumably, in combination with the formation of a planar antiferromagnetic domain wall as suggested by several authors, e.g. [14, 27]. This scenario is illustrated in figure 6.5a. When the ferromagnetic layer reverses, starting from the configuration with twisted antiferromagnetic spins, the planar domain wall in the antiferromagnet unwinds and assists the reversal. Therefore, the magnetization reversal occurs earlier than in the opposite direction leading to exchange bias. In the case of the trilayers, both ends of the antiferromagnetic layer are exchange coupled to ferromagnetic layers. Therefore, at both ends the spins of the antiferromagnet are dragged by the ferromagnetic spins during magnetization reversal. This leads to a complete rotation of the antiferromagnetic spin structure (figure 6.5b) erasing the pinning, which creates exchange bias in the bilayers.

Polarized neutron reflectivity data provide layer resolved information about the magnetization of the trilayers during the magnetization reversal at room temperature. As

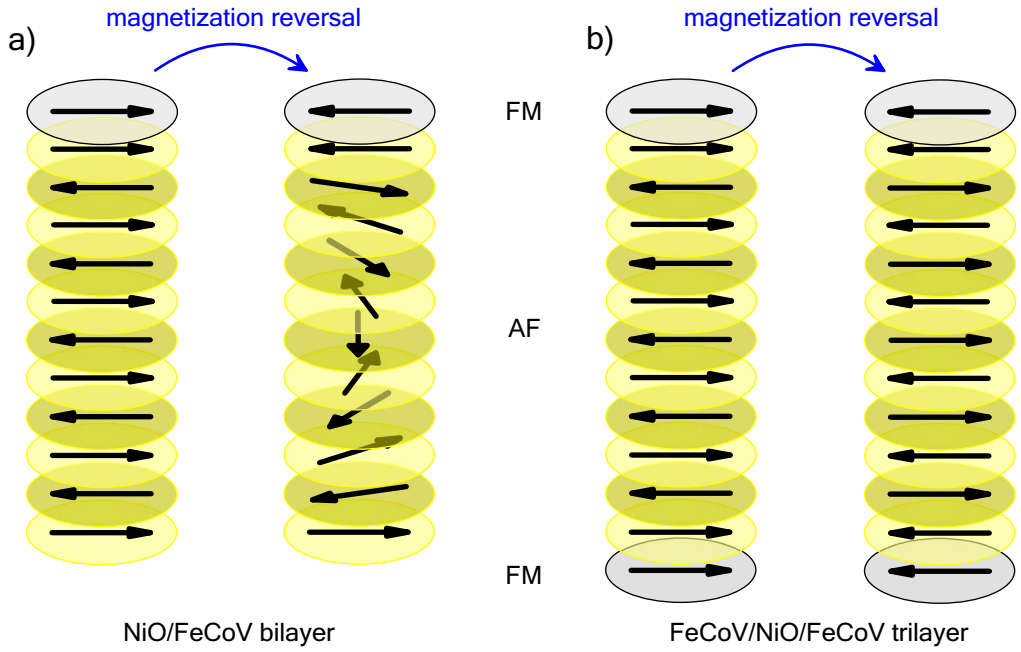

Figure 6.5: Illustration of the magnetization reversal at $T = 2K$ of a) NiO/FeCoV bilayer and b) FeCoV/NiO/FeCoV trilayer. In the case of the bilayer significant exchange bias is observed whereas the trilayers with $t_{NiO} \leq 10$ nm do not show exchange bias because the antiferromagnetic spins are dragged at either end leading to a complete rotation.

discussed above, it shows, that for $t_{NiO} \leq 20$ nm the magnetization reversal of the FeCoV layer at the bottom is initiated already at lower applied field than expected from its intrinsic properties known from FeCoV single layers and FeCoV/NiO bilayers (table 6.1). This suggests that the soft anisotropy of the top FeCoV layer is in competition with the high anisotropy in the bottom FeCoV layer because of exchange coupling of the ferromagnetic layers mediated by a rigid spin structure across the antiferromagnetic spacer. In more detail, the results from polarized neutron reflectometry show that for $t_{NiO} \leq 5$ nm the average magnetization of top and bottom FeCoV layer are identical in magnitude and orientation indicating that the domain pattern is identical in both ferromagnetic layers because of strong interlayer exchange coupling. An interaction between the ferromagnetic layers is also evident for $t_{NiO} = 20$ nm but a small difference between the magnetization vectors of top and bottom FeCoV layers is identified, which indicates a slightly relaxed coupling of the FeCoV layers compared to thinner NiO spacer layers. Nevertheless, the contribution of the internal antiferromagnetic spins is essential to understand the evolution of the magnetization of the FeCoV layers during reversal.

At this point, it can be concluded that the performed experiments provide evidence for interfacial coupling between the ferromagnetic FeCoV layers and the antiferromagnetic NiO spacer layer as well as the involvement of the internal antiferromagnetic spins. The strength of interfacial coupling can be assumed to be independent of the thickness of the NiO spacer since the analysis of the X-ray reflectivity shows for all samples very similar interface properties at the bottom of NiO as well as on the top of it. A different

strength at both sides of the antiferromagnet is indicated by the different values for exchange bias at low temperature, which is presumably a consequence of the thin oxide layer identified between bottom FeCoV and NiO layers. Identical interfaces between FeCoV and NiO layers above are apparent since the underlying structure is identical for all samples (FeCoV/NiO bilayers and FeCoV/NiO/FeCoV trilayers). Only a moderate increase of the roughness at the interface between NiO layers and the FeCoV layers on top of these is observed. Nevertheless, the NiO/FeCoV bilayers have rather similar magnetic properties supporting the conclusion that properties of these interfaces are independent of t_{NiO}. Hence, the observed dependence of the magnetization reversal of FeCoV/NiO/FeCoV trilayers on the thickness of the NiO spacer must be related to the contribution of the internal antiferromagnetic spins, which also depends on the thickness of the NiO layer.

Xi and White investigate in [26] theoretically the '*Coupling between two ferromagnetic layers separated by an antiferromagnetic layer*'. In their model they consider a twisting of the antiferromagnetic spins along the thickness direction (z), which is enforced by the rotation of one ferromagnetic layer FM(2) while the other one FM(1) is rigid. The total energy E_{SW} comprising the volume energy of the antiferromagnetic layer and the interfacial exchange coupling energies is written as

$$E_{SW} = \int_0^{t_{AF}} \left[A_{AF} \left(\frac{d\varphi}{dz} \right)^2 + K_{AF} sin^2\varphi \right] dz - J_{int(1)} cos(\Delta\varphi_{(1)}) - J_{int(2)} cos(\Delta\varphi_{(2)}) \tag{6.2}$$

where A_{AF} and K_{AF} are the exchange coupling constant and the uniaxial anisotropy constant of the antiferromagnetic layer with thickness t_{AF}. $J_{int(1)}$ and $J_{int(2)}$ are the interfacial exchange coupling constants between the antiferromagnet and the rigid FM(1) and the rotating ferromagnetic layers FM(2), respectively. $\Delta\varphi_{(1)}$ and $\Delta\varphi_{(2)}$ are the angles between adjacent antiferro- and ferromagnetic spins at either interface of the antiferromagnetic spacer. φ is the angle of individual antiferromagnetic spins with respect to their anisotropy axis. The minimization of E_{SW} defines the configuration of the antiferromagnetic spins dependent on the rotation angle of FM(2). For illustration see also figure 6.6.

Based on this model, Xi and White computed phase diagrams as functions of $J_{int(1)}$, $J_{int(2)}$ normalized by the antiferromagnetic domain wall energy σ_W and of t_{AF} normalized by the antiferromagnetic domain wall width δ_W. In general, the rotation of the ferromagnetic layer FM(2) drags the adjacent antiferromagnetic spins twisting the internal antiferromagnetic spins (see figure 6.4). In addition, angles $\Delta\varphi_{(i)}$ between adjacent antiferro- and ferromagnetic spins at either interface can form creating interfacial exchange energy. At a certain rotation angle of FM(2) the twist in the antiferromagnet generates a wall energy, which cannot be sustained by the interfacial couplings. At this point, the weaker interfacial coupling breaks up and the antiferromagnetic spins either recover their original orientation or they reverse to another equilibrium state. Xi and White distinguish two categories with $J_{int(1)} \leq \sigma_W$ or $J_{int(1)} > \sigma_W$, i.e. whether the coupling between antiferromagnet and rigid ferromagnetic layer is weaker or stronger then the twist in the antiferromagnet. In both categories recovering and reversing

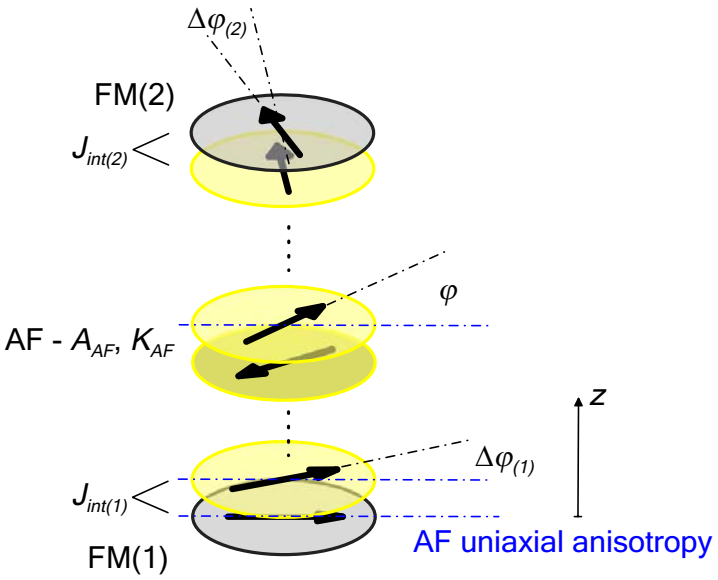

Figure 6.6: Definition of parameters in equation 6.2

regimes exist with the latter divided into a irreversible and reversible phase. The maximum twist angle of the antiferromagnetic spins is also a function of t_{AF} relative to δ_W.

Of particular interest for the present work is the category with strong interfacial coupling $J_{int(1)} > \sigma_W$ and also $J_{int(2)} > \sigma_W$. In this case, the authors report that FM(2) can be rotated beyond 180° while the coupling at both interfaces still sustains the twist in the antiferromagnet. Thus, the ferromagnetic layers can be aligned antiparallel accommodating a 180° domain wall in the antiferromagnet assuming no anisotropy of the rotating ferromagnetic layer at one end of the antiferromagnetic spacer and an absolutely rigid ferromagnetic layer at the other end of the spacer. In principle, this corresponds to the combination of a magnetically soft and hard layers separated by an antiferromagnetic spacer as in our work. A difference is that the hard ferromagnetic layer has only a finite rigidity, which adds additional complexity. Therefore, it is not only the relative strength of the interfacial coupling and the internal antiferromagnetic spin structure, which is of importance but also the anisotropy of the hard ferromagnetic layer relative to these parameters.

In a qualitative extension of the model of Xi and White, the dependence of the magnetization reversal of the FeCoV layers on t_{NiO} in the present work can be understood. In general, the FeCoV layer at the top of the trilayer is supposed to reverse first due to its lower coercivity. The reversal of the top FeCoV layer initiated by the applied field generates energy in the system because of the coupling to the magnetically hard FeCoV layer at the bottom. For small t_{NiO} ($\leq$ 10 nm) a twist of the antiferromagnetic spins would cause high exchange and anisotropy energies. The coupling at the interfaces is strong enough to remain stable but the anisotropy in the bottom FeCoV layer cannot sustain the magnetization in its original orientation. The situation is similar to the reversing regime described by Xi and White. There, the antiferromagnetic spins rotate

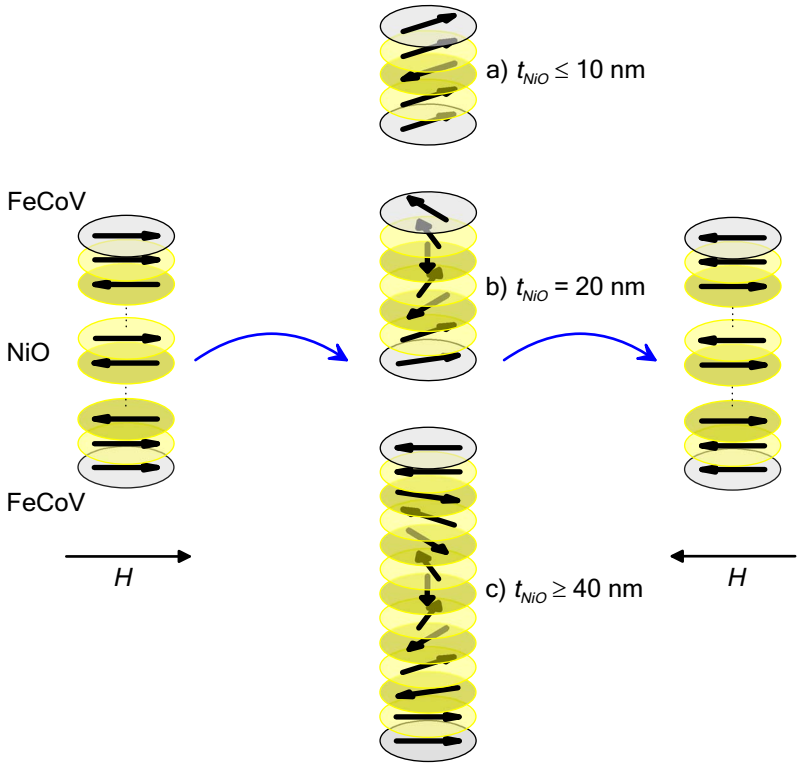

Figure 6.7: Magnetization reversal of FeCoV/NiO/FeCoV trilayers. The ferromagnetic layers are exchange coupled across the antiferromagnetic spacer, which can form a twist of the antiferromagnetic spins, dependent on t_{NiO}.

to another equilibrium state, which is also assumed to occur here but with the difference that the magnetization in the bottom FeCoV layer also follows the rotation. The complex interaction including the anisotropy of the top FeCoV layer and the exchange coupling energies described by equation 6.2 in combination with the distribution of local anisotropies in the bottom FeCoV layer discussed in section 5.1.2 leads to a gradual magnetization reversal as observed from the hysteresis loops. Dependent on the local contributions, some domains in the top layer reverse at small magnetic fields dragging the magnetization in the bottom FeCoV layer. Others are pinned unless a locally high anisotropy in the bottom layer is overcome. The first case explains the observation from polarized neutron reflectivity that the net magnetization of the bottom FeCoV layer is already reduced at lower applied field than expected. In general, it is inferred that the magnetization of top and bottom FeCoV layers reverses coherently within domains as a consequence of an exchange coupling mediated by a rigid spin structure of the antiferromagnet (figure 6.7a).

For $t_{NiO} = 20$ nm the antiferromagnetic spin structure can accommodate a larger twist until a critical amount of exchange and anisotropy energy is generated in the antiferromagnet (figure 6.7b). It is assumed that the twisted configuration is established at the first part of the magnetization reversal. In this range both ferromagnetic layers reverse but the magnetization of the bottom layer lags behind the magnetization of the top FeCoV layer. At the region of the small step the rotation of the magnetic

moments is blocked unless local anisotropies in the bottom FeCoV layer can be exceeded, assisted by the applied magnetic field (Zeeman interaction). Once this barrier is overcome, the magnetization of the bottom layer swings forward and its magnetization reversal is even further progressed than in the top FeCoV layer, as indicated from the results of polarized neutron reflectivities. A similar process is described by Xi and White where the antiferromagnetic spins at the interface to the rigid ferromagnetic layer rotate forward since the interfacial coupling cannot sustain the energy of the twist in the antiferromagnet. In the FeCoV/NiO/FeCoV trilayers, forward rotation of the antiferromagnetic spins drags the magnetic moments in the bottom FeCoV layer due to its finite anisotropy.

Polarized neutron reflectivity data of FeCoV/NiO/FeCoV trilayers with $t_{NiO} = 40$ and 60 nm reveal that within the step in the MH-loop the magnetization of top and bottom layers are aligned antiparallel. The top FeCoV layer reverses at the first transition at a small applied field followed by the bottom layer at a higher field. According the work of Xi and White an antiparallel configuration is possible for strong interfacial coupling at either interface, relative to the domain wall energy of the antiferromagnetic spacer. In this case the interfacial coupling can sustain the twist of the antiferromagnetic spins even for twist angles beyond 180°. Applied to the FeCoV/NiO/FeCoV trilayers with $t_{NiO} \geq 40$ nm it implies that the reversal of the top FeCoV layer initiates the formation of 180° domain wall in the antiferromagnetic spacer when the magnetization of the bottom FeCoV still remains in its original orientation (figure 6.7c).

It shall be noted that a realistic estimate for a 180° domain wall in NiO, available from literature [27, 29], is 40 nm. This is consistent with our observation that for $t_{NiO} \geq 40$ nm the magnetization of the ferromagnetic layers can be aligned antiparallel by applying a certain magnetic field. In addition, Xi and White [26] state that for values of the thickness of the antiferromagnetic spacer layer less than half of the width of 180° domain wall the critical interfacial coupling between the rotating ferromagnetic layer and the antiferromagnet decreases. This implies that in this thickness regime the antiferromagnetic spins prefer to rotate with the magnetization of the ferromagnet instead of twisting, i.e. they remain rigid. This is also consistent with our observation of a rigid antiferromagnet for $t_{NiO} \leq 10$ nm and the evolution of a twist of the antiferromagnetic spins for $t_{NiO} \geq 20$ nm.

Chapter 7

Conclusions - Outlook

In this work, I investigated the exchange coupling between two ferromagnetic layers spaced by an antiferromagnet on FeCoV/NiO (t_{NiO})/FeCoV trilayers. It was aimed to obtain an insight into the exchange coupling from a systematic study of the constituents of the trilayers, i.e. single layers and NiO-FeCoV bilayers of either sequence of deposition, as well as probing directly the magnetization reversal of individual ferromagnetic layers using polarized neutron reflectometry.

From X-ray reflectivity measurements, a detailed layer structure of the samples was deduced, refining models of the chemical depth profile. The models were developed systematically from FeCoV single layers to trilayers via NiO-FeCoV bilayers, which enabled to resolve finer details of the layers and the interfaces. A common base for the models of all samples could be established, from which the individual structures of the different samples were deduced in a consistent way. Similar conformity was found regarding the crystalline orientation of the samples from X-ray diffraction. Small differences in the out-of-plane texture exist dependent on the sequence of deposition of the materials but the diffraction pattern of trilayers comprises systematically the pattern of the constituents. In conclusion, the structural characterization confirms the consistent and high quality of the samples prepared by DC magnetron sputtering. Thus, the produced samples enable a systematic investigation and comparison of the magnetic properties from the elementary to the complex systems.

DC magnetization measurements on FeCoV single layers show intrinsic magnetic properties, which are consistent with previous investigations and reports, in particular a relative high coercivity compared to the bulk counterpart. When interfaced with antiferromagnetic NiO, modifications of the properties are observed, which are attributed to exchange coupling across the NiO-FeCoV interface. Although exchange bias is not observed at room temperature for $t_{NiO} < 40$ nm and only weak for thicker NiO layers, interfacial exchange coupling is evident from the distinct modification of magnetic properties when NiO is paramagnetic ($T > T_N$). Besides that, exchange coupling between FeCoV and NiO is also supported from the observation of exchange bias at low temperature indicating that the magnetic moments of both layers interact. In conclusion, the presence of interfacial exchange coupling but absence of exchange bias demonstrates that the spins of the antiferromagnet are rotated irreversibly when the magnetization of the ferromagnet reverses. According several authors [106, 107, 108], this is a consequence of strong interfacial coupling and a relative weak anisotropy of

the antiferromagnet and supports their prediction that exchange bias is only observable when the interfacial coupling energy is small compared to the domain wall energy of the antiferromagnet. The observation of exchange bias at a relatively low temperature, i.e. a low blocking temperature, is consistent with strong interfacial coupling as argued by Xi [109].

Another interesting result in this work is that trilayers with rather thin NiO spacers ($t_{NiO} \leq 10$) nm do not exhibit exchange bias at low temperature contrary to their bilayer counterparts. This fact indicates that the effect of exchange bias is not confined to the interfacial spins but involves the internal spins of the antiferromagnet. This observation supports models proposed by Mauri [14], Kiwi [15] and Stiles [27], which explain quantitatively the experimentally observed exchange bias fields by distributing the exchange coupling energy across the internal spins of the antiferromagnet.

Invaluable information about the configuration of the magnetization in individual ferromagnetic layers of the trilayers was obtained from polarized neutron reflectometry. For a full polarization analysis, a proper data reduction was required due to the finite efficiencies of the polarizer and analyzer supermirrors. A data reduction algorithm was developed and successfully implemented to retrieve the true reflectivity of the four spin dependent scattering processes. The results of polarized neutron reflectometry show that the reversal of both FeCoV layers occurs in a combined manner for small thicknesses of the NiO spacer indicating strong interlayer exchange coupling. In trilayers with thicker NiO spacers the magnetization reversal of top and bottom FeCoV layers occurs at distinct fields with an antiparallel alignment of their magnetization in between the individual reversal fields.

From the combined analysis of bulk magnetization measurements and polarized neutron reflectivity, it is inferred that the ferromagnetic layers are exchange coupled via the spin lattice of the antiferromagnetic spacer. The observed dependence of the magnetization reversal on the thickness of the NiO spacer can by explained in terms of the theoretical work of Xi and White on exchange coupled ferromagnetic layers separated by an antiferromagnet [26]. In order to apply their theoretical findings to the results of this work, a qualitative extension is needed. In contrast to their assumption that one ferromagnetic layer is absolutely rigid, it has to be considered that both ferromagnetic layers have different but finite rigidity in our case. In conclusion, it is inferred that during the magnetization reversal of the trilayers the spins of the antiferromagnetic spacer are twisted. The degree of twist depends on the thickness of the NiO layer. For thin spacer layers ($t_{NiO} \leq 10$) nm the antiferromagnetic spins are very rigid and only a small twist may form, resulting in a strong coupling between the ferromagnetic layers. The maximum twist angle increases with increasing t_{NiO} until a complete 180° domain wall can be accommodated across the NiO spacer facilitating the observed antiparallel configuration of the magnetization of the ferromagnetic layers for $t_{NiO} \geq 40$ nm.

The investigation of NiO-FeCoV films of the present work reveals interesting features, which can be explained satisfactorily so far. Nevertheless, some outstanding questions could not be addressed within this work. They are primarily on the influence of microstructure and thermal fluctuations on the magnetic properties of exchange biased

thin films. The present investigation was focused to resolve the structure of the films and their magnetization profile along the out-of-plane direction but a direct information is lacking regarding the microstructure and magnetic domains in the plane of the films.

Microstructural factors like grain size, strain, texture etc. are known to influence magnetic properties of materials. In thin films, their values and distribution in the plane play a significant role. The low coercivity of NiO/FeCoV bilayers may to some extent originate from a particular microstructure of the FeCoV layers. Their magnetic anisotropy has been inferred as a net anisotropy in the distribution of strain. The grain size of ferromagnets is also known to influence the coercivity [94]. In order to characterize the in-plane microstructure additional experiments are envisaged. Cross-sectional transmission electron microscopy would provide a direct image of the cross-section of the films resolving the vertical layer structure and the lateral grain size etc.. A challenge in these experiments is the extensive sample preparation. Lateral grain size, strain and texture can be probed using X-ray grazing incident diffraction. In principle, controlling the penetration of the X-ray via the incident angle of the beam enables depth sensitivity [65]. Thus, it should be possible to distinguish the lateral microstructure of top and bottom FeCoV layers in the trilayers.

The reduced magnetic moment of the ferromagnetic layers during the magnetization reversal, found from polarized neutron reflectivity data, indicates the formation of lateral domains. Domain imaging techniques like magnetic force microscopy or Lorentz microscopy would be desirable to trace local domain processes during the magnetization reversal. A very powerful technique to explore magnetic domains, in particular in buried layers, is off-specular polarized neutron reflectometry. In contrast to the domain imaging techniques mentioned before, off-specular reflectometry combines vertical and lateral sensitivity and provides information about the lateral size of domains and their lateral and vertical correlation. Recently, we performed these experiments at the reflectometer D17 at the Institut Laue-Langevin. Qualitatively, the results confirm the findings of this work. A quantitative analysis is very complex and extensive and presently beyond the scope of this work but aimed for future analysis.

X-ray resonant magnetic reflectometry is a well suited technique to probe the size and orientation of magnetic moments taking advantage of its element selectivity. In particular, X-ray Magnetic Linear Dichroism (XMLD) is sensitive to detect the deviation of magnetic moments, especially adequate to probe the twist of the spins in the antiferromagnetic spacer as inferred from the present investigations. Preliminary experiments were performed at BESSY recently and a continuation of these is in progress with the aim to trace directly the evolution of the antiferromagnetic spins during the magnetization reversal of the ferromagnets.

The importance of thermal effects, especially the anisotropy and exchange stiffness of the antiferromagnet, are visible from the magnetization measurements at room temperature and 2 K. In general, NiO and FeCoV were chosen to combine two materials with high ordering temperatures and high magnetic moments. It is expected that the high Néel temperature of NiO leads also to a high blocking temperature up to which

exchange bias will be observed. On the contrary, a reduction of the blocking temperature has been observed when the ferromagnet has a high Curie temperature. Our preliminary study of the blocking temperatures as a function of t_{NiO} in bilayers and trilayers also corroborate the idea of the formation of domain walls in the antiferromagnet and is in agreement with the theoretical findings of Xi et. al. [109]. Theoretically, it is argued that when the interfaced ferromagnet has a very high Curie temperature or when the interfacial exchange is very strong, the blocking temperature of the exchange biased system is much reduced relative to the Néel temperature of the antiferromagnet. In such a case, high magnetic moment of FeCoV (2.35 μ_B), leading to a strong interfacial exchange, combined with its very high Curie temperature (T_C = 1223 K) would eventually result in a dramatic reduction of the blocking temperature of the FeCoV/NiO system.

In fact, our experimental results show that the blocking temperature of NiO/FeCoV systems is below room temperature or around that and therefore much lower than the Néel temperature of NiO. A detailed study of the temperature dependence of exchange bias in NiO/FeCoV systems is foreseen to find the blocking temperature precisely and to evaluate its dependence on the thickness of the NiO layer and other microstructural factors. Nevertheless, it is inferred that the low blocking temperature is a consequence of strong interfacial coupling and a relatively low anisotropy of NiO. Apparently, the pinning of the NiO magnetic moments is rather weak at room temperature and the rotation of the ferromagnetic moments assisted by thermal activation causes a irreversible rotation of the antiferromagnetic spins and therefore no exchange bias. In contrast to that, a rigid antiferromagnet pinning a ferromagnetic layers is desired for technical applications. Therefore, other combinations of materials may be better candidates for application. Regarding fundamental studies, NiO/FeCoV films are very interesting because they constitute a combination of strong interfacial coupling and a relative soft spin structure of the antiferromagnet, as demonstrated in this work.

Appendix A

Parameter models for X-ray reflectivity

A.1 FeCoV/NiO bilayers

t_{NiO}	5 nm				60 nm			
	t [nm]	ρb_{at} [10^{11} cm^{-2}]	Σ_a [10^{10} cm^{-2}]	σ_{rms} [nm]	t [nm]	ρb_{at} [10^{11} cm^{-2}]	Σ_a [10^{10} cm^{-2}]	σ_{rms} [nm]
glass	-	1.96	0.17	0.19	-	1.96	0.17	0.51
glass-Ti	0.77	2.53	1.69	0.20	0.78	2.51	1.68	0.62
Ti	4.41	3.55	2.98	0.20	4.21	3.55	2.98	0.61
Ti-FeCoV	0.44	4.13	1.82	0.40	1.07	2.57	1.13	1.08
FeCoV	16.8	5.95	8.08	0.37	19.2	5.95	8.08	0.59
Oxide	0.51	3.25	0.77	0.35	0.18	1.52	0.36	0.51
NiO	3.96	5.03	0.85	0.48	61.4	4.94	0.83	1.49
NiOX	0.68	1.28	0	0.37	1.74	3.48	0	2.16

Table A.1: Model parameters for samples glass/Ti (5 nm)/FeCoV (20 nm)/NiO (t_{NiO}) with nominal thicknesses t_{NiO} = 5, 60 nm. The parameters of individual layers are the thickness t, the scattering length density ρb_{at} and the absorption cross-section $\Sigma_a = r_0 \rho f''$ for X-rays ($\lambda = 0.154$ nm) and the RMS value of the interfacial roughness σ_{rms}. The errors of the given values are of the order of 5 % (see table 4.1).

A.2 NiO/FeCoV bilayers

t_{NiO}	5 nm				10 nm				20 nm			
	t [nm]	ρb_{at} [10^{11} cm^{-2}]	Σ_a [10^{10} cm^{-2}]	σ_{rms} [nm]	t [nm]	ρb_{at} [10^{11} cm^{-2}]	Σ_a [10^{10} cm^{-2}]	σ_{rms} [nm]	t [nm]	ρb_{at} [10^{11} cm^{-2}]	Σ_a [10^{10} cm^{-2}]	σ_{rms} [nm]
glass	-	1.96	0.17	0.62	-	1.96	0.17	0.22	-	1.96	0.17	0.47
glass-NiO	1.04	2.72	1.82	0.56	1.64	2.29	1.54	0.59	1.39	2.48	1.66	0.53
NiO	3.69	4.84	0.82	0.42	10.4	4.57	0.77	0.91	20.1	4.63	0.78	1.21
FeCoV	17.4	5.95	8.08	0.51	19.4	5.95	8.08	0.86	20.1	5.95	8.08	1.01
Ti	2.51	3.80	3.19	0.48	2.82	3.88	3.26	0.72	3.00	4.12	3.46	1.30
TiO_2	4.05	3.22	1.61	0.58	4.49	3.28	1.64	0.69	4.54	3.27	1.64	0.81
TiO_xX	1.03	0.35	0	0.42	1.51	1.02	0	0.62	1.62	0.88	0	0.59

t_{NiO}	40 nm				60 nm			
	t [nm]	ρb_{at} [10^{11} cm^{-2}]	Σ_a [10^{10} cm^{-2}]	σ_{rms} [nm]	t [nm]	ρb_{at} [10^{11} cm^{-2}]	Σ_a [10^{10} cm^{-2}]	σ_{rms} [nm]
glass	-	1.96	0.17	0.32	-	1.96	0.17	0.29
glass-NiO	1.56	2.25	1.50	0.62	1.45	2.23	1.49	0.62
NiO	42.6	4.77	0.81	1.48	64.1	4.62	0.78	2.02
FeCoV	19.6	5.95	8.08	1.37	19.2	5.95	8.08	1.78
Ti	2.82	3.92	3.29	1.26	3.17	3.76	3.16	1.88
TiO_2	4.41	3.28	1.64	1.12	4.30	3.34	1.67	1.48
TiO_xX	1.53	0.89	0	0.86	2.03	0.76	0	1.79

Table A.2: Model parameters for samples glass/NiO (t_{NiO})/FeCoV (20 nm)/Ti (5 nm) with nominal thicknesses as given in the header of the table. The parameters of individual layers are the thickness t, the scattering length density ρb_{at} and the absorption cross-section $\Sigma_a = r_0 \rho f''$ for X-rays ($\lambda = 0.154$ nm) and the RMS value of the interfacial roughness σ_{rms}. The errors of the given values are of the order of 5 % (see table 4.1).

A.3 FeCoV/NiO/FeCoV trilayers

t_{NiO}	1.5 nm				5 nm				10 nm			
	t [nm]	ρb_{at} [10^{11} cm^{-2}]	Σ_a [10^{10} cm^{-2}]	σ_{rms} [nm]	t [nm]	ρb_{at} [10^{11} cm^{-2}]	Σ_a [10^{10} cm^{-2}]	σ_{rms} [nm]	t [nm]	ρb_{at} [10^{11} cm^{-2}]	Σ_a [10^{10} cm^{-2}]	σ_{rms} [nm]
glass	–	1.96	0.17	0.37	–	1.96	0.17	0.23	–	1.96	0.17	0.27
glass-Ti	0.59	2.34	1.57	0.17	0.77	2.34	1.57	0.29	1.02	2.34	1.57	0.27
Ti	3.97	3.55	2.98	0.71	3.89	3.55	2.98	0.29	4.13	3.55	2.98	0.57
Ti-FeCoV	1.23	3.86	1.70	0.40	1.50	3.86	1.70	0.36	1.28	3.86	1.70	0.38
FeCoV	18.5	5.95	8.08	0.51	18.6	5.95	8.08	0.64	18.6	5.95	8.08	0.57
Oxide	0.32	1.38	0.32	0.47	0.40	1.38	0.32	0.50	0.39	1.38	0.32	0.49
NiO	1.77	4.99	0.84	0.26	5.07	4.99	0.84	0.27	10.1	4.99	0.84	0.41
FeCoV	18.6	5.95	8.08	0.49	18.6	5.95	8.08	0.53	18.6	5.95	8.08	0.54
Ti	2.66	3.96	3.32	0.94	2.56	3.96	3.32	0.75	2.69	3.96	3.32	1.09
TiO_2	4.37	3.30	1.66	0.46	4.46	3.30	1.66	0.50	4.51	3.30	1.66	0.55
TiO_xX	1.41	1.18	0	0.39	1.80	1.18	0	0.49	1.67	1.18	0	0.38

t_{NiO}	20 nm				40 nm				60 nm			
	t [nm]	ρb_{at} [10^{11} cm^{-2}]	Σ_a [10^{10} cm^{-2}]	σ_{rms} [nm]	t [nm]	ρb_{at} [10^{11} cm^{-2}]	Σ_a [10^{10} cm^{-2}]	σ_{rms} [nm]	t [nm]	ρb_{at} [10^{11} cm^{-2}]	Σ_a [10^{10} cm^{-2}]	σ_{rms} [nm]
glass	–	1.96	0.17	0.06	–	1.96	0.17	0.18	–	1.96	0.17	0.10
glass-Ti	0.91	2.34	1.57	0.18	1.04	2.34	1.57	0.24	0.90	2.34	1.57	0.27
Ti	4.09	3.55	2.98	0.73	4.18	3.55	2.98	0.71	4.01	3.55	2.98	0.53
Ti-FeCoV	1.27	3.86	1.70	0.37	1.35	3.86	1.70	0.42	1.39	3.86	1.70	0.45
FeCoV	18.6	5.95	8.08	0.52	18.6	5.95	8.08	0.59	18.6	5.95	8.08	0.56
Oxide	0.35	1.36	0.32	0.47	0.37	1.38	0.32	0.54	0.32	1.38	0.32	0.60
NiO	20.0	4.99	0.84	0.60	40.0	4.99	0.84	1.04	59.6	4.99	0.84	1.43
FeCoV	18.8	5.95	8.08	0.66	18.8	5.95	8.08	0.97	19.2	5.95	8.08	1.36
Ti	2.71	3.96	3.32	1.07	2.66	3.96	3.32	0.98	2.62	3.96	3.32	1.00
TiO_2	4.42	3.30	1.66	0.58	4.38	3.30	1.66	0.89	4.53	3.30	1.66	1.16
TiO_xX	1.45	1.17	0	0.49	1.35	1.18	0	0.73	1.73	1.18	0	0.94

t_{NiO}	80 nm				100 nm			
	t [nm]	ρb_{at} [10^{11} cm^{-2}]	Σ_a [10^{10} cm^{-2}]	σ_{rms} [nm]	t [nm]	ρb_{at} [10^{11} cm^{-2}]	Σ_a [10^{10} cm^{-2}]	σ_{rms} [nm]
glass	–	1.96	0.17	0.48	–	1.96	0.17	0.56
glass-Ti	0.89	2.34	1.57	0.52	0.71	2.34	1.57	0.67
Ti	4.36	3.55	2.98	0.23	4.5	3.55	2.98	0.81
Ti-FeCoV	1.15	3.86	1.70	0.56	1.13	3.86	1.70	0.74
FeCoV	19.7	5.95	8.08	0.81	19.2	5.95	8.08	0.52
Oxide	0.40	1.38	0.32	0.72	0.17	1.38	0.32	0.52
NiO	85.3	4.99	0.84	2.52	110	4.99	0.84	3.24
FeCoV	19.4	5.95	8.08	2.27	19.6	5.95	8.08	2.90
Ti	3.88	3.96	3.32	1.67	2.80	3.96	3.32	4.62
TiO_2	3.68	3.30	1.66	2.24	4.33	3.30	1.66	2.06
TiO_xX	2.06	1.18	0	2.39	4.14	1.18	0	2.19

Table A.3: Model parameters for samples glass/Ti (5 nm)/FeCoV (20 nm)/NiO (t_{NiO})/FeCoV (20 nm)/Ti (5 nm) with nominal thicknesses as given in the header of the table. The parameters of individual layers are the thickness t, the scattering length density ρb_{at} and the absorption cross-section $\Sigma_a = r_0 \rho f''$ for X-rays ($\lambda = 0.154$ nm) and the RMS value of the interfacial roughness σ_{rms}. The errors of the given values are of the order of 5 % (see table 4.1).

Bibliography

[1] G. Prinz. Magnetoelectronics. *Sience*, 282:1660, 1998.

[2] P. Grünberg, R. Schrieber, Y. Pang, M.B. Brodsky, and H. Sowers. Layered magnetic structures: Evidence for antiferromagnetic coupling of Fe layers across Cr interlayers. *Phys. Rev. Lett.*, 57:2442, 1986.

[3] S.S.P. Parkin, N. More, and K.P. Roche. Oscillations in exchange coupling and magnetoresistance in metallic superlattice structures: Co/Ru, Co/Cr, and Fe/Cr. *Phys. Rev. Lett.*, 64:2304, 1990.

[4] P. Bruno. Theory of interlayer magnetic coupling. *Phys. Rev. B*, 67:411, 1995.

[5] M.N. Baibich, J.M. Broto, A. Fert, F. Nguyen Van Dau, F. Petroff, P. Eitenne, G. Creuzet, A. Friederich, and J. Chazelas. Giant magnetoresistance of (001)Fe/(001)Cr magnetic superlattices. *Phys. Rev. Lett.*, 61:2472, 1988.

[6] M. Julliere. Tunneling between ferromagnetic films. *Phys. Lett. A*, 54:225, 1975.

[7] J.S. Moodera and G. Mathon. Spin polarized tunneling in ferromagnetic junctions. *J. Magn. Magn. Mater.*, 200:248, 1990.

[8] J. Faure-Vincent, C. Tiusan, C. Bellouard, E. Popova, M. Hehn, F. Montaigne, and A. Schuhl. Interlayer magnetic coupling interactions of two ferromagnetic layers by spin polarized tunneling. *Surface Science*, 89:107206–1, 2002.

[9] P. Grünberg, D.E. Bürgler, R. Gareev, D. Olligs, M. Buchmeier, M. Breidbach, B. Kuanr, and R. Schreiber. Experiments on the relation between GMR and interface roughness and on the interlayer exchange coupling across semiconductors. *J. Phys. D: Appl. Phys.*, 35:2403, 2002.

[10] Y. Ohno, D.K. Young, B. Beschoten, F. Matsukura, H. Ohno, and D.D. Awschalom. Electrical spin injection in a ferromagnetic semiconductor heterostructure. *Nature*, 402:790, 1999.

[11] W.H. Meiklejohn and C.P. Bean. New magnetic anisotropy. *Phys. Rev.*, 102(5):1413, 1956.

[12] D. Lederman, C.A. Ramos, V. Jaccarino, and J.L. Cardy. Finite-size scaling in FeF_2/ZnF_2 superlattices. *Phys. Rev. B*, 48:8365, 1993.

[13] A.E. Berkowitz and K. Takano. Exchange anisotropy - a review. *J. Magn. Magn. Mat.*, 200:552, 1999.

[14] D. Mauri, H.C. Siegmann, P.S. Bagus, and E. Kay. Simple model for thin ferromagnetic films exchange coupled to an antiferromagnetic substrate. *J. Appl. Phys.*, 62:3047, 1987.

[15] M. Kiwi, J. Mejía-López, R.D. Portugal, and R. Ramrez. Exchange bias model for Fe/FeF: Role of domains in the ferromagnete. *Europhys. Lett.*, 48:573, 1999.

[16] A.P. Malozemoff. Random-field model of exchange anisotropy at rough ferromagnetic-antiferromagnetic interfaces. *Phys. Rev. B*, 35:3679, 1987.

[17] A. Scholl, M. Liberati, E. Arenholz, H. Ohldag, and J. Stöhr. Creation of an antiferromagnetic exchange spring. *Phys. Rev. Lett.*, 92:247201, 2004.

[18] T. Ambrose and C.L. Chien. Magnetic properties of exchange coupled NiFe/CoO/NiFe trilayers. *Appl. Phys. Lett.*, 65:1967, 1994.

[19] F.Y. Yang and C.L. Chien. Spiraling spin structure in an exchange-coupled antiferromagnetic layer. *Phys. Rev. Lett.*, 85:2597, 2000.

[20] F. Ernult, B. Dieny, and J.R. Regnard. Experimental study of the coupling between two ferromagnetic layers through an antiferromagnetic spacer. *J. Magn. Magn. Mater.*, 242:515, 2002.

[21] O. Zaharko, P.M. Oppeneer, H. Grimmer, M. Horisberger, H.-Ch. Mertins, D. Abramsohn, F. Schäfers, A. Bill, and H.-B. Braun. Exchange coupling in Fe/NiO/Co film studied by soft x-ray resonant magnetic reflectivity. *Phys. Rev. B*, 66:134406, 2002.

[22] Z.Y. Liu and S. Adenwalla. Oscillatory interlayer exchange coupling and its temperature dependence in $[Pt/Co]_3/NiO/[Co/Pt]_3$ multilayers with perpendicular anisotropy. *Phys. Rev. Lett.*, 91:037207, 2003.

[23] M.Ye. Zhuravlev, E.Y. Tsymbal, and S.S. Jaswal. Exchange model for oscillatory interlayer coupling and induced unidirectional anisotropy in $[Pt/Co]_3/NiO/[Co/Pt]_3$ multilayers. *Phys. Rev. Lett.*, 92:219703, 2004.

[24] J.C. Slonczewski. Overview of interlayer exchange theory. *J. Magn. Magn. Mater.*, 150:13, 1995.

[25] M. Rubinstein. Exchange coupling between two magnetic films separated by an antiferromagnetic spacer. *J. Magn. Magn. Mater.*, 85:5880, 1999.

[26] H. Xi and R.M. White. Coupling between two ferromagnetic layers separated by an antiferromagntic layer. *Phys. Rev. B*, 62(6):3933, 2000.

[27] M.D. Stiles and R.D. McMichael. Model for exchange bias in polycrystalline ferromagnet-antiferromagnet bilayers. *Phys. Rev. B*, 59:3722, 1999.

[28] H. Xi and R.M. White. Theory of the blocking temperature in polycrystalline exchange biased bilayers based on a thermal fluctuation model. *J. Appl. Phys.*, 94(9):5850, 2003.

[29] C.H. Lai, H. Matsuyama, R.L. White, T.C. Anthony, and G.G. Bush. Exploration of magnetization reversal and coerivity of epitaxial NiO {111}/NiFe films. *J. Appl. Phys.*, 79(6):6389, 1996.

[30] J.A.C. Bland, C. Daboo, B. Heinrich, Z. Celinski, and R.D. Bateson. Enhanced magnetic moments in bcc Fe films. *Phys. Rev. B*, 51:258, 1995.

[31] S. Hope, J. Lee, P. Rosenbusch, G. Lauhoff, J.A.C. Bland, A. Ercole, D. Bucknall, J. Penfold, H.J. Lauter, V. Lauter, and R. Cubitt. Thickness dependence of the total magnetic moment per atom in the Cu/Ni/Cu/Si(001)system. *Phys. Rev. B*, 55:11422, 1995.

[32] G.P. Felcher, R.T. Kampwirth, K.E. Gray, and R. Felici. Polarized neutron reflections: A new technique used to measure the magnetic field penetration depth in superconducting niobium. *Phys. Rev. Lett.*, 52:1539, 1984.

[33] A. Mansour, R.O. Hilleke, G.P. Felcher, R.B. Laibowitz, P. Chaudhari, and S.S.P. Parkin. Magnetic field penetration into the high temperature superconductor $YBa_2Cu_3O_{7-x}$. *Physica B*, 156:867, 1989.

[34] J.M. Reynolds, V. Nunez, A.T. Boothroyd, T. Freltoft, D.G. Bucknall, and J. Penfold. Penetration depth of $YBa_2Cu_3O_7$ measured by polarised neutron reflectometry. *Physica B*, 248:163, 1998.

[35] A. Barthélémy, A. Fert, M.N. Baibich, S. Hadjoudj, F. Petroff, P. Etienne, R. Cabanel, S. Lequien, F. Nguyen Van Dau, and G. Creuzet. Magnetic and transport properties of Fe/Cr superlattices. *J. Appl. Phys.*, 67:5908, 1990.

[36] J.F. Ankner and G.P. Felcher. Polarized-neutron reflectometry. *J. Magn. Magn. Mat.*, 200:741, 1999.

[37] G.P. Felcher, S.G.E. te Velthuis, A. Rühm, and W. Donner. Polarized neutron reflectometry: recent developments and perspectives. *Physica B*, 297:87, 2001.

[38] H. Zabel and K. Theis-Bröhl. Polarized neutron reflectivity and scattering studies of magnetic heterostructures. *J. Phys.: Condens. Matter*, 15:S505, 2003.

[39] C.H. Park, I.G. Kim, B.C. Lee, and J.I. Lee. Origin of the magnetic moment enhancement of the ordered $Fe_{50}Co_{50}$ alloys. *Phys. Stat. Sol.*, 241(7):1419, 2004.

[40] D. Gautard, G. Couderchon, and L. Coutu. 50-50 CoFe alloys: magnetic and mechanical properties. *J. Magn. Magn. Mater.*, 160:359, 1996.

[41] Z. Turgut, J.H. Scott, M.Q. Huang, S.A. Majetich, and M.E. McHenry. Magnetic properties and ordering in C-coated Fe_xCo_{1-x} alloy nanocrystals. *J. Appl. Phys.*, 83:6468, 1998.

[42] S. Chikazumi. *Physics of Magnetism*, page 161. Wiley, New York, 1964.

[43] B.G. Lyashenko. Neutron diffraction study of iron-cobalt alloy I. *Sov. Phys. Cryst.*, 6:443, 1962.

[44] T.B. Massalski. *Binary alloy phase diagrams*, volume 2. ASM International Metals Park, Ohio, 2 edition, 1996.

[45] R.H. Yu, S. Basu, Y. Zhang, and J.Q. Xiao. Magnetic domains and coercivity in FeCo soft magnetic alloys. *J. Appl. Phys.*, 85:6034, 1999.

[46] R.H. Yu, S. Basu, Y. Zhang, A. Parvizi-Majidi, and J.Q. Xiao. Pinning effect of the grain boundaries on magnetic domain wall in FeCo-based magnetic alloys. *J. Appl. Phys.*, 85:6655, 1999.

[47] VACUUMSCHMELZE GMBH & CO. KG. Weichmagnetische Kobalt-Eisen-Legierungen VACOFLUX 48 · VACOFLUX 50 · VACODUR 50 · VACOFLUX 17. www.vacuumschmelze.de/dynamic/de/home/produkte/halbzeugampteile/weichmagnetisch/kobalteisen.php, 2001.

[48] M.S. Kumar and P. Böni. Influence of interstitial nitrogen on the structural and magnetic properties of FeCoV/TiN_x multilayers. *J. Appl. Phys.*, 91:3750, 2002.

[49] M.S. Kumar, P. Böni, and M. Horrisberger. Perpendicular anisotropy, hysteresis and structural properties of nanostructured FeCoV/Ti multilayers. *Physica B*, 325:401, 2003.

[50] M. Senthil Kumar, V.R. Shah, C. Schanzer, P. Böni, T. Krist, and M. Horisberger. Polarized neutron reflectivity of FeCoV/Ti multilayers. *Physica B*, 350:e241, 2003.

[51] C. Schanzer, V.R. Shah, P. Böni, and T. Krist. Investigation of magnetization reversal in FeCoV/Ti multilayers. *Physica B*, 350:e221, 2003.

[52] D.G. Hwang, C.M. Park, and S.S. Lee. Exchange biasing in NiO spin valves. *J. Magn. Mat.*, 186:265, 1998.

[53] G.A. Slack. Crystallography and domain walls in antiferromagnetic NiO crystals. *J. Appl. Phys.*, 31:1571, 1960.

[54] A.J. Sievers and M. Tinkham. Far infrared antiferromagnetic resonance in MnO and NiO. *Phys. Rev.*, 129:1566, 1962.

[55] S. Blundell. *Magnetism in Condensed Matter*. Oxford Masters Series in Condensed Matter Physics. Oxford University Press, Oxford, 2001.

[56] E. Bauer and J.H. van der Merwe. Structure and growth of crystalline superlattices: From monolayer to superlattice. *Phys. Rev. B*, 33(6):3657, 1986.

[57] R. Behrisch. *Sputtering by Particle Bombardment I*, volume 47 of *Topics in Applied Physics*. Springer, Berlin, 1981.

[58] R. Behrisch. *Sputtering by Particle Bombardment II*, volume 47 of *Topics in Applied Physics*. Springer, Berlin, 1983.

[59] R. Behrisch. *Sputtering by Particle Bombardment III*, volume 47 of *Topics in Applied Physics*. Springer, Berlin, 1991.

[60] M. Horisberger. private communication, 2003.

[61] Quantum Desigen. PPMS application note - magnetometry. http://www.qdusa.com/pdf/brochures/mag.pdf, 2000.

[62] Quantum Desigen. PPMS hardware manual.

[63] Quantum Desigen. Magnetic property measurement system. http://www.qdusa.com/products/brochures/mpmsBro2.pdf, 2000.

[64] J. Daillant and A. Gibaud. *X-Ray and Neutron Reflectivity: Principles and Application*, chapter Specular Reflectivity from Smooth and Rough Surfaces, page 87. Springer, Berlin, Heidelberg, New York, 1999.

[65] V. Holý, U. Pietsch, and T. Baumbach. *High-Resolution X-ray Scattering from Thin Films and Multilayers*, volume 149 of *Springer Tracts in Modern Physics*. Springer, Berlin, Heidelberg, New York, 1999.

[66] J. Lekner. *Theory of reflection of electromagnetic and particle waves*. Martinus Nijhoff Publishers, Dordrecht, Boston, Lancaster, 1987.

[67] M.R. Fitzsimmons, S.D. Bader, J.A. Borchers, G.P. Felcher, J.K. Furdynad, A. Hoffmann, J.B. Kortright, I.K. Schuller, T.C. Schulthessg, S.K. Sinha, M.F. Toney, D. Weller, and S. Wolf. Neutron scattering studies of nanomagnetism and artificially structured materials. *J. Magn. Magn. Mater.*, 271:103, 2004.

[68] X.L. Zhou and S.H. Chen. Theoretical foundation of X-ray and neutron reflectometry. *Physics Reports*, 257:223, 1995.

[69] A. Fresnel. Mémoire sur la théorie mathématique des phénomènes électrodynamiques, uniquement déduite de l'expérience. *Mémoires de l'Académie*, 11:393, 1823.

[70] L.G. Parrat. Surface studies of solids by total reflection of x-rays. *Phys. Rev.*, 95(2):359, 1954.

[71] F. Ott. SimulReflec V1.52. http://www-llb.cea.fr/prism/programs/simulreflec/simulreflec.html, 2004.

[72] G.L. Squires. *Thermal Neutron Scattering*. Cambridge University Press, Cambridge, 1978.

[73] P. Böni, D. Clemens, M. Senthil Kumar, and C. Pappas. Applications of remanent supermirror polarizers. *Physica B*, 267-268:320, 1999.

[74] C. Fermon, F. Ott, and A.Menelle. *X-Ray and Neutron Reflectivity: Principles and Application*, chapter Neutron Reflectometry, page 161. Springer, Berlin, Heidelberg, New York, 1999.

[75] F. Tasset, P.J. Brown, E. Lelièvre-Berna, T. Roberts, S. Pujol, J. Allibon, and E. Bourgeat-Lami. Spherical neutron polarimetry with Cryopad-II. *Physica B*, 267-268:69, 1999.

[76] M.S. Kumar, P. Böni, and M. Horisberger. Induced magnetic anisotropy, stress and hysteresis in FeCoV/TiN$_x$ multilayers. *IEEE Transactions on Magnetics*, 35:3067, 1999.

[77] Ralph Siebrecht. *Untersuchung magnetischer $Fe_{1-x}Cr_x$/Cr-Übergitter mit dem Neutronenreflektometer ADAM.* PhD thesis, Fakultät für Physik und Astronomie an der Ruhr-Universität Bochum, Bochum, Dezember 2000.

[78] T. Gutberlet. private communication.

[79] D. Clemens, M. Gupta, J. Stahn, M. Könnecke, R. Steitz, and T. Gutberlet. New Options for Time-of-flight Reflectometry at AMOR. *http://num.web.psi.ch/reports/2002/pdf/b-8-04.pdf*, 2002.

[80] W. Kraus and G. Nolze. Powdercell for Windows, Version 2.4. http://www.bam.de/service/publikationen/publikationen.htm, 2000.

[81] NiO, card number 47-1749, JCPDS, International Center for Diffraction Data, Newton square PA, 1997.

[82] J.A. Thornton. Influence of apperatur geometry and deposition conditions on the structur and topography of thick sputtered coatings. *J. Vac. Sci. Tech.*, 11(4):666, 1974.

[83] Matthias Wuttig and Xiangdong Liu. *Ultrathin Metal Films*, volume 206, chapter Growth of Ultrathin Metal Films, page 5. Springer, Berlin Heidelberg, 2004.

[84] I. Ohnuma, H. Enoki, O. Ikeda, R Kainuma, H. Ohtani, B. Sundman, and K Ishida. Phase equilibria in the Fe-Co binary system. *Acta Mat.*, 50:379, 2002.

[85] P.F. Fewster. X-ray analysis of thin films and multilayers. *Rep. Prog. Phys.*, 59:1339, 1996.

[86] G.S.D Beach, A.E. Berkowitz, F.T. Parker, and D.J. Smith. Magnetically-soft, high moment, high resistiviy thin films using discontinous metal/native oxide multilayers. *Appl. Phys. Lett.*, 79(2):224, 2001.

[87] G.S.D Beach, A.E. Berkowitz, V.G. Harris, F.T. Parker, B. Ramadurai, and D.J. Smith. Properties of the native oxide in metal/native oxide multilayers. *J. Appl. Phys.*, 91(10):7526, 2002.

[88] G.S.D Beach, T.J. Silva, F.T. Parker, and A.E. Berkowitz. High-frequency charateristics of metal/native-oxide multilayers. *IEEE Transactions on magnetics*, 39(5):2669, 2003.

[89] M.T. Johnson, P.J.H. Bloemen, F.J.A. den Broeder, and J.J. de Vries. Magnetic anisotropy in metallic multilayers. *Rep. Prog. Phys.*, 59:1409, 1996.

[90] D. Clemens, A. Vananti, C. Terrier, P. Böni, B. Schnyder, S. Tixier, and M. Horisberger. Magnetic in-plane anisotropy in sputtered FeCo films and multilayers. *Physica B*, 234-236:500, 1997.

[91] M.S. Cohen. Anomalous Magnetic Films. *J. Appl. Phys*, 33:2968, 1962.

[92] C.L. Platt, A.E. Berkowitz, D.J. Smith, and M.R. McCartney. Correlation of coercivity and microstructure of thin CoFe films. *J. Appl. Phys.*, 88:2058, 2000.

[93] H.S. Jung, W.D. Doyle, J.E. Wittig, J.F. Al-Sharab, and J. Bentley. Soft anisotropic high magnetization Cu/FeCo films. *Appl. Phys. Lett.*, 81:2415, 2002.

[94] J.F. Löffler, J.P. Meier, B. Doudin, J.P. Ansermet, and W. Wagner. Random and exchange anisotropy in consolidated nanostructured Fe and Ni: Role of grain size and trace oxides on the magnetic properties. *Phys. Rev. B*, 57:2915, 1998.

[95] R. Alben, J.J. Becker, and M.C. Chi. Random anisotropy in amorphous ferromagnets. *J. Appl. Phys.*, 49:1653, 1978.

[96] E.M. Chudnovsky. *The Magnetism of Amorphous Metals and Alloys*, chapter 3. World Scientific, Singapore, 1995.

[97] E.M. Chudnovsky, W.M. Saslow, and R.A. Serota. Ordering in ferromagnets with random anisotropy. *Phys. Rev. B*, 33:251, 1986.

[98] J. Nogués and I.K. Schuller. Exchange bias. *J. Magn. Magn. Mat.*, 193:203, 1999.

[99] Z. Qian, J.M. Sivertsen, and J.H. Judy. Magnetic behavior of NiFe/NiO bilayers. *J. Appl. Phys.*, 83(11):6825, 1998.

[100] W. Zhu, L. Seve, R. Sears, B. Sinkovic, and S.S.P. Parkin. Field colling induced changes in the antiferromagnetic structure of NiO films. *Phys. Rev. Lett.*, 86(23):5389, 2001.

[101] T.J. Regan. *X-Ray absorption spectroscopy and microscopy study of ferro- and antiferromagnetic thin films, with applications to exchange anisotropy.* PhD thesis, Department of Applied Physics, Stanford University, 2001.

[102] H. Hoffmann. Theory of magnetization ripple. *IEEE Trans. Magn.*, MAG 4:32, 1968.

[103] Z.Y. Liu and S. Adenwalla. Ferromagnetic domain-wall behavior during reversal and thermally activated antiferromagnetic reversal in an exchange-biased NiO/NiFe bilayer. *Phys. Rev. B*, 67:184423, 2003.

[104] U. Rücker, E. Kentzinger, B. Toperverg, F. Ott, and T. Brückel. Layer-by-layer magnetometry of polarizing supermirrors. *Appl. Phys. A*, 74:S607, 2002.

[105] B.D. Schrag, A. Anguelouch, S. Ingvarsson, Gang Xiao, Y. Lu, P.L. Trouilloud, A. Gupta, R.A. Wanner, W.J. Gallagher, P.M. Rice, and S.S.P. Parkin. Néel "orange-peel" coupling in magnetic tunneling junction devices. *Appl. Phys. Lett.*, 77:2373, 2000.

[106] W.H. Meiklejohn. Exchange anisotropy-A Review. *J. Appl. Phys.*, 33:1328, 1962.

[107] H. Fujiwara, C. Hou, M. Sun, HS Cho, and K. Nishioka. Effect of exchange coupling of polycrystalline antiferromagnetic layers on the magnetization behavior of soft magnetic layers. *IEEE Trans. Magn.*, 35:3082, 1999.

[108] H. Xi and R.M. White. Antiferromagnetic thickness dependence of exchange biasing. *Phys. Rev. B*, 61:80, 2000.

[109] H. Xi. Theoretical study of the blocking temperature in polycrystalline exchange biased bilayers. *J. Magn. Magn. Mat.*, 288:66, 2004.

Acknowledgement

With these pages, an important and exciting period of my life ends. I like to use this occasion to acknowledge many people and their help. Here, I can do this only with words but words actually cannot describe how grateful I am. Please consider the following lines as a small effort to express something really big.

Prof. Dr. Peter Böni for simply everything. You provided me the possibility to realize this work. I had your support all the time. You provided a lot of freedom to try new things but you also took care that I stayed focused in my work. I appreciate that I'm a PhD student of you.

Dr. Shah Valloppilly for the last years. You were always there for discussions. You were always pushing me to expand my knowledge and to make it better and better. Due to your big eagerness to try new experiments, I learned many things. We had also a beautiful time exchanging Indian and Bavarian habits. It was my pleasure to share the time with you.

Dr. Hans-Benjamin Braun for all the discussions about our experimental results, the explanations of theoretical models, the collaborations for our papers and the proof reading of my work. I appreciate that you spent a lot of your time in educating me in magnetism.

Barbara Russ for all your support. You maintained the instruments perfectly and supported me in many aspects of the daily work. I could always approach you in case of technical problems and I knew that I did not need to be patient since I could always count on your immediate help. In addition, you contributed a lot that I felt absolutely comfortable at E21.

Prof. Dr. Rudolf Gross, **Dr. Matthias Opel** and **Dr. Andreas Erb** for the measurements at your SQUID magnetometer and the test experiments at your X-ray diffractometer. You were extremely complaisant to get time for experiments. It was also a great pleasure for me that I could present our work in your seminar.

Michael Horisberger for your absolutely kind support in the preparation of the samples. You prepared the sputter system perfectly at any of our requests and allowed us an extensive use. Thank you for all the help, which I have received since the first day of our collaboration.

Dr. Thomas Gutberlet and **Dr. Mukul Gupta** for the many hours, day and night, which you spent for us doing the polarized neutron reflectivity experiments. As you find in this work, the results are invaluable for our studies.

At this point I like also to acknowledge that part of this work is based on experiments performed at the Swiss Spallation Neutron Source, Paul Scherrer Institute, Villigen,

Switzerland. Beamtime for experiments at AMOR has been obtained on the basis of accepted proposals for two periods of twelve days. The second period has been supported by the European Commission under the 6th Framework Programme through the Key Action: Strengthening the European Research Area, Research Infrastructures, Contract n°: RII3-CT-2003-505925.

Prof. Dr. Winfried Petry for many years at FRM-II. I hope, I could support your work with mine. It was always a pleasure to discuss with you since I could always be sure to have your support. Thank you also for the good advice to choose the current topic for my thesis.

Dr. Erich Steichele for many years of collaboration. Looking back, I can say that you have defined the way of my career beginning when I got to know neutron supermirrors and neutron guides from you. I have learned so many things from you. I really appreciate the work with you. Thank you a lot for that.

My colleagues at E21 - **Dr. Alex Mirmelstein**, **Dr. Evgeni Clementyev**, **Verena Kargl**, **Sylvia Jones**, **Nikolas Arend**, **Daniel Lamago**, **Sebastian Mühlbauer**, **Florian Grünauer** for being together with me at E21. From each of you I requested help occasionally and received it. Either scientific discussions or talking about many other things, I enjoyed always that I could share this with you in particular.

Dr. Burkhard Schillinger for the X-ray diffractometer. You found it and you spent your time to bring me to Dortmund to check its condition. Finally, it was transferred to E21 and the measurements provided the base for this work.

My colleagues at FRM-II - **Holger Bamberger**, **Ralph Lorenz**, **Alfred Urban**, **Dominik Hohl**, **Swato** and **Eberhard Kahle** for a long and wonderful time at FRM-II, before I started my thesis and during that. Your help was enormous making it possible that I could fulfill my duties there. Despite the hard work, it was always a pleasure for me to spend time with you having nice discussions about many aspects of life.

More colleagues at FRM-II - **Dr. Ralph Gilles**, **Dr. Jürgen Neuhaus**, **Dr. Karl Zeitelhack**, **Dr. Anton Kastenmüller** and **Dr. Robert Georgii** for many successful collaborations. I felt always well to work with you since I knew that I would receive your support and kindness.

Still more colleagues at FRM-II - **Christian Herzog** and his team in the mechanical workshop of FRM-II for being always approachable when I needed support. I could count on your help. I enjoyed the Weisswurst essen with you a lot.

Last but not least colleagues at FRM-II - Mr. **Stephan Lukatsch** and Mr. **Guido Engelke** for the explanations and suggestions about what to do in one's career. I understood from you to reach my goals.

Dr. Joel Mesot, **Dr. Jochen Stahn** and **Dr. Murat Ay** for the warm wel-

come at LNS/PSI. You took care of me right from the beginning, which helped me a lot to integrate and to feel comfortable at PSI, my new place.

The **SNAG-lers** for a good time since I'm in Switzerland and hopefully in the future as well.

Melanie Hobelsberger-Dalton for your effort to teach me some more English in 3h. I hope, I could include as much as possible in this work.

Meinen Eltern **Brigitte** und **Manfred Schanzer** für viele Jahre die Ihr Euch um mich gekümmert und in denen Ihr mich unterstützt habt. Ich konnte in der Vergangenheit nicht viel bei Euch sein, habe aber nie und werde auch nie vergessen, wo mein zu Hause ist. Weil ein besseres kann es nicht geben.

Meinem Bruder **Robert Schanzer** und seiner Frau **Kerstin**, dass Ihr so nett seid. Bleibt bitte so. Ich hatte immer Eure Hilfe und hoffe, dass ich in Zukunft davon was zurückgeben kann. Ich wünsche Euch, dass Ihr auch so ein schönes Leben habt wie ich es habe.

Meinen Freunden **Gerhard Nöbauer**, **Josef Frauendorfer** und **Martin Kummer**, dass Ihr meine Freunde seid, obwohl ich ganz wenig Zeit habe und Ihr mich trotzdem nicht vergesst. Ich wünsche mir, dass das auch in Zukunft so ist.

Meiner **Eva** - bisher fiel es mir schon schwer zu schreiben, was ich sagen will. An Dich ist es gar nicht möglich. Es gibt keine Worte dafür. Aber das macht auch nichts, denn ich möchte es lieber schaffen, dass es Dir so gut geht, wie es mir geht, weil ich bei Dir sein darf. Ich freue mich auf viel mehr Zeit mit Dir. bbb

To all of you

Live long and in prosper